

JSCSEN 72(8-9) 737–919 (2007)

UDC 54:66

ISSN 0352–5139

Journal of the Serbian Chemical Society

VOLUME 72

NO 8-9

BELGRADE 2007



ISSN 0352-5139

J. Serb. Chem. Soc. Vol. 72, No. 8-9 (2007)

CONTENTS

Organic Chemistry and Biochemistry

- V. Nikolić, Lj. Nikolić, M. Stanković, A. Kapor, M. Popsavin and D. Cvetković:* A Molecular inclusion complex of atenolol with 2-hydroxypropyl- β -cyclodextrin; the production and characterization thereof..... 737
- D. Andrić, G. Tovilović, G. Roglić, V. Šoškić, M. Tomić and S. Kostić-Rajačić:* 6-[2-(4-Arylpiperazin-1-yl)ethyl]-4-halo-1,3-dihydro-2*H*-benzimidazole-2-thiones: synthesis and pharmacological evaluation 747
- S. Ž. Grbavčić, S. I. Dimitrijević-Branković, D. I. Bezbradica, S. S. Šiler-Marinković and Z. D. Knežević:* Effect of fermentation conditions on lipase production by *Candida utilis*.... 757

Inorganic Chemistry

- D. Poleti, Lj. Karanović, A. Kremenović and J. Rogan:* Disorder of lattice solvent molecules in the structure of hexaaqua(μ_2 -1,2,4,5-benzenetetracarboxylato)-bis(*N,N'*-2,2'-dipyridylamine)dinickel(II) hexahydrate DMSO solvate (Short communication)..... 767

Electrochemistry

- B. M. Babić, B. V. Kaluđerović, Lj. M. Vračar, V. Radmilović and N. V. Krstajić:* Characterization of a surface modified carbon cryogel and a carbon supported Pt catalyst 773
- N. D. Nikolić:* The effects of a magnetic field on the morphologies of copper and nickel deposits: the concept of "effective overpotential" 787

Analytical Chemistry

- L. Pavun, D. Malešev and D. Veselinović:* Spectrophotometric investigation of the uranyl-phenyl-ephriane system 799
- B. F. Abramović, V. B. Anderluh, F. F. Gaal and D. V. Šojić:* Derivative spectrophotometric determination of the herbicides picloram and triclopyr in mixtures 809
- D. Đ. Stojanović, J. S. Milinović and S. D. Nikolić-Mandić:* Interferences from titanium and zirconium during calcium determination by flame spectrometry 821

Chemical Engineering

- E. Djordjević, S. Kabelac and S. Šerbanović:* Mean heat transfer coefficients during the evaporation of 1,1,1,2-tetrafluoroethane (R-134a) in a plate heat exchanger 833
- Lj. Takić, V. Veljković, M. Lazić and S. Pejanović:* Ozone absorption in a mechanically stirred reactor 847

Materials

- M. R. Vukić, D. S. Veselinović and V. G. Marković:* Crystalline forms of silver iodide II. Determination of phase transformations 857
- S. Belošević, R. Mladenović, D. Dakić, M. Paprika, A. Erić, D. Djurović, M. Komatina, B. Grbić and N. Radić:* Properties and efficiency of a Pt/Al₂O₃ catalyst applied in a solid fuel thermo-accumulating furnace..... 869

Environmental Chemistry

- R. Djurović, M. Marković and D. Marković:* Headspace solid phase micro-extraction in the analysis of pesticide residues – kinetics and quantification prior to the attainment of partition equilibrium 879
- A. M. Žujić, B. B. Radak and D. A. Marković:* The characteristics of the air pollution of a transition economy city: the example of Belgrade 889

Metallurgy

- D. Živković, I. Katayama, D. Manasijević, H. Yamashita and N. Štrbac:* Thermodynamics and phase diagram calculation of some sections in the Ag-Bi-Sn system 901
- M. M. Antonijević, G. D. Bogdanović, S. M. Šerbula and S. M. Milić:* Influence of grain size on chalcopyrite ore leaching in acidic medium 911

Published by the Serbian Chemical Society
Karnegijeva 4/III, 11120 Belgrade, Serbia
Printed by the Faculty of Technology and Metallurgy
Karnegijeva 4, P.O. Box 35-03, 11120 Belgrade, Serbia



A molecular inclusion complex of atenolol with 2-hydroxypropyl- β -cyclodextrin; the production and characterization thereof

VESNA NIKOLIĆ^{1*#}, LJUBIŠA NIKOLIĆ^{1#}, MIHAJLO STANKOVIĆ^{1#}, AGNEŠ KAPOR²,
MIRJANA POPSAVIN^{3#} and DRAGAN CVETKOVIĆ¹

¹Faculty of Technology, Bulevar oslobođenja 124, 16000 Leskovac, ²Faculty of Science, Department of Physics, Trg Dositeja Obradovića 4, 21000 Novi Sad and ³Faculty of Science, Department of Chemistry, Trg Dositeja Obradovića 3, 21000 Novi Sad, Serbia

(Received 28 August 2006, revised 21 March 2007)

Abstract: The molecular inclusion complex of atenolol with 2-hydroxypropyl- β -cyclodextrin was synthesized using the coprecipitation method. The complex obtained was characterized by FT-IR, ¹H-NMR, ¹³C-NMR spectroscopy, as well as by DSC and X-ray diffraction analysis. The DSC analysis confirmed the existence of the complex with the endothermic atenolol melting peak at about 155 °C disappearing. The X-ray diffraction patterns of the complex and 2-hydroxypropyl- β -cyclodextrin were very similar, thus confirming the complete inclusion of the atenolol molecule within the cavity of the 2-hydroxypropyl- β -cyclodextrin. The peaks originating from atenolol were completely absent in the diffractogram of the complex. ¹H-NMR and ¹³C-NMR spectra showed certain changes in the chemical shifts of protons and C atoms from atenolol and 2-hydroxypropyl- β -cyclodextrin, indicating that a complex had been formed and also which protons participated in the hydrogen bonds which formed the complex. The atenolol solubility in water was improved (254 mg complex cm⁻³, *i.e.*, 37.5 mg atenolol cm⁻³), and in pH 3 HCl solution (251 mg complex cm⁻³, *i.e.*, 37 mg atenolol cm⁻³) when compared to pure atenolol, and even when compared to the atenolol complex with β -cyclodextrin. The increased solubility ensures greater bioavailability of the active component and, due to the low solubility, significantly corrects for the lack of the basic active substance and, simultaneously, increases its overall therapeutic effect, combined with reduced side effects.

Keywords: atenolol, 2-hydroxypropyl- β -cyclodextrin, inclusion complex, FT-IR, DSC, NMR, X-ray.

INTRODUCTION

Cyclodextrins and their derivatives build canal inclusion compounds, so-called “molecular inclusion compounds”. In these compounds, a single molecule can receive a molecule of another compound into the cavity of its large ring (canal ca-

* Corresponding author. E-mail: nvesna@yahoo.com

Serbian Chemical Society member.

doi: 10.2298/JSC0709737N

vity diameter 0.5–0.9 nm). In crystalline state, some spirally wound molecules of cyclodextrin are placed one above the other, thus forming longer canal where molecules of various organic substances can be located, representing so-called molecular encapsulation.^{1–9} There are a number of examples of molecular inclusion complexes of cyclodextrins and their derivatives, especially with respect to various types of drugs.

Ammar gave a description of the formation of an ampicillin and β -cyclodextrin complex, which eliminates one of the drawbacks of ampicillin, *i.e.*, its tendency to polymerize when alone in an aqueous solution.¹⁰ With most drugs, their bioavailability, *i.e.*, the absorption of the remedial substance is low due to their poor solubility and, therefore, their application is limited. This is the case with some antibiotics, such as polymixin and tetracycline hydrochloride.^{11,12} By forming a complex of naproxen (a steroid anti-inflammatory agent with an analgesic effect) and β -cyclodextrin, the absorption of the former is increased and, thus, its bioavailability.¹³ Heptacain, a local anesthetic, has better activity when in a complex with β -cyclodextrin because of its improved physico-chemical properties, *i.e.*, solubility, dissolution rate and membrane permeability.¹⁴ The chemical and photochemical stabilities of retinol, meclozin hydrochloride and nicedipin are improved after formation of inclusion complexes with cyclodextrins.^{11,15,16} In order to form an inclusion complex, the diameter of the guest molecule must correspond to the diameter of the host molecule cavity.¹¹ Drugs from the β -blocker group are characterized by poor solubility in aqueous and gastric fluids and, therefore, the low solubility rate and the variability of their bioavailability directly affect the efficiency of the drug.¹⁷ Consequently, in order to increase the solubility and solubility rate, atenolol was complexed into an inclusion complex with β -cyclodextrin, whereby a better, but still not completely satisfactory, solubility of the complex was achieved.¹⁸ For the same reason, celiprolol, a well known β -blocker, was complexed with β -cyclodextrin and a correction of the solubility of this drug was achieved.¹⁷ An improved solubility of felodipine was achieved by complexing with β -cyclodextrin.¹⁹ Prazosin hydrochloride, an α_1 -adrenoceptor antagonist used in clinical practice for the treatment of hypertension, vascular sclerosis and cardiac arrest, also has the problem of poor solubility in water, which is very important for its activity. By complexing this drug with β -cyclodextrin and hydroxypropyl- β -cyclodextrin, these complexes obtained solubility superior to those of the non-complexed drug.²⁰

In a patent application, a method for the separation of racemic atenolol by a solid-liquid separation method is given. Moreover, another patent gives a description of the slow release of some drugs from the corresponding forms, including atenolol, carvedilol and hydrochlorothiazide.^{21,22} A further patent gives a description of the increased bioavailability of atenolol in connection with cholic acid, but there is no data on inclusion type complexes with β -cyclodextrin derivatives

with the purpose of increasing the solubility of this drug.²³ 2-Hydroxypropyl- β -cyclodextrin was chosen for complexing atenolol because it has a better solubility in water at room temperature than β -cyclodextrin.³

EXPERIMENTAL

Reagents

Atenolol (*RS*)-2-{-4-[2-hydroxy-3-(isopropylamino)propoxy]phenyl}acetamide is a racemic mixture of (*R*)-(+ and (*S*)-(–) stereoisomers of 99.43 % purity, purchased from Ipca Laboratories Limited, India, while 2-hydroxypropyl- β -cyclodextrin (average molecular weight 1540 g mol⁻¹) was obtained from Sigma–Aldrich, Wisconsin.

Preparation of the inclusion complex by co-precipitation

Atenolol (266 mg) and 2-hydroxypropyl- β -cyclodextrin (1540 mg) were mixed and dissolved in 150 cm³ of the water. The solution was stirred at room temperature for 24 h, evaporated using rotary evaporator at 50 °C to a volume of approximately 20 cm³, and then dried in a desiccator above concentrated sulfuric acid at 25 °C.

Preparation of a physical mixture

A homogenous physical mixture was prepared by mixing atenolol and 2-hydroxypropyl- β -cyclodextrin in a 1:1 molar ratio in a mortar.

X-Ray crystallography

X-Ray diffraction analysis was performed on a Phillips X'Pert powder diffractometer under the following conditions: the samples were exposed to monochromatic CuK α radiation and analyzed in the 2θ range between 5 and 65° with a step of 0.05° and the recording time $\tau = 5$ s. The voltage and the strength of the electric current were 40 kV and 20 mA, respectively.

¹H-NMR and ¹³C-NMR spectroscopy

The ¹H-NMR and ¹³C-NMR spectra of the samples were recorded in a 5 mm diameter glass cuvette at room temperature on a Bruker AC 250 E NMR spectrometer, operating at frequencies of 250 and 62.5 MHz, respectively, by the pulse method and with multiple pulse repetitions. D₂O was used as the solvent.

Differential scanning calorimetry (DSC)

DSC Curves of the samples were recorded on a DuPont DSC differential scanning calorimeter in the temperature range 30–280 °C at a scanning rate of 10 °C min⁻¹. The measurements were performed on 5 mg of the sample in closed aluminum containers under a nitrogen atmosphere.

Fourier transformation infrared (FTIR) spectroscopy

The FTIR spectra of the samples were recorded in KBr pellets (0.6 mg sample, 140 mg KBr) in the wavenumber range 4000–400 cm⁻¹, on a Bomem Hartmann & Braun MB-series FTIR spectrophotometer.

RESULTS AND DISCUSSION

X-Ray crystallography

The diffractograms of atenolol (A), 2-hydroxypropyl- β -cyclodextrin (B), the molecular inclusion complex of 2-hydroxypropyl- β -cyclodextrin and atenolol (C), and the physical mixture (D) are shown in Fig. 1. A comparative analysis of these diffractograms shows that the diffractogram of the complex (C) is almost identical to that of 2-hydroxypropyl- β -cyclodextrin (B), confirming the hypothe-

sis that the atenolol molecule was included into the cavity of 2-hydroxypropyl- β -cyclodextrin, which shielded it completely from the X-rays. On the other hand, the commercially available, high purity (99.46 %) atenolol sample had a high degree of crystallinity, as evidenced by the very articulated peaks in its diffractogram. The diffractogram of 2-hydroxypropyl- β -cyclodextrin indicates the existence of two wide diffraction peaks in the range of about $2\theta = 10.516^\circ$ to $2\theta = 18.882^\circ$, which are not structured and show the existence of a disorganized crystal structure at great distances. The diffractogram of the physical mixture (D) confirms by the presence of the peaks of both components of the mixture that this really was a mixture of atenolol and 2-hydroxypropyl- β -cyclodextrin; the peaks arising from atenolol were absent in the diffractogram of the complex. The X-ray diffraction pattern of the complex confirms that atenolol is complexed as a molecular inclusion into the crystalline grid of the matrix, 2-hydroxypropyl- β -cyclodextrin.

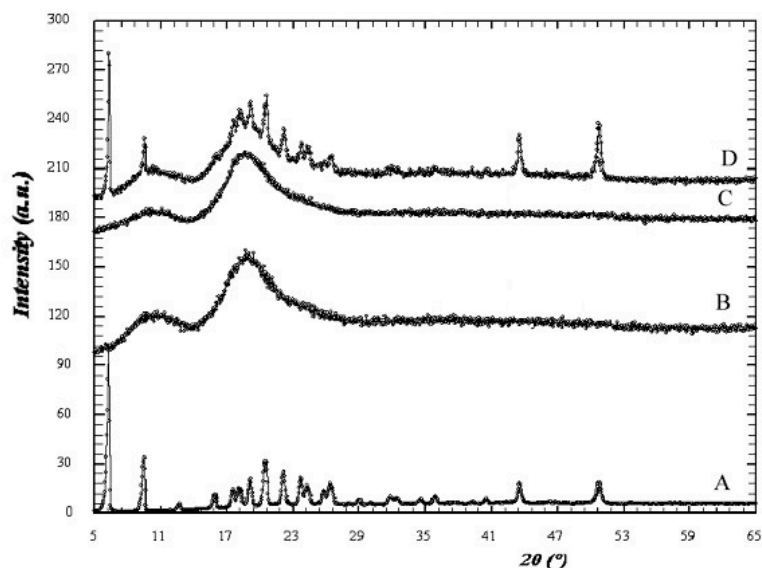


Fig. 1. X-ray diffractograms of atenolol (A), 2-hydroxypropyl- β -cyclodextrin (B), the inclusion complex of atenolol and 2-hydroxypropyl- β -cyclodextrin (C) and a mixture of atenolol and 2-hydroxypropyl- β -cyclodextrin (D).

NMR analysis

The $^1\text{H-NMR}$ analysis shows the occurrence of the molecular encapsulation of atenolol into the hydrophobic cavity of 2-hydroxypropyl- β -cyclodextrin because the spectra of the basic components are different from those of the molecular inclusion complex. The labeling of the C atoms in atenolol and 2-hydroxypropyl- β -cyclodextrin where the protons are situated is shown in Figs. 2 and 3 and the chemical shifts, as well as the changes in proton chemical shifts in the complex with respect to the pure components, are shown in Table I.

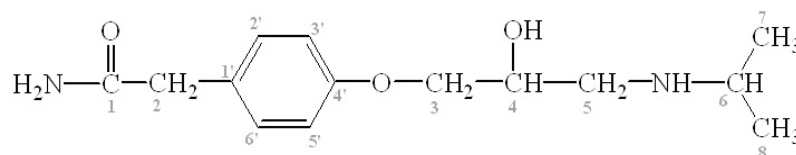
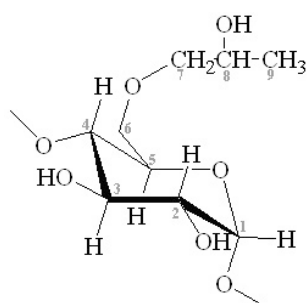


Fig. 2. Labeling of the C atoms in an atenolol molecule.

Fig. 3. Labeling of the C-atoms in the hydroxypropylglucose unit of a 2-hydroxypropyl- β -cyclodextrin molecule.TABLE I. Chemical shifts (δ) and changes of proton chemical shifts ($\Delta\delta$) in the $^1\text{H-NMR}$ spectra of atenolol, 2-hydroxypropyl- β -cyclodextrin, and the complex of atenolol with 2-hydroxypropyl- β -cyclodextrin

C atom	δ / ppm		$\Delta\delta$ / ppm
	Atenolol	Complex	
2	3.500 <i>s</i>	3.852 <i>s</i>	+0.352
3 and 4	4.000 <i>m</i>	4.200 <i>m</i>	+0.200
5 and 6	2.750 <i>m</i>	2.963 <i>m</i>	+0.213
7 and 8	1.017 <i>d</i>	1.179 <i>d</i>	+0.162
2' and 6'	6.958 <i>d</i>	7.037 <i>d</i>	+0.079
3' and 5'	7.208 <i>d</i>	7.296 <i>d</i>	+0.088
2-Hydroxypropyl- β -cyclodextrin		Complex	
1	5.137 <i>d</i>	5.200 <i>d</i>	+0.063
2 to 8	3.731 <i>m</i>	3.852 <i>m</i>	+0.121
9	1.108 <i>d</i>	1.179 <i>d</i>	+0.071

On the basis of these results it can be concluded that the protons from atenolol on the 2, 3, 4, 5, and 6 C atom had the greatest shifts ($\Delta\delta$ from 0.352 to 0.200) in the complex, which means that they participated to a great extent in the interaction with 2-hydroxypropyl- β -cyclodextrin. The other protons from atenolol also showed shifts, but they were slightly less in magnitude. The greatest proton shifts in 2-hydroxypropyl- β -cyclodextrin in the complex relative to the uncomplexed compound occurred at the H atoms bonded to carbons C₂ to C₈, while the shifts of those bonded to C₁ and C₉ were slight.

This analysis indicates an inclusion type of complexing between atenolol and 2-hydroxypropyl- β -cyclodextrin, in which hydrogen bonds, apart from physical factors, play an important role in the guest–host interactions.

The analysis of the ^{13}C -NMR results, also indicating the inclusion of the guest into the host cavity, show that the greatest chemical shifts after complexing occurred at the C₁, C₄, C₅, C₇, and C₈ atoms in atenolol, while in 2-hydroxypropyl- β -cyclodextrin, the greatest shifts were found at the C₁, C₄, and C₅ atoms. The differences in chemical shifts for each C atom in atenolol and in 2-hydroxypropyl- β -cyclodextrin with respect to the molecular inclusion complex are shown in Table II.

TABLE II. Chemical shifts and variations of the chemical shifts of the C-atoms in ^{13}C -NMR spectra of atenolol, 2-hydroxypropyl- β -cyclodextrin and the complex of atenolol with 2-hydroxypropyl- β -cyclodextrin

C-atom	δ / ppm		$\Delta\delta$ / ppm	δ / ppm		$\Delta\delta$ / ppm
	Atenolol	Complex		2-Hydroxypropyl- β -cyclodextrin	Complex	
1	180.818	179.912	-0.906	102.933	103.361	+0.428
2	43.585	43.897	+0.312	74.506	74.383	-0.123
3	73.312	73.405	+0.093	75.629	75.806	+0.177
4	71.342	70.660	-0.682	83.212	83.622	+0.410
5	51.011	51.526	+0.515	74.787	75.058	+0.271
6	50.922	51.030	+0.108	63.113	62.994	-0.119
7 and 8	23.844	23.420	-0.424	-	-	-
1'	130.521	130.762	+0.241	-	-	-
2' and 6'	117.883	117.651	-0.232	-	-	-
3' and 5'	133.285	133.079	-0.206	-	-	-
4'	160.143	160.308	+0.165	-	-	-
7	-	-	-	79.497	80.861	+1.364
8	-	-	-	69.219	69.224	+0.005
9	-	-	-	20.919	20.941	+0.022

DSC analysis

The DSC curves of atenolol (A), 2-hydroxypropyl- β -cyclodextrin (B), a mixture of atenolol and 2-hydroxypropyl- β -cyclodextrin (C), and the complex of atenolol and 2-hydroxypropyl- β -cyclodextrin (D) are shown in Fig. 4. A comparative analysis of the DSC curves also confirms the inclusion of the guest molecule into the cavity of the host. The DSC curve of the inclusion complex has no endothermic melting peak of racemic atenolol at about 155 °C, which is, on the other hand, present in the curve of atenolol and of the mixture of atenolol and 2-hydroxypropyl- β -cyclodextrin.

Infrared spectroscopy

By comparing IR spectrum of the inclusion complex of 2-hydroxypropyl- β -cyclodextrin and atenolol to those of the pure substances and the physical mixture, it can be concluded that there are no variations in the spectrum of the physical

mixture with respect to the spectra of the pure components, but that there are variations in the IR spectrum of the complex (Fig. 5). Namely, pure atenolol has a strong band at 1638 cm^{-1} , originating from C=O valence vibrations (amide band I), which, in the inclusion complex, has a significantly lower intensity and occurs at 1668 cm^{-1} , which results from this vibration being covered due to the inclusion of atenolol into the cavity of 2-hydroxypropyl- β -cyclodextrin. For the same reason, the band at 3180 cm^{-1} , originating from the NH valence vibrations, present in the spectrum of atenolol is absent in spectrum of the complex, as is the amide band III, originating from the C-N valence vibration coupled with NH bending vibrations, which is present in the spectrum of atenolol at 1417 cm^{-1} . Also, the band at 1516 cm^{-1} , originating from C=C valence vibrations of the aromatic part of the atenolol system, does not appear in the IR spectrum of the complex. This analysis is in accordance with the results of the previous methods used to analyze the complex and it confirms the realization of the inclusion of the atenolol molecule into the hydrophobic cavity of the host molecule, 2-hydroxypropyl- β -cyclodextrin, *i.e.*, the formation of the molecular inclusion complex.

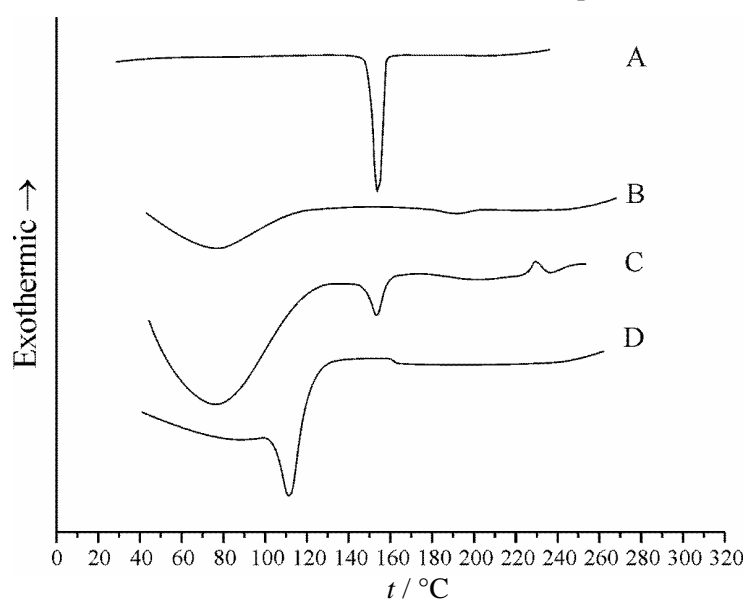


Fig. 4. DSC curves of atenolol (A), 2-hydroxypropyl- β -cyclodextrin (B), a mixture of atenolol and 2-hydroxypropyl- β -cyclodextrin (C), and the inclusion complex of atenolol with 2-hydroxypropyl- β -cyclodextrin (D).

Dissolution study

The room temperature solubility of pure atenolol in water is 0.3 mg cm^{-3} .²⁴ On complexing it with 2-hydroxypropyl- β -cyclodextrin, its solubility is increased to $254\text{ mg complex cm}^{-3}$, *i.e.*, to $37.5\text{ mg atenolol cm}^{-3}$, in water and 251 mg com-

plex cm^{-3} , *i.e.*, 37 mg atenolol cm^{-3} in a pH 3 solution of HCl. In this way, the bioavailability of the drug to the organism can be increased and the effect of the therapy can be achieved by administration a lower quantity of the substance.

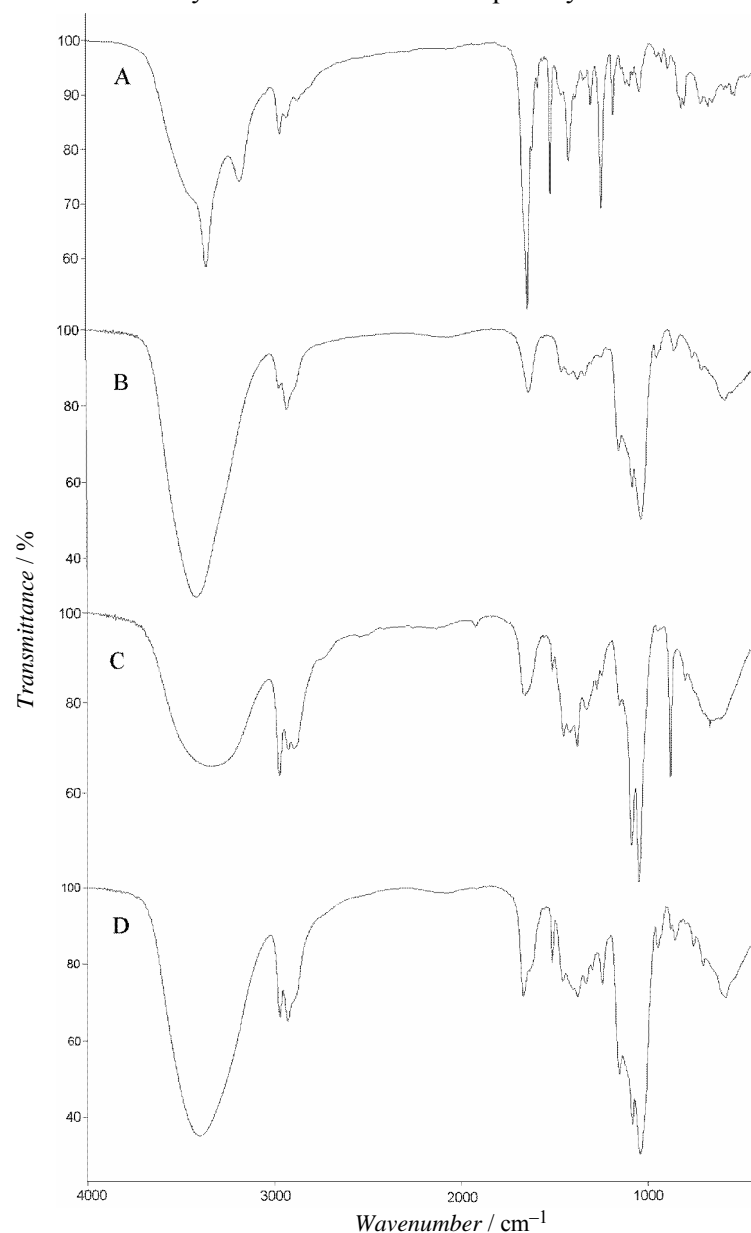


Fig. 5. FT-IR Spectra of atenolol (A), 2-hydroxypropyl- β -cyclodextrin (B), a mixture of atenolol and 2-hydroxypropyl- β -cyclodextrin (C), and the inclusion complex of atenolol and 2-hydroxypropyl- β -cyclodextrin (D).

CONCLUSIONS

From the point of view of pharmacologically active formulations with basic components of varied physical properties, inclusion complexes are of interest. In such supramolecular structures the active substance, in this case atenolol, which will have excellent solubility in this form, can be incorporated in an exact quantity, thus ensuring better bioavailability and functional value in medicine.

Compared to free atenolol of hard consistency and with poor solubility in water and, consequently, low bioavailability, the molecular inclusion complexes of atenolol with cyclodextrin derivatives are also solid, powdery substances containing the active substance in a form giving them manifold solubility, and consequently, better bioavailability and efficiency.

Acknowledgements: This paper was supported by the Ministry of Science of the Republic of Serbia through the project TR-6708B.

ИЗВОД

МОЛЕКУЛСКИ ИНКЛУЗОНИ КОМПЛЕКС АТЕНОЛОЛА СА 2-ХИДРОКСИПРОПИЛ- β -ЦИКЛОДЕКСТРИНОМ; ПОСТУПАК ДОБИЈАЊА И КАРАКТЕРИЗАЦИЈА

ВЕСНА НИКОЛИЋ¹, ЉУБИША НИКОЛИЋ¹, МИХАЛЛО СТАНКОВИЋ¹, АГНЕШ КАПОР²,
МИРЈАНА ПОПСАВИН³ и ДРАГАН ЦВЕТКОВИЋ¹

¹Технолошки факултет, Булевар Ослобођења 124, Лесковац, ²Природно-математички факултет, Делатман за физику, Трз Досијеја Обрадовића 4, Нови Сад и ³Природно-математички факултет, Делатман за хемију, Трз Досијеја Обрадовића 3, Нови Сад

Молекулски инклузиони комплекс атенолола са 2-хидроксипропил- β -циклодекстрином синтетисан је методом копреципитације. Добијени комплекс је окарактерисан методама FT-IR, DSC, ¹H-NMR, ¹³C-NMR и дифракцијом X-зрака. DSC анализа је потврдила постојање комплекса у коме нестаје ендотермни пик од топлења атенолола на око 155 °C. Дифрактограми комплекса и 2-хидроксипропил- β -циклодекстрина су веома слични чиме је потврђена потпуна заклоњеност молекула атенолола унутар шупљине 2-хидроксипропил- β -циклодекстрина. Пикови који потичу од атенолола на дифрактограму комплекса у потпуности нестају. ¹H-NMR и ¹³C-NMR спектри су показали извесне промене у хемијским померањима протона и C атома из атенолола и 2-хидроксипропил- β -циклодекстрина, што такође указује на стварање комплекса, као и на то који протони учествују у стварању водоничних веза којима је формиран комплекс. Постигнута је побољшана растворљивост комплексираниог атенолола у води (254 mg комплекса cm⁻³, тј. 37,5 mg атенолола cm⁻³) и у раствору HCl, pH 3 (251 mg комплекса cm⁻³, тј. 37 mg атенолола cm⁻³) у односу на чист атенолол, па чак и у односу на атенолол који је комплексирани β -циклодекстрином. Повећана растворљивост обезбеђује и већу биорасположивост активне компоненте и значајно коригује недостатак основне активне супстанце услед слабе растворљивости повећавајући њен укупни терапеутски учинак са смањеним споредним појавама.

(Примљено 28. августа 2006, ревидирано 21. марта 2007)

REFERENCES

1. A. R. Hedges, *Chem. Rev.* **98** (1998) 2035
2. V. T. Karathanos, I. Mourtzinou, K. Yannakopoulou, N. K. Andrikopoulos, *Food Chem.* **101** (2007) 652
3. H. J. Schneider, F. Hacket, V. Rudiger, *Chem. Rev.* **98** (1998) 1755

4. J. Szejtli, *Chem. Rev.* **98** (1998) 1743
5. M. Morgan Conn, J. Rebek, Jr., *Chem. Rev.* **97** (1997) 1647
6. P. Wallimann, T. Marti, A. Furer, F. Diederich, *Chem. Rev.* **97** (1997) 1567
7. K. Uekama, F. Hirayama, T. Irie, *Chem. Rev.* **98** (1998) 2045
8. F. Hapiot, S. Tilloy, E. Monflier, *Chem. Rev.* **106** (2006) 767
9. A. R. Khan, P. Forgo, K. J. Stine, V. T. D'Souza, *Chem. Rev.* **98** (1998) 1977
10. H. O. Ammar, S. A. El-Nahas, M. M. Ghorab, *Pharmazie* **51** (1996) 568
11. A. Angelova, C. R. Lefebvre, A. Baszkin, *J. Colloid Interface Sci.* **212** (1999) 275
12. S. T. Stankov, N. Lambov, E. Minkov, *Pharmazie* **47** (1992) 125
13. N. Celebi, M. Iscanoglu, T. Degim, *Pharmazie* **46** (1991) 863
14. K. Kralova, J. Cizmarik, J. Szejtli, *Pharmazie* **47** (1992) 460
15. M. Beričević, R. Senjković, *Pharmazie* **47** (1992) 202
16. J. Mielcarek, *Pharmazie* **51** (1996) 477
17. R. Ficarra, P. Ficarra, M. R. Di Bella, D. Raneri, S. Tommasini, M. L. Calabro, M. C. Gamberini, C. Rustichelli, *J. Pharm. Biomed. Anal.* **23** (2000) 33
18. R. Ficarra, P. Ficarra, M. R. Di Bella, D. Raneri, S. Tommasini, M. L. Calabro, A. Villari, S. Coppolino, *J. Pharm. Biomed. Anal.* **23** (2000) 231
19. J. Mielcarek, *J. Inclusion Phenom. Mol. Recognit. Chem.* **30** (1998) 243
20. L. Liu, S. Zhu, *J. Pharm. Biomed. Anal.* **40** (2006) 122
21. T. Yoshikazu, S. Nobuaki, K. Kazuhiro, EP 0 605 384 A1 (1994)
22. Z. Shuyi, W. Jin, WO 2005/030201 (2003)
23. P. James, C. Andrew, M. Dean, L. Kimberley, WO 2001/076531 (2001)
24. M. Moneghini, A. Carcano, G. Zingone, B. Perissutti, *Intern. J. Pharmaceutics* **175** (1998) 177.



6-[2-(4-Arylpiperazin-1-yl)ethyl]-4-halo-1,3-dihydro-2H-benzimidazole-2-thiones: synthesis and pharmacological evaluation

DEANA ANDRIĆ^{1*#}, GORDANA TOVILOVIĆ², GORAN ROGLIĆ^{1#}, VUKIĆ ŠOŠKIĆ^{3,4#},
MIRKO TOMIĆ² and SLAĐANA KOSTIĆ-RAJAČIĆ³

¹Faculty of Chemistry, University of Belgrade, Studentski trg 16, 11000 Belgrade, ²Department of Biochemistry, Institute for Biological Research, Bulevar Despota Stefana 142, 11060 Belgrade, ³Center for Chemistry, Institute for Chemistry, Technology and Metallurgy, Njegoševa 12, 11000 Belgrade; Serbia and ⁴Proteosys AG, Carl-Zeiss-Str. 51, 55129 Mainz, Germany

(Received 30 June 2006, revised 20 February 2007)

Abstract: Eight new compounds with halogen atom introduced into the benzimidazole-2-thione dopaminergic pharmacophore of 5-[2-(4-arylpiperazin-1-yl)ethyl]-1,3-dihydro-2H-benzimidazole-2-thiones with the arylpiperazine part of the molecule being selected according to known structure–affinity requirements, have been synthesized. All the new compounds were evaluated for the *in vitro* binding affinity at the dopamine (DA) D₁ and D₂ and serotonin 5-HT_{1A} receptors by the competitive radioassays, performed on synaptosomal membranes prepared from fresh bovine caudate nuclei and hippocampi. All the new compounds were strong competitors for the binding of the radioligands to the D₂ and 5-HT_{1A} receptors, with the most active of them having 34 and 170 time higher affinity than non-halogenated congeners in the D₂ DA receptor radioassays (compounds **9.1b** and **9.2b**, respectively). Divergently, these compounds were without significant affinities for the D₁ DA receptors.

Keywords: arylpiperazines, benzimidazole-2-thiones, dopamine receptors, serotonin receptors.

INTRODUCTION

For many years, the D₂ dopamine receptor (DAR) was a major target for neurobiological research and drug development, since DA antagonists have been proven to be efficient antipsychotics.¹ Since a great number of these compounds expressed undesirable side effects,^{2,3} the need for new drugs is increasing. It took nearly four decades to make a breakthrough in this field of effort. These second-generation derivatives, named as atypical antipsychotics, combined D₂ and 5-HT₂ antagonism.⁴ Newer atypical agents (*i.e.*, aripiprazole, bifeprunox, Fig. 1) differ

* Corresponding author. E-mail: deanad@chem.bg.ac.yu

Serbian Chemical Society member.

doi: 10.2298/JSC0709747A

in that they act as partial agonists at D₂ and 5HT_{1A} receptors, although they also interact with an array of other CNS targets.⁵ Such therapeutic strategy features the stabilization of dopamine function, instead of the inhibition of D₂ transmission caused by previous antipsychotic drugs.^{5,6}

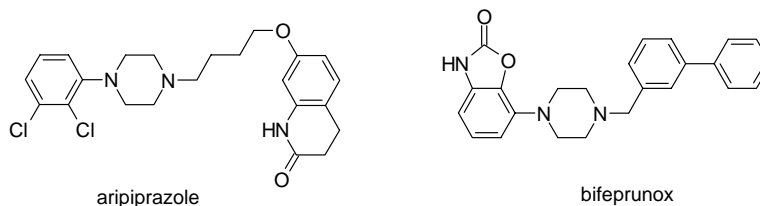


Fig. 1. Structures of aripiprazole and bifeprunox, atypical antipsychotics.

The work described herein presents the preparation of halogen derivatives of arylpiperazine-benzimidazole-2-thiones, ligands with mixed D₂/5-HT_{1A} activity. Arylpiperazines are a common structural motif included in various compounds for diverse pharmacological applications.⁷ Certain groups of arylpiperazines express ligand property at the specific G-protein coupled receptors (GPCRs).^{8,9} On the other hand, benzimidazole and their 2-substituted analogues possess a catechol moiety of biogenic catecholamine and are considered to be bioisosteres. Molecular modeling studies revealed that they both fit well into the binding pocket of D₂ DAR.^{10,11} The interactions of 5-{2-[4-(2-methoxyphenyl)piperazin-1-yl]ethyl}-1*H*-benzimidazole (presented in Fig. 2) are realized at first by the salt bridge between protonated N1 of the piperazine ring with Asp86 in the binding pocket, and a mixture of hydrogen bonds, electronic and bulk interaction, which are all largely affected by the electrostatic surface potential (electron density distribution; ESP) in benzimidazole ring.

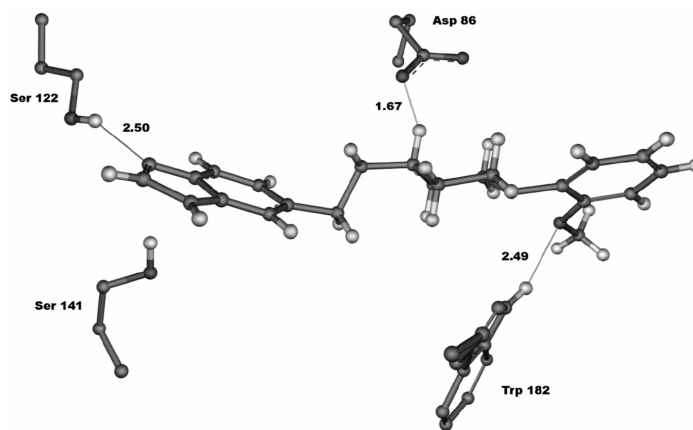


Fig. 2. Schematic representation of 5-{2-[4-(2-methoxyphenyl)piperazin-1-yl]ethyl}-1*H*-benzimidazole interaction with key amino acids in the binding site of the D₂ dopamine receptor.

In addition, ESP is influenced by the nature of substituents on the heterocyclic ring. This fact inspired us to insert halogen substituents into the benzimidazole pharmacophore, with the expectation that a mayor ESP perturbation will be achieved due to their large electron withdrawal effect. In recent publications, it was shown that high affinity D₂ DA/5HT_{1A} receptors ligands can be obtained by linking arylpiperazine and 2-substituted benzimidazole structural moieties through flexible linker.^{10,12,13} The effect of various substituents on the stabilization of the ligand–D₂ complex through hydrogen bond formation, edge-to-face interactions and steric interactions with amino acid residues in the binding pocket of D₂ DAR receptors was investigated.¹⁰

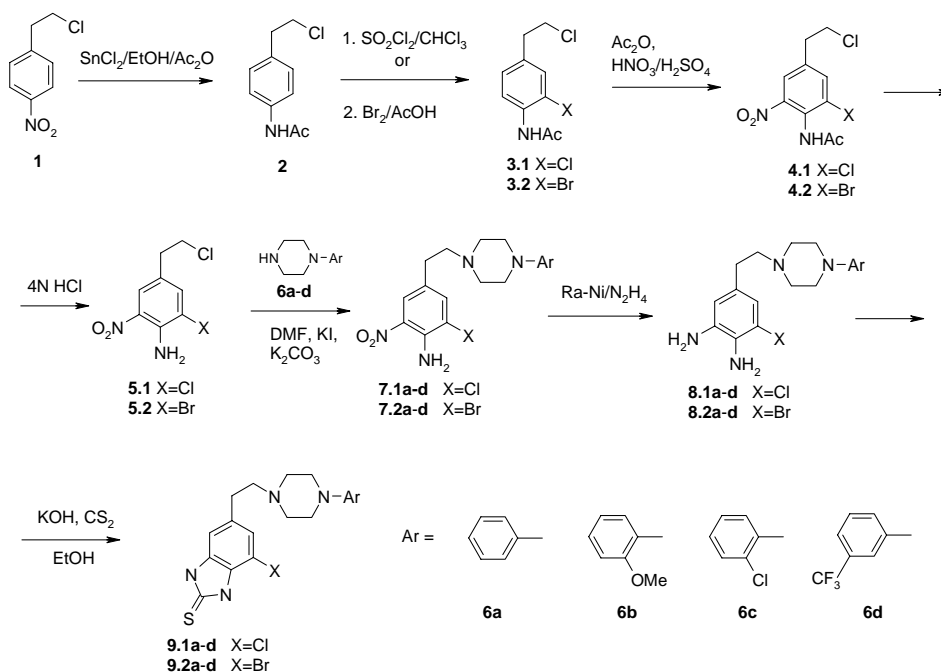
In this paper, the preparation of halogenated analogues together with their *in vitro* binding potencies at the D₁ and D₂ DAR and 5HT_{1A} receptors are presented. The effects of ligand halogenation on their dopaminergic/serotonergic activity are discussed.

RESULTS AND DISCUSSION

Eight new ligands, clasified as benzimidazole-2-thiones (compounds **9.1a–d** – **9.2a–d**), were synthesized (as shown in Scheme 1). Shortly, compound **1** was reduced with stannous chloride in absolute ethanol¹⁴ and the resulting amine was acylated without purification with acetanhydride to produce acetamide **2**. Compound **2** was converted either into corresponding halo-acetamides **3.1** or **3.2** using sulfuryl chloride¹⁵ or bromine in acetic acid, respectively. Nitration of halo-acetamides **3.1** and **3.2** in acetanhydride with 100 % nitric acid/sulfuric acid afforded the corresponding compounds **4.1** and **4.2**. After hydrolysis of acetamido group in 4 N HCl, the resulting products **5.1** and **5.2** readily alkylated aryl-piperazines in the presence of potassium carbonate and potassium iodide in dimethylformamide. The obtained arylpiperazines **7.1a–d** – **7.2a–d** were reduced with Ra-Ni/hydrazine¹⁶ to produce corresponding diamines **8.1a–d** – **8.2a–d**. Benzimidazole-2-thiones **9.1a–d** – **9.2a–d** used as target ligands, were prepared by refluxing the diamines **8.1a–d** – **8.2a–d** with carbon disulfide and KOH in ethanol.¹⁷

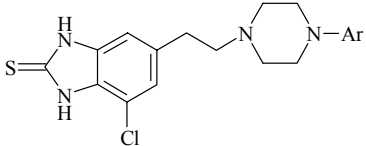
The affinities (K_i values, Table I) of the compounds towards DA (D₁ and D₂) and 5-HT (5-HT_{1A}) receptors were evaluated by *in vitro* binding assays. While none of the tested compounds were active displacers of [³H]SCH 23390 at the D₁ DAR, they all showed significant affinities at the D₂ and 5-HT_{1A} receptors. Generally, all the newly synthesized compounds are stronger ligands at the D₂ receptors than the corresponding parent compounds **9a–d**. The most active of them (compounds **9.1b** and **9.2b**) have affinities in the low picomolar range and belong to the category of the most active hitherto described dopaminergic ligands. The phenyl derivatives (**9.1a** and **9.2a**) as well as the 2-chlorophenyl (**9.1c** and **9.2c**) and 3-(trifluoromethyl)phenyl derivative **9.1d** expressed affinity for binding at 5-HT_{1A} receptors similar to the affinities of the parent compounds. The 2-methoxy-

phenyl derivative **9.1b** was the strongest competitor in the [³H]8-OH-DPAT binding assay too. The fact that the 3-(trifluoromethyl)phenyl ligand **9.1d** possesses greater affinity for the 5-HT_{1A} than for the D₂ receptors was exceedingly manifested as a tendency in the case of the bromo derivative **9.2d**, which was the most selective 5-HT_{1A} ligand.

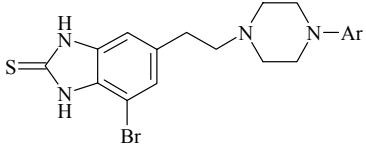


Scheme 1. Pathways for the synthesis of the ligands.

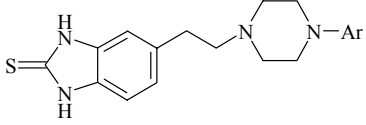
Taken together, these data confirm our previous observation that the affinity of the ligand for D₂ DA receptors depends both on the ESP of the benzimidazole pharmacophore¹¹ and on the choice of 1-arylpiperazine aryl groups. A positive ESP in the benzimidazole ring, induced by halogens and hydrogen bond acceptor groups (*e.g.* methoxy group) in the *ortho* position of 1-arylpiperazines, stabilizes the ligand–D₂ receptor complex.^{10,18} These two factors additively contributed to the high affinity towards D₂ DA receptors in the compounds **9.1b** and **9.2b**. The influence on the affinity towards 5-HT_{1A} receptors by the introduction of halogens into the benzimidazole pharmacophore of these ligands is diminished because the complete structure of the arylpiperazine part plays a predominant role. In conclusion, the here-presented fulfillment of the structural requirements for the DA and 5-HT ligand binding potency led to the expected rise of the affinity and selectivity for the tested compounds. Therefore, it seems that the binding characteristic of this kind of ligand can be predicted.

TABLE I. Chemical structure and K_i values* of the ligands


No	Ar	Formula	M.p. / °C	D ₁ K_i / nM	D ₂ K_i / nM	5HT _{1A} K_i / nM
9.1a	Ph	C ₁₉ H ₂₁ ClN ₄ S	247	>1000	4.9±1.1	12.9±2.2
9.1b	2-MeOPh	C ₂₀ H ₂₃ ClN ₄ OS	246	>1000	0.054±0.003	0.36±0.04
9.1c	2-ClPh	C ₁₉ H ₂₀ Cl ₂ N ₄ S	257	>1000	11.9±2.4	36.1±1.3
9.1d	3-CF ₃ Ph	C ₂₀ H ₂₀ ClF ₃ N ₄ S	239	>1000	44.8±3.0	15.2±2.1



No	Ar	Formula	M.p. / °C	D ₁ K_i / nM	D ₂ K_i / nM	5HT _{1A} K_i / nM
9.2a	Ph	C ₁₉ H ₂₁ BrN ₄ S	259	>1000	6.3±3.1	19.1±3.3
9.2b	2-MeOPh	C ₂₀ H ₂₃ BrN ₄ OS	236	>1000	0.01±0.005	1.7±0.2
9.2c	2-ClPh	C ₁₉ H ₂₀ BrClN ₄ S	254	>1000	7.1±1.5	76.5±5.7
9.2d	3-CF ₃ Ph	C ₂₀ H ₂₀ BrF ₃ N ₄ S	248	>1000	72.5±6.2	1.7±0.8



No	Ar	Formula	M.p. / °C	D ₁ K_i / nM	D ₂ K_i / nM	5HT _{1A} K_i / nM
9a	Ph	C ₁₉ H ₂₂ N ₄ S	238	>1000	15.2±2.0	13.4±2.8
9b	2-MeOPh	C ₂₀ H ₂₄ N ₄ OS	250	ND	1.7±0.4	2.9±1.1
9c	2-ClPh	C ₁₉ H ₂₁ N ₄ SCl	236	ND	20.7±2.2	80.1±8.4
9d	3-CF ₃ Ph	C ₂₀ H ₂₁ N ₄ SF ₃	265	>1000	134.0±15	10.7±3.2

*Values are the means ± S.E.M. of 3–4 independent experiments done in triplicate, performed at eight competing ligand concentrations (10⁻⁵–10⁻⁹ M) and [³H]SCH 23390 (D₁), [³H]spiperone (D₂) and [³H]8-OH-DPAT (5HT_{1A}).

EXPERIMENTAL

General

A Boetius PHMK apparatus (VEB Analytic, Dresden, Germany) was used to determine melting points, presented here as uncorrected. ¹H-NMR (at 200 MHz) and ¹³C-NMR (at 50 MHz) spectra were recorded on a Gemini 2000 spectrometer (Varian, Palo Alto, CA, USA) with CDCl₃ as a solvent, unless otherwise stated, are reported in ppm using tetramethylsilane as the internal standard. The IR spectra were run on a Perkin Elmer 457 Grating FT Infrared Spectrophotometer (Perkin Elmer, Beaconsfield, UK). The mass spectra were determined by a Finnigan Mat 8230 mass spe-

ctrometer (Finnigan, Bremen, Germany). For analytical thin-layer chromatography Merck (Darmstadt, Germany) F-256 plastic-backed thin-layer silica gel plates were used. Chromatographic purifications were performed on Merck-60 silica gel columns, 230–400 mesh ASTM, under medium pressure (dry column flash chromatography). All reagents and solvents used in this work were obtained from Aldrich and were used without further purification. Solutions were routinely dried over anhydrous Na₂SO₄ prior to evaporation.

Chemistry

4-(2-Chloroethyl)-2-Halo-6-nitrophenylamines (**5.1** and **5.2**), 1,3-dihydro-5-[2-(4-phenylpiperazin-1-yl)ethyl]-2H-benzimidazole-2-thione **9a** and 5-[2-(4-aryl)piperazin-1-yl]ethyl]-1,3-dihydro-2H-benzimidazole-2-thiones (**9b–c**) were prepared as previously described.^{11,19,20}

General procedure for the synthesis of 4-[2-(4-aryl)piperazin-1-yl]ethyl]2-halo-6-nitro-anilines

7.1a–d – 7.2a–d

To a solution of 10.0 mmol of either arylpiperazine in 50.0 ml DMF, 12.0 mmol of 4-(2-chloroethyl)-2-halo-nitroaniline (**5.1** or **5.2**), 6.0 g K₂CO₃ and 0.1 g of KI were added. The mixture was stirred at 80 °C for 12 h. After cooling, the precipitate was removed and the filtrate was evaporated *in vacuo*. The residue was dissolved in CH₂Cl₂ and obtained products purified by MPLC using CH₂Cl₂ as the eluent.

2-Chloro-6-nitro-4-[2-(4-phenylpiperazin-1-yl)ethyl]aniline (7.1a): Yield: 69 %; m.p. 104 °C; ¹H NMR: δ 2.57–2.80 (*m*, 8H), 3.20–3.25 (*m*, 4H), 6.45 (*s*, 2H, NH₂), 6.87–6.97 (*m*, 3H, ArH), 7.22–7.32 (*m*, 2H, ArH), 7.45 (*d*, 1H, *J* = 2.2 Hz, ArH), 7.97 (*d*, 1H, *J* = 2 Hz, ArH).

2-Bromo-6-nitro-4-[2-(4-phenylpiperazin-1-yl)ethyl]aniline (7.2a): Yield: 72 %; m.p. 110 °C; ¹H NMR: δ 2.57–2.80 (*m*, 8H), 3.20–3.25 (*m*, 4H), 6.51 (*s*, 2H, NH₂), 6.83–6.96 (*m*, 3H, ArH), 7.24–7.32 (*m*, 2H, ArH), 7.62 (*d*, 1H, *J* = 2 Hz, ArH), 8.01 (*d*, 1H, *J* = 2 Hz, ArH).

2-Chloro-4-[2-[4-(2-methoxyphenyl)piperazin-1-yl]ethyl]-6-nitroaniline (7.1b): Yield: 76 %; m.p. 97 °C; ¹H NMR: δ 2.59–2.81 (*m*, 8H), 3.10–3.21 (*m*, 4H), 3.87 (*s*, 3H, OCH₃), 6.45 (*s*, 2H, NH₂), 6.85–7.02 (*m*, 4H, ArH), 7.45 (*d*, 1H, *J* = 2 Hz, ArH), 7.97 (*d*, 1H, *J* = 2 Hz, ArH).

2-Bromo-4-[2-[4-(2-methoxyphenyl)piperazin-1-yl]ethyl]-6-nitroaniline (7.2b): Yield: 67 %; m.p. 95 °C; ¹H NMR: δ 2.58–2.79 (*m*, 8H), 3.12 (*s*, 4H), 3.87 (*s*, 3H, OCH₃), 6.51 (*s*, 2H, NH₂), 6.85–7.02 (*m*, 4H, ArH), 7.61 (*d*, 1H, *J* = 2 Hz, ArH), 8.00 (*d*, 1H, *J* = 2 Hz, ArH).

2-Chloro-4-[2-[4-(2-chlorophenyl)piperazin-1-yl]ethyl]-6-nitroaniline (7.1c): Yield: 79 %; m.p. 98 °C; ¹H NMR: δ 2.60–2.81 (*m*, 8H), 3.09–3.13 (*m*, 4H), 6.46 (*s*, 2H, NH₂), 6.93–7.09 (*m*, 2H, ArH), 7.19–7.27 (*m*, 1H, ArH), 7.36 (*dd*, 1H, *J* = 4 Hz, *J* = 2 Hz, ArH), 7.46 (*d*, 1H, *J* = 2 Hz, ArH), 7.98 (*d*, 1H, *J* = 2 Hz, ArH).

2-Bromo-4-[2-[4-(2-chlorophenyl)piperazin-1-yl]ethyl]-6-nitroaniline (7.2c): Yield: 76 %; m.p. 128 °C; ¹H NMR: δ 2.60–2.80 (*m*, 8H), 3.08–3.13 (*m*, 4H), 6.52 (*s*, 2H, NH₂), 6.94–7.09 (*m*, 2H, ArH), 7.19–7.23 (*m*, 1H, ArH), 7.36 (*dd*, 1H, *J* = 6.2 Hz, *J* = 1.8 Hz, ArH), 7.62 (*d*, 1H, *J* = 2 Hz, ArH), 8.02 (*d*, 1H, *J* = 2 Hz, ArH).

2-Chloro-6-nitro-4-(2-[4-[3-(trifluoromethyl)phenyl]piperazin-1-yl]ethyl)aniline (7.1d): Yield: 59 %; oil; ¹H NMR: δ 2.58–2.78 (*m*, 8H), 3.23–3.28 (*m*, 4H), 6.44 (*s*, 2H, NH₂), 7.08–7.21 (*m*, 3H, ArH), 7.42 (*t*, 1H, *J* = 8 Hz, ArH), 7.59 (*d*, 1H, *J* = 2 Hz, ArH), 7.97 (*d*, 1H, *J* = 2 Hz, ArH).

2-Bromo-6-nitro-4-(2-[4-[3-(trifluoromethyl)phenyl]piperazin-1-yl]ethyl)aniline (7.2d): Yield: 64 %; oil; ¹H NMR: δ 2.58–2.71 (*m*, 8H), 3.24–3.29 (*m*, 4H), 6.52 (*s*, 2H, NH₂), 7.05–7.39 (*m*, 4H, ArH), 7.62 (*d*, 1H, *J* = 2 Hz, ArH), 8.04 (*d*, 1H, *J* = 2 Hz, ArH).

General procedure for the synthesis of 2-amino-5-[2-(4-aryl)piperazin-1-yl]ethyl]3-halo-phenylamines **8.1a–d – 8.2a–d**

Raney-Ni (0.06–0.08 g) was added in small portions to a stirred solution of 2 mmol of nitro compound (**7.1a–d–7.2a–d**) in 5 ml EtOH, 10 ml 1,2-dichloroethane and 0.9 ml hydrazine hydrate

at 30 °C. After the addition of Ra-Ni was completed, the mixture was heated in a water bath (50 °C, 60 min) and filtered through celite. The filtrate was evaporated *in vacuo* and crude products were used for further syntheses.

Synthesis of 6-[2-(4-arylpiperazin-1-yl)ethyl]-4-chloro-1,3-dihydro-2H-benzimidazole-2-thiones (9.1a–d) and 6-[2-(4-arylpiperazin-1-yl)ethyl]-4-bromo-1,3-dihydro-2H-benzimidazole-2-thiones (9.2a–d)

Carbon disulfide (0.24 ml, 4 mmol) and KOH (0.25 g in 0.6 ml water) were added to 2 mmol of diamine (**8.1a–d** – **8.2a–d**) in 10 ml EtOH. After refluxing for 3 h, 0.3 ml of acetic acid in 3.3 ml water were added. The solvent was removed *in vacuo* and the residue chromatographed on silica gel.

4-Chloro-1,3-dihydro-6-[2-(4-phenylpiperazin-1-yl)ethyl]-2H-benzimidazole-2-thione (9.1a): Yield: 69 %; m.p. 247 °C; IR (cm⁻¹): 692, 1201, 1345, 1490, 1602, 2825; ¹H NMR (*d*₆DMSO): δ 2.65 (s, 6H), 2.84 (t, 2H, *J* = 8 Hz), 3.15 (s, 4H), 6.78 (t, 1H, *J* = 7.2 Hz, ArH), 6.92 – 7.00 (m, 3H, ArH), 7.12 (s, 1H, ArH), 7.17 – 7.25 (m, 2H, ArH), 12.75 (s, 1H, NH), 12.97 (s, 1H, NH). ¹³C NMR (*d*₆DMSO): δ 32.31 (CH₂), 48.36 (2CH₂), 52.83 (2CH₂), 59.82 (CH₂), 108.48 (CH), 113.22 (C-Cl), 115.53 (2CH), 118.98 (CH), 122.78 (CH), 128.64 (C), 129.14 (2CH), 133.85 (C), 136.75 (C), 151.29 (C-N), 169.48 (C=S). MS: *m/e* (100) 372.0 (M⁺). C₁₉H₂₁ClN₄S.

4-Bromo-1,3-dihydro-6-[2-(4-phenylpiperazin-1-yl)ethyl]-2H-benzimidazole-2-thione (9.2a): Yield: 73 %; m.p. 259 °C; IR (cm⁻¹): 758, 1198, 1344, 1486, 1601, 2827, 2946, 3427; ¹H NMR (*d*₆DMSO): δ 2.55 – 2.59 (m, 6H), 2.81 (t, 2H, *J* = 7.8 Hz), 3.09 – 3.14 (s, 4H), 6.77 (t, 1H, *J* = 7.2 Hz, ArH), 6.91 – 6.95 (m, 2H, ArH), 7.02 (s, 1H, ArH), 7.17 – 7.25 (m, 3H, ArH), 12.79 (s, 2H, NH). ¹³C NMR (*d*₆DMSO): δ 32.18 (CH₂), 48.31 (2CH₂), 52.79 (2CH₂), 59.78 (CH₂), 100.86 (C-Br), 108.89 (CH), 115.54 (2CH), 118.99 (CH), 125.73 (CH), 129.14 (2CH), 130.35 (C), 133.49 (C), 137.02 (C), 151.26 (C-N), 169.43 (C=S). MS: *m/e* (100) 415.9 (M-1). C₁₉H₂₁BrN₄S.

4-Chloro-1,3-dihydro-6-[2-[4-(2-methoxyphenyl)piperazin-1-yl]ethyl]-2H-benzimidazole-2-thione (9.1b): Yield: 75 %; m.p. 246 °C; IR (cm⁻¹): 650, 758, 1240, 1307, 1347, 1496, 2827; ¹H NMR (*d*₆DMSO): δ 2.63 (s, 6H), 2.82 (t, 2H, *J* = 7.8 Hz), 2.97 (s, 4H), 3.77 (s, 3H, OCH₃), 6.88 – 6.96 (m, 4H, ArH), 7.00 (d, 1H, *J* = 1 Hz, ArH), 7.10 (d, 1H, *J* = 1 Hz, ArH), 12.74 (s, 1H, NH), 12.94 (s, 1H, NH). ¹³C NMR (*d*₆DMSO): δ 31.99 (CH₂), 49.97 (CH₃), 52.95 (2CH₂), 55.49 (2CH₂), 59.66 (CH₂), 108.54 (CH), 112.09 (CH), 113.22 (C-Cl), 118.22 (CH), 121.03 (CH), 122.63 (CH), 125.76 (CH), 128.59 (C), 133.80 (C), 136.53 (C), 141.32 (C-O), 152.17 (C-N), 169.47 (C=S). MS: *m/e* (100) 402.2 (M⁺). C₂₀H₂₃ClN₄OS.

4-Bromo-1,3-dihydro-6-[2-[4-(2-methoxyphenyl)piperazin-1-yl]ethyl]-2H-benzimidazole-2-thione (9.2b): Yield: 68 %; m.p. 236 °C; IR (cm⁻¹): 758, 1196, 1240, 1344, 1495, 1603, 2823, 3434; ¹H NMR (*d*₆DMSO): δ 2.66 (s, 6H), 2.83 (t, 2H, *J* = 7.8 Hz), 2.98 (s, 4H), 3.77 (s, 3H, OCH₃), 6.88 – 6.93 (m, 4H, ArH), 7.02 (s, 1H, ArH), 7.23 (s, 1H, ArH), 12.76 (s, 1H, NH), 12.85 (s, 1H, NH). ¹³C NMR (*d*₆DMSO): δ 31.90 (CH₂), 49.97 (CH₃), 52.97 (2CH₂), 55.50 (2CH₂), 59.67 (CH₂), 100.87 (C-Br), 108.98 (CH), 112.09 (CH), 118.16 (CH), 121.05 (CH), 122.69 (CH), 125.73 (CH), 130.39 (C), 133.49 (C), 136.78 (C), 141.30 (C-O), 152.18 (C-N), 169.45 (C=S). MS: *m/e* (100) 447.4 (M⁺). C₂₀H₂₃BrN₄OS.

4-Chloro-6-[2-[4-(2-chlorophenyl)piperazin-1-yl]ethyl]-1,3-dihydro-2H-benzimidazole-2-thione (9.1c): Yield: 62 %; m.p. 257 °C; IR (cm⁻¹): 693, 933, 1348, 1485, 2937; ¹H NMR (*d*₆DMSO): δ 2.63 (s, 6H), 2.82 (t, 2H, *J* = 8 Hz), 2.98 (s, 4H), 6.99 – 7.17 (m, 4H, ArH), 7.25 – 7.42 (m, 2H, ArH), 12.73 (s, 1H, NH), 12.94 (s, 1H, NH). ¹³C NMR (*d*₆DMSO): δ 32.16 (CH₂), 50.93 (2CH₂), 52.90 (2CH₂), 59.66 (CH₂), 108.54 (CH), 113.24 (C-Cl), 121.05 (CH), 122.80 (CH), 124.07 (C), 127.81 (CH), 128.30 (CH), 128.59 (C), 130.56 (CH), 133.82 (C), 136.64 (C), 149.20 (C-N), 169.48 (C=S). MS: *m/e* (100) 406.0 (M⁺). C₁₉H₂₀Cl₂N₄S.

4-Bromo-1,3-dihydro-6-[2-[4-(2-chlorophenyl)piperazin-1-yl]ethyl]-2H-benzimidazole-2-thione (9.2c): Yield: 72 %; m.p. 254 °C; IR (cm⁻¹): 760, 1191, 1344, 1483, 1603, 2819, 3097; ¹H NMR

(d_6 DMSO): δ 2.62 (s, 6H), 2.81 (t, 2H, $J = 8$ Hz), 2.98 (s, 4H), 6.99 – 7.43 (m, 6H, ArH), 12.77 (s, 2H, NH). ^{13}C NMR (d_6 DMSO): δ 32.16 (CH_2), 51.00 (2CH_2), 52.93 (2CH_2), 59.80 (CH_2), 100.86 (C-Br), 108.96 (CH), 121.05 (CH), 124.05 (C), 125.71 (CH), 127.80 (CH), 128.30 (CH), 130.35 (C), 130.55 (CH), 133.47 (C), 137.04 (C), 149.25 (C-N), 169.48 (C=S). MS: m/e (100) 451.8 (M^+). $\text{C}_{19}\text{H}_{20}\text{BrClN}_4\text{S}$.

4-Chloro-1,3-dihydro-6-(2-{4-[3-(trifluoromethyl)phenyl]piperazin-1-yl}ethyl)-2H-benzimidazole-2-thione (9.1d): Yield: 68 %; m.p. 239 °C; IR (cm^{-1}): 697, 953, 1123, 1451, 1490, 1611, 2952; ^1H NMR (d_6 DMSO): δ 2.60 (s, 6H), 2.82 (t, 2H, $J = 7.8$ Hz), 3.23 (s, 4H), 6.99 – 7.24 (m, 5H, ArH), 7.42 (t, 1H, $J = 8$ Hz, ArH), 12.73 (s, 1H, NH), 12.95 (s, 1H, NH). ^{13}C NMR (d_6 DMSO): δ 32.20 (CH_2), 47.69 (2CH_2), 52.54 (2CH_2), 59.60 (CH_2), 108.56 (CH), 110.97 (CH), 113.22 (C-Cl), 114.80 (CH), 118.90 (CH), 122.80 (CH), 128.59 (C), 129.77 (CH), 130.17 (CH), 130.40 (C), 133.82 (C), 136.62 (C), 151.44 (C-N), 169.47 (C=S). MS: m/e (100) 440.0 (M^+). $\text{C}_{20}\text{H}_{20}\text{ClF}_3\text{N}_4\text{S}$.

4-Bromo-1,3-dihydro-6-(2-{4-[3-(trifluoromethyl)phenyl]piperazin-1-yl}ethyl)-2H-benzimidazole-2-thione (9.2d): Yield: 75 %; m.p. 248 °C; IR (cm^{-1}): 697, 952, 1314, 1348, 1451, 1487, 1607, 2947, 3049; ^1H NMR (d_6 DMSO): δ 2.53 – 2.58 (m, 6H), 2.81 (t, 2H, $J = 7.8$ Hz), 3.20 (s, 4H), 7.02 – 7.24 (m, 5H, ArH), 7.42 (t, 1H, $J = 8$ Hz, ArH), 12.79 (s, 2H, NH). ^{13}C NMR (d_6 DMSO): δ 32.22 (CH_2), 47.78 (2CH_2), 52.59 (2CH_2), 59.75 (CH_2), 100.88 (C-Br), 108.96 (CH), 110.94 (CH), 114.70 (CH), 118.88 (CH), 125.70 (CH), 128.55 (C), 129.77 (CH), 130.15 (C), 130.40 (C), 133.52 (C), 136.98 (C), 151.48 (C-N), 169.43 (C=S). MS: m/e (100) 484.0 ($\text{M}-1$). $\text{C}_{20}\text{H}_{20}\text{BrF}_3\text{N}_4\text{S}$.

Membrane preparation, binding assays and data analysis

Specific binding affinities (K_i values, Table I) of the thiones were determined exactly as described previously,^{17,21} by measuring the extent of displacement of specific tritiated ligands ($[^3\text{H}]\text{SCH 23390}$ for D_1 , CAS Number [87134–87–0], $[^3\text{H}]\text{spiperone}$ for D_2 , CAS Number [749–02–0], and $[^3\text{H}]\text{8-OH-DPAT}$ for 5HT_{1A} receptors, CAS Number [80300–08–9]; products of Amersham Buchler GmbH, Germany) to fresh membrane preparations of bovine caudate nuclei and hippocampi. The competitive radioassays were performed in sample triplicates, with a range of concentrations (10^{-5} – 10^{-9} M) of the selected compounds. Nonspecific binding was determined with the 1mM (+)-butaclamol (D_1 and D_2) and 10 μM serotonin (5HT_{1A}). The retained radioactivity was measured by introducing the dry filters into 5 ml toluene-based scintillation liquid and counting in a 1219 Rack-beta Wallac scintillation counter. Competition binding curves were constructed and analyzed by “Graph-Pad Prism” (v. 4.0).

Acknowledgments: This work was supported by the Ministry of Science, Technology and Development of Serbia, grants # 142009 and 143032.

ИЗВОД

6-[2-(4-АРИЛПИПЕРАЗИН-1-ИЛ)ЭТИЛ]-4-ХАЛО-1,3-ДИГИДРО-2H-БЕНЗИМИДАЗОЛ-2-ТИОНИ: СИНТЕЗА И ФАРМАКОЛОШКО ИСПИТИВАЊЕ

ДЕАНА АНДРИЋ¹, ГОРДАНА ТОВИЛОВИЋ², ГОРАН РОГЛИЋ¹, ВУКИЋ ШОШКИЋ^{3,4},
МИРКО ТОМИЋ² и СЛАЂАНА КОСТИЋ-РАЈАЧИЋ³

¹Хемијски факултет, Универзитет у Београду, Студенски брџ 16, 11000 Београд, ²Одсек за биохемију, Институт за биолошка истраживања “Синиша Станковић”, Булевар Деспојина Сидефана 142, 11060 Београд, ³Центар за хемију, ИХТМ, Њеђошева 12, 11000 Београд и

⁴Proteosys AG, Carl-Zeiss-Str. 51, 55129 Mainz, Germany

Синтетисано је осам нових једињења код којих је атом халогена уведен у бензимидазол-2-тионску допаминергичку фармакофору 5-[2-(4-арилпиперазин-1-ил)етил]-1,3-дихидро-2H-бензимидазол-2-тиона са арилпиперазинским делом молекула изабраним сходно познатим захтевима о односу структуре и реактивности. За сва новосинтетисана једињења је одре-

Њен афинитет везивања за допаминске (D_1 и D_2) и 5-HT_{1A} рецепторе у *in vitro* експериментима конкуренције са радиолигандима. Као извор допаминских и 5-HT_{1A} рецептора су коришћене синаптозомалне мембране изоловане из говеђег нуклеуса каудатуса и хипокампуса. Сва новосинтетисана једињења показала су се као јаки конкуритори [^3H]спиперона и [^3H]8-ОН-ДРАТ, од којих најактивнија (**9.1b** и **9.2b**) поседују 34 и 170 пута већи афинитет ка D_2 ДА рецепторима од полазних, нехалогенованих једињења. Са друге стране, ова једињења не поседују значајан афинитет ка D_1 допаминским рецепторима.

(Примљено 30. јуна 2006, ревидирано 20. фебруара 2007)

REFERENCES

1. P. G. Strange, *Pharmacol. Rev.* **53** (2001) 119
2. D. E. Casey, *Int. Clin. Psychopharmacol.* **10**(S3) (1995) 105
3. A. Wieck, P. Haddad, *Brit. Med. J.* **324** (2002) 250
4. H. Y. Meltzer, S. Matsubara, J.-C. Lee, *Psychopharmacol. Bull.* **25** (1989) 390
5. J. A. Lieberman, *CNS Drugs* **18** (2004) 251
6. C. Cosi, E. Carilla-Durand, M. B. Assie, A. M. Ormiere, M. Maraval, N. Leduc, A. Newman-Tancredi, *Eur. J. Pharmacol.* **535** (2006) 135
7. R. A. Glendon, *Drug Dev. Res.* **26** (1992) 251
8. R. Perrone, E. Berardi, N. A. Colabufo, *J. Med. Chem.* **42** (1999) 490
9. A. Mouithys-Mickalad, J. H. Poupaert, S. Spampinato, *Bioorg. Med. Chem. Lett.* **12** (2002) 1149
10. V. Šukalović, M. Zlatović, D. Andrić, G. Roglić, S. Kostić-Rajačić, V. Šoškić, *Arzneim. Forsch./Drug Res.* **55** (2005) 145
11. V. Šukalović, D. Andrić, G. Roglić, S. Kostić-Rajačić, V. Šoškić, *Arch. Pharm. Pharm. Med. Chem.* **337** (2004) 376
12. V. Šukalović, M. Zlatović, D. Andrić, G. Roglić, S. Kostić-Rajačić, V. Šoškić, *Arch. Pharm. Pharm. Med. Chem.* **337** (2004) 502
13. D. Andrić, G. Tovilović, G. Roglić, Đ. Vasković, V. Šoškić, M. Tomić, S. Kostić-Rajačić, *J. Serb. Chem. Soc.* **72** (2007) 429
14. F. D. Bellamy, K. Ou, *Tetrahedron Lett.* **23** (1984) 839
15. L. Florvall, V. Hillegaart, A. Malmberg, A. Wijkstroem, S. Ahlenius, *Eur. J. Med. Chem.* **31** (1996) 133
16. R. S. Mali, S. G. Tilve, *Synth. Commun.* **19** (1989) 1825
17. Z. Tuče, V. Šoškić, J. Joksimović, *Drug Design Discovery* **11** (1994) 251
18. V. Šoškić, J. Joksimović, *Curr. Med. Chem.* **5** (1998) 493
19. S. Dukić, M. Vujović, V. Šoškić, J. Joksimović, *Arzneim. Forsch.* **47** (1997) 239
20. S. Dukić, S. Kostić-Rajačić, D. Dragović, V. Šoškić, J. Joksimović, *J. Pharm. Pharmacol.* **49** (1997) 1036
21. H. Gozlan, S. El Mestikaway, S. Pichat, J. Glowinski, M. Hamon, *Nature* **305** (1983) 140.



Effect of fermentation conditions on lipase production by *Candida utilis*

SANJA Ž. GRBAVČIĆ, SUZANA I. DIMITRIJEVIĆ–BRANKOVIĆ[#], DEJAN I. BEZBRADICA[#],
SLAVICA S. ŠILER–MARINKOVIĆ[#] and ZORICA D. KNEŽEVIĆ*[#]

Faculty of Technology and Metallurgy, Department of Biotechnology and Biochemical Engineering, Karnegijeva 4, 11000 Belgrade, Serbia

(Received 5 October 2006, revised 6 March 2007)

Abstract: A wild yeast strain isolated from spoiled soybean oil and identified as *Candida utilis* initially presented rather low lipase activity (approximately 4 IU dm⁻³) in submerged culture in a universal yeast medium containing 2 % malt extract. Studies were undertaken to improve the lipase production. The best yields of lipase were obtained with a medium supplemented with caprylic and oleic acids as inducers, but higher concentrations of the former (> 0.5 %) had a negative effect on the lipase production and cell growth. The type of nitrogen source seemed also to be very important. The highest lipolytic activity of 284 IU dm⁻³ was achieved after 5 days of fermentation in a medium containing oleic acid and hydrolyzed casein as carbon and nitrogen sources, respectively, and supplemented with Tween 80[®]. It was shown that optimization of the fermentation conditions can lead to a significant improvement in the lipase production (more than 70-fold higher compared to the initial value obtained in the non-optimized medium).

Keywords: *Candida utilis*, lipase production, media optimization, hydrolyzed casein, oleic acid.

INTRODUCTION

Lipases (triacylglycerol acylhydrolases EC 3.1.1.3) are a class of hydrolases which catalyze the hydrolysis of triglycerides to glycerol and free fatty acids on an oil–water interface.^{1,2} In addition, lipases catalyze the hydrolysis and transesterification of other esters,³ the syntheses of esters and exhibit enantioselective properties.⁴ Their ability to perform very specific chemical transformations (bio-transformations) has made them increasingly popular in industries where less specific chemical processes produce unwanted by-products, such as the food, detergent, cosmetic and pharmaceutical industries. In recent years, increasing attention has been paid to the conversion of processing industry wastes by microbial lipases or their use as biosensors.^{5,6}

* Corresponding author. E-mail: zknez@tmf.bg.ac.yu

[#] Serbian Chemical Society member.

doi: 10.2298/JSC0709757G

The rapidly increasing market for compounds produced by lipases has resulted in a growing demand to identify lipases with novel and specific properties. Each application requires unique lipase properties with respect to specificity, stability, temperature and pH. Often an industrial process can be modified to accommodate the limitations of an enzyme but this is costly and a better approach is to find an enzyme more suited to the existing process. Therefore, the screening of microorganisms with lipolytic activity could enable the discovery of a lipase with convenient properties for its potential industrial application.¹

Microbial commercial lipases are mainly produced from *Pseudomonas*,⁷ *Mucor*,⁴ *Geothricum*,⁶ *Rhizopus*⁸ and *Candida* sp.^{9,10,11} In a number of studies, it has been reported that the production of lipase can be significantly increased by the careful selection of the nitrogen and carbon sources for microbial growth and the optimization of the composition of the growth medium.^{9,10,12} Most importantly, since lipase is an inducible extracellular enzyme, by application of a proper inducer the lipase production can be considerably increased.¹³ Although fermentation conditions have been widely studied and documented, only limited research was directed towards *Candida utilis* lipase. On the other hand, the great nutrition value of this microorganism has been well recognized.¹⁴ It appears that among the nine different microorganisms isolated in this study from spoiled soybean oil, it was the best lipase producer. Therefore, the use of this microorganism could lead to the development of a process for achieving high lipolytic activity and gaining a nutritionally valuable biomass. In this work an attempt was made to select a suitable fermentation medium and optimize its components to increase the production of lipase by the yeast *Candida utilis*.

EXPERIMENTAL

Materials

The substrate solution for the determination of the lipase activity was an emulsion of triolein (Sigma, St. Louis MO) in Triton X-100[®] (Sigma, St. Louis MO). Malt extract, yeast extract, peptone, meat extract and maltose were obtained from Torlak (Institute of Immunology and Virology, Serbia). Bovine serum albumin and Folin-Ciocalteu's Phenol Reagent, used for the determination of the protein concentration, were products of Sigma (St. Louis, USA). Oleic acid, Tween 80[®], dodecane and palmitic acid were also obtained from Sigma (St. Louis, USA). KH₂PO₄, MgSO₄·7H₂O and NaOH were products of Lachema (Neratovice, Czech Republic). All other employed chemicals were of analytic grade.

Microorganisms and growth media

The microorganism used in this study was yeast previously isolated from spoiled soybean oil. The yeast was identified as *Candida utilis* according to the identification scheme of Lodder.¹⁵ As a part of the culture collection (Microbiological Laboratory of the Faculty of Technology and Metallurgy, Belgrade), the yeast was maintained on agar slanted at 4 °C. The yeast strain, grown in a medium containing 2 % of malt extract for 24 h at 30 °C (approximately 1.2×10⁷ cells cm⁻³), was used for the inoculum. In the study of the effect of carbon source on lipase production, a medium containing 2 % of malt extract was also used.

The following basal medium was used for lipase production (per dm³): yeast extract 30.0 g; KH₂PO₄ 10.0 g; MgSO₄·7H₂O 1.0 g; maltose 5.0 g and Tween 80[®] 1 cm³ with the pH adjusted to 6.0. Optimization of enzyme production was carried out by altering the nitrogen sources at a concentration of 3.0 % (w/v). All samples were in duplicates and the experiments were repeated at least twice to ensure reproducibility.

Lipase production

The culture was grown in 100 cm³ Erlenmeyer flasks containing 50 cm³ of fermentation media inoculated with 1 % (v/v) (0.5 cm³) of cell suspension and incubated at 28 °C on a rotary shaker (120 rpm) for 120 h.

Determination of lipase activity

Extracellular lipase activity was measured in culture supernatants after centrifugation (3200 rpm for 20 min). The substrate solution for lipase activity determination was an emulsion of triolein in Triton X-100[®]. The assay mixture consisting of 3 cm³ of substrate solution, 2.5 cm³ of distilled water, 1 cm³ of Tris–HCl buffer (pH 7.7) and 1 cm³ of culture supernatant was incubated for 60 min. at 37 °C. The reaction was stopped by the addition of 3 cm³ of methanol. The fatty acids released were determined by titration with 0.5 M NaOH in the presence of phenolphthalein as indicator. For each test run, a blank control was done separately in which case the reaction was stopped with methanol (3 cm³) immediately after the addition of the supernatant to the assay mixture. One unit was defined as the enzyme required for releasing 1 μmol of fatty acid per minute at 37 °C.

Determination of cell growth

Determination of yeast cell growth was performed by spreading a suitably diluted cell suspension on malt agar plates and counting the yeast cell colonies after 48 h of incubation at 30 °C.

Determination of protein concentration

The protein concentration was determined according to Lowry method using bovine serum albumin as the standard.¹⁶ The protein concentration was determined from a standard curve which was constructed for each measurement.

RESULTS AND DISCUSSION

Preliminary study

The yeast strain isolated from spoiled soybean oil presented the highest lipolytic activity among several different microorganisms after 5 days of incubation at 28 °C on agar plates containing tributyrine. It was identified as *Candida utilis* by its morphology and biochemical properties.¹⁵

In a preliminary study, the effects of other conditions of the fermentation process, such as temperature, initial pH of the medium and inoculum concentration, on the yield of lipase were investigated in a medium containing 2 % malt extract. It seems that the optimal temperature and pH range was 27–29 °C and 5.9–6.1, respectively, whereas the inoculum concentration did not significantly affect the enzyme yield (data not shown). Therefore, the effect of the composition of the fermentation media and the concentrations of the components was investigated with the temperature and pH fixed at their optimal values (28 °C and pH 6.0) with an inoculum concentration of 1 % (v/v).

Optimization of the composition of the culture medium

Production of the lipase by *Candida utilis* can be optimized by designing the growth medium or conditions which have a positive effect on the genetic regulation of the synthesis of the enzyme. There are two major regulatory mechanisms involved in lipase synthesis: carbohydrate catabolite repression and induction by lipase substrates and products (fatty acids and lipids). Accordingly, the choice of fermentation medium is of crucial importance for the elimination or reduction of catabolite repression and induction of lipase biosynthesis.

Effect of carbon sources and inducers. Studies on the fermentation conditions for the production of extracellular lipases by many microorganisms, such as *Candida rugosa*, *Yarrowia lipolytica*, showed that the addition of lipid substances enhanced the level of lipase produced. Fatty acids are generally considered to be the most effective inducers for lipase biosynthesis.^{12,17} In initial experiments, the fermentation of lipase by *Candida utilis* in batch cultures with different carbon sources was studied in order to determine the influence of different inducers on the production of lipase. Different fatty acids, as well as the other possible inducers, were added at a concentration of 0.1 % (w/v). The obtained data is shown in Fig. 1.

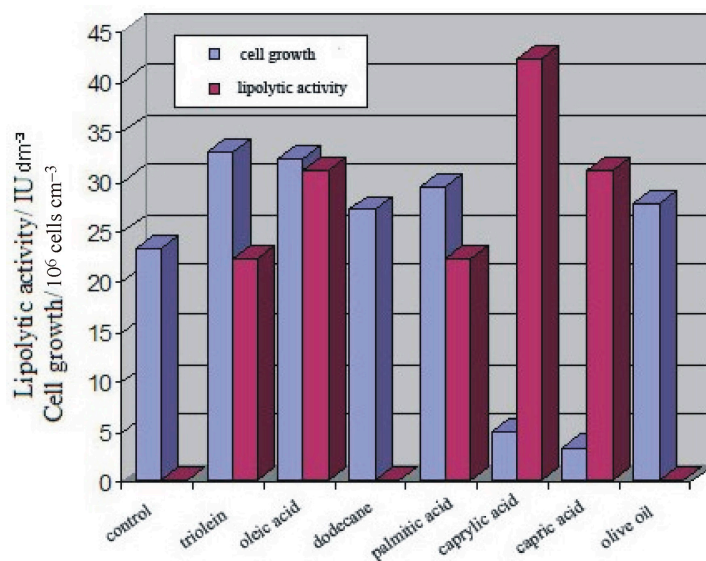


Fig. 1. Effects of carbon sources as inducers on lipase production and cell growth. Fermentation conditions: 2 % malt extract medium, 28 °C, 120 h.

It was concluded that the highest lipase activity was obtained in a medium supplemented with oleic and caprylic acids. The addition of olive oil and dodecane did not improve the production of lipase. The lipase activity and cell growth were not in strict correlation. Namely, the short-chain inducers (capric and caprylic acid) inhibited cell growth, but improved lipase production.

According to the obtained results, a second experiment was conducted to study the effect of the concentrations of caprylic and oleic acid in the concentration range 0.1–0.9 %. This series of experiments was also performed in 2 % malt extract media. As indicated in Fig. 2, increasing the oleic acid concentration up to 0.5 % enhanced the production of lipase, as well as the total amount of proteins produced and cell growth.

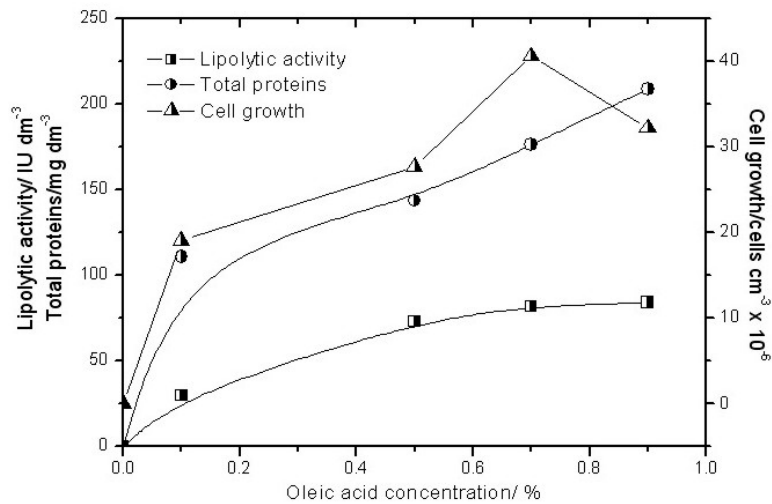


Fig. 2. Effect of oleic acid concentration on lipase production, cell growth and total proteins. Fermentation conditions: 2 % malt extract medium, 28 °C, 120 h.

It seems that caprylic acid is a better inducer than oleic acid at a concentration of 0.1 % (Fig. 1). However, higher concentrations of caprylic acid (Fig. 3) had a negative effect on lipase production and cell growth, which indicated its possible toxicity and, therefore, caprylic acid was excluded from further experiments. The inhibitory effect of caprylic acid at higher concentrations was previously registered for other yeasts, such as *C. rugosa*.¹³

Increasing the oleic acid concentration had a favorable effect only up to 0.5 %, and a further increase did not lead to an enhancement of the yield of lipolytic activity (Fig. 2). This may be due to the reduced oxygen transfer into the medium caused by the low solubility of oleic acid at high concentration. Low oxygen supplies can alter the yeast metabolism and, consequently, production of lipase.

It is a well known fact that surfactants can increase permeability of the yeast membrane, facilitating the export of various compounds, including enzymes, out of the cell.¹² Therefore, the effect of the addition of the surfactant Tween 80[®] to the growth medium containing 1 % of oleic acid was investigated. It was evidenced that the yield of lipolytic activity was two times higher in the presence than in the absence of the surfactant. Additionally, it was shown that in the presence of Tween 80[®], increasing the oleic acid concentration up to 6 % led to a con-

comitant increase of the lipase activity (Fig. 4). It is plausible that the presence of the surfactant led to more effective oxygen transport in the medium, as well as better dispersion of the oleic acid in the growth substrate, which made it readily accessible to the microbial cells.

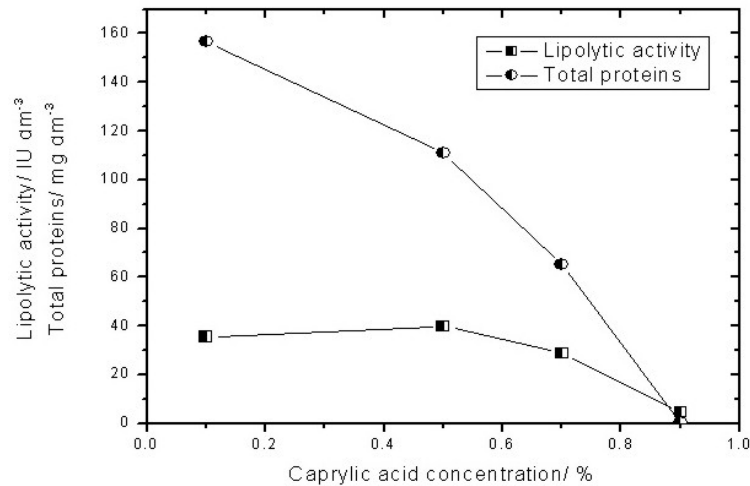


Fig. 3. Effect of caprylic acid concentration on lipase production and total proteins. Fermentation conditions: 2 % malt extract medium, 28 °C, 120 h.

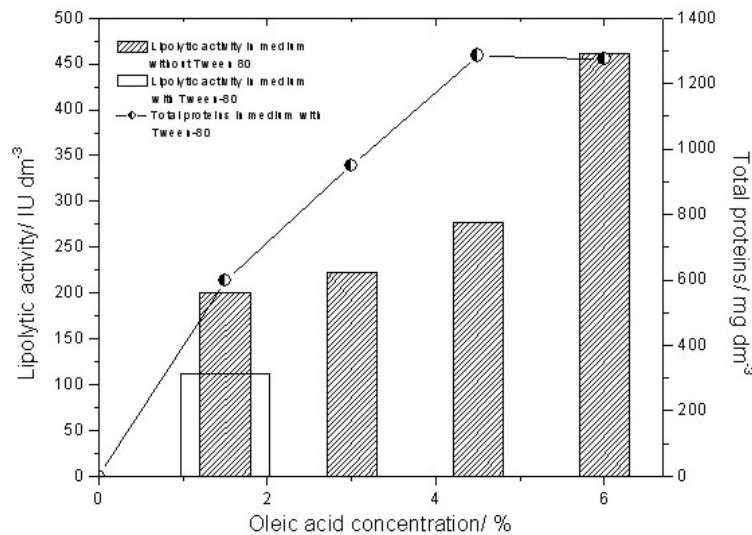


Fig. 4. Combined effect of oleic acid concentration and Tween 80[®] on lipase production and total proteins. Fermentation conditions: yeast extract 3 % (w/v); KH₂PO₄ 1 % (w/v); MgSO₄·7H₂O 0.01 % (w/v); maltose 0.5 % (w/v), 28 °C, Tween 80[®] 0.1 % (v/v), 120 h.

Effects of nitrogen sources. In previous experiments, yeast extract was used as a nitrogen source. Literature data shows that the production of lipases can be

improved by a suitable selection of a nitrogen source depending on the studied microorganism. For example, yeast extract stimulated lipase production by *Cryptococcus* sp., while urea was the best nitrogen source for lipase production by *Y. lipolytica*.^{1,10} In terms of medium optimization, different organic nitrogen sources at a concentration of 3 % (w/v) were investigated instead of yeast extract. The influence of the source of organic nitrogen is shown in Fig. 5.

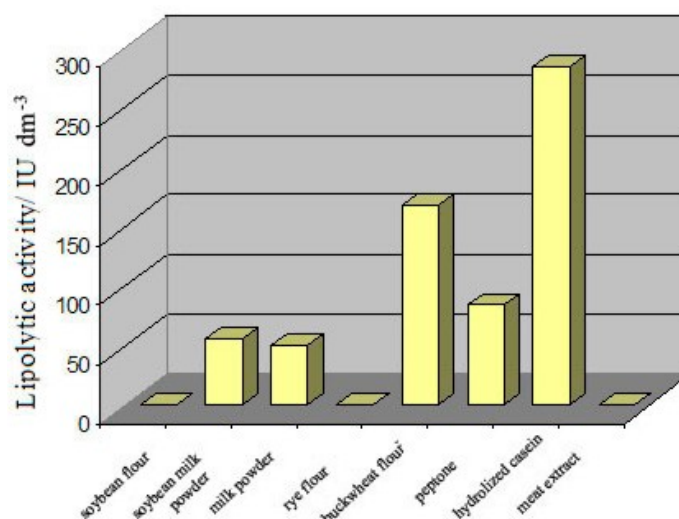


Fig. 5. Effect of nitrogen sources on lipase production. Fermentation conditions: oleic acid 6 % (w/v); KH_2PO_4 1 % (w/v); $\text{MgSO}_4 \cdot 7\text{H}_2\text{O}$ 0.01 % (w/v); maltose 0.5 % (w/v) and Tween 80[®] 0.1 % (v/v), 28 °C, 120 h.

The highest yield of lipolytic activity of 284 IU dm⁻³ was achieved in a growth medium with hydrolyzed casein as the nitrogen source. A satisfactory yield of lipase activity was achieved in a medium containing buckwheat flour (166 IU dm⁻³), while other nitrogen sources did not stimulate lipase production. The favorable effect of hydrolyzed casein on lipase production was previously reported in a study focused on mutant *Candida* sp.⁹

Fermentation of lipase

According to the obtained results, the fermentation was performed in a medium with hydrolyzed casein as the nitrogen source enriched with Tween 80[®] and oleic acid (6 % w/v). This medium was used to study the kinetics of the production of lipase and the relationship between enzyme secretion, protein production and cell growth.

The kinetics of lipase production, total produced proteins and cell growth during 7 days of fermentation are shown in Fig. 6. The exponential phase of cell growth ceased after 4 days and subsequently the cell concentration decreased rapidly. On the other hand, the increase of lipase activity and total produced pro-

teins was prolonged. Therefore, the maximum lipase activity appeared during the late logarithmic phase, after 5 days of fermentation, which corresponded with the maximum of the total produced proteins. A similar behavior was observed in the production of lipase with *Antrodia cinnamomea*¹⁸ and *C. rugosa*.^{19,20}

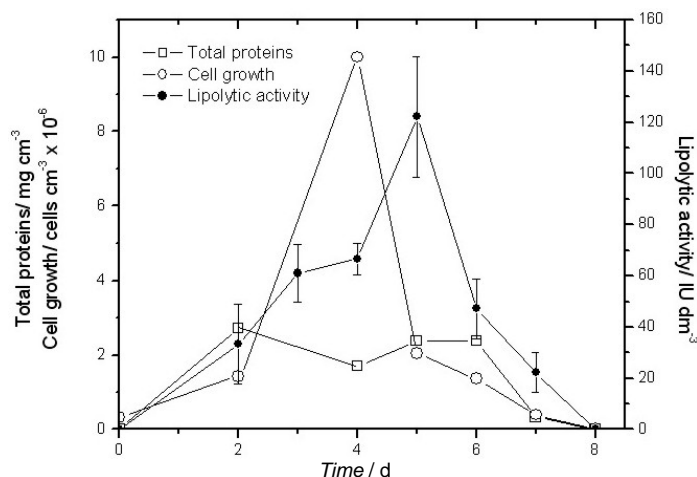


Fig. 6. The time course of lipase production, total proteins and cell growth in the optimized medium. Fermentation conditions: oleic acid 6 % (w/v); hydrolyzed casein 3 % (w/v); KH_2PO_4 1 % (w/v); $\text{MgSO}_4 \cdot 7\text{H}_2\text{O}$ 0.01 % (w/v); maltose 0.5 % (w/v) and Tween 80[®] 0.1 % (v/v), 28 °C.

After reaching the lipase production peak, the lipase activity decreased more rapidly than the total produced proteins. It is plausible that the rapid decrease in the lipolytic activity is a consequence of the detrimental effect of proteolytic enzymes released from the yeast cells after cell death.

CONCLUSIONS

In this study, the effects of different factors, such as composition of fermentation medium and addition of inducers, on lipase production by the yeast *Candida utilis* were investigated. Among the examined inducers, the highest lipolytic activity was achieved with oleic and caprylic acids. However, caprylic acid was toxic to yeast cells in concentrations above 0.5 %, while oleic acid exhibited favorable effect on lipase production in concentrations up to 6%.

Among different nitrogen sources, good results were achieved with pepton and buckwheat flour, but the highest lipolytic activity was achieved in a medium containing hydrolyzed casein.

The kinetics of lipase production was studied in the optimized medium and it was observed that the maximum lipase production was achieved after an exponential phase of cell growth, after five days of fermentation. It can be concluded that significant extracellular lipase activity can be achieved using *Candida utilis* and that the obtained lipase activity can be notably enhanced by optimization of the composition of the growth medium.

ИЗВОД

УТИЦАЈ УСЛОВА ФЕРМЕНТАЦИЈЕ НА ПРОДУКЦИЈУ ЛИПАЗЕ ИЗ *Candida utilis*

САЊА ГРБАВЧИЋ, СУЗАНА ДИМИТРИЈЕВИЋ–БРАНКОВИЋ, ДЕЈАН БЕЗБРАДИЦА,
СЛАВИЦА ШИЛЕР–МАРИНКОВИЋ И ЗОРИЦА КНЕЖЕВИЋ

Технолошко–металуршки факултет, Карнегијева 4, 11000 Београд

У раду је испитана могућност производње липазе помоћу дивљег соја квасца изолованог из поквареног сојиног уља и идентификованог као *Candida utilis*. Овај микроорганизам је показао малу липолитичку активност када је узгајан у 2 % сладном бујону као универзалном квашчевом медијуму (око 4 IU dm⁻³). Испитани су утицаји различитих фактора као што су састав хранљиве подлоге и додаток одређених индуктора и стимулатора продукције липаза на повећање липолитичке активности. Олеинска и каприлна киселина су се показале као најефикаснији индуктори продукције липазе. У малим концентрацијама (до 0,5 %) каприлна киселина је показала већи утицај на производњу липазе од олеинске киселине, да би при већим концентрацијама имала токсичан утицај на ћелијски раст. Процес је оптимизован и са аспекта извора азота. Највећа липолитичка активност од 284 IU dm⁻³ остварена је након 5 дана ферментације у оптимизованој подлози која је садржала олеинску киселину и хидролизат казеина као изворе угљеника и азота и Tween 80® као стимулатор продукције ензима. Показано је да се пажљивим избором састава хранљиве подлоге може значајно повећати продукција липаза (више од 70 пута у поређењу са почетном вредношћу добијеном у неоптимизованој подлози).

(Примљено 5. октобра 2006, ревидирано 6. марта 2007)

REFERENCES

1. N. R. Kamini, T. Fujii, T. Kurosu, H. Iefuji, *Process Biochem.* **36** (2000) 317
2. Z. Knežević, S. Šiler–Marinković, L. Mojović, *Appl. Microbiol. Biotechnol.* **49** (1998) 267
3. D. Bezbradica, D. Mijin, S. Šiler–Marinković, Z. Knežević, *J. Mol. Catal. B: Enzym.* **38** (2006) 11
4. H. Abbas, A. Hiol, V. Deyris, L. Comeau, *Enzyme Microb. Technol.* **31** (2002) 968
5. W. O. B. Silva, S. Mitidieri, A. Schrank, M. H. Vainstein, *Process Biochem.* **40** (2005) 321
6. J. Vakhlu, A. Kour, *Electron J. Biotechnol.* **9** (2006) 68
7. A. Makhzoum, J. Z. Knapp, R. K. Owusu, *Food Microbiol.* **12** (1995) 277
8. A. Hiol, M. D. Jonzo, N. Rugani, D. Druet, L. Sarda, L. Comeau, *Enzyme Microb. Technol.* **26** (2000) 421
9. T. Tan, M. Zhang, B. Wang, C. Ying, L. Deng, *Process Biochem.* **39** (2003) 459
10. S. Benjamin, A. Pandey, *Bioresour. Technol.* **55** (1996) 167
11. M. A. Gordillo, J. L. Montesinos, C. Casas, *Chem. Phys. Lipids* **93** (1998) 131
12. E. Dalmau, J. L. Montesinos, M. Lotti, C. Casas, *Enzyme Microb. Technol.* **26** (2000) 657
13. N. Obradors, J. L. Montesinos, F. Valero, F. J. Lafuente, C. Sola, *Biotechnol. Lett.* **15** (1993) 357
14. B.–K. Lee, J. K. Kim, *Aquacult. Eng.* **25** (2001) 111
15. J. Lodder, *The yeast – a taxonomic study*, American Elsevier Publishing Company, New York, 1974
16. O. H. Lowry, N. J. Rosebrough, A. L. Farr, R. J. Randall, *J. Biol. Chem.* **193** (1951) 265
17. G. Corzo, S. Revah, *Bioresour. Technol.* **70** (1999) 173
18. E.–S. Lin, H.–C. Ko, *Enzyme Microb. Technol.* **37** (2005) 261
19. R. V. Muralidhar, R. R. Chirumamila, R. Marchant, P. Nigam, *Biochem. Bioeng. J.* **9** (2001) 17
20. R. K. Saxena, P. K. Gosh, R. Gupata, W. S. Davidson, S. Bradoo, R. Gulati, *Curr. Sci.* **77** (1999) 101.



SHORT COMMUNICATION

Disorder of lattice solvent molecules in the structure of hexaaqua(μ_2 -1,2,4,5-benzenetetracarboxylato)-bis(2,2'-dipyridylamine)dinickel(II) hexahydrate DMSO solvate

DEJAN POLETI^{1*#}, LJILJANA KARANOVIĆ², ALEKSANDAR KREMENOVIĆ² and JELENA ROGAN^{1#}

¹Faculty of Technology and Metallurgy, Karnegijeva 4, 11000 Belgrade and

²Faculty of Mining and Geology, Đušina 7, 11000 Belgrade, Serbia

(Received 4 December 2006, revised 15 March 2007)

Abstract: The crystal structure of the complex $[\text{Ni}_2(\text{btc})(\text{dipya})_2(\text{H}_2\text{O})_6]\cdot 6\text{H}_2\text{O}\cdot \text{DMSO}$ (btc = tetra-anion of 1,2,4,5-benzenetetracarboxylic acid, dipya = 2,2'-dipyridylamine) was refined in the triclinic system, space group $P\bar{1}$, using low temperature (170 K) X-ray diffraction data. The compound consists of binuclear complex entities and lattice solvent molecules making pseudo-layers parallel to the 101 plane and channels parallel to the *b*-axis. The observed structural features were compared with the previously reported results and formula $[\text{Ni}_2(\text{btc})(\text{dipya})_2(\text{H}_2\text{O})_6]\cdot 4\text{H}_2\text{O}$ based on room temperature X-ray diffraction data. A possible arrangement of the disordered lattice solvent molecules located in the structural channels is described and discussed. It is concluded that the layout of these molecules is non-centrosymmetric, although the remaining and main part of the structure is centrosymmetric.

Keywords: nickel(II) complex, 1,2,4,5-benzenetetracarboxylate ion, 2,2'-dipyridylamine, crystal structure, lattice solvent molecules, disorder.

INTRODUCTION

Due to the presence of eight oxygen atoms as potential donor atoms, the tetra-anion of 1,2,4,5-benzenetetracarboxylic acid (btc) is interesting as a ligand suitable for the preparation of inorganic-organic framework structures. In such complexes, btc exhibits a great variety of coordination modes, acting from a simple bidentate ligand bridging two metal centers to a 12-dentate ligand coordinated up to 10 transition metal atoms.^{1–3} As the consequence of the bulkiness of the ligand and the almost free rotation of its COO groups, cavities of different shape and dimensions are characteristic for btc complexes. Some cavities are empty, others are filled by H₂O molecules or different ions. However, complexes with well-defined channels are not so common. Two recent illustrative examples are

* Corresponding author. E-mail: dejan@tmf.bg.ac.yu

Serbian Chemical Society member.

doi: 10.2298/JSC0709767P

$\text{K}(\text{H}_3\text{O})[\text{Fe}_2(\text{btc})\text{F}_2]\cdot 3.5\text{H}_2\text{O}$ with small channels filled with K^+ and H_3O^+ ions, as well as H_2O molecules,⁴ and $(\text{H}_3\text{NC}_3\text{H}_6\text{NH}_3)[\text{Cu}(\text{btc})]\cdot 2\text{H}_2\text{O}$ with two channels of different dimensions containing either 1,3-propanediammonium ions or H_2O molecules.⁵

Another example is the title complex having channels that occupy 17 % of the unit cell volume (190 \AA^3) with an effective cross section of about $2 \times 4 \text{ \AA}$. This property classifies the complex as a microporous material and a potential hydrogen storage medium. In fact, the structure of the complex based on single crystal X-ray diffraction data collected at room temperature was published recently with the formula reported as $[\text{Ni}_2(\text{btc})(\text{dipya})_2(\text{H}_2\text{O})_6]\cdot 4\text{H}_2\text{O}$ (dipya=2,2'-dipyridylamine).⁶ However, during that refinement a problem was experienced with the modeling of some disordered solvent molecules present in the channels parallel to the *b*-axis (Fig. 1a). For this reason, the contribution of these molecules to the structural model was removed using the procedure SQUEEZE implemented in the program PLATON.⁷ At the same time, TG analysis also confirmed the presence of additional lattice solvent molecules. To resolve this ambiguity, it was necessary to recollect X-ray diffraction data at a low temperature (170 K), and the results of this new structure determination are reported here.

RESULTS AND DISCUSSION

Projection of the structure along the *b*-axis and the shape of the molecules of the complex are shown in Figs. 1 and 2, respectively. Two pseudo-layers parallel to the 101 plane, one containing complex units (A) and the other containing solvent molecules only (B), together with channels extending along the *b*-axis, are clearly visible in the crystal packing (Fig. 1a). Within the pseudo-layers A, the complex units are connected by hydrogen bonds and face-to-face π - π stacking interactions, whereas only hydrogen bonds exist within the pseudo-layers B and between pseudo-layers A and B.

In comparison to the room temperature results,⁶ a predictable decrease of the unit cell volume ($\approx 1.4\%$) and atomic displacement parameters was observed at the low temperature. In addition, one O atom from the uncoordinated COO group, which had a very elongated displacement ellipsoid at room temperature, was found to be split in two nearby positions [Fig. 2; $d(\text{O}101-\text{O}102) = 0.689(8) \text{ \AA}$]. However, in addition to the expected H_2O molecules, one dimethyl sulphoxide, DMSO, molecule (DMSO was present in the reaction mixture as a solvent) with a half occupancy was located in the channels. In this way, as shown by the refinement of the low temperature data, the correct formula of the complex is $[\text{Ni}_2(\text{btc})(\text{dipya})_2(\text{H}_2\text{O})_6]\cdot 6\text{H}_2\text{O}\cdot \text{DMSO}$ and not $[\text{Ni}_2(\text{btc})(\text{dipya})_2(\text{H}_2\text{O})_6]\cdot 4\text{H}_2\text{O}$, as reported previously⁶ for the "squeezed", solvent-free data.

The corrected formula was also confirmed by the results of thermogravimetry, TG (the TG curve was published in ref. 6 as Fig. 5). The first step of dehy-

dration occurred in a nearly horizontal step between 53 and 85 °C with the release of two H₂O molecules (mass loss found 3.6 %, calcd. 3.4 %). Very likely, it concerns two disordered and loosely bound lattice H₂O molecules. Dehydration continued up to 126 °C, when all 12 H₂O molecules were lost (found 21.2 %, calcd. 21.5 %). The DMSO molecule was slowly released between 126 and 292 °C (total mass loss for 12H₂O + DMSO: found 29.3 %, calcd. 30.6 %) when an inflection point on the TG curve was observed. Degradation of the desolvated product continued with the loss of btc ligand up to 430 °C (total mass loss: found 58.6 %, calcd. 58.9 %), with possibly decarboxylation (loss of CO₂) as the first step. Subsequently, the complex showed a slow mass loss and the residue did not reach constant mass up to 700 °C.

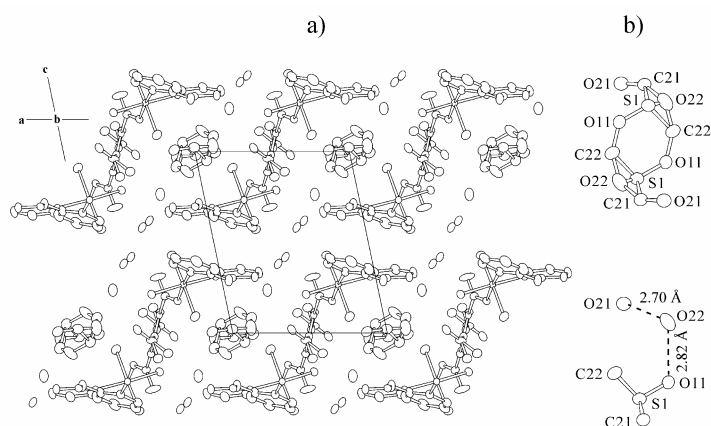


Fig. 1. (a) Crystal packing showing the pseudo-layers of the complex units and lattice solvent molecules, as well as channels extending along the *b*-axis; (b) an enlarged view showing the content of channels as obtained by the crystal structure analysis (top), and a possible arrangement of the disordered H₂O and DMSO molecules (bottom).

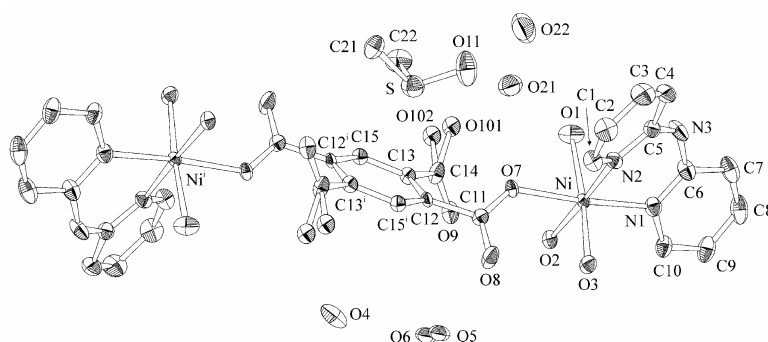


Fig. 2. A view of the centrosymmetric binuclear complex unit with the atomic numbering scheme (displacement ellipsoids are drawn at the 50 % probability level). For the sake of clarity, only the asymmetric part of the lattice solvent molecules is shown and the hydrogen atoms are omitted. Symmetry code: (i) $-x+1, -y+1, -z+2$.

Since the channel solvent molecules (O21, O22 and DMSO) are situated around the symmetry center, they are close to each other (Fig. 1b, top) and cannot co-exist simultaneously, which is in agreement with their half occupancy. Although it was easy to find a plausible layout giving quite reasonable hydrogen bond lengths (dashed lines in Fig. 1b, bottom), this also means that the channel solvent molecules can be allocated over the whole structure in a number of ways. Therefore, this minor part of the structure is non-centrosymmetric, although, as also indicated by the reflection statistics, the remaining and predominant part is centrosymmetric. However, all further attempts to resolve this disorder by refining the structure in space group $P1$ instead of $P\bar{1}$ resulted in higher R -indices and non-positive definite displacement ellipsoids. Very probably, the lack of straightforward conclusions could be related to the diffuse character of the lattice solvent molecules and their negligible contribution to the structural model.

EXPERIMENTAL

The complex was prepared as described previously.⁶ Elemental analysis was performed by standard analytical micromethods. Found (calcd.) %: C, 38.71 (38.27); H, 4.73 (5.02); N 8.18 (8.37). The experimental density was determined at room temperature by the floatation method. TG analysis (30–700 °C range) was performed on a Perkin–Elmer model TGS-2 thermo balance in a dry N₂ atmosphere (flow rate 60 cm³ min⁻¹) at a heating rate of 10 °C min⁻¹.

X-ray diffraction data were collected at 170 K on a STOE IPDS 2 single crystal diffractometer (MoK α radiation, $\lambda = 0.71073$ Å) using a light blue plate-like crystal of approximate dimensions 0.23×0.15×0.06 mm. The data were corrected for Lp and for absorption (integration method, $T_{\min} = 0.8240$, $T_{\max} = 0.9604$). The structure was refined (program SHELXL97)⁸ starting from the known structural model⁶ by the full-matrix least-squares method with anisotropic displacement parameters for all non-H atoms. The hydrogen atoms were treated in three different ways: (a) those connected to C atoms were placed at the geometrically calculated positions and refined using a riding model, (b) those from coordinated and fully occupied H₂O molecules (O1–O4, Fig. 2), as well as the amine H were found in ΔF maps and refined isotropically and (c) the positions of the H atoms from disordered lattice H₂O molecules (O21, O22, O5 and O6, Fig. 2) were determined by comparison of ΔF maps and the positions determined by the Nardelli method.⁹ The latter H atoms are involved in the structural model with all parameters fixed. The refined occupancies of water O5 and O6 atoms [Fig. 2; $d(\text{O5–O6}) = 0.68(3)$ Å] were 0.79(2) and 0.21(2), respectively. Occupancies of DMSO and some other lattice H₂O molecules (O21 and O22, Fig. 2) were tested in independent refinements; in all cases the occupancies were near to 0.5 and the refinement was finished with these values fixed to 0.5. The final results of crystal structure determination are summarized as follows.

Empirical formula: C₃₂H₅₀N₆Ni₂O₂₁S; $M_r = 1004.26$; crystal system: triclinic; space group: $P\bar{1}$; unit cell parameters: $a = 9.290(1)$, $b = 10.863(1)$, $c = 11.997(2)$ Å, $\alpha = 67.40(1)$, $\beta = 77.04(1)$, $\gamma = 84.79(1)^\circ$; unit cell volume: $V = 1089.2(3)$ Å³; $Z = 1$; calculated density: $\rho_x = 1.531$ g cm⁻³; experimental density (room temperature): $\rho_m = 1.49(2)$ g cm⁻³; absorption coefficient: $\mu = 0.998$ mm⁻¹; $F(000) = 524$; range for data collection: $1.88^\circ < \theta < 25.35^\circ$; index ranges: $-11 \leq h \leq 11$, $-13 \leq k \leq 13$, $-13 \leq l \leq 14$; reflections collected: 14262; reflections independent: 3980 ($R_{\text{int}} = 0.0800$); number of refined parameters: 344; number of restraints: 11; $S = 1.165$; R indices [$I > 2\sigma(I)$]: $R_1 = 0.0592$, $wR_2 = 0.1065$; R indices (all data): $R_1 = 0.0826$, $wR_2 = 0.1135$; the largest difference peak and hole: 0.99 and -0.46 e Å⁻³.

Supplementary materials

CCDC 627247 contains the supplementary crystallographic data for this paper. These data can be obtained free of charge from The Cambridge Crystallographic Data Center via www.ccdc.cam.ac.uk/data_request/cif.

Acknowledgements: The financial support of the Ministry for Science of the Republic of Serbia (Grants No. 142030 and 141027) is gratefully acknowledged. The authors are indebted to Dr. Volker Kahlenberg, Institut für Mineralogie und Petrographie, Leopold Franzens Universität Innsbruck, Austria, for providing the diffractometer facilities.

ИЗВОД

НЕУРЕЂЕНОСТ МОЛЕКУЛА РАСТВАРАЧА У СТРУКТУРИ ХЕКСААКВА(μ_2 -1,2,4,5-БЕНЗЕНТЕТРАКАРБОКСИЛАТО)-БИС(2,2'-ДИПИРИДИЛАМИН)ДИНИКАЛ(II)-ХЕКСАХИДРАТА-DMSO СОЛВАТА

ДЕЈАН ПОЛЕТИ¹, ЉИЉАНА КАРАНОВИЋ², АЛЕКСАНДАР КРЕМЕНОВИЋ² и ЈЕЛЕНА РОГАН¹

¹Технолошко-металуршки факултет, Карнегијева 4, 11000 Београд и

²Рударско-геолошки факултет, Ђушица 7, 11000 Београд

Кристална структура комплекса $[\text{Ni}_2(\text{btc})(\text{dipa})_2(\text{H}_2\text{O})_6]\cdot 6\text{H}_2\text{O}\cdot \text{DMSO}$ (btc = тетраанјон 1,2,4,5-бензентетракарбоксилне киселине, dipa = 2,2'-дипиридиламин) утањена је у триклиничном систему, просторна група $P\bar{1}$, на основу података добијених рендгенском дифракцијом на ниској температури (170 К). Једињење се састоји од бинуклеарних комплексних јединки и некоординираних молекула растварача, који формирају псеудо-слојеве паралелне равни 101 и канале паралелне *b*-оси. Структурне карактеристике комплекса упоређене су са раније објављеним резултатима и формулом $[\text{Ni}_2(\text{btc})(\text{dipa})_2(\text{H}_2\text{O})_6]\cdot 4\text{H}_2\text{O}$, који су били засновани на подацима прикупљеним на собној температури. У раду је описан и дискутован могући распоред неуређених молекула растварача који се налазе у раније поменутих каналама. Закључено је да распоред тих молекула мора бити нецентросиметричан, иако је преостали и највећи део структуре центросиметричан.

(Примљено 4. децембра 2006, ревидирано 15. марта 2007)

REFERENCES

1. H. Kumagai, C. J. Kepert, M. Kurmoo, *Inorg. Chem.* **41** (2002) 3410
2. L.-J. Zhang, J.-Q. Xu, Zh. Shi, X.-L. Zhao, T.-G. Wang, *J. Solid State Chem.* **32** (2003) 32
3. H. Kumagai, K. W. Chapman, C. J. Kepert, M. Kurmoo, *Polyhedron* **22** (2003) 1921
4. M. Sonselme, M. Riou-Cavellec, G. Férey, *Solid State Sci.* **4** (2002) 1419
5. D. Poleti, Lj. Karanović, *J. Serb. Chem. Soc.* **70** (2005) 1441
6. J. Rogan, D. Poleti, Lj. Karanović, *Z. Anorg. Allg. Chem.* **632** (2006) 133
7. a) P. v. d. Sluis, A. L. Spek, *Acta Crystallogr.* **A46** (1990) 194; b) A. L. Spek, *Acta Crystallogr.* **A46** (1990) c34
8. G. M. Sheldrick, *Program for the refinement of crystal structures, SHELXL97*, University of Göttingen, Germany, 1997
9. M. Nardelli, *J. Appl. Cryst.* **32** (1999) 563.



Characterization of a surface modified carbon cryogel and a carbon supported Pt catalyst

BILJANA M. BABIĆ¹, BRANKA V. KALUĐEROVIĆ¹, LJILJANA M VRAČAR²,
VELIMIR RADMILOVIĆ³ and NEDELJKO V. KRSTAJIĆ^{2*}

¹Vinča Institute of Nuclear Sciences, P.O.B. 522, 11001 Belgrade, ²Faculty of Technology and Metallurgy, University of Belgrade, Karnegijeva 4, 11120 Belgrade, Serbia and ³National Center for Electron Microscopy, LBLN University of California, Berkeley, USA

(Received 27 November 2006, revised 22 January 2007)

Abstract: A carbon cryogel, synthesized by carbonization of a resorcinol/formaldehyde cryogel and oxidized in nitric acid, was used as catalyst support for Pt nanoparticles. The Pt/C catalyst was prepared by a modified polyol synthesis method in an ethylene glycol (EG) solution. Characterization by nitrogen adsorption showed that the carbon cryogel support and the Pt/C catalyst were mesoporous materials with high specific surface areas ($S_{\text{BET}} > 400 \text{ m}^2 \text{ g}^{-1}$) and large mesoporous volumes. X-Ray diffraction of the catalyst demonstrated the successful reduction of the Pt precursor to metallic form. TEM Images of the Pt/C catalyst and Pt particle size distribution showed that the mean Pt particle size was about 3.3 nm. Cyclic voltammetry (CV) experiments at various scan rates (from 2 to 200 mV s^{-1}) were performed in 0.5 mol dm^{-3} HClO_4 solution. The large capacitance of the oxidized carbon cryogel electrode, which arises from a combination of the double-layer capacitance and pseudocapitance, associated with the participation of surface redox-type reactions was demonstrated. For the oxidized carbon cryogel, the total specific capacitance determined by $1/C$ vs. $v^{0.5}$ extrapolation method was found to be 386 F g^{-1} . The hydrogen oxidation reaction at the investigated Pt/C catalyst proceeded as an electrochemically reversible, two-electron direct discharge reaction.

Keywords: carbon cryogel, platinum catalyst, hydrogen oxidation, fuel cell.

INTRODUCTION

Porous carbon, due to its high surface area and pore accessibility, excellent thermal and chemical stability, as well as good electrical conductivity, is an extremely attractive and competitive material for application in electrochemistry.

Carbon aerogels and cryogels are a special class of materials,^{1–4} which are usually formed from the sol–gel polycondensation of resorcinol and formaldehyde, followed by supercritical or freeze drying, and subsequent pyrolysis. The resulting carbon aerogels and cryogels are electrically conductive, in contrast to all other

* Corresponding author. E-mail: nedeljko@tmf.bg.ac.yu
doi: 10.2298/JSC0709773B

types of organic and inorganic aerogels, which are generally insulating materials. The need to control the structure and properties of porous carbon aerogels and cryogels has led to their increased use as electrode materials in advanced energy storage devices and other electrochemical devices.^{5,6}

Interest in the application of a carbon aerogels as catalyst supports results from their unique electronic and morphological structure and their high surface area, the last characteristic being essential for the optimal activity of a catalyst for electrochemical reactions, since they occur on the surface of the particles. An increase in surface area of Pt/C catalyst is usually achieved by deposition of nano-sized Pt particles on a highly porous carbon support, using a variety of preparation methods.^{7–12}

It is now generally accepted that the size and distribution of the catalyst particles are affected by the physical structure of the support (porosity and surface area) and the nature of the catalyst precursor. Since carbon aerogels and cryogels have a large specific surface and many unsaturated carbon atoms, these atoms react with heteroatoms from environment (O, H, N). The chemical properties of these materials arise mostly from incorporation of oxygen, forming oxides, carboxylic, phenolic, lactonic and etheric groups which are responsible for the acid/base and the redox properties of a carbon material. Surface modification (oxidation) of these materials gives a more hydrophilic surface with a relatively large number of oxygen containing surface groups.¹³ Modification of the surface chemistry results in a significant change in the loading capacity. However, conflicting results concerning the influence of oxidative pretreatments of the carbon on the catalyst dispersion have regularly been reported in the literature. According to some references, for carbon supported platinum catalysts prepared by the impregnation method, both the dispersion and resistance to sintering increase with increasing number of oxygen surface groups on the support.^{14–17} The opposite conclusion was also reported for similar catalytic systems, namely, that the presence of oxygen surface groups on the carbon leads to lower metal dispersions and lower resistance to sintering.^{18–20}

In this article, the preparation and electrochemical characterization of a new type of oxidized carbon cryogel employed as a catalyst support for Pt nanoparticles is reported. The relation between the specific surface area of the carbon support and the particle size distribution of the Pt catalyst, as well as the effect of carbon oxygen surface groups on their dispersion and, consequently, on their catalytic activity for the hydrogen oxidation reaction were investigated.

EXPERIMENTAL

Carbon support and catalyst preparation

The carbon cryogel was synthesized by polycondensation of resorcinol and formaldehyde, according to a method described in the literature.²¹ Sodium carbonate was used as the basic catalyst. The solution was prepared from resorcinol (R), (99 % purity, Merck) and formaldehyde (F), 36 % methanol stabilized (Fluka Chemie), sodium carbonate (C), p.a. quality (Merck) and deionized water (W). The molar ratio between R and F was 0.5, the molar ratio between R and C was 100 and fi-

nally, the mass ratio between R and W was 20. The mixture was decanted into a glass tube, sealed and placed 2 days at 25 °C, 1 day at 50 °C and 4 days at 85 °C. The RF gel was immersed in a 10-times volume of *t*-butanol and rinsed to give the liquid contained in the gel with *t*-butanol. The sample was freeze-dried at -30 °C for 24 h. The vacuum during twenty hours of freeze-drying was around 4 mbar. The carbon cryogel was prepared by carbonization of the gel in a conventional furnace, in nitrogen flow, at 800 °C and the furnace was cooled at room temperature after pyrolysis.

To study the influence of surface oxidation, 250 mg of carbon cryogel was immersed in 50 cm³ of 5 mol dm⁻³ HNO₃, for 3 h, at room temperature. Subsequently the sample was filtered, washed with distilled water and dried at 80 °C for 8 h.

The modified ethylene glycol method (EG) for the preparation of the Pt catalyst²² can be described as follows: hexachloroplatinic(IV) acid (H₂PtCl₆) solution was dissolved in ethylene glycol (EG) solution containing 5 vol % of water. To adjust the pH of the solution to the value of 12, the required amount of 1.0 mol dm⁻³ NaOH (in EG) was added immediately to the EG solution. The so-prepared solution was added dropwise, under mechanical stirring to an ultrasonically dispersed carbon ethylene glycol solution. The temperature was increased to 130 °C and kept constant for 2 h in order that the platinum salt could be adequately reduced to platinum metal. The whole preparation process was conducted under a dynamic argon atmosphere. After filtration and washing, the filter cake was dried under vacuum at 60 °C for 12 h. The Pt loading of the all catalysts was always 20 wt. %. The Pt/C catalysts were finally heat-treated at 300 °C under a H₂ atmosphere for 1 h.

Characterization of the oxidized carbon cryogel and oxidized carbon cryogel with Pt nanoparticles

Adsorption and desorption isotherms of N₂ of the carbon cryogel were measured at -196 °C using the gravimetric McBain method. From the isotherms, the specific surface area, S_{BET} , pore size distribution, mesopore including external surface area, S_{meso} , and micropore volume, V_{mic} , for the samples were calculated. The pore size distribution was estimated by applying the BJH (Barret, Joyner, Halenda) method²³ to the desorption branch of the isotherms and the mesopore surface and micropore volume were estimated using the high resolution α_s plot method.²⁴⁻²⁶ The micropore surface, S_{mic} , was calculated by subtracting S_{meso} from S_{BET} .

Oxidized carbon cryogel and C/Pt catalyst were characterized by recording their powder X-ray diffraction (XRD) patterns on a Siemens D500 X-ray diffractometer using CuK α radiation with a Ni filter. The 2θ angular regions between 5 and 80° were examined at a scan rate of 0.02° s⁻¹, with an angular resolution of 0.02°.

Transmission electron microscopy (TEM) measurements were performed at the National Center for Electron Microscopy (NCEM) using FEI (Fillips electronic instruments) CM200 super-twin and CM300 ultra-twin microscopes operating at 200 and 300 kV and equipped with the Gatan 1k×1k and 2k×2k CCD cameras, respectively. Specimens for transmission electron microscopy were prepared by suspending the catalyst powder in ethanol using an ultrasonic bath. This suspension was dropped onto clean holey carbon grids and dried in air. The particle size distributions were determined from images of, an average, 20 different regions of the catalyst; each region contained 10–20 particles. The particle shape was determined by real space crystallography using high-resolution images taken from particles near or on the edge of the carbon substrate, and/or by numerical Fourier filtering of the digitized image intensity spectrum of particles on top of the carbon.

Cell and electrode preparation

Two milligram of sample was ultrasonically suspended in 1.0 ml of a water–methanol mixture (v/v = 1/1) and 50 μ l of Nafion solution (5 wt. % Aldrich solution) to prepare a sample ink. Then, 12.5 μ l of ink was transferred with an injector to a clean gold disk electrode (6 mm diameter, with an area of 0.28 cm²). After volatilization of the water–methanol, the electrode was heated at 80 °C for 10 min.

A conventional RDE and three-compartment cell were used. The working electrode compartment was separated from the other two compartments by fritted glass discs. All measurements were

performed in $0.5 \text{ mol dm}^{-3} \text{ HClO}_4$ solution (Spectrograde, Merck), prepared in highly pure water at $20 \text{ }^\circ\text{C}$. The counter electrode was a platinum sheet of 5 cm^2 geometric area. A platinum plated Pt reversible hydrogen electrode (RHE) in the same solution as the working electrode was used as the reference electrode.

Electrode characterization

Electrochemical characterization was performed using an EG&G 273 instrument. Cyclic voltammetry was performed in $0.5 \text{ mol dm}^{-3} \text{ HClO}_4$ saturated with high purity nitrogen which was continuously bubbled through the working electrode compartment. The CVs were recorded in the potential range from 0.03 to 1.20 V (RHE) at a rotating speed of 2500 rpm at a scan rate in the range from 2 to 200 mV s^{-1} .

RESULTS AND DISCUSSION

Adsorption isotherms – BET experiments

Nitrogen adsorption isotherms for the oxidized carbon cryogel and Pt/C catalyst, as the amount of N_2 adsorbed as function of the relative pressure at $-196 \text{ }^\circ\text{C}$, are shown in Fig. 1. According to the IUPAC classification, the isotherms are of type-IV with a small hysteresis loop which is associated with mesoporous materials. The specific surface area, calculated by the BET equation, S_{BET} , is listed in Table I, together with the corresponding value for the non-oxidized sample, which was given in a previous paper.²¹ In comparison with this result, it is obvious that surface oxidation with nitric acid leads to decrease of the overall specific surface (from 573 to $440 \text{ m}^2 \text{ g}^{-1}$), until the process of loading of the Pt nanoparticles increased the specific surface area of the oxidized sample. On the contrary, the value of S_{BET} and mesoporous surface area of non-oxidized carbon cryogel support decreased with the addition of nano-sized Pt particles.

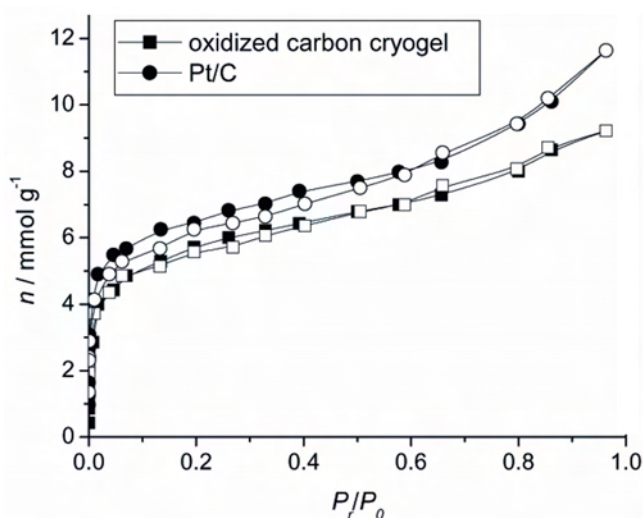


Fig. 1. Nitrogen adsorption isotherms, as the amount of N_2 adsorbed as a function of the relative pressure for oxidized carbon cryogel and Pt/C samples. Solid symbols – adsorption, open symbols – desorption.

The pore size distribution of the oxidized carbon cryogel and Pt/C samples are shown in Fig. 2. The distribution has a single peak and the value for the pore

radius of the maximum of observed curves, r_{peak} , was between 1–2 nm. Both samples (support and catalyst) had sharp and similar pore size distributions.

TABLE I. Porous properties of the carbon cryogel support and Pt/C samples

Sample	S_{BET} $m^2 g^{-1}$	S_{meso} $m^2 g^{-1}$	S_{micro} $m^2 g^{-1}$	V_{micro} $cm^3 g^{-1}$	C_{tot} $F g^{-1}$
Oxidized carbon cryogel	440	145	295	0.14	386
Oxidized carbon cryogel + 20 wt. % Pt	501	185	316	0.15	–
Non-oxidized carbon cryogel ²¹	573	258	315	0.15	124
Non-oxidized carbon cryogel + 20 wt.% Pt	517	234	283	0.13	–

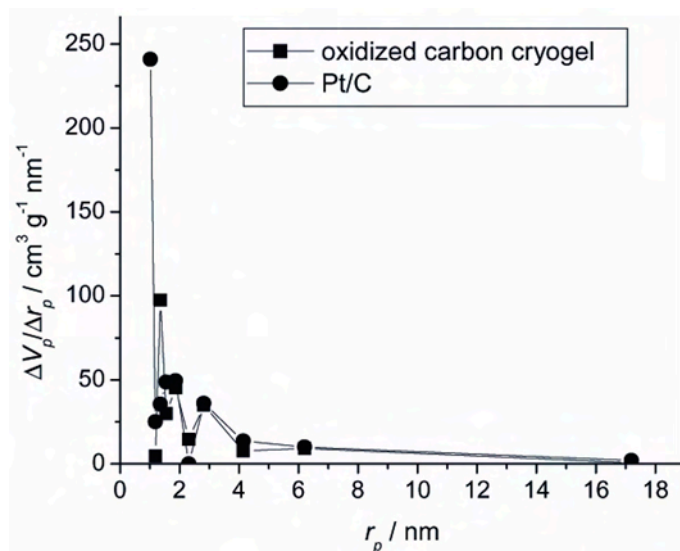


Fig. 2. Pore size distribution of the oxidized carbon cryogel and Pt/C catalyst.

The α_s plots, obtained on the basis of the standard nitrogen adsorption isotherms for the support and catalyst are shown in Fig. 3. The straight line in the medium α_s region gives a mesoporous surface area including the contribution of external surface, S_{meso} , determined by its slope, until the micropore volume, V_{mic} , is determined by the intercept. The calculated porosity parameters (S_{meso} , S_{mic} and V_{mic}) are given in Table I and they show that the mesoporous specific surface decreased as a consequence of surface oxidation.²¹ Pt loading also slightly increased mesoporous surface.

It is well known¹⁵ that oxidation treatments of carbons lead to the formation of different surface acid groups, mainly carboxylic, anhydride, lactone, phenol and carbonyl groups. Carboxylic and anhydride groups are considered as strong acid ones, while the other ones display weaker acid properties. Moreover, it has been reported that the stronger acid groups lead to CO_2 desorption at low temperatures during temperature-programmed desorption (TPD) experiments, in contrast to the weaker acid sites which lead to CO -desorption at higher temperatures.¹⁵ The oxida-

tive treatment of the carbon cryogel with HNO_3 solution, as was previously mentioned, results in a reduction of the specific surface area and porosity of the support.

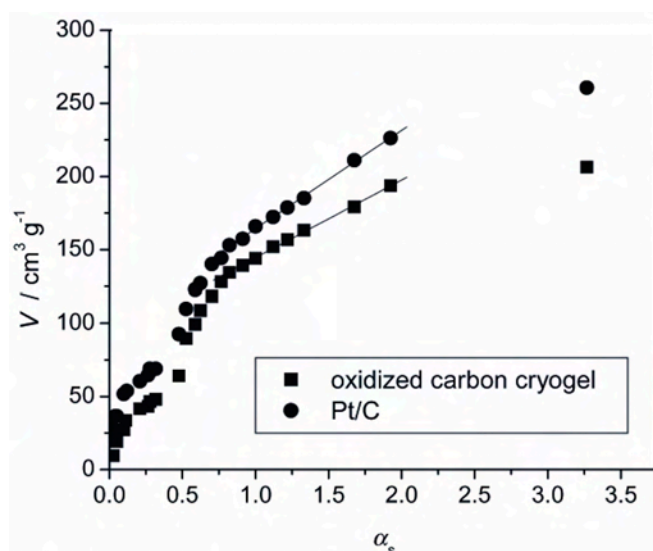


Fig. 3. α_s Plots for the nitrogen adsorption isotherm of the oxidized carbon cryogel and Pt/C catalyst, based on the standard isotherm of non-porous carbon.

During the activation process of Pt/C samples under a H_2 atmosphere at $300\text{ }^\circ\text{C}$ complex processes could take place at the oxidized carbon support. Thus, the decomposition of strong acid groups into CO_2 and their transformation into CO by combination with atomic hydrogen produced by dissociation of H_2 on the metallic Pt particles.¹⁵ The increase in the porosity and specific surface area of the oxidized carbon cryogel sample after Pt loading and the final activation process could be explained by the decomposition of the oxygenated surface groups and formation of gaseous products (CO_2 and CO), which increase the pore volume.

XRD Analysis of Pt catalyst

The XRD patterns of the oxidized carbon cryogel and the Pt/C samples are shown in Fig. 4. XRD Pattern of the oxidized carbon cryogel, *i.e.*, without characteristic peaks, proves the amorphous structure of the carbon material. The characteristic diffraction peaks of face centered cubic (fcc) phase Pt for the Pt/C catalyst demonstrate that a successful reduction of the Pt precursor to metallic Pt had been achieved. The diffraction peaks at about 39° and 46° , due to the Pt (111) and (200) plane, respectively, represent the typical character of a crystalline Pt face that is a fcc phase. There are no other distinct reflection peaks in all patterns in the investigated 2θ range than the two peaks already mentioned above, indicating that in these in-house supported Pt catalysts, the Pt fcc crystal structure prevailed.

TEM Analysis

The low magnification TEM micrograph (Fig. 5) shows a very uniform size distribution of the Pt particles, with a mean particle size of about 3.3 nm. The hi-

stogram of Pt particle size distribution of Pt/C catalyst was obtained based on measurements of over 300 Pt particles.

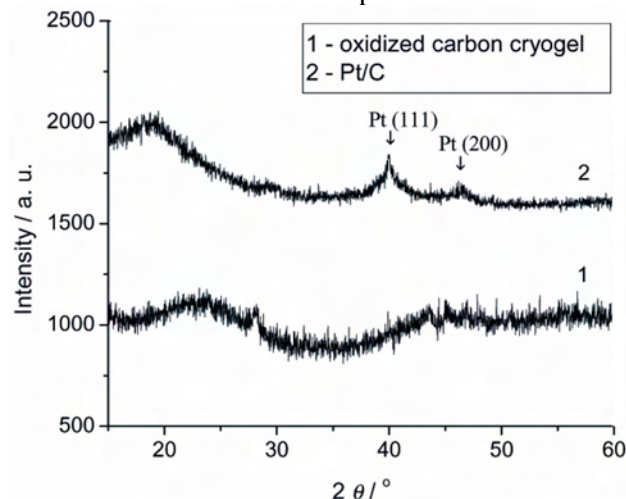


Fig. 4. XRD Patterns of the oxidized carbon cryogel and Pt/C catalyst.

The atomically resolved image in Fig. 6 shows rows of Pt atoms with a spacing corresponding to the (200) and (111) planes of the face centered cubic Pt nanoparticles, as indicated in the corresponding digital diffractograms, also shown in Fig. 6. The Pt particles have the common cubo-octahedral shapes. Twinned particles were observed occasionally with the same (111) twinning plane as in some other Pt based catalysts.²⁷

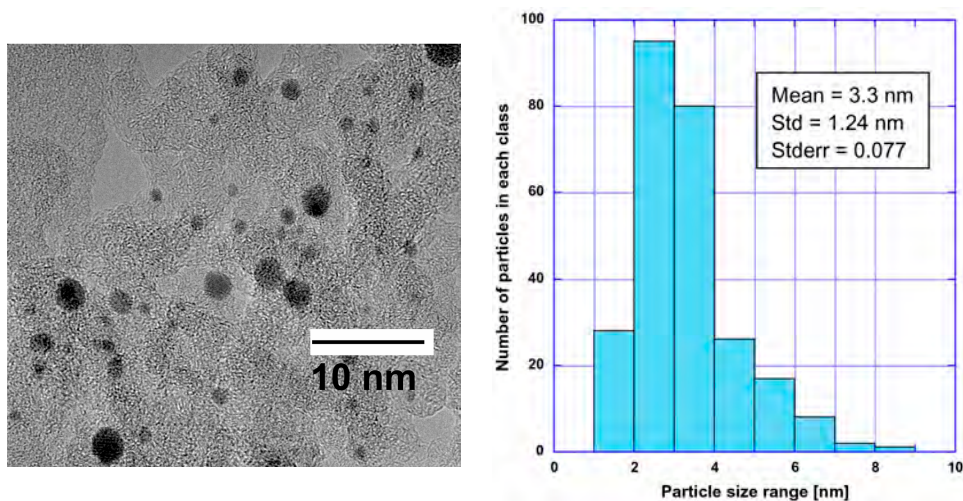


Fig. 5. TEM Micrographs of Pt nanoparticles on the oxidized carbon cryogel (Pt/C catalyst). The lower magnification shows the spread of the Pt particle size distribution. The corresponding size histogram is also shown.

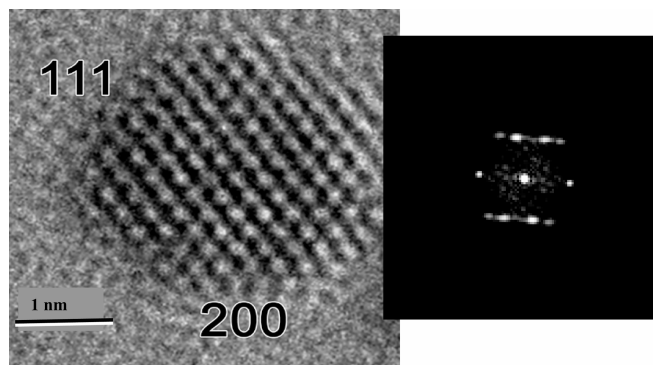


Fig. 6. High resolution image showing one-dimensional lattice fringes of the (111) lattice planes in Pt.

Cyclic voltammetry experiments

Cyclic voltammograms (CV) of the oxidized carbon cryogel (C) and Pt/C samples, at different scan rates ($2\text{--}200\text{ mV s}^{-1}$) are shown in Figs. 7a and 7b, respectively. The cyclic voltammetry experiments showed that, due to the oxidation process, the basic voltammogram is different from that observed for a non-oxidized carbon cryogel.²¹ The voltammograms of the oxidized sample show, to some extent, deviation from a rectangular shape and the presence of reversible redox peaks connected with pseudo-Faradic reactions. Chemical treatment of the carbon cryogel with nitric acid significantly increased the voltametric charge. Although the oxidation process decreased the specific surface, the overall voltametric charge increased remarkably due to redox processes of the functional groups on the surface (pseudocapacitance).

The specific capacitance decreased with increasing the scan rate (Fig. 7). It was shown²¹ that the voltametric charge and/or capacitance, should be a linear function of $\nu^{-0.5}$ and the reciprocal capacitance should be a linear function of $\nu^{0.5}$. The extrapolation of the $1/C - \nu^{0.5}$ line to $\nu^{0.5} \rightarrow 0$ gives the capacitance at an infinity slow scan rate, *i.e.*, under the conditions of reversibility. Under the condition of a slow scan rate, it was assumed that the charging process is able to reach equilibrium at the whole surface (external and internal), meaning that the specific capacitance measured at this scan rate corresponds to the total capacitance. For the oxidized carbon cryogel, the so-determined total specific capacitance was found to be 386 F g^{-1} (the total specific capacitance of the non-oxidized carbon cryogel was 124 F g^{-1}). Literature data show that the specific capacitances of other carbon materials^{28–33} are significantly lower than the present measured value and for this reason the present result could be very important for further investigations and applications of surface modified carbon cryogels in supercapacitors.

Cyclic voltammetry measurements on the Pt/C electrode were performed to determine the electrochemical surface area of the Pt and to elucidate the adsorption properties of the catalyst. The electrochemically active surface area of the ca-

talyst was calculated from the charge associated with the anodic desorption peak of underpotential deposited (UPD) hydrogen at the Pt nano-sized particles. The base line was taken by extrapolation of the double-layer region of the voltammogram. The electrochemically active surface area of the catalysts (S_{easa}) was calculated from the measured charge assuming $210 \mu\text{C cm}^{-2}$ as the charge of full coverage with adsorbed hydrogen. The electrochemical surface area for this electrocatalyst was found to be 2.36 cm^2 ($47 \text{ m}^2 \text{ g}^{-1}$).

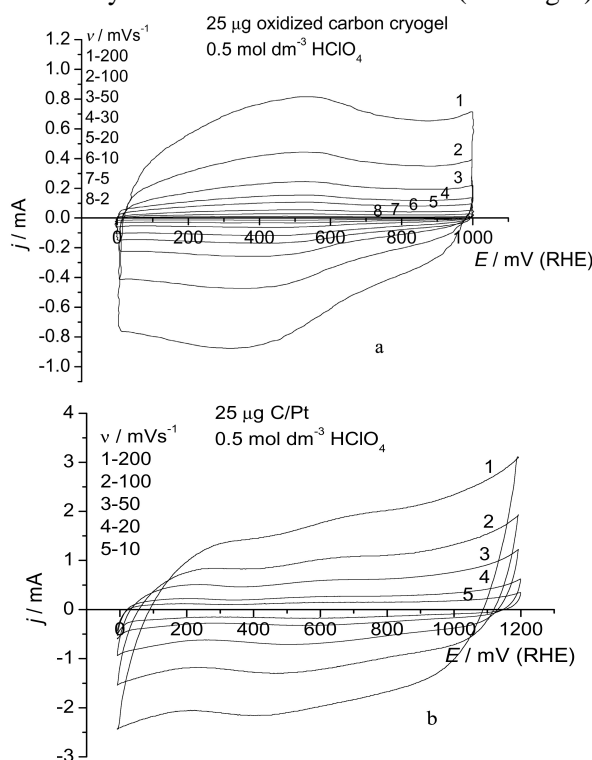


Fig. 7. Cyclic voltammograms of the oxidized carbon cryogel and Pt/C catalyst a) oxidized carbon cryogel b) Pt/C in $0.5 \text{ mol dm}^{-3} \text{ HClO}_4$ solution at 293 K.

The total surface area of Pt catalyst, S_{tot} , was calculated from the corresponding values of the mean particle size, d , and the density of Pt metal, $\rho = 4.24 \text{ cm}^3$. The Pt utilization efficiency for the RDE was determined using the following equation: $\text{Pt}_{\text{u.e.}} = S_{\text{easa}} / S_{\text{tot}}$. The Pt utilization efficiency was 56 %. However, the Pt utilization efficiency on the non-oxidized carbon cryogel support was around 88 %.²¹ This means that the presence of carboxyl surface groups on the oxidized carbon cryogel support, under the present conditions, results in a lower utilization efficiency and a lower metal dispersion during the reduction of the anionic precursor, PtCl_6^{2-} in ethylene glycol at 130 °C. Electrostatic repulsion between the anionic entities and the acid groups of the oxidized carbon support can explain the low dispersion of Pt particles. This interpretation is in line with that proposed for a series of Pt catalysts supported on graphitized carbon blacks.¹⁵ The-

se results also indicate that the control of the final metallic dispersion of a high surface area carbon-supported Pt catalyst also depends on the presence of oxygen surface groups on the carbon support.

Kinetics of the hydrogen oxidation at the Pt/C catalyst

The hydrogen oxidation polarization curves for several rotation speeds, obtained at a scan rate of 2 mV s^{-1} in $0.5 \text{ mol dm}^{-3} \text{ HClO}_4$ solution, on the Pt/C electrode are presented in Fig. 8. The current is increased rapidly with potential on each curve, reaching a limiting value at a potential of *ca.* 60 mV (RHE).

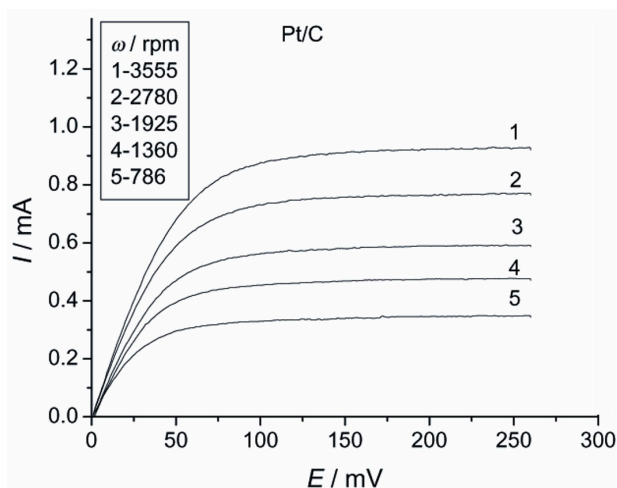


Fig. 8. Current vs. potential curves of the electrocatalytic oxidation of H_2 on the Pt/C catalyst ($T = 293 \text{ K}$, $\nu = 2 \text{ mV s}^{-1}$), on RDE electrode, in $0.5 \text{ mol dm}^{-3} \text{ HClO}_4$ solution under a H_2 atmosphere.

In order to obtain information about the kinetics of the HOR on the investigated electrode, the RDE polarization data were analyzed in terms of mass transport corrected Tafel diagrams. The kinetic equations used for such an analysis were derived considering the reversible or irreversible nature of the electrochemical reaction.

The kinetic equations for a reversible and an irreversible electrochemical reaction³⁴ can respectively be given as:

$$E = E_1^\ominus - \frac{2.303RT}{nF} \log \left(\frac{I_D - I}{I_D} \right) \quad (1)$$

$$E = E_2^\ominus + \frac{2.303RT}{\alpha nF} \log \left(\frac{I_D I}{I_D - I} \right) \quad (2)$$

where E_1^\ominus and E_2^\ominus are current independent constants and α is the charge transfer coefficient. Equation (1) is used to obtain mass transport corrected Tafel diagrams if the reaction is assumed to be reversible, while Eq. (2) is employed to obtain mass transport corrected Tafel diagrams if the reaction is irreversible. If one or another condition is satisfied, according to Eqs. (1) or (2), the plots $E - \log [(I_L - I)/I_L]$

or $E - \log [I_L \times I / (I_L - I)]$, respectively, should be linear with the points independent of the rotation rate.

It is clear that linear plots practically independent of the rotation speed were obtained when reversible kinetic were assumed (Fig. 9). The slope of the linear plot is very close to the theoretical value of 29 mV dec^{-1} . However, there is no agreement with the prediction of Eq. (2). In this case, the linear relationship of $E - \log [I_L \times I / (I_L - I)]$ is also established in the potential range where the correction for the reverse reaction is not necessary, but the linear plots depend on the rotation speed and the slopes are around 28 mV dec^{-1} , which is only half of the predicted value of 58 mV dec^{-1} . Therefore, the most reasonable assumption that electrochemical hydrogen oxidation reaction at the investigated Pt/C catalyst is reversible seems to be experimentally justified.

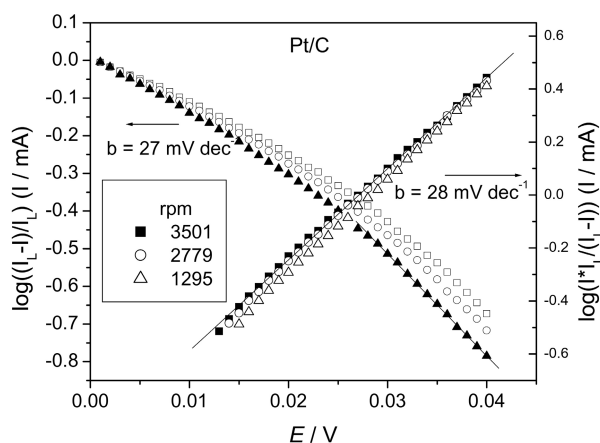


Fig. 9. Plots of $E - \log [(I_L - I)/I_L]$ and $E - \log [I_L \times I / (I_L - I)]$. Data taken from the RDE plots in Fig. 8.

The mechanism of the HOR has been extensively studied in acidic and base solutions.^{35,36} The chance of extracting $2 e^-$ directly from H_2 in a direct discharge reaction is usually considered low. However, the kinetic analysis conducted in this paper shows that the HOR occurs as a reversible two-electron direct discharge reaction at the investigated Pt/C catalyst.

CONCLUSION

The effect of the specific surface area and oxygen surface groups of a carbon support on the catalytic properties of Pt/C were investigated using an oxidized carbon cryogel. The catalyst was prepared by a modified polyol synthesis method and heat-treatment under a hydrogen atmosphere at $300 \text{ }^\circ\text{C}$. The results show that the specific surface area of the oxidized carbon cryogel support (S_{BET}) decreases after oxidation with HNO_3 . However, the calculated total specific capacitance determined from CV experiments significantly increased from 124 to 386 F g^{-1} due to oxidative-reductive processes on the surface functional groups (pseudocapacitance).

The presence of oxygen surface groups on the carbon led to low metal dispersions and utilization efficiency (56 %). The mean Pt particle size on the oxidi-

zed carbon cryogel was 3.3 nm. These results also indicate that the control of the final metallic dispersion of a high surface area, carbon-supported metal catalyst depends also on the presence of oxygen surface groups on the carbon support.

Analysis of the hydrogen oxidation reaction showed that this reaction occurs at the investigated Pt/C catalyst as a reversible two-electron direct discharge reaction.

Acknowledgements: This study was supported by the Ministry of Science of the Republic of Serbia, under Contracts No. 142016 and 142038 and partially by the Office of Basic Energy Sciences of the U.S. Department of Energy under contract No. DE-AC0376SF00098.

ИЗВОД

КАРАКТЕРИЗАЦИЈА ПОВРШИНСКИ МОДИФИКОВАНОГ УГЉЕНИЧНОГ КРИОГЕЛА И ПЛАТИНА/УГЉЕНИК КАТАЛИЗАТОРА

БИЉАНА М. БАБИЋ¹, БРАНКА В. КАЛУЂЕРОВИЋ¹, ЉИЉАНА М. ВРАЧАР²,
ВЕЛИМИР РАДМИЛОВИЋ³ и НЕДЕЉКО В. КРСТАЈИЋ²

¹Институт за нукларне науке "Винча", б. бр. 522, 11000 Београд, ²Технолошко-металуришки факултет,
Карнегијева 4, 11120 Београд и ³National Center for Electron Microscopy,
LBLN University of California, Berkeley, USA

Угљенични криогел, синтетизован карбонизацијом резорцинол/формалдехид криогела и оксидован у азотној киселини употребљен је као носач катализатора за наночестице платине. Платина/угљеник катализатор припремљен је модификованом полиол методом, у раствору етилен-гликола. Карактеризација адсорпцијом азота показала је да су угљенични криогел и платина/угљеник катализатор мезопорозни материјали високе специфичне површине (> 400 m² g⁻¹) и мезопорозне запремине. Метода рентгенске дифракције показала је да је постигнута редукција прекурсора платине до металног облика. ТЕМ анализа платина/угљеник катализатора и расподела величине честица платине показује да је средњи пречник честица око 3,3 nm. Испитивања методом цикличне волтаметрије, при различитим брзинама промене потенцијала (2 – 200 mV s⁻¹), показала су да електрода од оксидованог угљеничног криогела има веома висок капацитет који потиче од комбинације капацитета двојног слоја и псеудо-капацитета. Укупан специфични капацитет оксидованог угљеничног криогела износи 386 F g⁻¹. Реакција оксидације водоника на наночестицама платине одвија се по механизму реверзибилне директне оксидације.

(Примљено 27. новембра 2006, ревидирано 22. јануара 2007)

REFERENCES

1. R. W. Pekala, *J. Mater. Sci.* **24** (1989) 3221
2. R. W. Pekala, C. T. Alviso, X. Lu, J. Gross, *J. Non-Cryst. Solids* **188** (1995) 34
3. H. Tamon, H. Ishizaka, T. Yamamoto, T. Suzuki, *Carbon* **37** (1999) 2049
4. T. Yamamoto, T. Sugimoto, T. Suzuki, S. R. Mukai, H. Tamon, *Carbon* **40** (2002) 1345
5. B. Babić, D. Đokić, N. Krstajić, *J. Serb. Chem. Soc.* **70** (2005) 21
6. K. L. Yang, S. Yiacuomi, C. Tsouris, *J. Electroanal. Chem.* **540** (2003) 159
7. Y. Yang, Y. Zhou, C. Cha, W. M. Carrol, *Electrochim. Acta* **38** (1993) 2333
8. Y. Gao, F. Naguchi, T. Mitamura, H. Kita, *Electrochim. Acta* **37** (1992) 1327
9. Y. Takusu, N. Ohashi, X.-G. Zhang, Y. Murukami, H. Minagawa, S. Sato, K. Yahikozawa, *Electrochim. Acta* **41** (1996) 2595
10. S. Hirano, J. Kim, S. Srinivasan, *Electrochim. Acta* **42** (1997) 1587

11. M. T. Reetz, W. Helbig, *J. Am. Chem. Soc.* **116** (1994) 7401
12. C. Prado–Burguete, A. Linares–Solano, F. Rodríguez–Reinoso, C. S. M de Lecea, *J. Catal.* **115** (1989) 98
13. Lj. R. Radović, F. Rodríguez–Reinoso, in *Chemistry and Physics of Carbon*, P. A. Throver, Ed., Dekker, New York, Vol. 25 (1996) p. 243
14. G. C. Torres, E. L. Jablonski, G. T. Baronetti, A. A. Castro, S. R. de Miguel, O. A. Scelza, M. D. Blanco, M. A. Peña Jiménez, J. L. G Fierro, *Appl. Catal. A* **161** (1997) 213
15. S. R. de Miguel, O. A. Scelza, M. C. Román–Martínez, C. S. M de Lecea, D. Cazorla–Amoros, A. Linares–Solano, *Appl. Catal. A* **170** (1998) 93
16. D. J. Suh., T. J. Park, S. K. Ihm, *Carbon* **31** (1993) 427
17. F. Coloma, A. Sepúlveda–Escribano, J. L. Fierro, F. Rodríguez–Reinoso, *Langmuir* **10** (1994) 750
18. M. C. Román–Martínez, D. Cazorla–Amorós, A. Linares–Solano, C. S. M. Lecea, *Carbon* **33** (1995) 3
19. P. Ehrburger, O. P. Majahan, P. L. Walker, *J. Catal.* **43** (1976) 61
20. A. Guerrero–Ruiz, P. Badenes, I. Rodríguez–Ramos, *Appl. Catal. A* **173** (1998) 313
21. B. Babić, B. Kaluderović, Lj. Vračar, N. Krstajić, *Carbon* **42** (2004) 2617
22. B. M. Babić, Lj. M. Vračar, V. Radmilović, N. V. Krstajić, *Electrochim. Acta* **51** (2006) 3820
23. E. P. Barret, L. G. Joyner, P. P. Halenda, *J. Am. Chem. Soc.* **73** (1951) 373
24. K. Kaneko, C. Ishii, M. Ruike, H. Kuwabara, *Carbon* **30** (1992) 1075
25. M. Kruk, M. Jaroniec, K. P. Gadakaree, *J. Colloid Interface Sci.* **192** (1997) 250
26. K. Kaneko, C. Ishii, H. Kanoh, Y. Hanzawa, N. Setoyama, T. Suzuki, *Adv. Coll. Interface Sci.* **76–77** (1998) 295
27. V. Radmilovic, T. J. Richardson, S. J. Chen, P. N. Ross, *J. Catal.* **232** (2005) 199
28. W. Li, G. Reichenauer, J. Fricke, *Carbon* **40** (2002) 2955
29. W. Li, H. Probstle, J. Fricke, *J. Non–Cryst. Solids* **325** (2003) 1
30. J. M. Miller, B. Dunn, T. D. Tran, R. W. Pekala, *J. Electrochem. Soc.* **144** (1997) L309
31. R. W. Pekala, J. C. Farmer, C. T. Alviso, T. D. Tran, S. T. Mayer, J. M. Miller, B. Dunn, *J. Non–Cryst. Solids* **225** (1998) 74
32. C. Schmitt, H. Probstle, J. Fricke, *J. Non–Cryst. Solids* **285** (2001) 277
33. H. Probstle, C. Schmitt, J. Fricke, *J. Power Sources* **105** (2002) 189
34. A. J. Bard, L. Faulkner, *Electrochemical Methods, Fundamentals and Applications*, Ch. 8, John Wiley & Sons, New York, 1981, p.256
35. N. M. Marković, B. N. Grgur, P. N. Ross, *J. Phys. Chem. B* **101** (1997) 5405
36. N. M. Marković, T. S. Sarraf, H. A. Gasteiger, P. N. Ross, *J. Chem. Soc. Faraday Trans.* **92** (1996) 3719.



The effects of a magnetic field on the morphologies of nickel and copper deposits: the concept of “effective overpotential”

NEBOJŠA D. NIKOLIĆ**

ICTM – Institute of Electrochemistry, University of Belgrade,
Njegoševa 12, P.O.B. 473, 11001 Belgrade, Serbia

(Received 1 December 2006, revised 6 March 2007)

Abstract: The morphologies of nickel and copper deposits obtained without applied magnetic fields, and with both parallel and perpendicular applied magnetic fields were examined by the scanning electron microscopy (SEM) technique. Changes in the morphologies of the metals caused by the effect of the magnetic fields are explained by the concept of “effective overpotential”. The morphologies of the nickel and copper deposits obtained under parallelly oriented magnetic fields were similar to those obtained at some lower cathodic potentials without an applied magnetic field. The magnetic field with a perpendicular orientation to the electrode surface increased the dispersity of the nickel and copper deposits. Nickel and copper deposits obtained under this orientation of the magnetic field were similar to those obtained at some higher cathodic potentials without an applied magnetic field.

Keywords: electrodeposition, magnetic field, copper, nickel, SEM.

INTRODUCTION

The effects of a magnetic field on electrochemical processes can be divided into three categories, *i.e.*, those relating to mass transport, electrode kinetics and morphology of the metal deposits.^{1–17} The effect of a magnetic field on electrochemical processes is usually observed through the magnetohydrodynamic (MHD) effect. The origin of this effect lies in the Lorentz force, $F_L = i \times B$, where i is the current density and B is the magnetic field.¹ During electrolysis, this force acts on the migration of ions and induces a convective flow of the electrolyte close to the electrode surface. The largest effect of this force and, consequently, the largest MHD effect are achieved with magnetic fields parallelly oriented to the electrode surface (*i.e.*, when the external magnetic field is oriented perpendicularly to the direction of the ion flux). On the contrary, when a magnetic field is applied perpendicular to the electrode surface, the Lorentz force is zero.

In addition to the Lorentz force, magnetically induced forces which have an effect on electrochemical processes are the magnetic gradient force and the para-

* E-mail: nnikolic@tmf.bg.ac.yu

Serbian Chemical Society member.

doi: 10.2298/JSC0709787N

magnetic force. These are gradient forces and they depend on the magnitude of the magnetic field and not on its direction.^{9,17} Other forces of possible significance in magnetoelectrolysis are the gravitational force $\Delta\rho_g$, which drives natural convection, and the damping force (this force depends on the conductivity of the electrolyte and its velocity, v).⁹

The concept of “effective overpotential” was recently proposed in order to explain the morphologies of electrodeposited copper obtained under conditions of strong hydrogen co-deposition.¹⁸ According to this concept, at high overpotentials when hydrogen evolution is sufficiently vigorous, the electrodeposition process actually occurs at an overpotential which is effectively lower (and for that reason, it is called the “effective overpotential” of the electrodeposition process) than that applied. Then, the morphologies of the deposits become, at the macro level, similar to those obtained at some lower overpotentials when hydrogen evolution does not exist. It was estimated¹⁹ that the quantities of evolved hydrogen enabling the validity of the concept of “effective overpotential” correspond to the average current efficiencies of hydrogen evolution above 10.0 % of about 80.0 mA cm⁻². These quantities of evolved hydrogen were sufficient to cause stirring of the solution in the near-electrode layer, decreasing thereby the thickness of the cathode diffusion layer and increasing the limiting diffusion current density, which lead to a change of the hydrodynamic conditions in the solution.

Bearing in mind that both vigorous hydrogen evolution and an applied magnetic field have an effect on the hydrodynamic conditions in a plating solution, it is logical to assume that the concept of “effective overpotential” can be applied for the case of electrodeposition under imposed magnetic fields. The first report on a possible correlation between the effects of a magnetic field and the concept of “effective overpotential” was recently given¹⁶ for the case of iron electrodeposition under a perpendicularly oriented magnetic field. Nevertheless, a detailed analysis of this correlation was necessary and the aim of this study was its investigation. The effect of magnetic fields on the electrodeposition of magnetic (nickel) and non-magnetic (copper) metals, both under imposed parallel and perpendicular fields will be examined.

EXPERIMENTAL

Working conditions

Nickel was electrodeposited from the following solution: NiSO₄·6H₂O, 262.5 g l⁻¹; NiCl₂·6H₂O, 45 g l⁻¹; H₃BO₃, 37.5 g l⁻¹ and coumarin, 0.060 g l⁻¹ at pH 4.5.

Nickel was deposited potentiostatically at room temperature at cathodic potentials of -1000, -1200 and -1300 mV/SCE, with a counter electrode of electrolytic nickel (99.99 %).

Copper was electrodeposited from 0.2 M CuSO₄ in 0.5 M H₂SO₄, (pH 1.5), at room temperature at a cathodic potential of -500 mV/SCE, with a counter electrode of electrolytic copper (99.99%).

The electrodeposition was performed onto copper electrodes. The positions of electrodes in the electrochemical cells were same in the all cases. The quantities of the electrodeposited metals were 16 mA h cm⁻².

Equipment

The deposition of nickel and copper was performed by use of a bipotentiostat, model AFCBP 1, Pine Instruments Company. The electrochemical cell was plunged into a uniform magnetic field of 500 Oe, which was perpendicular or parallel to the electrode surface using the magnetic system model M-50, MMR Technologies, Inc. The nickel and copper deposits were examined by a scanning electron microscope, model Philips SEM-FEG-XL 30.

A schematic illustration of the electrochemical cell, including the field directions, ion velocity, v , and the flux of ions, J , is given elsewhere.¹²

RESULTS AND DISCUSSION

The nickel deposits obtained at a cathodic potential of -1300 mV/SCE without an applied magnetic field, as well as with both a parallelly and perpendicularly oriented applied magnetic field of 500 Oe, are shown in Fig. 1.

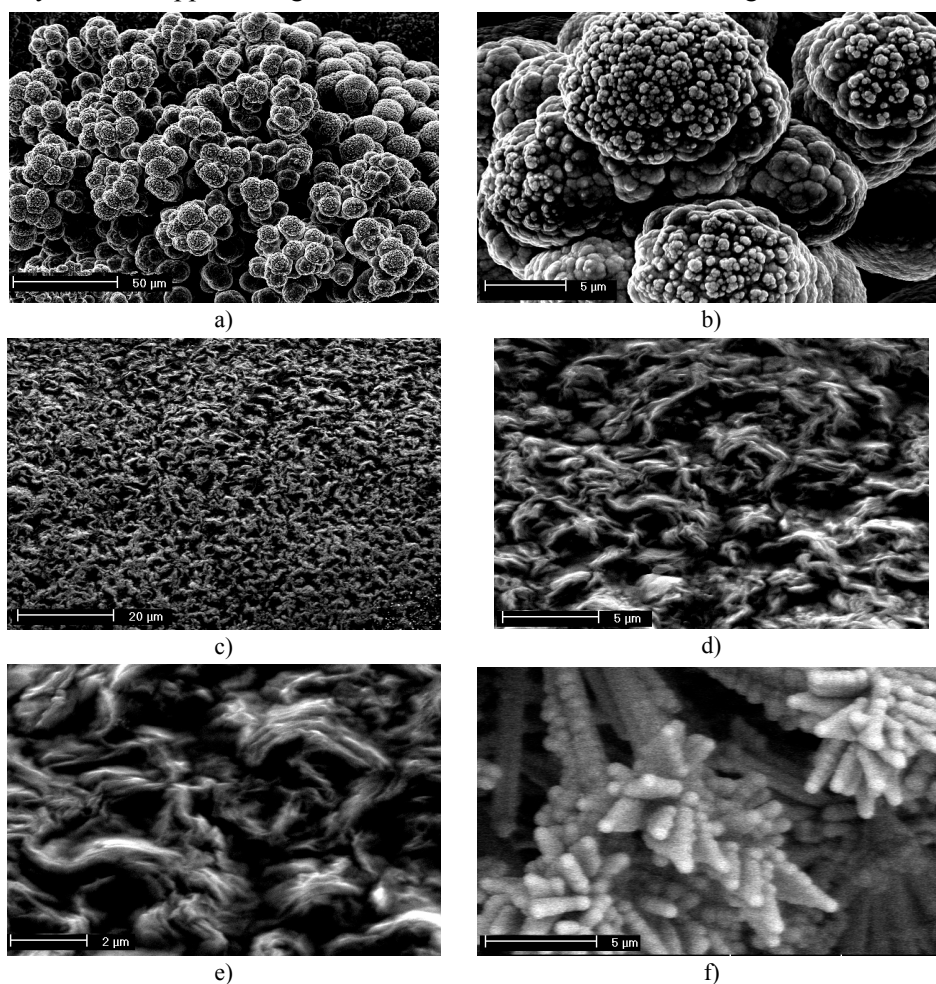


Fig. 1. Nickel deposits obtained at a cathodic potential of -1300 mV/SCE without: a) and b) and with: c), d) and e) a parallelly, and f) a perpendicularly oriented magnetic field of 500 Oe.

Fig. 1a shows that the nickel deposit obtained without an imposed magnetic field had a shrub-like structure. This shrub-like nickel structure consisted of bunched nickel grains. In addition, every nickel grain consisted of very small, probably nano-sized, nickel grains, as shown in Fig. 1b.

The nickel deposit obtained at the same cathodic potential but with the parallel magnetic field is shown in Figs. 1c–1e. This deposit had a porous structure without bunched nickel grains.

The nickel deposit obtained at the same cathodic potential under the perpendicular magnetic field is shown in Fig. 1f. This nickel deposit had a very developed dendritic 3D structure. The structure of this deposit consisted of thin nickel branches or filaments which terminated in flower like aggregates of nickel. The flower like aggregates of nickel also consisted of thin nickel branches (or filaments) made of small, probably nano-sized nickel grains, like a rosary.

The copper deposits obtained at a cathodic potential of -500 mV/SCE without an applied magnetic field, as well as with both a parallel and perpendicularly oriented applied magnetic field, are shown in Fig. 2.

It can be seen from Fig. 2 that the copper deposits obtained without (Figs. 2a and 2b) and with the perpendicular field (Figs. 2e and 2f) had dendritic structures. The copper deposit obtained with the parallel field (Figs. 2c and 2d) had a cauliflower-like structure.

The application of the concept of “effective overpotential” for the case of a change in the hydrodynamic conditions caused by the effects of a magnetic field means that the morphologies of the nickel and copper deposits obtained under parallel fields (the largest MHD effect) should be, at a macro level, similar to those obtained at some lower overpotentials or potentials without an imposed magnetic field. This assumption will be considered below.

The nickel deposit obtained at a cathodic potential of -1200 mV/SCE without an applied magnetic field is shown in Fig. 3a. It can be seen that there is a similarity at a macro level between the morphology of this nickel deposit and the morphology of the nickel deposit obtained at a potential of -1300 mV/SCE under the parallel magnetic field (Figs. 1c – 1e). Both nickel deposits are without dendritic and globular parts and with clearly visible nickel grains. The only difference lies in the compactness of the deposits, which is a consequence of the larger nucleation rate and more intensive hydrogen evolution at a potential of -1300 mV/SCE than at a potential of -1200 mV/SCE.

Also, the concept of “effective overpotential” can be illustrated by the comparison of the nickel deposit obtained at a cathodic potential of -1200 mV/SCE under the parallel magnetic field with the nickel deposit obtained at -1000 mV/SCE without an imposed magnetic field. The morphologies of these nickel deposits are shown in Figs. 3b and 3c. The morphology of the nickel deposit obtained at a potential of -1200 mV/SCE under the parallel field is shown in Fig. 3b, while the

morphology of the nickel deposit obtained at -1000 mV/SCE without applied magnetic fields is shown in Fig. 3c. From Figs. 3b and 3c, it can be observed that there is similarity at the macro level between these nickel deposits. The boundaries between adjacent nickel grains cannot be observed. Nevertheless, the nickel deposit obtained at -1200 mV/SCE under the parallel field (Fig. 3b) was more similar to that obtained at -1000 mV/SCE without an applied magnetic field than to that obtained at -1200 mV/SCE without an imposed magnetic field (Fig. 3a).

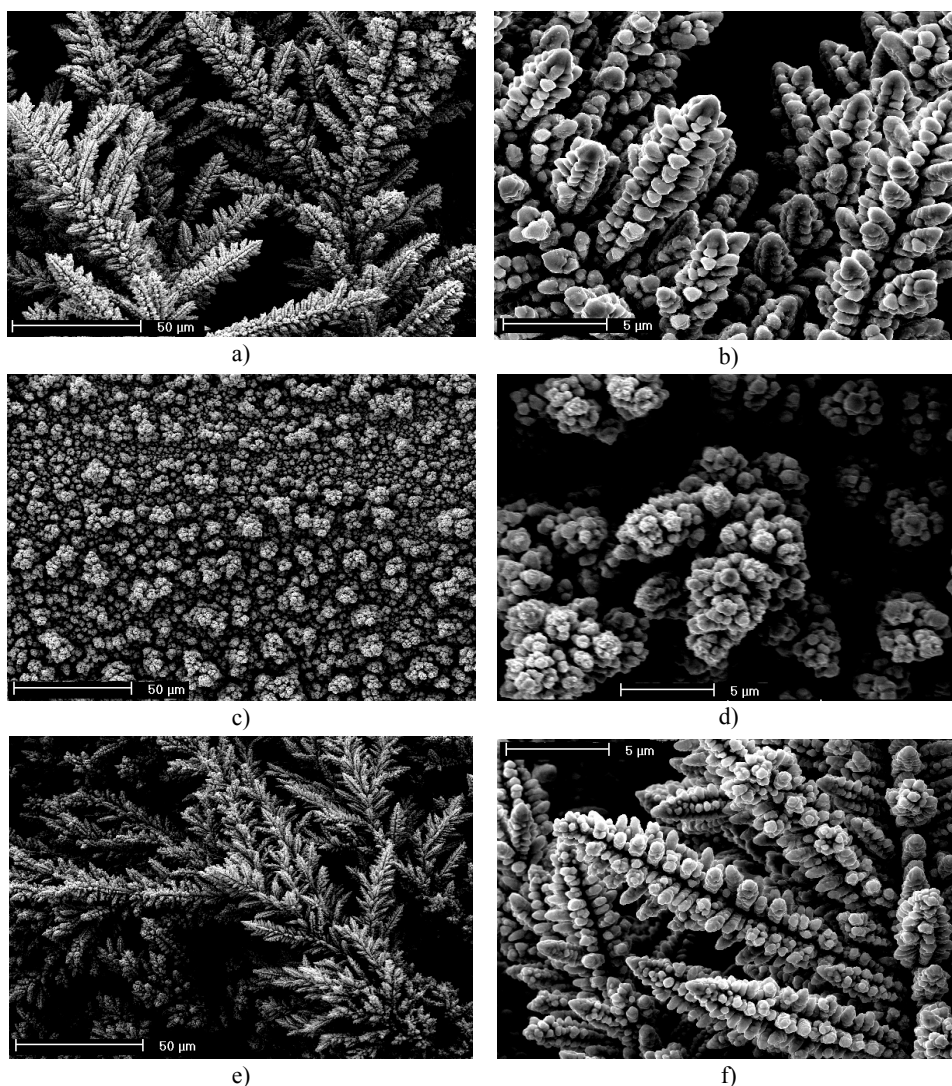


Fig. 2. Copper deposits obtained at a cathodic potential of -500 mV/SCE without: a) and b) and with: c) and d) a parallelly, and e) and f) a perpendicularly oriented magnetic field of 500 Oe.

This concept can also be applied for the case of the electrodeposition of copper. As mentioned earlier, the morphology of the copper deposit obtained at a cathodic potential of -500 mV/SCE under the parallel field had a cauliflower-like structure (Figs. 2c and 2d), while the morphology of the copper deposit obtained without an applied magnetic field had a very dendritic structure (Figs. 2a and 2b). It is known that dendritic structures are main characteristic of electrodeposition under conditions of full diffusion control, while cauliflower-like structures are characteristic of a dominant diffusion control in a mixed control of the electrodeposition process.²⁰

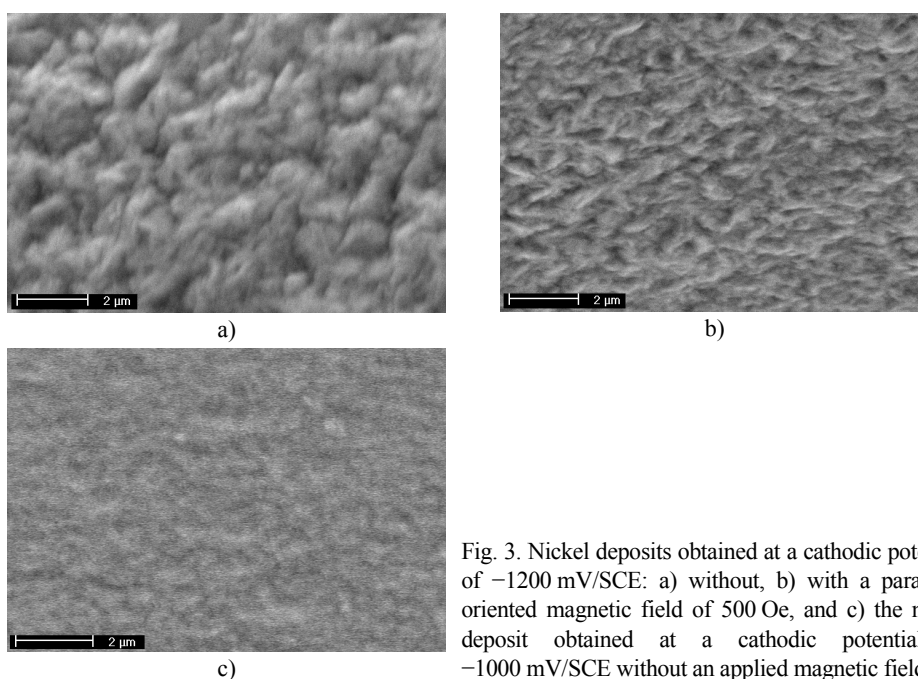


Fig. 3. Nickel deposits obtained at a cathodic potential of -1200 mV/SCE: a) without, b) with a parallelly oriented magnetic field of 500 Oe, and c) the nickel deposit obtained at a cathodic potential of -1000 mV/SCE without an applied magnetic field.

Thus, it can be seen that the application of a parallel magnetic field of 500 Oe led to a shifting of the formation of characteristic morphological forms toward lower cathodic potentials by about 100 – 200 mV. Hence, the obtained morphologies of the nickel and copper deposits can be explained by the concept of “effective overpotential” in the manner below.

The deposition overpotential, η , in the region of mixed activation/diffusion control is given by Eq. (1):²⁰

$$\eta = \frac{b_c}{2.3} \ln \frac{i}{i_0} + \frac{b_c}{2.3} \ln \frac{1}{1 - (i/i_L)} \quad (1)$$

where b_c is the cathodic Tafel slope and i_0 and i_L are the exchange and the limiting current densities, respectively. The activation part of the deposition overpotential required for the charge transfer, η_a , is given by Eq. (2):

$$\eta_a = \frac{b_c}{2.3} \ln \frac{i}{i_0} \quad (2)$$

and the remaining overpotential, η_{diff} , given by Eq. (3):

$$\eta_{\text{diff}} = \frac{b_c}{2.3} \ln \frac{1}{1 - (i/i_L)} \quad (3)$$

is due to mass transfer limitations (diffusion limitation primarily).

The influence of magnetic field appears to be restricted to the diffusion-limited regions. During electrolysis under parallel fields, the Lorentz force induces convective flow of the electrolyte close to electrode surface. A magnetically stimulated convection leads to a decrease in the thickness of the diffusion layer, thus the diffusion-limited current is increased. This will lead to a decrease in the degree of diffusion control of the electrodeposition process, because the current density of the electrodeposition process increases with increasing limiting diffusion current density at a fixed value of overpotential η , and then, η_a should be larger in the presence than in the absence of the effect of a magnetic field. If the applied overpotential remains the same, η_{diff} must decrease. This is only a qualitative analysis, while a quantitative analysis of the change of hydrodynamic conditions has been given elsewhere.¹⁸

As a rule, it was adopted that the limiting diffusion current density depends on magnetic field, as $i_L \propto B^{1/3}$.³ According to Eqs. (1) and (3), increasing the limiting current density leads to a decrease of the degree of diffusion control of the deposition process (a decrease of diffusion part in Eqs. (1) and (3)), and then, the electrodeposition process occurs at some overpotential which is effectively lower. This overpotential at which a metal electrodeposition occurs when the change in the hydrodynamic conditions is caused by the effect of an imposed magnetic field (*i.e.*, by the magnetohydrodynamic effect) represents the "effective overpotential" of the electrodeposition process.

This effect of the parallel field is equivalent to those achieved by vigorous hydrogen evolution,¹⁸ rotating the electrode⁹ or vigorous stirring of the electrolyte.⁹

The second special case is that of a magnetic field perpendicular to the plane surface of the electrode. According to MHD theory, for this orientation of a magnetic field to the electrode surface, the Lorentz force is zero, and then, changes in growth processes are not expected (*i.e.*, the expected MHD effect is zero). In this set-up the observed effects can result either from the non-homogeneity of the magnetic field (magnetic field gradient or a ferromagnetic electrode in magnetic induction, or an electrode composed of a magnetized material), or from an effect of the magnetic forces on the concentration gradients of electrochemical species.¹⁷ Hence, the main forces involved when magnetic fields are applied perpendicular to the electrode surface are the magnetic gradient force (which depends

on the field gradient, ∇B) and the paramagnetic force (this force is caused by concentration gradients, ∇c , of paramagnetic ions, Cu^{2+} , Fe^{2+} , Co^{2+} , Ni^{2+} , *etc.*).

The difference between the morphologies of nickel and copper deposits obtained with the perpendicular field (Fig. 1f and Figs. 2e and 2f, respectively) and those obtained without an applied magnetic field (Figs. 1a and 1b, and Figs. 2a and 2b, respectively) is clearly visible. This difference is larger in the case of the electrodeposition of nickel than in case of copper electrodeposition. The nickel deposit obtained under the perpendicular field had a very developed 3D dendritic structure (Fig. 1f), unlike shrub-like nickel structure (Figs. 1a and 1b) obtained without an applied magnetic field. On the other hand, although both copper deposits had dendritic structures, there was a difference in the ramification of these copper dendrites. The copper deposit obtained under the perpendicular field had a somewhat more ramified structure (Figs. 2e and 2f) than the copper deposit obtained without the imposed magnetic field (Figs. 2a and 2b).

The concept of "effective overpotential" applied to the case of electrodeposition under perpendicular fields means that the electrodeposition process occurs at an overpotential which is effectively higher than the overpotential without an applied magnetic field.

There is the opposite effect to the case of metal electrodeposition under parallel fields. The changes in the morphologies under perpendicularly oriented magnetic fields were similar to those obtained when limiting diffusion current density was decreased. In fact, the possibility of decreasing limiting currents with a perpendicular field was reported recently.²¹ Grant *et al.*²¹ showed that a uniform magnetic field perpendicularly oriented to the microelectrode surface in order to induce rotational flow of the electrolyte causes either an increase or a decrease in the voltammetric limiting currents (from -37 to $+119\%$), depending solely on the size of the electrode. For inlaid disc electrodes with radii less than $100\ \mu\text{m}$, the magnetic field driven flow results in a decrease of the transport limited current, as a consequence of rotational solution flow adjacent to the surface, preventing gravity-driven natural convection. Some similar local effects on electrodeposition on a small scale profile can probably be expected in the case of electrodeposition of both, nickel and copper, similar to the change of mass transfer conditions described by Bockris *et al.*^{22,23}

In the absence of the MHD effect, it is clear that the main forces responsible for the change of morphologies of nickel and copper deposits under perpendicularly oriented magnetic fields are the paramagnetic and magnetic gradient forces. As already mentioned, the paramagnetic force is caused by concentration gradients of paramagnetic Cu^{2+} and Ni^{2+} ions and the effect of this force does not depend on the direction of the magnetic field. The obtained morphologies of nickel and copper deposits under perpendicular fields are similar to those obtained by electrodeposition processes from solutions with lower concentrations of the depositing ions without an applied magnetic field.

The cause of larger change in the morphology of the nickel deposit under the perpendicular field than the change in the morphology of the copper deposit is probably the magnetic character of metallic nickel. Changes in the morphologies of ferromagnetic electrodeposits under perpendicularly oriented magnetic fields are ascribed to some magnetic properties, such as, for example, magnetoresistance^{11,12,15,16} or magnetic anisotropy.⁸

The possible reason for the change in the morphologies of the nickel and copper deposits under perpendicularly oriented magnetic fields is the vigorous evolution of hydrogen at -1300 mV/SCE and -500 mV/SCE, respectively. The fact that the change in the morphology of the nickel deposit under the perpendicular field is only observed by electrodeposition of nickel at -1300 mV/SCE¹⁵ (and not at lower cathodic potentials) clearly indicates to the contribution of the vigorous hydrogen evolution to the change in the morphologies of nickel and copper deposits at high potentials. It can be concluded that the growth of these very developed dendritic deposits is controlled by convective phenomenon caused by the magnetic field and diffusion effects.

For example, Shannon *et al.*⁷ also showed that for a weak value of an applied magnetic field, a change in the morphology of nickel deposits is possible with both parallel and perpendicular fields. This change was ascribed to the existence of a metastable hydrodynamic condition in the plating solution. This metastable condition is subjected to local disturbances *via* the applied magnetic fields and gas evolution. The magnetic field, in addition to acting on the paramagnetic Ni ions, influences the flow dynamics and stability of the evolved gas bubbles.

The larger change in the morphology of the nickel deposit than the change in the morphology of the copper deposit obtained under perpendicular fields can also be ascribed to some other processes characterised only for electrodeposition of nickel. For example, the electrodeposition of nickel was performed from neutral solutions²⁴ and there is a possible effect of local changes of the pH in the vicinity of the electrode due to the co-deposition of the corresponding hydroxides with nickel. In the case of electrodeposition of metals from acid solutions (which is the case of copper from a sulphate solution), there is no effect of local changes of the pH on the morphology of the electrodeposited metals because hydrogen evolution causes only a small change of the pH in the vicinity of the electrode.

In any case, the changes in the morphologies of the nickel and copper deposits caused by the effect of the perpendicularly oriented magnetic field clearly indicate that there was some additional energy introduced by the magnetic field of this orientation. In the case of nickel, this energy was larger than in the case of copper, which is probably the consequence of the magnetic properties of nickel (*i.e.*, the fact that nickel is a ferromagnetic metal).

Finally, the subject of this work was only the analysis of the morphologies of the nickel and copper deposits obtained without and with both parallelly and per-

pendicularly oriented imposed magnetic fields. The obtained metal morphologies are explained very well by the concept of “effective overpotential”. The possible kinetic reasons for the change in the morphologies of the metals under the imposed magnetic fields were not considered.

CONCLUSIONS

Analysis of the morphologies of nickel and copper deposits obtained without and with both parallel and perpendicular fields showed that the concept of “effective overpotential” can be applied for the case when a change of the hydrodynamic conditions is caused by the effect of the magnetic fields (*i.e.*, by the magnetohydrodynamic effect).

The nickel and copper deposits obtained under a parallel magnetic field were similar, at the macro level, to those obtained at lower deposition overpotentials without an applied magnetic field. For example, the nickel deposits obtained at -1200 mV/SCE and -1300 mV/SCE with the parallel field were similar to those obtained at -1000 mV/SCE and -1200 mV/SCE without an applied field, respectively.

On the other hand, the analysis of the morphologies of the nickel deposits obtained under the perpendicularly oriented magnetic field showed that the morphologies of these deposits were similar, at the macro level, to those obtained at some higher overpotentials, but without an applied magnetic field.

Acknowledgement: This work was supported by the Ministry of Science of the Republic of Serbia under the research project: “Deposition of ultrafine powders of metals and alloys and nano-structured surfaces by electrochemical techniques” (No. 142032G).

ИЗВОД

УТИЦАЈ ПРИМЕЊЕНИХ МАГНЕТНИХ ПОЉА НА МОРФОЛОГИЈЕ ТАЛОГА НИКЛА И БАКРА: КОНЦЕПТ “ЕФЕКТИВНЕ ПРЕНАПЕТОСТИ”

НЕБОЛША Д. НИКОЛИЋ

ИХТМ – Центар за електрохемију, Њеџишева 12, 11000 Београд

Техником скенирајуће електронске микроскопије (СЕМ) су биле испитане морфологије талога никла и бакра добијене без примењеног, као и са паралелно и вертикално оријентисаним магнетним пољима. Промене морфологија талога никла и бакра под утицајем примењених магнетних поља су објашњене концептом “ефективне пренапетости”. Морфологије талога никла и бакра добијене у паралелно оријентисаном магнетном пољу су биле сличне онима добијеним на неким нижим катодним потенцијалима без примењених магнетних поља. Примена магнетног поља са вертикалном оријентацијом према електродној површини је повећала дисперзност талога никла и бакра. Талози никла и бакра добијени под овом оријентацијом магнетног поља су били слични онима добијенима на неким вишим катодним потенцијалима без примењеног магнетног поља.

(Примљено 1. децембра 2006, ревидирано 6. марта 2007)

REFERENCES

1. J. A. Shercliff, *A Textbook of Magnetohydrodynamics*, Pergamon Press, Oxford, 1965
2. O. Devos, A. Olivier, J. P. Chopart, O. Aaboubi, G. Maurin, *J. Electrochem. Soc.* **145** (1998) 401

3. R. Aogaki, K. Fueki, T. Mukaibo, *Denki Kagaku* **43** (1975) 504
4. O. Aaboubi, J.-P. Chopart, J. Douglade, A. Olivier, C. Gabrielli, B. Tribollet, *J. Electrochem. Soc.* **137** (1990) 1796
5. G. Hinds, J. M. D. Coey, M. E. G. Lyons, *Electrochem. Commun.* **3** (2001) 215
6. I. Mogi, M. Kamiko, S. Okubo, G. Kido, *Physica B* **201** (1994) 606
7. J. C. Shannon, Z. H. Gu, T. Z. Fahidy, *J. Electrochem. Soc.* **144** (1997) L314
8. S. Bodea, L. Vignon, R. Ballou, P. Molho, *Phys. Rev. Lett.* **83** (1999) 2612
9. G. Hinds, F. E. Spada, J. M. D. Coey, T. R. Ni Mhiochain, M. E. G. Lyons, *J. Phys. Chem. B* **105** (2001) 9487
10. H. Matsushima, T. Nohira, I. Mogi, Y. Ito, *Surf. Coat. Technol.* **179** (2004) 245
11. N. D. Nikolic, Hai Wang, Hao Cheng, C. A. Guerrero, N. Garcia, *J. Magn. Magn. Mater.* **272–276** (2004) 2436
12. N. D. Nikolić, Hai Wang, Hao Cheng, C. Guerrero, E. V. Ponizovskaya, Genhua Pan, N. Garcia, *J. Electrochem. Soc.* **151** (2004) C577
13. A. Krause, M. Uhlemann, A. Gebert, L. Schultz, *Electrochim. Acta* **49** (2004) 4127
14. A. Bund, A. Ispas, *J. Electroanal. Chem.* **575** (2005) 221
15. N. D. Nikolić, *J. Serb. Chem. Soc.* **70** (2005) 1213
16. N. D. Nikolić, *J. Serb. Chem. Soc.* **71** (2006) 1083
17. K. L. Rabah, J.-P. Chopart, H. Schloerb, S. Saulnier, O. Aaboubi, M. Ulemann, D. Elmi, J. Amblard, *J. Electroanal. Chem.* **571** (2004) 85
18. N. D. Nikolić, K. I. Popov, Lj. J. Pavlović, M. G. Pavlović, *J. Electroanal. Chem.* **588** (2006) 88
19. N. D. Nikolić, K. I. Popov, Lj. J. Pavlović, M. G. Pavlović, *Sensors* **7** (2007) 1
20. K. I. Popov, S. S. Djokić, B. N. Grgur, *Fundamental Aspects of Electrometallurgy*, Kluwer Academic/Plenum Publishers, New York, 2002
21. K. M. Grant, J. W. Hemmert, H. S. White, *J. Electroanal. Chem.* **500** (2001) 95
22. A. R. Despić, J. W. Diggle, J. O`M. Bockris, *J. Electrochem. Soc.* **115** (1968) 507
23. J. W. Diggle, A. R. Despić, J. O`M. Bockris, *J. Electrochem. Soc.* **116** (1969) 1503
24. S. Djordjević, M. Maksimović, M. Pavlović, K. Popov, *Galvanotehnika*, Tehnička knjiga, Beograd, 1997., p. 11 (in Serbian).

Spectrophotometric investigation of the uranyl–phenylephrine system

LEPOSAVA PAVUN^{1*#}, DUŠAN MALEŠEV¹ and DRAGAN VESELINOVIĆ^{2#}

¹Faculty of Pharmacy, University of Belgrade, Serbia, Vojvode Stepe 450, Belgrade and ²Faculty of Physical Chemistry, University of Belgrade, Studentski trg 12, Belgrade, Serbia

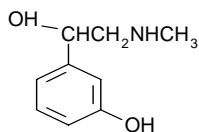
(Received 2 October 2006, revised 9 March 2007)

Abstract: Using spectrophotometric methods and pH-metric measurements, it was found that the uranyl ion and phenylephrine form a 1:2 complex in the pH region 2.50–4.25 with two absorption maxima at 314.2 nm and 340.6 nm. The thermodynamic stability constant at $I = 0$ and $T = 298$ K (room temperature) of the $\text{UO}_2(\text{II})$ –phenylephrine complex, $\text{UO}_2(\text{C}_9\text{H}_{12}\text{O}_2\text{N})_2$, is $\log \beta_2^0 = 14.0$ and $\Delta G_2^\ominus = -79.6$ kJ mol⁻¹. A linear dependence of the absorbance at 340.6 nm on the concentration of phenylephrine was obtained in the range from 0.0025 mol dm⁻³ to 0.0245 mol dm⁻³ using a solution of 0.025 mol dm⁻³ $\text{UO}_2(\text{NO}_3)_2$ at pH = 3.90 and $I = 0.075$ mol dm⁻³. The measurement error was 2.1 %.

Keywords: complex, uranyl ion, phenylephrine, thermodynamic stability constant.

INTRODUCTION

Phenylephrine ((*R*)-1-(3-hydroxyphenyl)-2-(methylamino)ethanol, $\text{C}_9\text{H}_{13}\text{O}_2\text{N}$) is a white crystalline powder, and belongs to the group of medicines called sympathomimetics. It acts by stimulating the alpha-receptors in certain areas of the body. It is used locally, as a decongestant, for non-specific and allergic conjunctivitis, sinusitis and nasopharyngitis.^{1,2}



Phenylephrine

Phenylephrine has been investigated spectrophotometrically using interactions with 1-nitroso-2-naphthol,³ ninhydrin in sulfuric acid⁴ and nitrobenzene derivatives.⁵ On the other hand, due to the presence of an amino group and a phenyl group in the molecule ($pK_a(-\text{OH}) = 8.9$ and $pK_a(-\text{NH}_2^+) = 10.1$),¹ phenyl-

* Corresponding author. E-mail: leposava.pavun@pharmacy.bg.ac.yu

Serbian Chemical Society member.

doi: 10.2298/JSC0709799P

ephine forms a complex with Fe^{3+} ($\text{Fe}^{3+}/\text{phenylephrine} = 2:1$).^{6,7} However, there are no data in the literature about complexes of phenylephrine and the UO_2^{2+} ion or other metal ions. The purpose of the present work was to investigate the UO_2^{2+} -phenylephrine complex and the possibility of the employment of the complex for the spectrophotometric determination of phenylephrine in aqueous media.

EXPERIMENTAL

Reagents and solutions

Uranyl nitrate (Fluka A.G.), HNO_3 , NaOH , NaNO_3 (Merck) and phenylephrine hydrochloride (Zdravlje, Serbia), all *p.a.*, were used without further purification.

Uranyl nitrate solution was standardized gravimetrically, by precipitation with oxine (8-hydroxyquinoline).⁸

A solution of phenylephrine hydrochloride was prepared by dissolving a precisely measured mass of dry phenylephrine hydrochloride in deionized water. The phenylephrine hydrochloride had previously been dried in a desiccator over silica gel. This solution was stored in a refrigerator.

All solutions were prepared by dilution of $0.0100 \text{ mol dm}^{-3}$ solutions of $\text{UO}_2(\text{NO}_3)_2$ and $0.0500 \text{ mol dm}^{-3}$ solutions of phenylephrine hydrochloride.

The pH of all solutions was adjusted using HNO_3 or NaOH solutions, and the ionic strength of the final solutions was kept constant by addition of the required volume of a 1 mol dm^{-3} solution of NaNO_3 .

Apparatus

The spectrophotometric measurements were performed on a Beckman DU-650 spectrophotometer, using 1 cm quartz cells. The pH values were measured using a pH-meter (pHM-28 Radiometer) and a combined electrode (accuracy ± 0.01 pH units). Buffers solutions (Radiometer), pH 4.01 and pH 7.00 at 25 °C, were used for calibrating the pH-meter.

RESULTS AND DISCUSSION

Absorption spectra

Phenylephrine and the uranyl(II) ion formed a complex in the pH interval 2.50 – 4.25. Above pH 4.25, the solution of the complex turns orange and a sediment, *i.e.*, the hydroxide products of the uranyl(II) ions, is formed. Phenylephrine is stable at $\text{pH} \leq 7$.

The absorption spectra (Fig. 1) were recorded using the solutions of $0.002 \text{ mol dm}^{-3}$ $\text{UO}_2(\text{NO}_3)_2$ and $0.040 \text{ mol dm}^{-3}$ phenylephrine and their mixture, where the concentrations of components were the same as in the single solutions, at a constant pH 4.00 and ionic strength (0.03 mol dm^{-3}). Water was used as the blank.

Also, the calculated spectrum of the complex, $\Delta A = f(\lambda)$, (Fig. 1, curve 4), was obtained using the following equation for the calculation of the complex absorbance, ΔA :

$$\Delta A = A_M - A_U - A_P \quad (1)$$

where A_U , A_P and A_M are the absorbance of the solutions of $\text{UO}_2(\text{NO}_3)_2$, phenylephrine and their mixture, respectively, at the corresponding wavelengths (λ).

The absorption spectrum of the complex has two maxima, the more intensive one being at 314.2 nm and the other one at 340.6 nm. All measurements were per-

formed at 340.6 nm since the absorbance of the $\text{UO}_2(\text{NO}_3)_2$ solution increases abruptly at lower wavelengths.

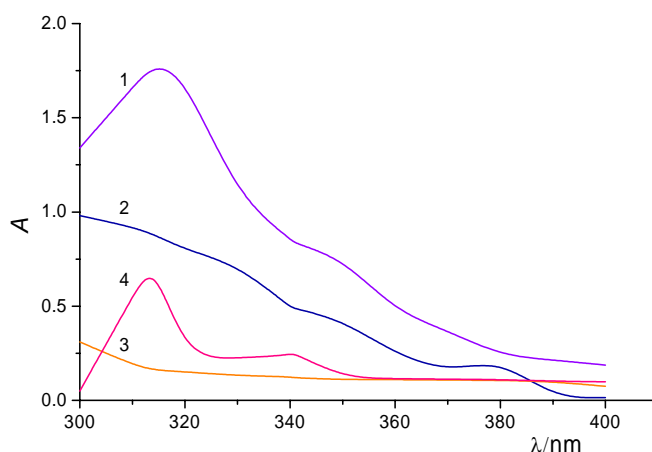


Fig. 1. Absorption spectra. 1: mixture $0.002 \text{ mol dm}^{-3} \text{UO}_2(\text{NO}_3)_2$ and $0.040 \text{ mol dm}^{-3}$ phenylephrine; 2: $0.002 \text{ mol dm}^{-3} \text{UO}_2(\text{NO}_3)_2$; 3: $0.020 \text{ mol dm}^{-3}$ phenylephrine; blank was water; 4: Calculated absorption spectra of the complex (ΔA).

The absorption spectrum of the UO_2^{2+} -phenylephrine complex was recorded in pH range from 2.50 to 4.25 (Fig. 2, curves 1–3), using the previously described procedure. The positions of absorption maxima are independent of pH, indicating the formation of only one type of complex in this pH interval.

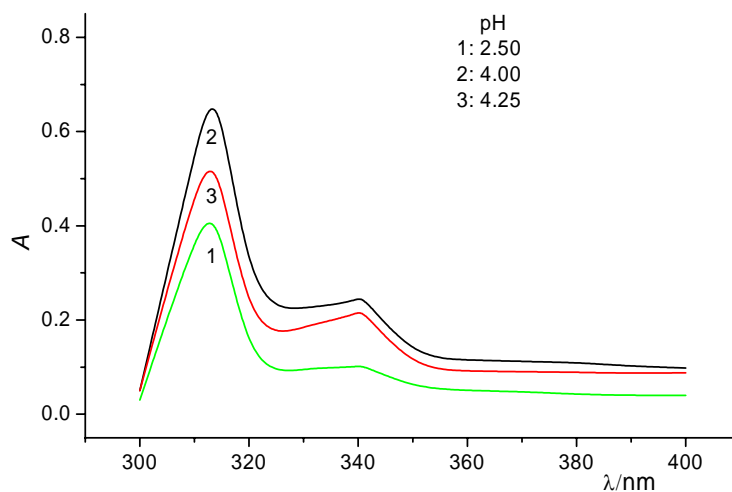


Fig. 2. Absorption spectra of the complex at different pH values; $0.002 \text{ mol dm}^{-3} \text{UO}_2(\text{NO}_3)_2$ and $0.040 \text{ mol dm}^{-3}$ phenylephrine.

The dependence of the absorbance of the complex and the components on pH was investigated at three different values of ionic strength, *i.e.*, at 0.025, 0.050

and $0.075 \text{ mol dm}^{-3}$. The absorbances of solutions of $0.002 \text{ mol dm}^{-3} \text{ UO}_2(\text{NO}_3)_2$, $0.040 \text{ mol dm}^{-3}$ phenylephrine and the mixture (containing the components at concentrations the same as in the individual solutions) were measured at 340.6 nm .

For each ionic strength, three curves $A = f(\text{pH})$ were obtained for solutions $\text{UO}_2(\text{NO}_3)_2$, phenylephrine and their mixture. By subtracting the relevant absorbances of the solution $\text{UO}_2(\text{NO}_3)_2$ and phenylephrine from their mixture, fourth curve $\Delta A = f(\text{pH})$ was obtained (Fig. 3). This curve represents the change of the complex absorbance on pH. The pH region $4.00\text{--}4.20$ was used for this investigation of the complex.

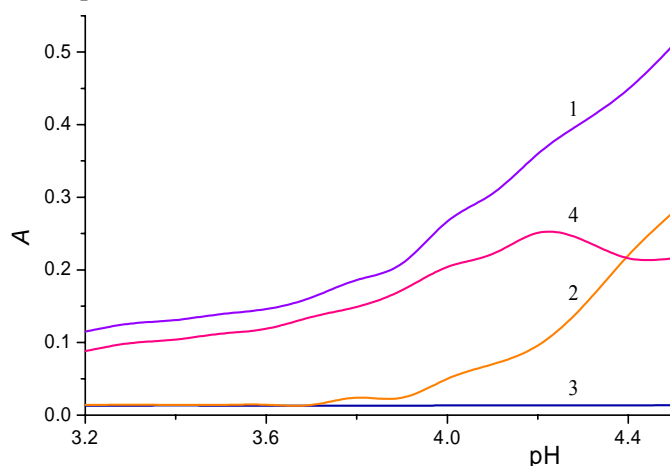


Fig. 3. Dependence of the absorbance on pH: Curve 1: mixture $0.002 \text{ mol dm}^{-3} \text{ UO}_2(\text{NO}_3)_2$ and $0.040 \text{ mol dm}^{-3}$ phenylephrine; Curve 2: $0.002 \text{ mol dm}^{-3} \text{ UO}_2(\text{NO}_3)_2$; Curve 3: $0.040 \text{ mol dm}^{-3}$ phenylephrine; the blank was water; Curve 4: $\Delta A = f(\text{pH})$; $\lambda = 340.6 \text{ nm}$, $I = 0.025 \text{ mol dm}^{-3}$.

Composition of the complex

The stoichiometric ratio of uranyl ion and phenylephrine in complex was determined by the method of molar ratios.⁹ The absorbances of solutions containing a constant concentration of $\text{UO}_2(\text{NO}_3)_2$ ($0.005 \text{ mol dm}^{-3}$) and different concentrations of phenylephrine ($0.0025\text{--}0.0200 \text{ mol dm}^{-3}$) were measured at 340.6 nm at a constant value of pH 4.00 and of ionic strength (0.05 mol dm^{-3}). The blank was the value of a $0.005 \text{ mol dm}^{-3}$ solution of $\text{UO}_2(\text{NO}_3)_2$. A straight line, $A = f(c(\text{phen})/c(\text{UO}_2^{2+}))$, with an intercept at $c(\text{phen})/c(\text{UO}_2^{2+}) = 2$ was obtained, which showed that the stoichiometric ratio of uranyl ion : phenylephrine in the complex was 1:2 (Fig. 4).

The composition of the complex was also determined by the method of variation of equimolar solutions.¹⁰ The absorbances of the series of solutions formed by mixing equimolar solutions $\text{UO}_2(\text{NO}_3)_2$ and phenylephrine ($0.025 \text{ mol dm}^{-3}$) at a constant value of pH 3.75 and of ionic strength (0.05 mol dm^{-3}) were measured at 340.6 nm , *i.e.*, the Job's method¹⁰ was employed. The blank was a solution of $\text{UO}_2(\text{NO}_3)_2$ with the same concentration and pH as in the employed mix-

ture. On the curve of the dependence of the absorbencies of these solutions on the molar fractions of the UO_2^{2+} ion, there was a maximum at the molar fraction of $\text{UO}_2^{2+} = 0.33$ (Fig. 5), which confirms that the composition of the complex was $\text{UO}_2^{2+}/\text{phenylephrine} = 1:2$.

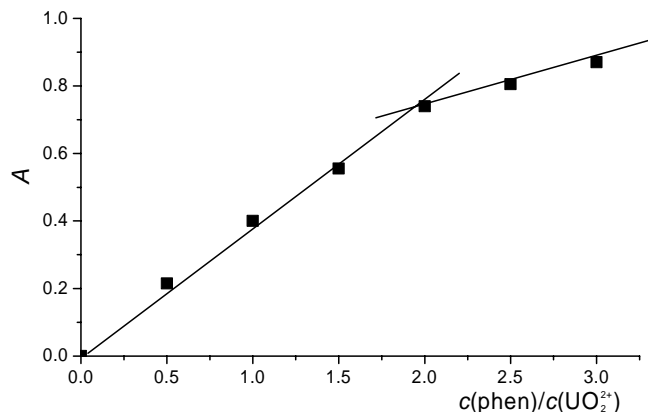


Fig. 4. Method of molar ratios. Dependence of absorbance on molar ratio $c(\text{phen})/c(\text{UO}_2^{2+})$; pH 4.00, $0.005 \text{ mol dm}^{-3} \text{UO}_2(\text{NO}_3)_2$; $0.0025\text{--}0.020 \text{ mol dm}^{-3}$ phenylephrine; Blank: $0.005 \text{ mol dm}^{-3} \text{UO}_2(\text{NO}_3)_2$; $\lambda = 340.6 \text{ nm}$; pH 4.02 ± 0.01 ; $I = 0.03 \text{ mol dm}^{-3}$.

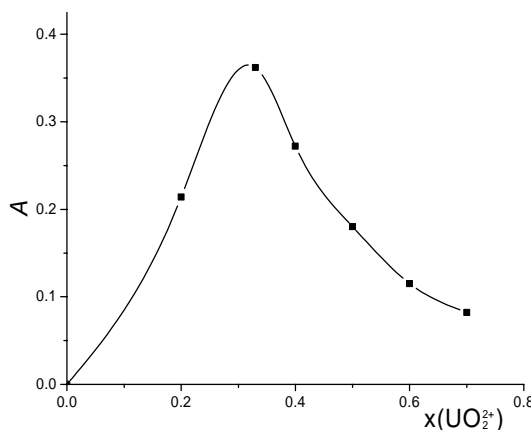


Fig. 5. Method of variations of equimolar solutions (Job's method). Change of absorbance with mol fraction of $x(\text{UO}_2^{2+})$. $c^0(\text{UO}_2^{2+}) = c^0(\text{phen}) = 0.025 \text{ mol dm}^{-3}$; blank is solution of $\text{UO}_2(\text{NO}_3)_2$ with the same concentrations and pH as in mixtures. $\lambda = 340.6 \text{ nm}$; pH 3.75 ± 0.01 ; $I = 0.05 \text{ mol dm}^{-3}$.

Infrared spectra of phenylephrine and of the complex

To find the position where the uranyl ion is linked to phenylephrine, the IR spectra of phenylephrine and of the isolated complex were recorded, using the KBr pellet method, in wave number region from 4000 to 800 cm^{-1} (Fig. 6). The complex was prepared by mixing solutions of $\text{UO}_2(\text{NO}_3)_2$ and phenylephrine in the molar ratio 1:2 and heating on a water bath ($80 \text{ }^\circ\text{C}$) with stirring for 0.5 h. After standing overnight at room temperature, the orange sediment was dried in desiccator over silica gel.

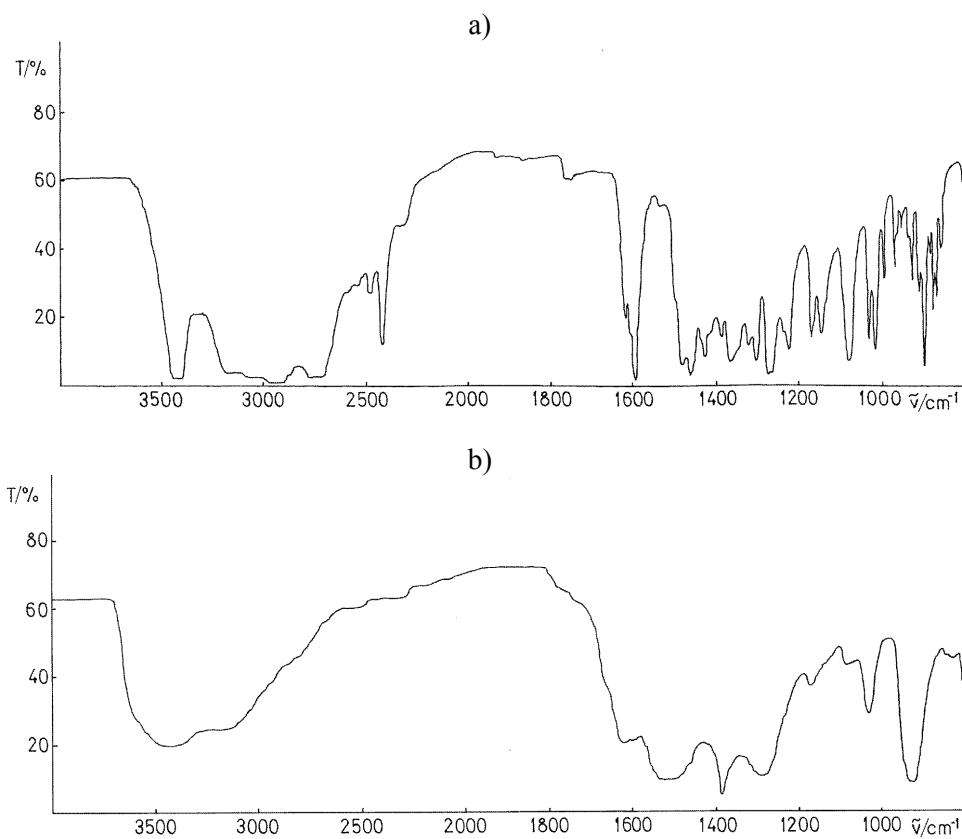
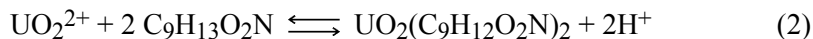


Fig. 6. IR Spectra of a) phenylephrine and b) complex (KBr pellets).

Bands ascribed to bending vibrations of phenolic OH groups in the wave number region $1280 - 930 \text{ cm}^{-1}$ were not present in the spectrum of the complex. This fact indicates that complex formation of UO_2^{2+} with phenylephrine occurs through the phenolic OH group.

Stability constant of the complex

It was found by measuring the pH of a $0.005 \text{ mol dm}^{-3}$ $\text{UO}_2(\text{NO}_3)_2$ solution and of a $0.010 \text{ mol dm}^{-3}$ phenylephrine solution, as well as their mixture containing the same concentrations as in single solutions that $c(\text{H}^+)_{\text{mixture}} > c(\text{H}^+)_{\text{uranyl}} + c(\text{H}^+)_{\text{phen}}$. This means that phenylephrine participated in the formation of the complex according to the reaction:



whereby an H^+ ion is released from the phenyl group.¹¹

The stability constant of the complex $\text{UO}_2(\text{C}_9\text{H}_{12}\text{O}_2\text{N})_2$ was determined at pH 3.90, combining the Bjerrum method (Eqs. (2) and (3)),¹² with Eqs. (4)–(6).^{13–15}

The highest complex concentration which matches the values A_{\max} and $\text{pH} \approx 4.20$ is on the maximum of the curve $\Delta A = f(\text{pH})$ (Fig. 2). It was not possible to calculate concentration of the complex, $c(\text{Complex})$, from A_{\max} using the Bjerrum method. Since the overall concentration of phenylephrine, $c_0(\text{HC}_9\text{H}_{12}\text{O}_2\text{N})$, *i.e.*, $c_0(\text{HL}^+)$, in the mixture was 20 times higher than the concentration of UO_2^{2+} ions, it can be considered that most of the UO_2^{2+} ions were bound in the complex, *i.e.*, the overall concentration of uranyl ions, $c_0(\text{UO}_2^{2+})$ equaled the concentration of the complex ($c(\text{Complex}) \approx c_0(\text{UO}_2^{2+})$). Therefore, the molar absorptivity, a , was calculated from the equation:

$$a = \frac{A_{\max}}{c_0(\text{UO}_2^{2+})} \quad (3)$$

The concentrations of the complex, UO_2^{2+} , and $\text{C}_9\text{H}_{13}\text{O}_2\text{N}$ (c_L) were calculated at $\text{pH} 3.90$ from the following equations:

$$c(\text{Complex}) = \frac{A}{a} \quad (4)$$

$$c_0(\text{UO}_2^{2+}) = c(\text{UO}_2^{2+}) + c(\text{Complex}) \quad (5)$$

$$c_0(\text{HL}^+) = c(\text{HL}^+) + c_L + 2c(\text{Complex}) \quad (6)$$

$$k_{d_1} = \frac{c(\text{H}^+)c_L}{c(\text{HL}^+)} \quad (7)$$

where k_{d_1} is the first dissociation constant of the phenolic hydroxylic groups of phenylephrine in aqueous solution.¹

According to Eq. (2), the stability constant of the complex, β_2 , is:

$$\beta_2 = \frac{c(\text{Complex})}{c(\text{UO}_2^{2+})c_{L^-}^2} \quad (8)$$

The stability constant β_2 was calculated for three different ionic strengths (Table I).

TABLE I. The concentration stability constants, β_2 , of the UO_2^{2+} -phenylephrine complex $\text{UO}_2(\text{C}_9\text{H}_{12}\text{O}_2\text{N})_2$ at different values of ionic strength I , $\text{pH} 3.90$, $T = 298 \text{ K}$

$I / \text{mol dm}^{-3}$	$\beta_2 \times 10^{-13}$	$\log \beta_2$
0.025	1.89	13.28
0.050	1.67	13.22
0.075	1.55	13.19

The thermodynamic stability constant of the complex, β_2^0 , was determined by extrapolation of the curve $\log \beta_2 = f(I^{0.5})$ (Fig. 7) and its value was 1.0×10^{14} . The thermodynamic parameter, the chemical potential, ΔG_2^\ominus , for the formation of the complex at room temperature (25°C) was calculated using the equation:

$$\Delta G_2^\ominus = -RT \ln \beta_2^0 = -79.6 \text{ kJ mol}^{-1} \quad (9)$$

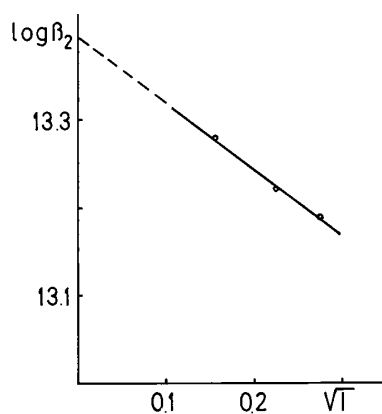


Fig. 7. Dependence of the stability constant, β_2 , of the $\text{UO}_2(\text{II})$ –phenylephrine complex on ionic strength I , $T = 298 \text{ K}$.

Possibility for quantitative determination of phenylephrine

The relatively high value of the stability constant of the uranyl(II)–phenylephrine complex enables the quantitative determination of phenylephrine from the absorbance of the complex at 340.6 nm. A curve of the dependence of the absorbance of the complex on the concentration of phenylephrine was constructed using solutions containing a constant concentration of $\text{UO}_2(\text{NO}_3)_2$ ($0.025 \text{ mol dm}^{-3}$) and different concentrations of phenylephrine at pH 3.90 and a constant ionic strength of $0.075 \text{ mol dm}^{-3}$. Water was used as the blank. A linear dependence of the absorbance of the complex on the concentration of phenylephrine was obtained in the interval 0.0025 – $0.0245 \text{ mol dm}^{-3}$. The regression equation $y = 7.88x - 0.0095$ was calculated with a high correlation coefficient of $r = 0.9997$. The accuracy of the method was determined for three different phenylephrine concentrations (Table II).

TABLE II. The spectrophotometric determination of phenylephrine

$c_{\text{phen}} / \text{mol dm}^{-3}$		$SD \times 10^4$	$CV / \%$
Taken	Found		
0.0050	0.0048	3.30	2.1
0.0125	0.0125	2.33	1.9
0.0225	0.0226	2.74	1.9

Due to the fact that the UO_2^{2+} ion forms complexes with other compounds (such as rutin,¹⁶ 3-hydroxyflavone¹¹ and hesperidin¹⁵) and these complexes have high absorbances in the spectral domain of the investigated UO_2^{2+} –phenylephrine complex, it is necessary to exclude these compounds from the investigated solutions.

CONCLUSION

The thermodynamic stability constant at $25 \text{ }^\circ\text{C}$ of the $\text{UO}_2(\text{II})$ –phenylephrine complex $\log \beta_2^0 = 14.0$ and $\Delta G_2^0 = -79.6 \text{ kJ mol}^{-1}$ indicate the formation of a stable complex. Since the absorbance of the complex at 340.6 nm is linear function of

the phenylephrine concentration without a large excess of UO_2^{2+} ions, spectrophotometric measurements can be used for the quantitative determination of phenylephrine in aqueous solutions without interfering compounds. Also, the high stability constant of the complex indicates that the complex could be used for other purposes, such as the extraction or desorption of uranyl ions.

ИЗВОД

СПЕКТРОФОТОМЕТРИЈСКО ИСПИТИВАЊЕ УРАНИЛ-ФЕНИЛЕФРИН СИСТЕМА

ЛЕПОСАВА ПАВУН¹, ДУШАН МАЛЕШЕВ¹ и ДРАГАН ВЕСЕЛИНОВИЋ²

¹Институт за физичку хемију, Фармацеутички факултет, Универзитет у Београду, Војводе Степе 450, Београд и ²Факултет за физичку хемију, Универзитет у Београду, Студентски брз 12, Београд

Применом спектрофотометријских метода и рН-метријских мерења утврђено је да $\text{UO}_2(\text{II})$ -јон и фенилефрин граде 1:2 комплекс у области рН 2,50 – 4,25 са два апсорпциона максимума на 314,2 nm и 340,6 nm. Термодинамичка константа стабилности комплекса $\text{UO}_2(\text{II})$ -фенилефрин, $\text{UO}_2(\text{C}_9\text{H}_{12}\text{O}_2\text{N})_2$, на $I = 0$ и на собној температури (25 °C) износи $\log \beta_2^0 = 14,0$, а $\Delta G_2^0 = -79,6 \text{ kJ mol}^{-1}$. Линеарна зависност апсорбације од концентрације фенилефрина у воденом раствору $\text{UO}_2(\text{NO}_3)_2$ концентрације $0,025 \text{ mol dm}^{-3}$ на 340,6 nm добијена је у интервалу $0,0025\text{--}0,0245 \text{ mol dm}^{-3}$ на рН 3,90 и $I = 0,075 \text{ mol dm}^{-3}$. Грешка мерења износи 2.1 %.

(Примљено 2. октобра 2006, ревидирано 9. марта 2007)

REFERENCES

1. A. C. Moffat, J. V. Jackson, M. S. Moss, *Clarke's Isolation and Identification of Drugs*, The Pharmaceutical Press, London, 1986, p. 893
2. E. Mutschler, H. Dernardorf, *Drug Actions*, Medipharm Scientific Publishers, Stuttgart, 1995, pp. 222 and 226
3. K. G. Bhansali, *Indian J. Pharm. Sci.* **41** (1979) 153
4. I. Muszalska, M. Zajac, G. Wrobel, M. Nogowska, *Acta Pol. Pharm.* **57** (2000) 247
5. E. H. El-Mossalamy, *Spectrochim. Acta A* **60** (2004) 1161
6. D. Malešev, D. Veselinović, Z. Radović, L. Pavun, *Arh. Farm.* **1–2** (1995) 9
7. L. Pavun, D. Malešev, D. Veselinović, *Arh. Farm.* **53** (2003) 27
8. I. Vogel, *Quantitative Inorganic Analysis*, Longmans, Green and Co, London, 1951, p. 471
9. J. Yoe, A. Jones, *Ind. Eng. Chem. Anal. Ed.* **16** (1944) 111
10. H. Irving, T. Pierce, *J. Chem. Soc.* (1959) 2565
11. D. Malešev, Z. Radović, M. Jelikić Stankov, *Monatsh. Chem.* **121** (1990) 455
12. J. Inczédy, *Analytical Applications of Complex Equilibria*, Horwood and Willy, New York, 1976, p. 137
13. D. Malešev, Z. Radović, M. Jelikić Stankov, *Monatsh. Chem.* **122** (1991) 429
14. D. Malešev, Z. Radović, M. Jelikić Stankov, *Spectrosc. Letters* **26** (1993) 1985
15. V. Kuntić, M. Kosanić, D. Malešev, Z. Radović, U. Mioč, *J. Serb. Chem. Soc.* **63** (1998) 565
16. V. Kuntić, D. Malešev, Z. Radović, M. Kosanić, *J. Agric. Food Chem.* **46** (1998) 5139.



Derivative spectrophotometric determination of the herbicides picloram and triclopyr in mixtures

BILJANA F. ABRAMOVIĆ^{1*#}, VESNA B. ANDERLUH^{1#},
FERENC F. GAÁL^{1,2#} and DANIELA V. ŠOJIC^{1#}

¹Faculty of Sciences, Department of Chemistry, Trg D. Obradovića 3, 21000 Novi Sad and

²Academy of Sciences and Arts of Vojvodina, Dunavska 37, 21000 Novi Sad, Serbia

(Received 14 July 2006, revised 13 March 2007)

Abstract: A derivative spectrophotometric method for the determination of the herbicides picloram (4-amino-3,5,6-trichloropicolinic acid) and triclopyr (3,5,6-trichloro-2-pyridyloxyacetic acid) in mixtures was developed in this work. Derivative spectrophotometric determination of the selected herbicides was preceded by investigations concerning the influence of pH, in the pH interval from 1 to 9. At pH 3.2, picloram and triclopyr solutions are stable under daylight for nine months. This pH was used for all subsequent determinations. It was also found that the use of the first derivative of the spectra at 232 nm was optimal for the determination of picloram, while use of the second derivative of the spectra at 211 nm was best suited for the determination of triclopyr. The calibration curves are linear in the concentration range 0.8 – 13 $\mu\text{g cm}^{-3}$ with correlation coefficients –0.9998 for picloram and 0.9996 for triclopyr. The limit of detection of the developed method is 0.08 $\mu\text{g cm}^{-3}$ for picloram and 0.03 $\mu\text{g cm}^{-3}$ for triclopyr. Derivative spectrophotometry was shown to be an appropriate method for the determination of picloram and triclopyr in mixtures and in pesticide formulations, unlike the deconvolution method.

Keywords: picloram, triclopyr, mixture, derivative spectrometry, zero-crossing method, deconvolution.

INTRODUCTION

Picloram (4-amino-3,5,6-trichloropicolinic acid, M_r 241.46, Fig. 1a) and triclopyr (3,5,6-trichloro-2-pyridyloxyacetic acid, M_r 256.47, Fig. 1b) are selective systemic herbicides, in the chemical class of pyridine compounds, used worldwide to control most annual and perennial broad-leaved weeds in lawns, turf, pastures, rights-of-ways and various crops, such as wheat, barley and oats.¹ They are used in the form of salts or esters as active components in different pesticide formulations individually and in mixtures. These formulations, besides the active components, generally, also contain one or more inert ingredients, such as liquid hydrocarbons, ethylene glycol, diethylene glycol monoethyl ether, polyglycol, ethanol etc.²

* Corresponding author. E-mail: abramovic@ih.ns.ac.yu

Serbian Chemical Society member.

doi: 10.2298/JSC0709809A

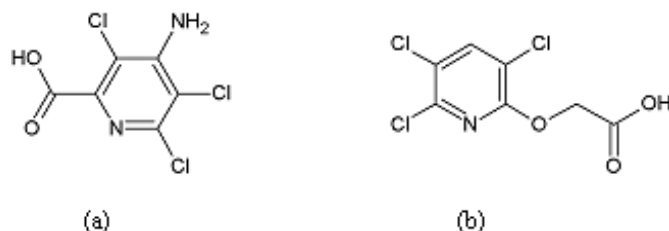


Fig. 1. Structures of (a) picloram and (b) triclopyr.

AOAC for determination of picloram and/or triclopyr provides the only official method for the determination of picloram and 2,4-D (2,4-dichlorophenoxyacetic acid) in mixtures in pesticide formulations, by applying a liquid chromatographic method.³

Spectrophotometric analysis, on the other hand, offers a fast and reliable method for solving different analytical problems. However, in conventional quantitative spectrophotometric methods based on the measurement of the absorbance of the analyte at a given wavelength, it is very common, especially in analysis of complex mixtures, for the analyte to be accompanied by other compounds exhibiting interfering signals. In such cases, the derivative method offers a useful means for improving the resolution of the determination of mixtures, because it enhances the detectability of minor spectral features.⁴⁻⁷ Namely, derivative spectrophotometry is based on use of derivative spectra which are generated from the zero-order spectra. Separation of overlapped signals and elimination of background caused by presence of other compounds in a sample can be achieved by derivatization, enabling the determination of one or more analytes without prior separation or purification.⁴⁻⁷ Derivative spectrophotometry is an analytical technique which has proven to be of great use for obtaining qualitative and quantitative information from spectra composed of unresolved bands by using the first or higher derivatives of the absorbance with respect to wavelength. It emphasizes subtle spectral features by enabling the resolution of multi-component elements and reducing the effect of spectral background interferences. This technique offers an alternative approach to the enhancement of sensitivity and specificity in the analysis of mixtures. The derivative transformation allows discernment against broad band interferences which arise from turbidity or non-specific matrix absorption.

As already stated, picloram and triclopyr are commercially available in pesticide formulations, either individually or in mixtures, as well as with inert ingredients. For this reason, the objective of this work was to develop a derivative spectrophotometric method for their determination in mixtures. The developed method was validated by determination of these herbicides in synthetic mixtures, as well as in formulations. In addition, the aim of this work was to compare the results obtained by derivative spectrophotometry to those obtained by using the deconvolution mode of the software provided with the spectrophotometer.

EXPERIMENTAL

Chemicals and solutions

Picloram (97.4 %) and triclopyr (99.8 %) were both purchased as analytical standards from Riedel–de Haën. Boric acid, *p.a.*, was purchased from Kemika, Zagreb, phosphoric acid, 85 %, *p.a.*, from Lachema, Neratovice, while sodium hydroxide, *p.a.*, was purchased from ZorkaPharm, Šabac. All solutions were made using doubly distilled water.

Stock solutions of the investigated herbicides ($\sim 250 \mu\text{g cm}^{-3}$) were prepared for the investigations. Standard solutions for the construction of the calibration curve ($0.8\text{--}13 \mu\text{g cm}^{-3}$) were prepared by measuring the required volumes of stock solutions into 10 cm^3 volumetric flasks. Then, 2 cm^3 of Britton–Robinson (BR) buffer pH 3.2 were added and the solutions were made to mark with doubly distilled water. For investigations of the influence of pH on the absorbance of picloram and triclopyr, solutions containing $13 \mu\text{g cm}^{-3}$ of each herbicide and 2 cm^3 of BR buffer of the appropriate pH value, in the interval from 1.0 to 9.0, were prepared. In the case of investigation of stability of solutions of picloram and triclopyr, two series of solutions containing $\sim 25 \mu\text{g cm}^{-3}$ of herbicides at pH 3.2 were prepared. One series was left to stand in the light, near a window, while the other was a control series which was for that reason left in the dark, also at room temperature. Spectra were recorded periodically during 9 months.

The three investigated synthetic binary mixtures were obtained by measuring appropriate volumes of stock solutions into 10 cm^3 volumetric flasks to make mixtures in which picloram and triclopyr were in the following concentrations: $4 \mu\text{g cm}^{-3}$ picloram and $12 \mu\text{g cm}^{-3}$ triclopyr (mixture 1), $6 \mu\text{g cm}^{-3}$ picloram and $6 \mu\text{g cm}^{-3}$ triclopyr (mixture 2) and $12 \mu\text{g cm}^{-3}$ picloram and $4 \mu\text{g cm}^{-3}$ triclopyr (mixture 3). These solutions also contained 2 cm^3 of pH 3.2 BR buffer.

Furthermore, the developed method was used for the determination of triclopyr in Garlon 3A, a formulation of this herbicide which, besides triclopyr in form of the triethylamine salt, contained ethanol, triethylamine and ethylenediaminetetraacetic acid as inert ingredients. The content of the acid equivalent of triclopyr was 31.8 %. For this purpose, a stock solution of Garlon 3A, in which the triclopyr concentration was $\sim 250 \mu\text{g cm}^{-3}$, was prepared. This solution was further diluted to prepare solutions with triclopyr concentrations of $\sim 12 \mu\text{g cm}^{-3}$. These determinations were also carried out at pH 3.2 by addition of BR buffer.

Unfortunately, a formulation containing a mixture of picloram and triclopyr is not available for purchase on the Serbian market. For this reason, such a mixture was prepared by adding a solution of picloram to an appropriate aliquot of Garlon 3A in an amount to obtain a mixture which contained triclopyr and picloram in the ratio 3:1; the ratio in which these two herbicides are found in commercially available Grazon[®]DS. In the said formulation, triclopyr is present as the butoxy-ethylester and picloram as the hexyloxypropylamine salt.

Analytical procedure

Spectra of all solutions were recorded in the wavelength region from 200 to 325 nm on an Anthelie version 2 spectrophotometer (Secomam, France), in 1 cm quartz cells with a fixed slit width (1 nm) at scan rate 1200 nm min^{-1} . Triclopyr was determined either from zero-order spectra at 232 nm or from the second derivative of the spectra at 211 nm, while picloram was determined from the first derivative of the spectra at 232 nm. The derivatives of the spectra were smoothed by the adjacent averaging method, using 5 data points for smoothing.

In addition to recording the spectra of the investigated compounds, advantage was taken of the deconvolution mode of the software provided with the spectrophotometer. In this case, calibration was performed with standard solutions of picloram and triclopyr, each having concentration of $13 \mu\text{g cm}^{-3}$. Calibration was followed by recording the spectra of the sample. Subsequently, the concentration of each herbicide in the mixtures automatically appears on the display of the spectrophotometer.

RESULTS AND DISCUSSION

Optimization of working conditions

The derivative spectrophotometric determination of the selected herbicides was preceded by investigations concerning the influence of pH, in the pH interval from 1 to 9. These investigations were carried out individually for each herbicide (Fig. 2). The dependence of the absorption spectra with the medium acidity indicates that picloram and triclopyr are involved in acid–base reactions. It was observed that there were no significant changes in the shape of the spectra in the pH interval from 3.2 to 9.0. All further determinations were carried out at pH 3.2. Bearing in mind that, according to literature data, the pK_a value for picloram is in the interval 2.2–3.6,^{8–10} and for triclopyr 2.68–3.89,¹¹ it can be concluded that dissociation of the carboxyl group occurred at the employed pH value.

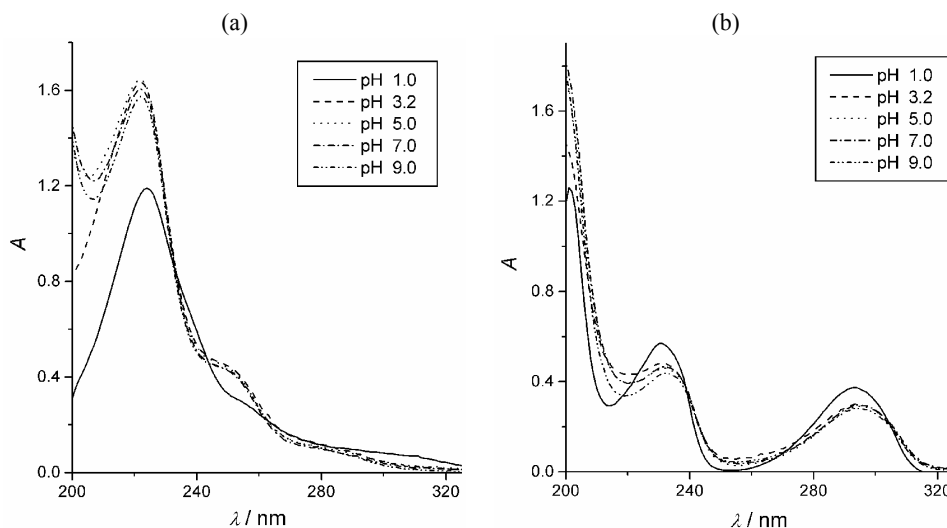


Fig. 2. The influence of pH on the appearance of $12.60 \mu\text{g cm}^{-3}$ picloram (a) and $12.50 \mu\text{g cm}^{-3}$ triclopyr (b) zero-order derivative spectra.

To additionally optimize the working conditions, investigations were undertaken to determine whether the investigated compounds degrade in the presence of light during the time necessary to perform the analysis. Firstly, since there are literature data¹ indicating photodegradation of these herbicides, the spectrum of each compound was recorded five times in a row, in the wavelength region from 200 to 325 nm, to determine if any degradation occurred during the recording of the spectrum. This was found not to be the case, *i.e.*, there were no relevant changes in the peak shape, position or intensity for both herbicides, indicating that no degradation occurred during the recording of the spectrum. Secondly, two series of solutions were prepared with the aim to determine if any degradation of the investigated herbicides occurs under normal laboratory conditions, *i.e.*, at room temperature in day-

light. One series was left to stand in the light, near a window, while the other was the control series which was, for that reason, left in the dark, also at room temperature. No significant changes occurred in either series of solutions within nine months and it can, therefore, be concluded that the analyses can be carried out under normal laboratory conditions, without the use of special working conditions.

Determination

After the preliminary investigations, the absorption spectra of triclopyr and picloram (Fig. 3) were recorded individually and in a mixture in the region between 200 and 325 nm. As a result of the similarity of the structures of the investigated compounds, their absorption spectra partially overlap and the analysis of their mixtures by direct measurement of the absorbance signals was not possible. For this reason, the use of first to fourth order derivative spectra for the determination of each herbicide, as well as their mixtures was tested. One of the frequently used methods in derivative spectrometry is the "zero-crossing" method,^{4-7,12-17} which calls for the determination of one component at the wavelength at which the derivative spectrum of the other passes through zero. This method was used in the present study. Thus, it was found that the use of the first derivative of the spectra at 232 nm (Fig. 4a, curve 1) was optimal for the determination of picloram, while the use of the second derivative of the spectra at 211 nm (Fig. 4b, curve 2) was best suited for the determination of triclopyr, since at these wavelengths practically no interferences were present. The use of higher order derivatives of the spectra (third and fourth derivative) did not give satisfactory results due to the high signal to noise ratio and, for this reason, these derivatives of the spectra were not employed further.

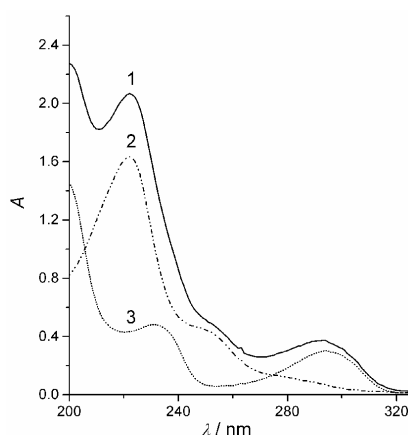


Fig. 3. Absorption spectra of (1) mixture of $12.60 \mu\text{g cm}^{-3}$ picloram and $12.50 \mu\text{g cm}^{-3}$ triclopyr; (2) $12.60 \mu\text{g cm}^{-3}$ picloram; (3) $12.50 \mu\text{g cm}^{-3}$ triclopyr. pH 3.2.

Calibration curves were constructed from the first and second derivatives of the picloram and triclopyr spectra, respectively, at the chosen wavelengths. The regression coefficients and linearity ranges of the calibration curves, obtained by

the linear fit of the acquired data using the least squares method, are presented in Table I. The same table presents the limits of detection (LOD) and quantification (LOQ), which were calculated for both herbicides from the first and second derivatives of the spectra of 20 blank measurements and the slopes of the corresponding calibration curves. Namely, the LOD was determined as the analyte concentration giving a signal equivalent to three times the standard deviation of the blank signal, while for the LOQ this concentration was taken to be equal to ten times the standard deviation of the blank signal.

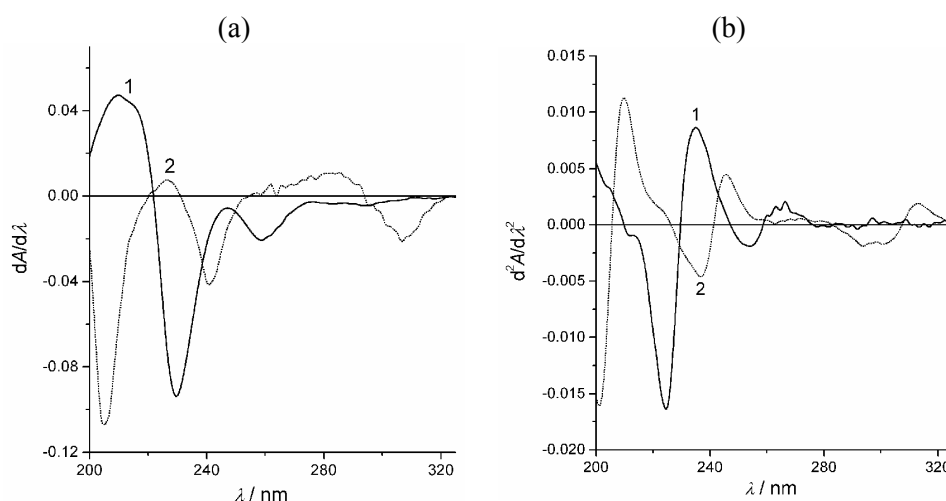


Fig. 4. Derivative spectra of (1) $12.60 \mu\text{g cm}^{-3}$ picloram and (2) $12.50 \mu\text{g cm}^{-3}$ triclopyr: (a) first and (b) second. pH 3.2.

After establishing the optimal working conditions for the determination of the selected herbicides, the developed method was applied to the analysis of three synthetic binary mixtures of picloram and triclopyr. Bearing in mind that triclopyr appears in the commercially available formulations in form of the triethanolamine salt or butoxyethyl ester, and picloram as the hexyloxypropyl amine salt and that they rapidly dissociate/hydrolyse in water to the triclopyr acid/anion,¹⁸ *i.e.*, picloram acid/anion (in dependence on the pH of solution), and triethanolamine, butoxyethanol, *i.e.*, hexyloxypropyl amine, the use of triclopyr and picloram as the analytical standards for the preparation of the synthetic binary mixtures was justified. The composition of these mixtures was chosen to simulate the composition of commercially available formulations. Namely, in commercially available formulations, the ratios of triclopyr and picloram varies from 2:1 to 3:1. Furthermore, the ratios of triclopyr and picloram were chosen with the aim of establishing the influence of the composition of the mixture on the analysis results. The first and second derivatives of the spectra for all three mixtures are presented in Fig. 5 and the results of these determinations together with the accuracy and precision data are presented in

Table II. On comparing the results obtained for the investigated mixtures according to the t -test, it can be seen that there was no significant difference between the taken and found concentration of the analyzed compounds at the 0.05 level, except in the case of picloram in mixture 3, where there was no significant difference at the 0.01 level. It can, thus, be concluded that the applied method can satisfactorily be employed for the determination of the above said herbicides.

TABLE I. Statistical analysis of calibration graphs in the determination of picloram and triclopyr by derivative spectrophotometry method

Parameter	Picloram	Triclopyr	
Derivative	first	zero	second
Wavelength, nm	232	232	211
Concentration range, $\mu\text{g cm}^{-3}$	0.8–13	1.6–13	0.8–13
LOD, $\mu\text{g cm}^{-3}$	0.08	0.04	0.03
LOQ, $\mu\text{g cm}^{-3}$	0.28	0.13	0.11
<i>Regression equation^a</i>			
Slope (b)	-6.76×10^{-3}	5.10×10^{-2}	1.27×10^{-3}
Standard deviation of slope (S_b)	6.72×10^{-5}	1.76×10^{-3}	1.95×10^{-5}
Intercept (a)	-8.40×10^{-4}	1.52×10^{-2}	3.69×10^{-4}
Standard deviation of intercept (S_a)	5.01×10^{-4}	1.38×10^{-2}	1.53×10^{-4}
Standard error of estimations (S_e)	5.84×10^{-4}	1.61×10^{-2}	1.79×10^{-4}
Correlation coefficient (r)	-0.9998	0.9991	0.9996

^a $Y = a + bc$, where c is concentration in $\mu\text{g cm}^{-3}$ and Y is A (zero derivative), $dA/d\lambda$ (first derivative) and $d^2A/d\lambda^2$ (second derivative). The linearity for picloram and triclopyr determined by a six-point calibration.

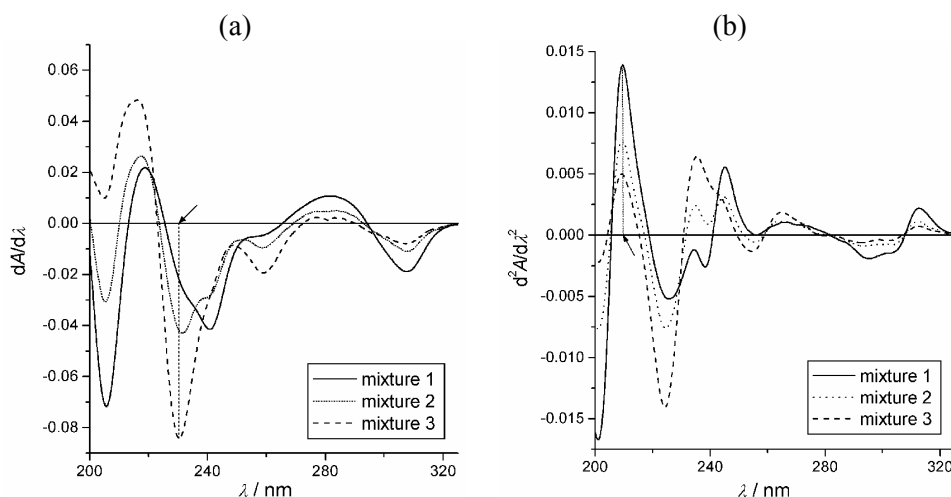


Fig. 5. Derivative spectra for mixtures of picloram and triclopyr: first derivative (a) and second derivative (b). pH 3.2. Mixture 1— $4 \mu\text{g cm}^{-3}$ picloram and $12 \mu\text{g cm}^{-3}$ triclopyr; mixture 2— $6 \mu\text{g cm}^{-3}$ picloram and $6 \mu\text{g cm}^{-3}$ triclopyr; mixture 3— $12 \mu\text{g cm}^{-3}$ picloram and $4 \mu\text{g cm}^{-3}$ triclopyr.

TABLE II. Results of the determination of picloram and triclopyr content in synthetic mixtures ($n = 6$)

Mixture	Found concentration $\mu\text{g cm}^{-3}$		Recovery %		RSD %		t -Test ^a	
	Picloram	Triclopyr	Picloram	Triclopyr	Picloram	Triclopyr	Picloram	Triclopyr
1	4.22	12.28	99.8	100.4	2.51	1.68	0.16	0.52
2	6.38	6.40	100.2	100.4	1.65	0.78	0.33	1.17
3	11.98	4.30	99.3	100.4	0.59	0.69	3.07	1.35

^a $t_{0.05;5} = 2.57$; $t_{0.01;5} = 4.03$.

The same synthetic mixtures were then analyzed by applying the deconvolution mode of the spectrophotometer (Table III). It can be concluded from the results of the t -test, that when the picloram content was determined, in all cases, there was a significant difference at the 0.01 level, while the accuracy was better in the case of the determination of triclopyr, *i.e.*, for the mixture 1 and 3, there was no significant difference at the 0.05 level and for mixture 2, there was no significant difference at the 0.01 level. Therefore, the deconvolution mode of analysis is not entirely applicable to the analysis of the investigated mixtures, *i.e.*, better results are obtained using the developed method.

TABLE III. Results of the determination of picloram and triclopyr content in synthetic mixtures (deconvolution mode of the spectrophotometer) ($n = 6$)

Mixture	Found concentration $\mu\text{g cm}^{-3}$		Recovery %		RSD %		t -Test ^a	
	Picloram	Triclopyr	Picloram	Triclopyr	Picloram	Triclopyr	Picloram	Triclopyr
1	4.42	12.18	104.6	99.5	1.62	1.20	6.68	1.04
2	6.25	6.56	98.1	102.9	1.16	2.27	4.14	3.06
3	11.78	4.35	97.6	101.5	0.89	2.36	6.66	1.51

^a $t_{0.05;5} = 2.57$; $t_{0.01;5} = 4.03$.

The developed method was applied for the determination of triclopyr in Garlon 3A. In this case, the suitability of the zero-order spectra, second derivative spectra and the deconvolution mode were investigated. Namely, since Garlon 3A contains only triclopyr, the possibility of using zero-order spectra for determination of its content was investigated. Statistical analysis of the calibration graph for the determination of triclopyr by the zero-order spectrophotometric method is given in Table I. Since the employed spectrophotometer can also operate in the deconvolution mode, the results obtained by this method were compared to those obtained from the zero-order and second derivative spectra. The results of these determinations are presented in Table IV. From the relative standard deviation (RSD) values, as well as from the results of the t -test, it can be concluded that zero-order and second derivative spectra can be satisfactorily used for determination of triclopyr in Garlon 3A. However, the deconvolution mode is not at all appropriate for the determination of triclopyr in the pesticide formulation.

TABLE IV. Results of the determination of triclopyr content in Garlon 3A ($n = 6$)

Mode of determination	Found ^a g	Recovery %	RSD %	t -Test ^b
Zero-order	31.62	99.42	1.16	1.22
Derivative	31.80	99.99	0.48	0.04
Deconvolution	37.85	119.04	0.62	63.4

^aNominal value for pesticide formulation is 31.8 g per 100 g. ^b $t_{0.05;5} = 2.57$; $t_{0.01;5} = 4.03$.

Furthermore, the developed method was used for the determination of picloram and triclopyr in a mixture made by the addition of picloram to the solution of Garlon 3A. The results of these determinations are presented in Table V. As can be seen, the recoveries obtained from derivative spectra were somewhat higher than 100 % for both determined herbicides. Nevertheless, there was no significant difference between the taken and found concentration at the 0.05 level for picloram, and no significant difference at the 0.01 level for triclopyr. However, in case of the deconvolution method, the results are significantly higher in both cases. It can be concluded that this method is not at all appropriate for the determination of picloram and triclopyr in this type of mixture.

TABLE V. Results of the determination of picloram and triclopyr content in a mixture of Garlon 3A and picloram ($n = 6$)

Mode of determination	Found concentration $\mu\text{g cm}^{-3}$		Recovery %		RSD %		t -Test ^a	
	Picloram	Triclopyr	Picloram	Triclopyr	Picloram	Triclopyr	Picloram	Triclopyr
Derivative	4.14	12.54	101.0	101.3	2.17	0.80	0.33	3.92
Deconvolution	5.48	15.91	133.6	128.5	1.85	0.95	33.3	50.8

^a $t_{0.05;5} = 2.57$; $t_{0.01;5} = 4.03$.

CONCLUSIONS

A derivative spectrophotometric method using the zero-crossing method was developed for the determination of the herbicides picloram and triclopyr in mixtures at pH 3.2. For the determination of picloram, the first derivative was used by measuring the signal at 232 nm, while the second derivative was used for the determination of triclopyr by measuring the signal at 211 nm. The developed method was successfully used to determine picloram and triclopyr in synthetic mixtures, as well as in a triclopyr formulation Garlon 3A and Garlon 3A spiked with picloram, which indicates the possibility of application of the method not only for these mixtures and pesticide formulations, but for many others as well.

Acknowledgment: The authors acknowledge the financial support of the Provincial Secretariat for Science and Technological Development, Novi Sad (Grant No 114-451-01338/2006-1) and the Ministry of Science and Environment Protection of the Republic of Serbia (Project No ON142029).

ИЗВОД

ДЕРИВАТИВНО СПЕКТРОФОТОМЕТРИЈСКО ОДРЕЂИВАЊЕ ХЕРБИЦИДА
ПИКЛОРАМА И ТРИКЛОПИРА У СМЕШИБИЉАНА Ф. АБРАМОВИЋ¹, ВЕСНА Б. АНДЕРЛУХ¹, FERENC F. GAÁL^{1,2} и ДАНИЕЛА В. ШОЈИЋ¹¹Природно–мајеминички факултет, Дејарман за хемију, Трџ Д. Обрадовића 3, 21000 Нови Сад и²Војвођанска академија наука и уметности, Дунавска 37, 21000 Нови Сад

Пиклорам (4-амино-3,5,6-трихлорпиридин-2-карбоксилна киселина) и триклопир (3,5,6-трихлор-2-пиридилдоксисирћетна киселина) су селективни системични хербициди, који се у заштити биља примењују за уништавање једногодишњих и вишегодишњих широколисних коро­ва. Како се на тржишту у пестицидним формулацијама могу наћи појединачно и у смеши, у овом раду је развијена деривативна спектрофотометријска метода за њихово селективно одређивање у смеши. У циљу оптимизације одређивања одабраних хербицида, најпре је испитан утицај рН на изглед њихових спектара, у интервалу од 1 до 9 рН јединица. При рН 3,2 раствори пиклорама и триклопира су стабилни на дневној светлости 9 месеци. Сва даља одређивања су вршена при рН 3,2. Нађено је да је за одређивање пиклорама оптимално користити први извод спектра, мерењем сигнала на 232 nm, док је за одређивање триклопира оптимална примена другог извода спектра, мерењем сигнала на 211 nm. Линеаран опсег мерења је од 0,8 до 13 $\mu\text{g cm}^{-3}$ за оба хербицида са коефицијентом корелације од $-0,9998$ за пиклорам и $0,9996$ за триклопир. Граница детекције разрађених поступака је $0,08 \mu\text{g cm}^{-3}$ за пиклорам и $0,03 \mu\text{g cm}^{-3}$ за триклопир. Деривативна спектрофотометријска метода се показала погодном за одређивање пиклорама и триклопира у смеши и у формулацијама пестицида, за разлику од деконволуционе методе.

(Примљено 14. јула 2006, ревидирано 13. марта 2007)

REFERENCES

1. C. Tomlin, Ed., *The Pesticide Manual*, 10th Ed., Crop Protection Publications, 1995
2. Dow AgroSciences, *Garlon Family of Herbicides*, Technical Fact Sheet, 2002, Dow AgroSciences LLC V01-101-011 (9/02) cii 010-50020
3. AOAC, Official Method 976.03, Picloram and 2,4-D in pesticide formulations, Liquid chromatographic method (2000)
4. G. V. Popović, L. B. Pfendt, V. M. Stefanović, *J. Serb. Chem. Soc.* **65** (2000) 457
5. J. Karpińska, *Talanta* **64** (2004) 801
6. C. B. Ojeda, F. S. Rojas, *Anal. Chim. Acta* **518** (2004) 1
7. A. Y. El-Sayed, N. A. El-Salem, *Anal. Sci.* **21** (2005) 595
8. FAO specifications and evaluations for agricultural pesticides, Picloram, 4-amino-3,5,6-trichloropyridine-2-carboxylic acid, <http://www.fao.org/ag/agp/agpp/Pesticid/Specs/docs/Pdf/new/picloram.pdf> (2007 Feb 24)
9. Environmental & Workplace Health, http://www.hc-sc.gc.ca/ewh-semt/pubs/water-eau/doc_sup-appui/picloram-piclorame/index_e.html (2007 Feb 24)
10. M. C. Corredor, J. M. Rodríguez Mellado, M. Ruiz Montoya, *J. Electrochem. Soc.* **153** (2006) E33
11. Triclopyr – Revised Human Health and Ecological Risk Assessments Final Report, http://www.fs.fed.us/foresthealth/pesticide/risk_assessments/0303_triclopyr.pdf (2007 Feb 24)
12. K. Wróbel-Zasada, K. Wróbel-Kaczmarczyk, P. L. López-de-Alba, L. López-Martínez, M. A. García-López, *Talanta* **43** (1996) 1055
13. R. Corbella Tena, M. A. Rodríguez Delgado, M. J. Sanchez, F. Garcia Montelongo, *Talanta* **44** (1997) 673

14. F. Onur, C. Yücesoy, S. Dermis, M. Kartal, G. Kökdil, *Talanta* **51** (2000) 269
15. A. El-Gindy, A. Ashour, L. Abdel-Fattah, M. M. Shabana, *J. Pharm. Biomed. Anal.* **25** (2001) 299
16. S. Saglik, O. Sagirli, S. Atmaca, L. Ersoy, *Anal. Chim. Acta* **427** (2001) 253
17. K. Karljickovic-Rajic, D. Novovic, V. Marinkovic, D. Agbaba, *J. Pharm. Biomed. Anal.* **32** (2003) 1019
18. EPA, Reregistration Eligibility Decision (RED), Triclopyr, EPA 738-R-98-011, <http://www.epa.gov/REDS/2710red.pdf> (2007 Feb 24).



Interferences from titanium and zirconium during calcium determination by flame spectrometry

DIMITRIJE Đ. STOJANOVIĆ^{1#}, JELENA S. MILINOVIĆ^{1*#} and
SNEŽANA D. NIKOLIĆ-MANDIĆ^{2#}

¹*Institute of Pesticides and Environmental Protection, Zemun and* ²*Faculty of Chemistry, University of Belgrade, Studentski trg 16, 11000 Belgrade, Serbia*

(Received 8 December 2006, revised 12 February 2007)

Abstract: Titration methods based on an inhibition effect were used to investigate the interferences from Ti and Zr in the determination of Ca by atomic absorption and flame emission spectrometry using an air–acetylene flame. Changes either in the absorption or emission signal of Ca were continuously registered on a computer display and characteristic titration curves were obtained. The mole ratios between Ti or Zr and Ca at characteristic points on titration curves were used to explain the quantitative changes occurring in the solution being titrated and aspirated into the flame. In order to investigate procedures for eliminating these interferences, a method of atomic absorption inhibition release titration was used. For this purpose, a solution of La, as a releasing agent with a very low Ca concentration, used as an indicator, was continuously titrated with the solution of Ti as inhibitor. A comparative study of the activity of Ba, Sr and La as releasing agents was investigated during titration of Ca with Zr solution. Based on the calculated mole ratios between Zr and Ba, Sr or La, the effectiveness of these agents in eliminating the interferences was determined. Possible reactions occurring during evaporation of the aerosol in the air–acetylene flame are represented by chemical equations.

Keywords: interference, calcium determination, titanium and zirconium, flame atomic absorption and emission spectrometry, titration method, releasing action.

INTRODUCTION

Interferences causing lower results during calcium determination by atomic absorption (emission) flame spectrometry in the presence of Ti or Zr have been reported in the literature.¹ Titanium and zirconium, being the inhibiting agents during the flame spectrometric determination of Ca, are assumed to form thermostable products with this alkaline earth metal.² This so-called inhibition effect is especially evident in low-temperature flames.³

In this study, titration based on the inhibition effect⁴ was used to investigate

[#] Serbian Chemical Society active member.

* Corresponding author. E-mail: jmilinovic@verat.net

doi: 10.2298/JSC0709821S

the interferences from Ti or Zr during the determination of calcium in an air–acetylene flame. Definite volumes of standard solutions of titanium or zirconium (titrand solution) were continuously titrated against a standard solution of CaCl_2 and *vice versa*. Simultaneously, as the titrand solution was aspirated into an air–acetylene flame, changes in absorption or emission of the Ca signal (422.7 nm) were monitored on a computer display. Titration curves with distinct characteristic points were obtained. The mole ratios between the inhibitors (Ti or Zr) and calcium at these inflection points were used to explain the processes occurring during evaporation of the aerosol in the flame.

It is important to note that the term “titration” is used here to designate an operation, *i.e.*, a procedure employed for the study of processes occurring in a flame, rather than to its conventional sense in volumetric analysis.

Interferences from Ti or Zr during the determination of calcium are commonly eliminated by addition of La.⁵ Also, Sr or Ba can be used to eliminate chemical interferences during calcium determination.^{6,7}

The continuous titration method, termed atomic absorption inhibition release titration⁸ was employed in a study of the elimination of interferences from Ti and Zr during the determination of Ca. For this purpose, a solution of La with a very low concentration of Ca, as an indicator, was continuously titrated with Ti. Changes in the atomic absorption signal of the indicator (Ca) were automatically recorded and titration curves with distinct inflection points compared to the blank curves were obtained. The determined mole ratios between Ti and La were used to explain the releasing action of La. The activity of Ba, Sr and La in the elimination of interferences was investigated during titration with a Zr solution, in the presence of Ca as indicator. Based on calculated mole ratios between Zr and corresponding releasing agents, their effectiveness in the elimination of interferences was determined. Possible reactions occurring during evaporation of an aerosol in an air–acetylene flame are presented by chemical equations.

The aim of this study was to summarize the quantitative results obtained in a study of reactions occurring between Ti and Ca or Zr and Ca, and thus advance our understanding of the changes in equilibrium occurring during the evaporation of an aerosol in an air–acetylene flame. Also, the releasing action of La in the elimination of interferences by Ti during the determination of Ca was studied. An investigation of the effectiveness of Ba, Sr and La in eliminating interferences from Zr has a scientific rationale, as well as an economic one, because the market prices of Ba, Sr or La salts vary significantly.

EXPERIMENTAL

Instrumentation and chemicals

A SpectrAA 220 Varian atomic absorption (emission) flame spectrometer was used for all the titration measurements. The spectrometer was attached to computer which enabled the automatic monitoring of changes either in the absorption or emission of the Ca signal. During the titration, the

titrand solution was stirred with a magnetic stirrer and a beaker with the titrant solution was connected to a peristaltic pump (LKB Bromma). The titrant solution was added at constant flow rate (about 3 ml min^{-1}) from a microburette through a tap connected by a capillary to the peristaltic pump. The rate of titrant addition was approximately equal to the rate of titrand aspiration into the flame, in order to minimize changes in volume during the titration.

Continual titration measurements were performed in an air–acetylene flame, with a 0.7 cm burner height, following the procedure described previously.^{9,10} Changes in emission of Ca (at 422.7 nm) occurring during titration were followed using a 0.2 nm slit width. Changes in the calcium atomic absorption (at 422.7 nm) were followed employing a hollow cathode lamp (Varian) for Ca, operating at 10.0 mA.

Highly purified, deionized water used for the preparation of all dilute standard solutions, was obtained using an Elga PURELAB Option-R 7/15 water purification unit. Standard Ca, Ba and Sr solutions were prepared by dissolving previously dried appropriate carbonates (*p.a.* Merck and *p.a.* Carlo Erba, Milano) in the minimal volume of 2M HCl or HNO₃. The La(III) solution was prepared from lanthanum chloride heptahydrate (LaCl₃·7H₂O, *p.a.* 98 % BDH laboratory reagents, England).

Standard solutions of Ti and Zr were prepared by dissolving TiCl₄ (Baker, USA), *i.e.*, Zr(NO₃)₄ (*p.a.* Merck). The concentrations of Ti and Zr in these solutions were determined gravimetrically *via* the corresponding dioxides, using the cupferron method.¹¹

RESULTS AND DISCUSSION

The study of the interferences from titanium

In order to study the interferences from titanium, a TiCl₄ solution, in the $10\text{--}50 \mu\text{g Ti ml}^{-1}$ concentration range, was titrated with a CaCl₂ solution in which the calcium concentration was $500 \mu\text{g Ca ml}^{-1}$. The titration curves in this case had a characteristic shape with a significant inflection domain labelled by point a (Fig. 1).

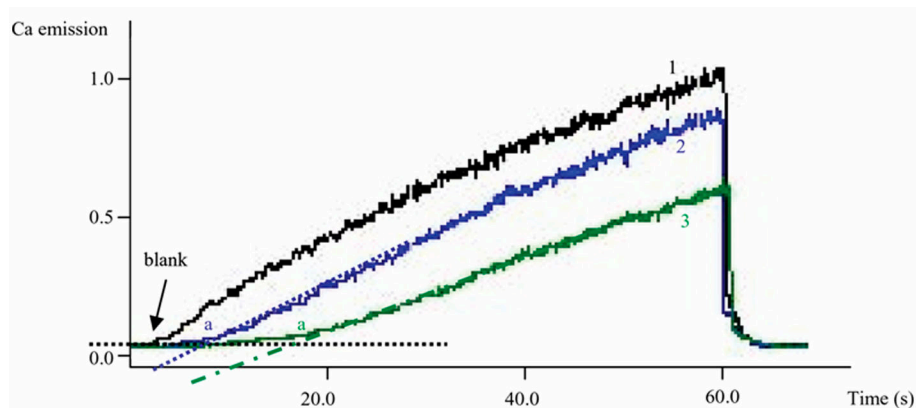


Fig. 1. Titration of 50 ml water (1), $10 \mu\text{g Ti ml}^{-1}$ (2) and $50 \mu\text{g Ti ml}^{-1}$ (3) with CaCl₂ standard solution ($500 \mu\text{g Ca ml}^{-1}$).

At the beginning of titration, the Ca emission at 422.7 nm changed only slightly, *i.e.*, Ti exerted a considerable depressive effect on the calcium emission. This occurs because Ti reacts with Ca and thermostable products are simultaneously formed during the evaporation of the aerosol. Further addition of the titrant ($500 \mu\text{g Ca ml}^{-1}$) leads to a rapid increase in the emission signal, which enables the

graphical determination of the titration end-point a. In order to calculate mole ratios Ti/Ca at point a, it is necessary to subtract the volume of CaCl₂ added during the titration of 50 ml deionized water, the so-called blank volume (Fig. 1, curve 1).

Calculation of mole ratios between Ti and Ca at the characteristic point a (Table I) showed them to be variable. Namely, mole ratios Ti/Ca increase with increasing concentration of Ti in titrand solution, which indicates the occurrence of an equilibrium change during the formation of thermostable mixed oxides, *i.e.*, CaO·5TiO₂ and CaO·6TiO₂:

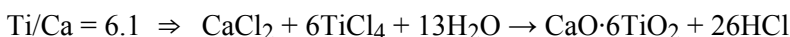
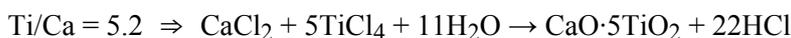


TABLE I. Mole ratios Ti/Ca obtained by titration of TiCl₄ solution with CaCl₂ solution (500 µg Ca ml⁻¹)

Ti concentration / µg ml ⁻¹	Mole ratios Ti/Ca at the inflection point a of the titration curves
10	3.5
20	4.3
30	5.2 ^a
40	6.1
50	6.2

^aThe relative standard deviation (RSD) value for five replicates is 7.0 %.

The formation of these mixed oxides with variable contents of CaO and TiO₂, which are introduced into flame as aerosol particles, indicates strongly the possible reactions occurring in the air-acetylene flame (disregarding possible influences of the combustion of the flame gases). Hence, the interference observed during Ti titration with CaCl₂ solution, can be ascribed to the much slower evaporation of the obtained calcium titanates, with respect to CaCl₂.¹²

When a reverse titration was performed, *i.e.*, when a solution of CaCl₂ was titrated with a titanium solution, the flame emission of Ca at the beginning of titration increased rapidly, depending on the calcium concentration in the titrand solution (Fig. 2). After a brief period, the Ca emission sharply decreased, which enables the determination of the so-called threshold of sensitivity of the indicator present – emission at 422.7 nm (point a).

On further addition of TiCl₄, the emission decreased gradually (depending on the Ti concentration in the titrant solution), because of the formation of new stoichiometric compounds between Ca and Ti, which enables the determination of the titration end-point b. The mole ratios Ti/Ca at points a and b were calculated and are presented in Table II.

In contrast, in the case of the titration of Ti with calcium solution, the mole ratios between Ti and Ca decreased with increasing calcium concentration (as titrand), which indicates that the formed thermostable mixed oxides have a higher CaO content.^{13,14} It was observed that the Ti/Ca values (at point b) increased

with increasing concentration of Ti as titrant when the Ca concentration was constant, which proves that the composition of the mixed oxides depends on both the titrand and titrant concentration. The calculated mole ratios at the first point (a) designate the threshold of the Ca flame emission signal and it was registered that Ti inhibited Ca even when its concentration in the solution was ten times lower than Ca concentration (Table II, Ti/Ca = 0.1).

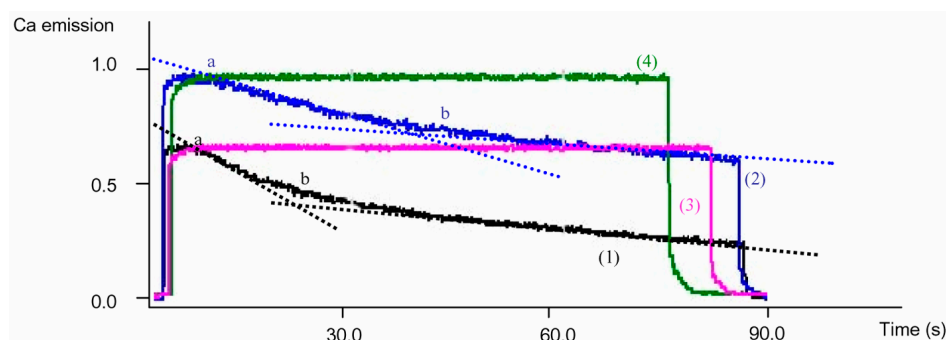


Fig. 2. Titration of $10 \mu\text{g Ca ml}^{-1}$ (1) and $20 \mu\text{g Ca ml}^{-1}$ (2) with TiCl_4 standard solution ($500 \mu\text{g Ti ml}^{-1}$) and aspiration of $10 \mu\text{g Ca ml}^{-1}$ (3) and $20 \mu\text{g Ca ml}^{-1}$ (4) as blank curves.

TABLE II. Mole ratios Ti/Ca obtained by titration of a CaCl_2 solution with a TiCl_4 solution

Ca concentration / $\mu\text{g ml}^{-1}$	Mole ratios Ti/Ca at the inflection points of the titration curves					
	Titrant concentration / $\mu\text{g Ti ml}^{-1}$					
	200		400		500	
	a	b	a	b	a	b
5	0.1	1.0	0.2	1.2	0.2	1.5
10	0.1 ^A	0.7 ^B	0.2 ^C	0.9 ^D	0.1 ^E	1.0 ^F
15	0.1	0.6	0.1	0.7	0.1	0.9
20	0.1	0.5	0.1	0.7	0.1	0.7

RSD values for five replicates are: ^A0.4, ^B2.1, ^C0.8, ^D4.6, ^E2.2 and ^F4.5 %.

It should be mentioned that similar results were obtained during the monitoring of the Ca absorption signal at 422.7 nm. Also, mole ratios Ti/Ca remained almost the same when the titrations of Ti with Ca, and *vice versa*, were performed by monitoring the emission signal at 622.0 nm (CaO band).

The study of interferences from zirconium

The processes occurring during Zr titration with a calcium chloride solution are described by the titration curves shown in Fig. 3. In contrast to the titration of TiCl_4 , the titration curves in this case show a sharp increase in the calcium absorption signal, rather than a gradual one. The existence of two distinct inflection points, a and b, on the titration curves clearly indicates that inhibition was present, but it is less intensive in comparison to Ti as the inhibitor.

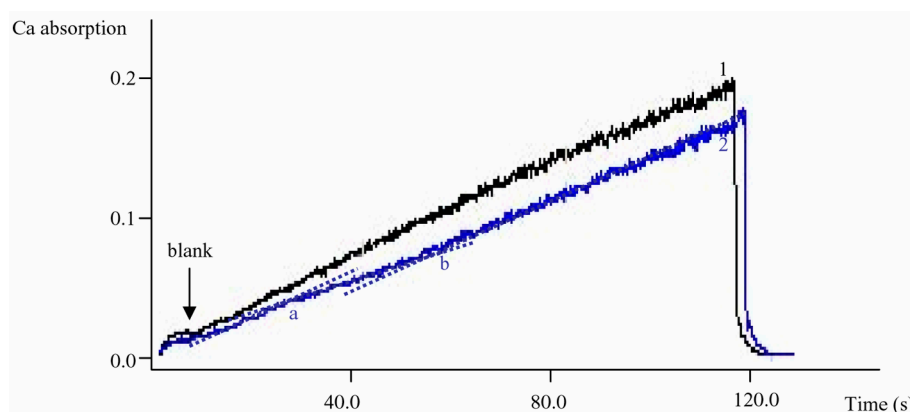


Fig. 3. Titration of 50 ml water (1) and $8 \mu\text{g Zr ml}^{-1}$ (2) with CaCl_2 standard solution ($100 \mu\text{g Ca ml}^{-1}$).

The mean values of the mole ratios Zr/Ca calculated at point a (Table III) indicate the possible formation of a mixed sesquioxide between Ca and Zr during the evaporation of the aerosol (irrespective of whether the absorption, *i.e.*, emission, at 422.7 nm or emission at 622.0 nm was measured):



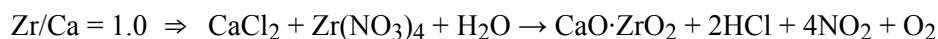
TABLE III. Mole ratios Zr/Ca obtained by titration of a $\text{Zr}(\text{NO}_3)_4$ solution with a CaCl_2 or $\text{Ca}(\text{NO}_3)_2$ solution ($100 \mu\text{g Ca ml}^{-1}$)

Zr concentration / $\mu\text{g ml}^{-1}$	Mole ratios Zr/Ca at the inflection points of the titration curves			
	Titrant			
	CaCl_2		$\text{Ca}(\text{NO}_3)_2$	
	a	b	a	b
8	1.6	1.0	1.7 ^A	1.0
10	1.4 ^B	1.0 ^C	1.3 ^D	0.9 ^E
12	1.4	0.9	1.6	0.9
15	1.3 ^A	0.9	1.4	1.0
18	1.4	0.7 ^A	1.4	0.9
Mean values	1.4 ^F	1.0 ^G	1.4 ^H	0.9 ^I

^AThese values are not taken into account.

RSD values for five replicates and the mean values are: 10.4^B, 4.2^C, 8.7^D, 5.3^E, 8.7^F, 5.0^G, 10.9^H and 4.9^I %.

Undoubtedly, at the second inflection point, b, the mean stoichiometric ratios (Table III) show that calcium metazirconate – $\text{CaO} \cdot \text{ZrO}_2$ was formed (melting point 2550 °C).¹⁵ The possible reaction occurring between Ca and Zr in the evaporating aerosol can be presented as follows:



In the case of Ca titration with $\text{Zr}(\text{NO}_3)_4$ solution, the titration curves have three pronounced inflection points (Fig. 4). The first one (point a) enables the de-

termination of the earlier-mentioned threshold of the indicator sensitivity, *i.e.*, Ca emission (422.7 nm) in the presence of the inhibitor Zr, and it is very similar to the one obtained by titration with titanium.

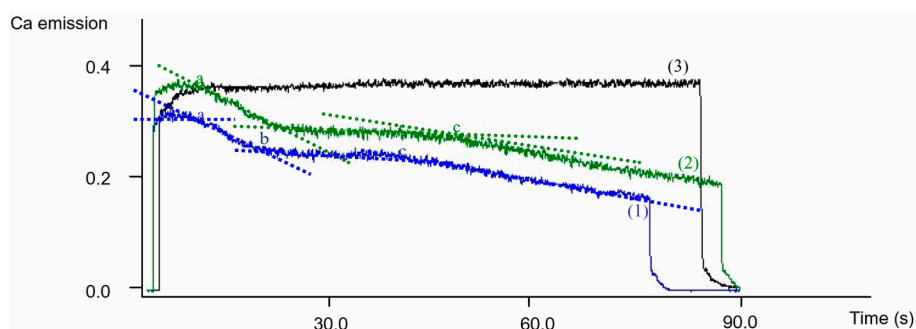


Fig. 4. Titration of 4 $\mu\text{g Ca ml}^{-1}$ (1) and 5 $\mu\text{g Ca ml}^{-1}$ (2) with $\text{Zr}(\text{NO}_3)_4$ standard solution (400 $\mu\text{g Zr ml}^{-1}$) and aspiration of 5 $\mu\text{g Ca ml}^{-1}$ (3) as blank curve.

The mean mole ratios within the respective points b and c are obviously very similar, regardless of the changing titrand (Ca) or titrant (Zr) concentrations (Table IV).

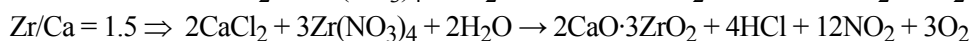
TABLE IV. Mole ratios Zr/Ca obtained by titration of a CaCl_2 solution with a $\text{Zr}(\text{NO}_3)_4$ solution

Ca concentration / $\mu\text{g ml}^{-1}$	Mole ratios Ti/Ca at the inflection points of the titration curves					
	Concentration / $\mu\text{g Zr ml}^{-1}$					
	300			400		
	a	b	c	a	b	c
4	0.1	0.7	1.5	0.2	0.7	1.5
5	0.2 ^A	0.6 ^B	1.4 ^C	0.2 ^D	0.6 ^{E, F}	1.4 ^G
8	0.2	0.7	1.5	0.2	0.7	1.6
10	0.2	0.7	1.5	0.2	0.6	1.6
12	0.2	0.6	1.5	0.2	0.6	1.4
15	0.2	0.6	1.4	0.2	0.7	1.3 ^H
Mean values	0.2 ^I	0.6 ^J	1.5 ^K	0.2 ^L	0.6 ^{M, N}	1.5 ^O

RSD values for five replicates and mean values are: 1.7^A, 2.6^B, 6.9^C, 1.6^D, 1.9^E, 6.2^G, 3.7^I, 5.0^J, 4.7^K, 0^L, 5.0^M and 8.9^O%.
^HThis value was not taken into account.

The 95 % confidence limits for the titration end-point and mean values are: $(0.65 \pm 0.02)^F$ and $(0.6 \pm 0.1)^N$.

On the basis of the mean mole ratios of Zr/Ca, obtained at inflection points b and c, it can be concluded that mixed sesquioxides: $2\text{CaO} \cdot 3\text{ZrO}_2$ and $3\text{CaO} \cdot 2\text{ZrO}_2$ are formed in air-acetylene flame through the following possible reactions (disregarding possible influences of the combustion of the flame gases):



As was mentioned earlier concerning the formation of Ca titanates, the depression of the absorption (or emission) signal of Ca in the presence of Zr can be

explained in the same manner. Namely, in this case, the interference effect of Zr must be attributable to the slower volatilization of the formed thermostable calcium zirconates.¹⁵

A study of releasing action of some common reagents in eliminating interferences from Ti and Zr

In order to investigate the releasing action of La in eliminating interferences from Ti, a lanthanum chloride solution (in the presence of $4 \mu\text{g Ca ml}^{-1}$ as indicator) was titrated with a TiCl_4 solution containing $400 \mu\text{g Ti ml}^{-1}$, whereby the Ca absorption at 422.7 nm was followed. The obtained titration curves are characterized by an inflection point a (Fig. 5). The absorption of Ca evidently increased at first and then, during the reaction of La with Ti, it remained nearly constant (until the inflection point a was attained). Thereafter, with further addition of titanium, the absorption of Ca commences to decrease, due to the reaction of Ca as indicator.

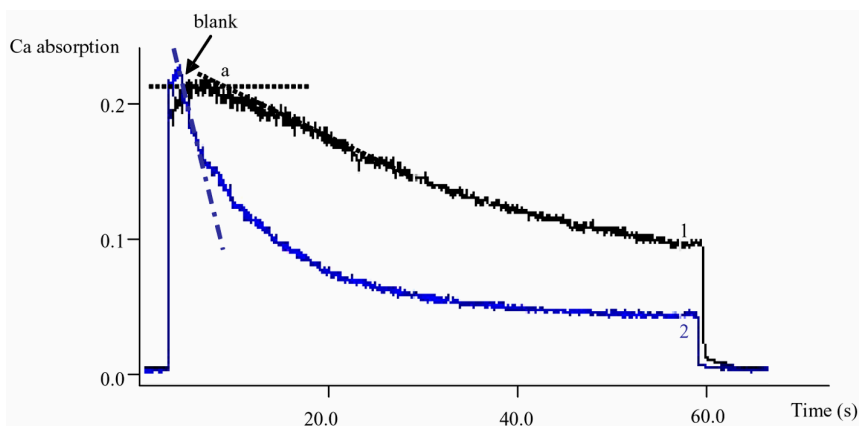


Fig. 5. Titration of $20 \mu\text{g La ml}^{-1}$ in presence of $4 \mu\text{g Ca ml}^{-1}$ (1) and $4 \mu\text{g Ca ml}^{-1}$ as a blank (2) with TiCl_4 standard solution ($400 \mu\text{g Ti ml}^{-1}$).

The mole ratios Ti/La can be determined at point a by subtracting the blank volume, which refers to the titration of $4 \mu\text{g Ca ml}^{-1}$ without La, with the same concentration of Ti, as inhibitor (Fig. 5, curve 2). The mole ratios between Ti and La at point a remained nearly constant, which suggests that a thermostable compound is formed between lanthanum and titanium – $\text{La}_2\text{O}_3 \cdot \text{TiO}_2$ (Table V).

The effectiveness of Ba, Sr and La as releasing agents was investigated during titration with Zr solution as inhibitor. For this purpose, standard solutions of Ba, Sr or La with $2 \mu\text{g Ca ml}^{-1}$ (as indicator) were titrated with $500 \mu\text{g Zr ml}^{-1}$. The changes in the Ca absorption were continuously registered and at the characteristic inflection points, mole ratios of Zr and the releasing agent were determined (Table VI).

It is evident from the mean mole ratios shown in Table VI that Zr reacts with barium approximately in a 1:3, with strontium in a 1:1, and with lanthanum in a

1:2 ratio. Based on these quantitative data, the releasing agents may be sequenced as: Sr > La > Ba regarding their effectiveness in eliminating the interference of Zr during the determination of Ca. This is because 97.3 g Sr, 277.8 g La and as much as 457.8 g Ba, are required to eliminate the interference from about 91.2 g Zr in the form of $Zr(NO_3)_4$.

TABLE V. Mole ratios Ti/La obtained by titration of lanthanum chloride in the presence of $4 \mu\text{g Ca ml}^{-1}$ (as indicator) with a $TiCl_4$ solution ($400 \mu\text{g Ti ml}^{-1}$)

La concentration / $\mu\text{g ml}^{-1}$	Mole ratios Ti/La
5	0.5
10	0.6
15	0.5
20	0.5 ^a
25	0.6

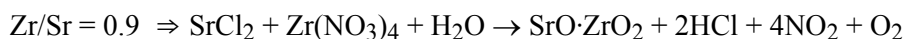
^aRSD value for five replicates is 3.4 %.

TABLE VI. Mole ratios Zr/Ba, Zr/Sr and Zr/La obtained by the titration of the corresponding releasing agents in presence of $2 \mu\text{g Ca ml}^{-1}$ (as indicator) with a $Zr(NO_3)_4$ solution ($500 \mu\text{g Zr ml}^{-1}$)

Ba, Sr, La Concentration / $\mu\text{g ml}^{-1}$	Mole ratios Zr/Ba	Mole ratios Zr/Sr	Mole ratios Zr/La
10	0.3	1.0 ^a	0.6
20	0.3	0.9	0.5
25	0.4	0.9	0.5
30	0.3 ^b	0.8	0.5 ^c
Mean values	0.3 ^d	0.9 ^e	0.5 ^f

RSD values for five replicates and mean values are: 3.2^a, 0.8^b and 1.4^c, 4.3^d, 7.1^e and 4.3^f %.

According to the calculated mean mole ratio values presented in Table VI, the reactions between the releasing elements (Ba, Sr or La) and Zr most probably occurring during evaporation of the aerosol in an air–acetylene flame, disregarding the effects of combustion of the flame gases, can be expressed as follows:



CONCLUSIONS

Titration methods based on an inhibition effect were used for the study of the interferences from Ti and Zr during Ca determination by flame spectrometry in air–acetylene flame. Titration curves of a characteristic shape with distinct inflection points were obtained. The mole ratios Ti/Ca or Zr/Ca at these points were used to explain the processes occurring during evaporation of the aerosol in the flame. It may be concluded that variable thermostable mixed oxides $xCaO \cdot yTiO_2$ are formed during the determination of Ca in the presence of Ti. The values of the x and y coefficients vary, depending on the concentration of the element

being titrated (titrand) or the concentration of the element in the titrant solution. Unlike Ti, during Ca determination in the presence of Zr, it seems that thermostable mixed oxides with a constant composition are formed, such as $3\text{CaO}\cdot 2\text{ZrO}_2$, $2\text{CaO}\cdot 3\text{ZrO}_2$ and $\text{CaO}\cdot \text{ZrO}_2$. The formation of these oxides probably occurs due to a much higher melting point of zirconates.

Elimination of the interference of Ti during the determination of Ca with La as the releasing agent was examined using the continuous atomic absorption inhibition release titration method. Releasing action of La occurs through reactions based on a change of the equilibrium in the evaporating aerosol, which results in the formation of thermostable mixed oxide $\text{La}_2\text{O}_3\cdot \text{TiO}_2$. The different releasing actions of Ba, Sr and La were investigated during calcium titration with $\text{Zr}(\text{NO}_3)_4$. It can be concluded that Zr reacts with Ba at an approximately 1:3, with Sr at 1:1 and with La at 1:2 mole ratio. These quantitative data suggest the following sequence series: $\text{Sr} > \text{La} > \text{Ba}$, considering the releasing action in the elimination of the interference of Zr. This parameter is important both in scientific and economic terms.

Acknowledgement: The authors are grateful to the Ministry of Science of the Republic of Serbia for financial support.

ИЗВОД

СМЕТЊЕ ОД ТИТАНА И ЦИРКОНИЈУМА ПРИ ОДРЕЂИВАЊУ КАЛЦИЈУМА ПЛАМЕНОМ СПЕКТРОМЕТРИЈОМ

ДИМИТРИЈЕ Ђ. СТОЈАНОВИЋ¹, ЈЕЛЕНА С. МИЛИНОВИЋ¹ и СНЕЖАНА Д. НИКОЛИЋ-МАНДИЋ²

¹Институт за исељивање и заштитну животну средину, Банатска 316, 11080 Београд-Земун и

²Хемијски факултет, Универзитет у Београду, Студентски брз 16, 11000 Београд

У овом раду су за проучавање сметњи од титана и цирконијума, при одређивању калцијума атомском апсорпционом и емисионом пламеном спектрометријом, разрађене методе титрације, које се базирају на ефекту инхибиције. У том циљу одређене запремине раствора инхибитора, Ti или Zr, континуално су титроване раствором калцијума и обрнуто, уз симултано распршивање титранда у ваздух-ацетиленски пламен. Истовремено, праћене су промене у апсорпцији, односно емисији калцијума на дисплеју рачунара. На овај начин су добијене титрационе криве са израженим превојним тачкама, у којима су израчунати молски односи између инхибитора (титана, односно цирконијума) и калцијума. Добијени молски односи су искоришћени за објашњење квантитативних промена до којих долази у току испаравања капи раствора у пламену. Упоредна проучавања поступака за елиминисање сметњи од Ti и Zr су вршена методом атомске апсорпционе "ослобађајуће" инхибиторске титрације. У том циљу, раствори "ослобађајућих" реагенаса (баријума, стронцијума или лантана) су титровани раствором цирконијума уз регистровање промена у апсорпцији Ca, као индикатора. Утврђено је да La уклања сметње од Ti и Zr при одређивању калцијума, реагујући са Ti и Zr у молском односу 1:2, при чему Ca остаје "слободан". На исти начин, доказано је да Ba и Sr реагују са Zr у различитим односима, у току спектрометријског одређивања Ca. На бази израчунатих молских односа између цирконијума и баријума, односно стронцијума или лантана, утврђено је да се одговарајући "ослобађајући" реагенси, према ефикасности у сузбијању сметњи, могу сврстати у низ: $\text{Sr} > \text{La} > \text{Ba}$, што је значајно како са научног, тако и са економског становишта.

(Примљено 8. децембра 2006, ревидирано 12. фебруара 2007)

REFERENCES

1. J. Y. Hwang, L. Sandonato, *Anal. Chim. Acta* **48** (1969) 188
2. W. Price, *Spectrochemical Analysis by Atomic Absorption*, Heyden and Son Ltd., London, 1979, p. 133
3. W. R. Looyenga, C. O. Huber, *Anal. Chem.* **43** (1971) 498
4. D. Stojanović, V. Vajgand, *Spectrochim. Acta* **39B** (1984) 767
5. J. Yofe, R. Avni, M. Stiller, *Anal. Chim. Acta* **28** (1963) 331
6. D. Stojanović, J. Winefordner, *Anal. Chim. Acta* **124** (1981) 295
7. D. Stojanović, V. Vajgand, S. Nikolić, *J. Serb. Chem. Soc.* **56** (1991) 39
8. D. Stojanović, V. Vajgand, S. Nikolić, *Spectrochim. Acta* **42B** (1987) 915
9. D. Stojanović, V. Vajgand, *J. Serb. Chem. Soc.* **62** (1997) 649
10. D. Đ. Stojanović, J. S. Milinović, S. D. Nikolić-Mandić, *44th Meeting of the Serbian Chemical Society*, Book of Abstracts, 2006, p. 23
11. J. Mendham, R. Denney, J. Barnes, M. Thomas, *Vogel's Textbook of Quantitative Chemical Analysis*, 6th Ed., Prentice Hall, New York, 2000, p. 473
12. B. Smets, *Analyst* **105** (1980) 482
13. G. Pfaff, *Chem. Mater.* **6** (1994) 58
14. R. M. Vezikova, V. M. Gropyyanov, *Refract. Ind. Ceram.* **34** (1993) 87
15. C. Cano, M. Osendi, M. Belmonte, P. Miranzo, *Surf. Coat. Technol.* **201** (2006) 3307.



Mean heat transfer coefficients during the evaporation of 1,1,1,2-tetrafluoroethane (R-134a) in a plate heat exchanger

EMILA DJORDJEVIĆ^{1*#}, STEPHAN KABELAC² and SLOBODAN ŠERBANOVIĆ^{1#}

¹Faculty of Technology and Metallurgy, University of Belgrade, Karnegijeva 4, 11120 Belgrade, Serbia and ²Helmut Schmidt University of Federal Armed Forces, Holstenhofweg 85, D-22043 Hamburg, Germany

(Received 8 February 2007)

Abstract: In this study the transfer coefficient of evaporation heat of the refrigerant 1,1,1,2-tetrafluoroethane (R-134a) in a vertical plate heat exchanger was experimentally investigated. The results are presented as the dependancy of the mean heat transfer coefficient for the whole heat exchanger on the mean vapor quality. The influences of mass flux, heat flux and flow configuration on the heat transfer coefficient were also taken into account and a comparison with previously published experimental data and literature correlations was made.

Keywords: plate heat exchanger, evaporation, 1,1,1,2-tetrafluoroethane, heat transfer coefficient.

INTRODUCTION

In the last decades, one of the applications of the plate heat exchangers has been as evaporators or condensers in many refrigeration, air conditioning and heat pump systems when the fluid acting as a heat source or heat sink was a liquid. This is due to their high thermal performance and compactness. For these purposes various chlorofluorocarbon (CFC) and hydrochlorofluorocarbon (HCFC) refrigerants were used as working fluids. However, due to the serious depletion of the ozone layer in the atmosphere and global warming problems, the use of CFC refrigerants was forbidden and the same destiny is soon awaiting the most extensively used HCFC refrigerant R-22.

As replacements, various new refrigerants, such as R-134a, R-143a, R-125, R-410a, R-410b, R-507 have been developed during the past years, which necessitates knowledge of their thermodynamic, thermophysical and heat transfer properties.

Moreover, better comprehension of the heat transfer characteristics during evaporation and condensation of the new refrigerants is also essential for the design of evaporators and condensers.

* Corresponding author. E-mail: emila@tmf.bg.ac.yu

Serbian Chemical Society member.

doi: 10.2298/JSC0709833D

The available literature data on two-phase heat transfer, especially for the new refrigerants in plate heat exchangers, are relatively scarce. In the past few years some experimental data have been published the evaporation and condensation of R-134a and R-410a in a vertical plate heat exchanger.^{1–6} Evaporation of ammonia⁷ and R-22⁸ has also been the subject of experimental investigation. Previously, heat transfer during the boiling process had been investigated on different plate geometries, with several refrigerants (R-12, R-22, R-113 and R-717) being used as working fluids.⁹

Several studies have been published on the heat transfer during evaporation and condensation of the refrigerant R-22 in micro-fin tubes of various outer diameter.^{10–12} Also, heat transfer during evaporation and condensation inside horizontal smooth tubes has been examined for a series of refrigerants, including R-12 and R-134a,¹³ and R-22, R-410a and R-407c.^{14,15}

A short literature review of previous investigations on boiling or evaporation of different refrigerants in plate heat exchangers is given in Table I.

TABLE I. Previous investigations of evaporation or boiling in a plate heat exchangers

Ref.	Substance	Plate type	Mass flux kg m ⁻² s ⁻¹	Heat flux or heat rate
1	R-134a	Herringbone type PHE	55, 70	11 and 15 kW m ⁻²
3	R134-a	Herringbone type PHE	50–200	0–35
4	R-410a	Herringbone type PHE	50–100	10 and 20 kW m ⁻²
6	R-410a	Herringbone type PHE	50–125	5–35 kW m ⁻²
16	NH ₃	Herringbone type PHE	9–25	10–30 kW m ⁻²
9	R-22, R-12, R-113, R-717	Herringbone type PHE	–	1–20 kW m ⁻² 0.3–23 kW m ⁻² 1.5–17 kW m ⁻²
23	R-22, R-134a, R-134a/R-32, R-134a/R-125/R-134a	Semi-welded PHE, Nickel-brazed PHE	50–200	12–20 kW
7	NH ₃	Herringbone type PHE	0.5–9.5	12–185 kW
8	R-22	Herringbone type PHE with enhanced surfaces	25.5–36.3	14.7–21.9 kW m ⁻²

The experimental system used in the present investigation includes two vertical plate heat exchangers – an evaporator and a condenser. The experiments were conducted under various test conditions – temperature, pressure and volume flow rate, employing the refrigerant R-134a. The collected data enabled the calculation of both the mean and local values of the heat transfer coefficients, as well as the pressure drops in the plate heat exchangers. In the study presented here, focus was directed on an experimental investigation of heat transfer and pressure drop of the refrigerant R-134a in the evaporator.

EXPERIMENTAL

The experimental system (Fig. 1) was used to investigate the evaporation and condensation of the refrigerant R-134a in a vertical plate heat exchanger (PHE). It includes two main loops – a refrigerant loop and a water–glycol loop, as well as a data acquisition unit.

During the experiments, the temperatures, pressures and flow rates were measured in both loops.

Refrigerant loop

The refrigerant loop contains an evaporator (1), a separation vessel (2), an expansion valve (3), an inner heat exchanger (4), a compressor (5), two oil separators (6), a condenser (7), a refrigerant collector with level indicator (8), two sight glasses and two volume flowmeters, one at the evaporator inlet and the other just before the expansion valve.

A vertical plate and frame heat exchanger is used as the evaporator (1). A liquid refrigerant enters the evaporator at a temperature just a few degrees below the saturation point. In order to obtain various test conditions of R-134a, especially the vapor quality at the exit, pressure, flow rate and imposed heat flux, various water–glycol flow rates were used and the compressor power was changed. It is also possible to investigate the influence of flow direction on heat transfer and pressure drop by changing the direction of the water–glycol flow from concurrent to countercurrent with a four-way valve (9). The flow direction of the refrigerant is always bottom up.

After partial evaporation in the plate heat exchanger, the two-phase refrigerant flow enters the separator (2). The liquid part is collected at the bottom of the vessel, together with the liquid fraction behind the expansion valve and directed back to the evaporator. The volume flow rate in this inner cycle is measured at the evaporator inlet by a calibrated Krohne Ultrasonic Flowmeter (type UFM 3030) with an accuracy of $\pm 1\%$. Vapor from the top of the vessel is superheated in the double-pipe inner heat exchanger (4) by heat transfer from the “hot” liquid refrigerant flowing on the other side.

After the heat exchanger, the superheated R-134a vapor passes through a compressor (5) and oil separators (6) before entering the condenser (7). In this set-up, a Bock F16/2051 compressor is used, which offers the choice of working with two, four or with all six cylinders, thus achieving different pressures and flow rates of the refrigerant. A detailed investigation was performed¹⁶ in order to check the efficiency of the used oil separators. Typically the oil content behind the separators was less than 0.2 mass %.

Another vertical plate heat exchanger functions as a countercurrent flow condenser (7). The superheated refrigerant vapor, which enters the condenser at the top, is completely condensed by the time it reaches the bottom and exits as a sub-cooled liquid. The water–glycol mixture passes through the condenser in the opposite direction, from bottom to top.

From the condenser, the liquid R-134a first flowed to the collector vessel (8), where the liquid level was constant during stationary operation, visually monitored on a sight glass and measured by the level indicator, and then to the inner heat exchanger (4) and the expansion valve (3). After reduction of the pressure, so that partial evaporation occurs in the expansion valve, the two-phase refrigerant flow enters the separation vessel (2), where the cycle is completed.

Before the expansion valve, the volume flow rate of R-134a was measured again by a turbine flow meter, thus enabling the overall energy balance for the refrigerant loop to be checked and the vapor qualities after expansion and evaporation calculated. Additionally, energy balances were calculated for the evaporator and the condenser, as separate units, using both the refrigerant and the water–glycol side. The results showed good agreement between the energy input and output (less than 2 % difference) for all cases reported here.

For temperature measurement, Pt100 thermometers are situated in the middle of the flow, at the evaporator inlet and outlet, the condenser inlet and outlet, the compressor inlet and outlet and in front of the expansion valve. The pressure in the system is measured by two types of pressure transducers – with measuring ranges 0–10 bar and 0–16 bar and a measuring accuracy of $\pm 0.5\%$.

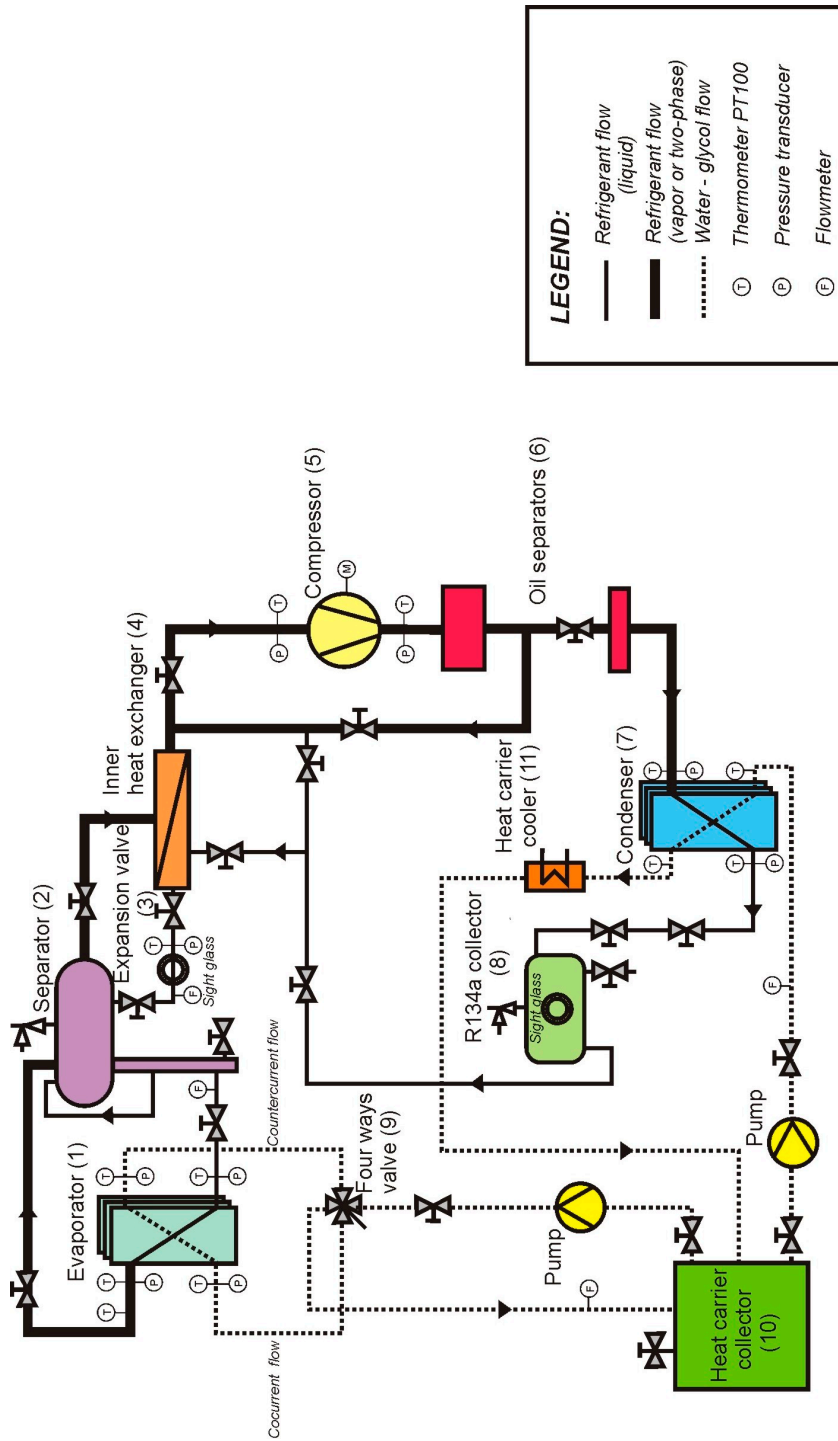


Fig. 1. Experimental setup.

Water-glycol loop

The water-glycol loop consists of two sub-cycles, one connected with the evaporator and the other with the condenser. A mixture with 30.6 mass % of glycol is transported from the heat carrier collector (10) to the plate heat exchangers by flow regulated pumps. After passing through the evaporator in either concurrent or countercurrent flow, the cooled water-glycol mixture returns to the tank. In the condenser, sub-cycled hot water-glycol flow is partially cooled with external cooling water in a brazed plate heat exchanger (11) (type Gea Ecobraze AB) and then returned to the tank. This external cooling compensates the energy input from the compressor so as to keep the overall setup in a stationary state.

For temperature measurement of the heating/cooling fluid, at the inlets and outlets of both heat exchangers, Pt100 thermometers are used, while the pressure is measured by pressure transducers having a measurement range of 0–4 bar and an accuracy of $\pm 0.5\%$. The flow rate in the evaporator sub-cycle is measured by a turbine flowmeter with an accuracy of $\pm 1.5\%$ and in the condenser sub-cycle by a Trimec Multipulse Positive Displacement MP025 flowmeter, with an accuracy of $\pm 0.5\%$. The resistance thermometers, the pressure transducers and the flow meters were repeatedly calibrated.

Data acquisition

The data acquisition system includes a recorder (Kethley 2750 Multimeter), a power supply and a personal computer. The temperature and voltage data are recorded and the collected data signals are then transmitted through a GPIB interface to a computer for further analysis. The experiment is monitored and controlled, and a preliminary balance check is performed by a routine written in LabVIEW[®] program.

It usually takes approximately 20 minutes for the system to reach stationary state. During this initial period and during the experiments, the acquisition unit scans all data channels every 10 or 20 s. For further calculations of the heat transfer coefficients and pressure drop, the mean, time averaged value of the data for each channel is used.

Plate heat exchangers

The plate heat exchangers used in this study are formed by 4 double-plate cassettes (type NT150S) produced by GEA Ecoflex in a frame. The plate characteristics are given in Table II and a schematic representation in Fig. 2.

TABLE II. Plate dimension

Length L_p / mm	872
Width B_p / mm	486
Amplitude a / mm	1.6
Wave length λ / mm	12
Plate thickness δ_p / mm	0.6
Thermal conductivity λ_p / $\text{W m}^{-1} \text{K}^{-1}$	15
Corrugation angle / °	63.26

Refrigerant flow passes inside the cassettes while the water-glycol mixture flows through the channels formed between the cassettes. As sealing against leakage into the environment, EPDM (Ethylene Propylene Diene Monomer) strips are used, while the inlet and outlet ports are sealed with Neopren (Polychloroprene) strips. Thermocouples (type K, 0.5 mm diameter) are welded along the plate surface, in a vertical line on the two middle cassettes, for local temperature measurement. On one of the plates, the thermocouples are used for measuring the wall temperature and on the other for measuring the fluid temperature, thus enabling direct calculation of local heat transfer coefficients on the water-glycol side. The three thermocouples placed near the central horizontal line of

the plates (position 3 in Fig. 2) measure the temperature in the middle of the plate, but also near the edges, which gives a better insight into the flow distribution.

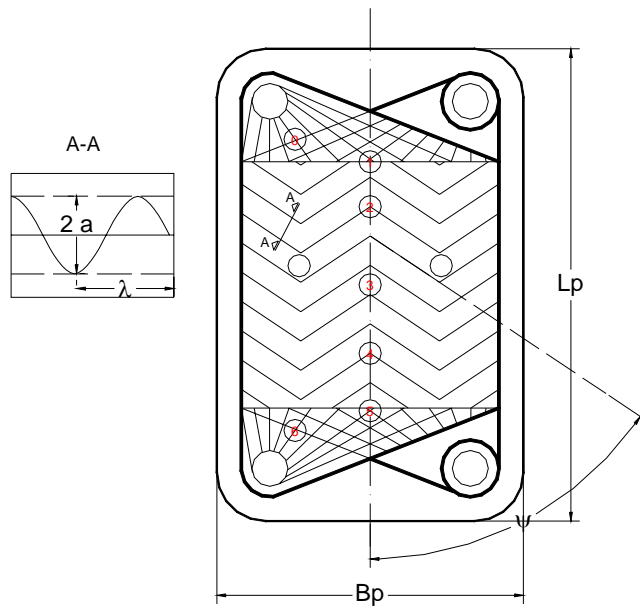


Fig. 2. Geometry of the plates.

Only two thermocouples were installed on each of the two outer cassettes: for measuring the inlet and outlet temperatures, thus enabling a check as to whether the flow distribution between the cassettes is even or not.

Beside measurements by the thermocouples, the temperature of both fluids is measured at the inlet and outlet by Pt100 resistance thermometers, in order to calculate mean heat transfer coefficients. Pressure transducers are also connected to the inlet and outlet of the plate heat exchangers.

Data reduction

Estimation of the mean heat transfer coefficients for the evaporator requires knowledge of the single phase water–glycol heat transfer coefficients. In the course of the analysis, literature correlations, correlation established on the basis of local measurements and a correlation suggested by the plate producer, were used for the calculation of this coefficient and the calculated values were compared.

The overall heat transfer coefficient can be expressed by the equation:

$$U = \frac{Q_h}{A\Delta T_{\text{lmtd}}} \quad (1)$$

As the con- or countercurrent flow in the plates was perfect, there was no need for a correction factor in Eq. (1).

The logarithmic mean temperature difference was calculated from the inlet and outlet temperatures of both fluids, measured by Pt100 thermometers:

$$\Delta T_{\text{lmtd}} = \frac{\Delta T_1 - \Delta T_2}{\ln \frac{\Delta T_1}{\Delta T_2}} \quad (2)$$

For the countercurrent flow, the temperature differences are:

$$\Delta T_1 = T_{h,i} - T_{r,o} \quad (3)$$

$$\Delta T_2 = T_{h,o} - T_{r,i}$$

and for the concurrent flow, these differences can be defined as:

$$\Delta T_1 = T_{h,i} - T_{r,i} \quad (4)$$

$$\Delta T_2 = T_{h,o} - T_{r,o}$$

where the index h is used for the heating fluid, water/ethylene-glycol mixture and the index r for the refrigerant.

The heat transferred can be calculated from the equation:

$$Q_h = m_h c_{p,h} (T_{h,i} - T_{h,o}) \quad (5)$$

The available heat transfer area can be expressed as follows:

$$A = 2L_p B_p \Phi N \quad (6)$$

where N is the number of cassettes. For a further explanations see the Nomenclature and Fig. 2.

Finally, the mean heat transfer coefficient for the refrigerant can be determined from the following equation in which the fouling resistances are omitted, since the experiments involved new plates with clean surfaces:

$$\frac{1}{\alpha_r} = \frac{1}{U} - \frac{1}{\alpha_h} - \frac{\delta_p}{\lambda_p} \quad (7)$$

The vapor quality at the outlet can be calculated either from the heat transferred in the evaporator:

$$x_o = \frac{1}{\Delta h_v} \left(\frac{Q_h}{m_r} - c_{p,r} (T_r^{\text{sat}} - T_{r,i}) \right) \quad (8)$$

or from the previously-mentioned overall balance for the refrigerant loop. Agreement between the values calculated by these two approaches was satisfactory, with differences of less than 1 % for all runs. It should be mentioned here that, for the the graphical representation of obtained results given in the Results and Discussion section, instead of the exit value of the vapor quality, the mean vapor quality in the evaporator was used.

Uncertainty analysis was conducted using a formula proposed by Kline and McClinton.¹⁷ These evaluation results are summarized in TABLE III.

TABLE III. Estimated uncertainties

Parameter	Uncertainty
Geometry of the plates	
Length, width	±0.3 % (max)
Area	±4.5 %
Measuring instruments	
Temperature, PT100	±0.1 °C
Temperature, TC	±0.4 °C
Pressure transducers	±1 %
Water flowrate – turbine	±1.5 %
Water flowrate – multipulse positive displacement flowmeter	±0.5 %
R-134 Flowrate – ultrasonic flowmeter	±1 %
R-134 Flowrate – turbine	±2 %

TABLE III. Continued

Parameter	Uncertainty
Evaporation heat transfer	
Heat flux	$\pm(4-7.5 \%)$
Vapor quality	$\pm(5-8.5 \%)$
Evaporation heat transfer coefficient	$\pm(10-15 \%)$
Friction factor	$\pm(15-17 \%)$

RESULTS AND DISCUSSION

In the present study of R-134a evaporation in a vertical plate heat exchanger, a series of experiments were conducted under different test conditions.¹⁸ The evaporation temperature was varied from -8.85 to 11.08 °C (saturation pressure from 0.21 to 0.43 MPa), the values of the refrigerant mass flux were between 40 and 90 $\text{kg m}^{-2} \text{s}^{-1}$ and the imposed heat flux was gradually increased from 9 to 15 kW m^{-2} . The experiments involved both concurrent and countercurrent flow of the fluids through the evaporator. The working conditions of pressure, mass flux, heat flux and flow configuration during the series of experiments discussed in this paper are summarized in Table IV. The thermophysical properties of R-134a necessary for the calculation of the heat transfer coefficient were taken from the REFPROP database.¹⁹ The calculated values of the mean heat transfer coefficient are presented in graphical form in terms of their variation with the mean vapor quality x_m in the plate heat exchanger. The mean vapor quality is defined and calculated as the arithmetic mean value between the inlet and the outlet vapor qualities.

TABLE IV. Working conditions during the experiments

Name	Flow direction	p / MPa	Flux	
			q / kW m^{-2}	m / $\text{kg m}^{-2} \text{s}^{-1}$
TEST 1	Concurrent	0.34–0.43	9–11.3	50–60
TEST 1a	Countercurrent	0.34–0.43	9–11.3	50–60
TEST 2	Concurrent	0.34–0.43	9–11.3	60–70
TEST 3	Concurrent	0.34–0.43	9–11.3	70–80
TEST 4	Concurrent	0.34–0.43	9–11.3	80–90
TEST 4a	Countercurrent	0.34–0.43	9–11.3	80–90
TEST 5	Countercurrent	0.26–0.30	11.6–13.5	40–50
TEST 6	Countercurrent	0.26–0.30	11.6–13.5	50–60
TEST 7	Countercurrent	0.26–0.30	11.6–13.5	60–70
TEST 8	Countercurrent	0.26–0.30	13.7–14.9	50–60
TEST 9	Countercurrent	0.26–0.30	13.7–14.9	60–70
Yan	Countercurrent	0.675	11	55 and 70

Previous measurements¹ involving the evaporation of the refrigerant R-134a were conducted in a plate heat exchanger of a smaller size, different geometry, with less single plates and at room temperature ($25-31$ °C). The results presented

in this study were obtained on a plate heat exchanger with larger number of plates, in order to approach closer the real exploitation conditions, and at lower temperatures. However, a comparison of current data with the earlier values (working conditions under which these values were obtained are also given in Table IV) shows a satisfactory agreement.

In order to calculate the two-phase evaporation heat transfer coefficient, it was necessary to first determine the single-phase values from the local temperature measurements. The results of these measurements are shown in Fig. 3 as a function of Reynolds number. In the final step, the heat transfer coefficients on the single phase, water-glycol mixture, side were correlated using the equation:

$$Nu_h = 0.39515 Re_h^{0.6244} Pr_h^{1/3} \quad (9)$$

while for the calculation of the Nu and Re numbers, the following definitions were used:

$$Nu_h = \frac{\alpha_h D_h}{\lambda_h} \quad (10)$$

$$Re_h = \frac{\rho_h u_h D_h}{\mu_h} \quad (11)$$

The agreement between the values calculated from the above equations and experimental results is good, having a relative percentage deviation of approximately 2 %, as can be seen in Fig. 3.

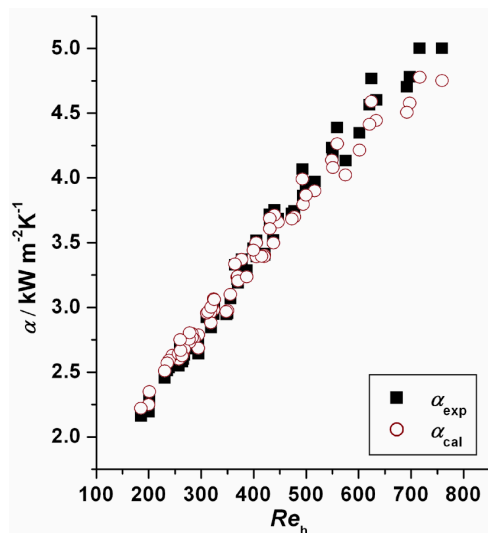


Fig. 3. Single phase water-ethylene-glycol heat transfer coefficient.

The influences of the mass flux of the refrigerant and the imposed heat flux on the heat transfer during evaporation are now closely analyzed. Selected data are shown in Fig. 4, which shows the dependence of heat transfer coefficient on

vapor quality for four different mass fluxes. It can be noticed that the heat transfer coefficient increases with the vapor quality, at least for the presented range of values. This tendency could be explained by the fact that with higher vapor quality, the thickness of liquid film decreases, and since this film represents an additional resistance to heat transfer, the influence on the heat transfer coefficient becomes favorable.

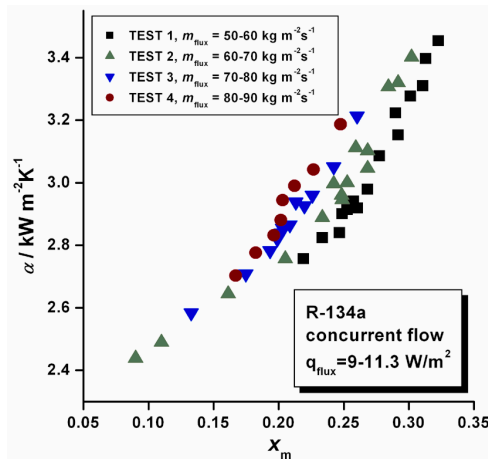


Fig. 4. Influence of mass flux on the heat transfer coefficient, concurrent flow.

The results shown in Fig. 4 for the four investigated mass fluxes during concurrent flow, indicate that the heat transfer coefficient rises with increasing mass flux. This is the consequence of the fact that a higher mass flux also means a higher velocity of the two-phase flow and better heat transfer. A similar tendency can also be noticed in the case of countercurrent flow (Fig. 5), which suggests that the convective boiling regime is dominant.

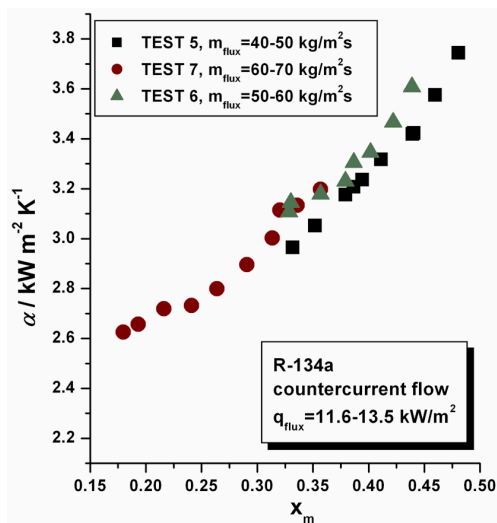


Fig. 5. Influence of mass flux on the heat transfer coefficient, countercurrent flow.

The effects of heat flux on the heat transfer coefficient are shown in Fig. 6. Two heat fluxes are compared under the same conditions of mass flux, system pressure and flow direction. The increase in heat flux induces a rise in heat transfer coefficient, although the effect seems to be less significant than that of mass flux. Such a behavior would indicate a dominance of the nucleate boiling regime.

The final conclusion could be that since the presented values of heat transfer coefficient are the mean values for the whole heat exchanger, both mechanisms occur along the plate and each of them is dominant in one section of the plate.

When the influence of flow direction on heat transfer is considered, under the same conditions of mass flux, heat flux and system pressure, the experiments showed that the heat transfer coefficients for concurrent flow are higher than in the case of countercurrent flow. This tendency, shown in Fig. 7, could be explained by the fact that in concurrent flow, temperature difference in the first part of the plate is higher than in the case of countercurrent flow. As a result, nucleate boiling, which is characterized by high heat transfer coefficients, occurs faster and better heat transfer is to be expected.

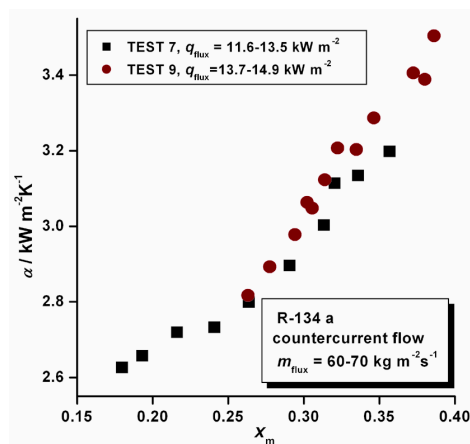


Fig. 6. Influence of heat flux on the heat transfer coefficient.

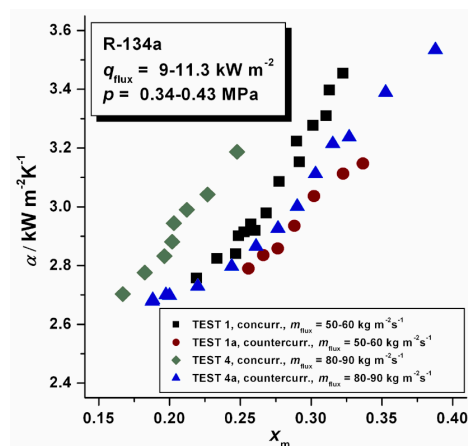


Fig. 7. Influence of flow direction on the heat transfer coefficient.

The results of a series of measurements under various experimental conditions are compared with the literature values¹ and presented in Fig. 8. These previously measured data correspond to experiments conducted with the same refrigerant, but under different test conditions and on a plate heat exchanger of different geometry (120 mm × 45 mm, with three single plates, forming two flow channels, one for each fluid).

Another comparison of the experimental data presented in this study with values calculated from literature correlations is given in Fig. 9.

The results marked with VDI and Martin were calculated from Eq. (7), with the value of the single-phase heat transfer coefficient calculated by different cor-

relations available in the literature.^{20,21} The results labeled as Danilova and Steiner were directly calculated from the equation for the heat transfer coefficient during evaporation suggested by these authors.^{9,22}

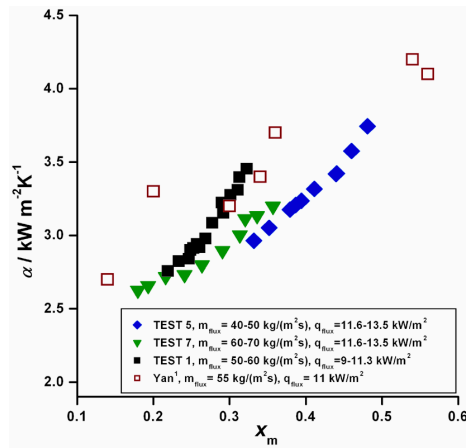


Fig. 8. Comparison with previous experimental data.³

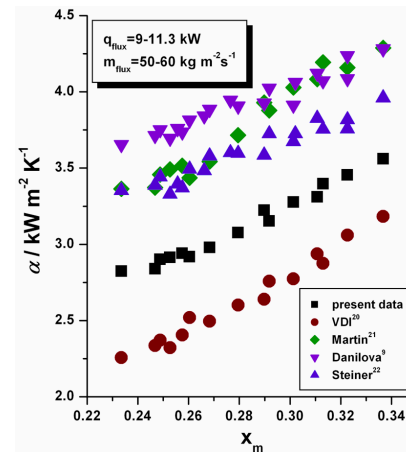


Fig. 9. Comparison of the current experimental data with correlations from the literature.

CONCLUSIONS

The results presented in this study show that all the analyzed factors, *i.e.*, mass flux, heat flux and flow configuration, influence, to some extent, the heat transfer coefficient during the process of evaporation. Since both mass flux and heat flux cause an increase in the heat transfer coefficient, it could be concluded that the boiling regime changes from nucleate boiling to convective boiling along the plate. The mean value of heat transfer coefficient given in this study would thus include the influence of both evaporation mechanisms. In order to determine in which section of the plate the dominate boiling regime changes from nucleate to convective; measurements of the local temperatures along the plate were undertaken. The collected data will enable the calculation of quasi-local heat transfer coefficients and give a better insight into the boiling process, which will be the subject of a future study.

Acknowledgement: The experimental measurements presented in this study were conducted in the Laboratory of the Institute of Thermodynamics at the Helmut Schmidt University of the Federal Armed Forces in Hamburg, Germany.

NOTATIONS

- A – Heat transfer area, m^2
- a – Amplitude of plate corrugation, m
- B – Width, m
- c_p – Specific heat, $J\ kg^{-1}\ K^{-1}$
- D_h – Hydraulic diameter, m

L – Length, m
 m – Mass flow rate, kg s^{-1}
 m_{flux} – Mass flux, $\text{kg m}^{-2}\text{s}^{-1}$
 N – Number of cassettes
 Nu – Nusselt number
 p^{sat} – Saturation pressure, Pa
 Pr – Prandtl number
 Q – Total heat transfer rate, W
 q – Heat flux in one segment from the water mixture side, W m^{-2}
 Re – Reynolds number
 T – Temperature, $^{\circ}\text{C}$
 T^{sat} – Saturation temperature, $^{\circ}\text{C}$
 U – Overall heat transfer coefficient, $\text{W m}^{-2} \text{K}^{-1}$
 u – Velocity, m s^{-1}
 x_{m} – Mean vapor quality
 u_{m} – Mean flow velocity, m s^{-1}

Greek letters

α – Heat transfer coefficient, $\text{W m}^{-2} \text{K}^{-1}$
 δ_{p} – Thickness of the plate, m
 Δh_{v} – Enthalpy of vaporization, J kg^{-1}
 ΔT_{lmtd} – Logarithmic mean temperature difference, $^{\circ}\text{C}$
 Φ – Area enhancement factor due to corrugation
 λ – Wave length of plate corrugation, m
 λ_{h} – Thermal conductivity of hot fluid mixture, W/mK
 λ_{p} – Thermal conductivity of plate material, $\text{W m}^{-1} \text{K}^{-1}$
 μ – Viscosity, Pa s
 ρ – Density, kg m^{-3}
 ψ – Angle of plate corrugation, deg

Subscripts

ch – Channel
 i – Inlet
 h – Hot water–glycol mixture
 o – Outlet
 p – Plate
 r – Refrigerant

ИЗВОД

СРЕДЊИ КОЕФИЦИЈЕНТ ПРЕЛАЗА ТОПЛОТЕ ПРИ ИСПАРАВАЊУ 1,1,1,2-ТЕТРАФЛУОРЕТАНА (R-134a) У ПЛОЧАСТОМ РАЗМЕЊИВАЧУ ТОПЛОТЕ

ЕМИЛА ЂОРЂЕВИЋ¹, СТЕРНАН КАВЕЛАС² и СЛОБОДАН ШЕРБАНОВИЋ¹

¹Технолошко–механички факултет, Универзитет у Београду, Карнегијева 4, 11120 Београд и ²Helmut Schmidt University of Federal Armed Forces, Holstenhofweg 85, D–22043 Hamburg, Germany

У овом раду је експериментално истраживан коефицијент прелаза топлоте при двофазном току расхладног флуида 1,1,1,2-тетрафлуоростана (R-134a) у вертикалном плочастом размењивачу топлоте. Резултати су представљени као зависност средњег коефицијента прелаза топлоте за цео апарат од средњег степена сувоће x_{m} . Утицаји масеног флукса, топлотног

флукса и конфигурације тока флуида на коефицијент прелаза топлоте су такође узети у обзир а направљено је и поређење са предходно објављеним експерименталним подацима и корелацијама из литературе.

(Примљено 8. фебруара 2007)

REFERENCES

1. Y. Y. Yan, T. F. Lin, *ASME J. Heat Transfer*. **121** (1999) 118
2. Y. Y. Yan, H. C. Lio, T. F. Lin, *Intern. J. Heat Mass Transfer* **42** (1999) 993
3. Y. Y. Hsieh, L. J. Chiang, T. F. Lin, *Intern. J. Heat Mass Transfer* **45** (2002) 1791
4. Y. Y. Hsieh, T. F. Lin, *ASME J. Heat Transfer* **125** (2003) 852
5. W. S. Kuo, Y. M. Lie, Y. Y. Hsieh, T. F. Lin, *Intern. J. Heat Mass Transfer* **48** (2005) 5205
6. Y. Y. Hsieh, T. F. Lin, *Intern. J. Heat Mass Transfer* **45** (2002) 1033
7. D. Sterner, B. Sundén, *Heat Transfer Engin.* **27** (2006) 45
8. G. A. Longo, A. Gasparella, R. Sartori, *Intern. J. Heat Mass Transfer* **47** (2004) 4125
9. D. N. Danilova et al., *Kholodilnaya Tekhnika* **4** (1981) 25
10. L. M. Schlager, M. B. Pate, A. E. Bergles, *Intern. J. Refrigeration* **12** (1989) 6
11. L. M. Schlager, M. B. Pate, A. E. Bergles, *ASME J. Heat Transfer* **112** (1990) 1041
12. W. Xiaomin, W. Xiaoling, W. Weicheng, *J. Enhanced Heat Transfer* **11** (2004) 275
13. S. J. Eckels, M. B. Pate, *Intern. J. Refrigeration* **14** (1991) 70
14. T. Ebisu, K. Torikoshi, *ASHRAE Transcript*. **121** (1998) 556
15. K. Torikoshi, T. Ebisu, *ASHRAE Transcriptions* **99** (1993) 90
16. M. Andre, *Heat Transfer by the evaporation of NH₃ in a plate heat exchanger*, PhD Thesis (in German), Hannover University, Germany, 2004
17. S. J. Kline, F. A. McClintock, *Mechan. Engin.* **75** (1953) 3
18. E. Djordjević, S. Kabelac, S. Šerbanović, *5th International Conference of the Chemical Societies of the South-East European Countries*, Ohrid, Macedonia, *Proceedings*, 2006, p. 218
19. M. O. McLinden, S. A. Klein, E. W. Lemmon, A. P. Peskin, *NIST thermodynamic and transport properties of refrigerant mixtures – REFPROP*, Version 6.0, NIST, Boulder, 1998
20. H. Martin in *VDI – Wärmeatlas*, Springer Verlag, Heidelberg, 2002, p. Mm1
21. H. Martin, *Chem. Eng. Proc.* **35** (1996) 301
22. D. Steiner in *VDI – Wärmeatlas*, Springer Verlag, Heidelberg, 2002, p. Hbb1
23. S. Wellsandt, *Heat transfer and pressure drop in a plate type evaporator*, PhD Thesis, Chalmers University of Technology, Gothenburg, Sweden, 2001.



Ozone absorption in a mechanically stirred reactor

LJILJANA TAKIĆ¹, VLADA VELJKOVIĆ^{1#}, MIODRAG LAZIĆ^{1#} and SRĐAN PEJANOVIĆ^{2*#}

¹University of Niš, Faculty of Technology, Leskovac and ²University of Belgrade, Faculty of Technology and Metallurgy, Karnegijeva 4, Belgrade, Serbia

(Received 19 June 2006, revised 27 December 2006)

Abstract: Ozone absorption in water was investigated in a mechanically stirred reactor, using both the semi-batch and continuous mode of operation. A model for the precise determination of the volumetric mass transfer coefficient in open tanks without the necessity of the measurement the ozone concentration in the outlet gas was developed. It was found that slow ozone reactions in the liquid phase, including the decomposition of ozone, can be regarded as one pseudo-first order reaction. Under the examined operating conditions, the liquid phase was completely mixed, while mixing in a gas phase can be described as plug flow. The volumetric mass transfer coefficient was found to vary with the square of the impeller speed.

Keywords: ozone, absorption, stirred reactor, volumetric mass transfer coefficient.

INTRODUCTION

When ozone from a gas mixture is absorbed in water of different quality, the appearance of free ozone in the water means that there are no fast reactions of ozone with substances originally present in the water. Very simple Equations describe the ozone transfer from a gas mixture to water in stirred tanks in which liquid phase is completely mixed. For the continuous mode of operation, the Equation is:

$$G_{\text{IN}} c_{G_{\text{IN}}} - G_{\text{OUT}} c_{G_{\text{OUT}}} = K_L a V (c_L^* - c_L) \quad (1)$$

and for the semi-batch mode:

$$\frac{dc_L}{d\tau} = K_L a (c_L^* - c_L) - r_L \quad (2)$$

where r_L is the overall rate of the slow ozone reactions in the liquid phase. In the case of distilled water r_L represents the ozone self-decomposition rate. The value of r_L may be easily determined by using Eq. (3), which also holds for the continuous mode of operation:

$$G_{\text{IN}} c_{G_{\text{IN}}} - G_{\text{OUT}} c_{G_{\text{OUT}}} = L c_L + r_L V \quad (3)$$

* Author to whom correspondence should be addressed. E-mail: srdjap@tmf.bg.ac.yu

Serbian Chemical Society member.

doi: 10.2298/JSC0709847T

In Eqs. (1) and (3), G and L represent the gas and liquid volumetric flow rates, respectively, and c_G and c_L the ozone concentration in the gas and liquid phase, respectively. However, the experimental determination of the volumetric mass transfer coefficient from Eqs. (1) or (2) requires the ozone concentration in the liquid phase, which is in equilibrium with ozone partial pressure in the gas phase, to be known. This concentration, c_L^* , is the product of the solubility ratio s , and average ozone concentration in the gas bubbles present in the gas–liquid dispersion in the reactor, \bar{c}_G , according to the Henry law:

$$c_L^* = s \bar{c}_G \quad (4)$$

A variety of data for the equilibrium concentration of ozone in water as a function of temperature is reported in the literature.^{1–11} The influence of pH and ionic strength of the liquid phase on the equilibrium ozone concentration was also considered.^{11,12}

Literature values of the solubility of ozone in water, converted to a solubility ratio at 20 °C and pH 7, are summarized in Table I.

TABLE I. Literature values of the solubility ratio

Reference	s
1	0.340
2	0.334
3	0.355
4	0.290
5	0.309
6	0.245
7	0.243
8	0.241
9	0.251
10	0.240
11.1	0.257
11.2	0.270
11.3	0.240
11.4	0.200
11.5	0.210
11.6	0.220

The values of solubility ratios from Table I can be summarized into two groups. In the first group, values of around 0.3 and above are predicted,^{1–5} while in the second group, the values are in the range from 0.2 to 0.27.^{6–11}

The value of the solubility ratio suggested by Bin,¹⁰ which approximately represents the mean value of the distribution ratios predicted in the literature,^{6–11} and has been adopted by IOA, was used in this work.

On the other hand, the average ozone concentration in gas bubbles present in a gas–liquid dispersion in reactor, \bar{c}_G , depends on the mixing status in the gas phase. It is evident that the value of the equilibrium ozone concentration calculated on the basis of the ozone concentration in the effluent gas will be lower than that calculated from the ozone concentration in the influent gas. Consequently, these different approaches may result in different obtained values of the volumetric mass transfer coefficients and, furthermore, in different behaviors of the volumetric mass transfer coefficient when some of the operating conditions are changed (impeller speed, power input or superficial gas velocity). In this way, different authors suggested different correlations for predicting the volumetric mass transfer coefficient as a function of power consumption or impeller speed in stirred tank reactors.

Ouederni *et al.*⁶ suggested the value of volumetric mass transfer coefficient to vary with impeller speed to the power 0.67, while Anselmi *et al.*¹³ suggested the exponent 2. Mallevalle *et al.*¹⁴ and Bouaifi *et al.*¹⁵ suggested that the volumetric mass transfer coefficient vary with the specific power input to the power of 0.5, while Qiu *et al.*¹⁶ suggested exponent 0.4 and Yocum¹⁷ 0.46.

Our assumption was that there is not one reason for the behavior of the ozone and oxygen volumetric mass transfer coefficients to differ when the impeller speed is changed.

Pejanović¹⁸ found that the oxygen volumetric mass transfer coefficient varied with the square of the impeller speed in the same stirred tank reactor as used in this study.

This fact was the basis for the determination of the mixing level in the gas phase in this reactor.

The main objective of this work was to establish a model for precise determination of the ozone volumetric mass transfer coefficient in opened mechanically stirred tanks, without the necessity of measuring the ozone concentration in the effluent gas.

EXPERIMENTAL

The experimental set up is schematically shown in Fig. 1. A closed reactor was used for the continuous mode of operation, while semi-batch experiments were performed in an open tank.

The impeller speeds and gas flow rates were chosen in the ranges which provide that mechanical sucking be avoided.

An ozone generator Ozone Lab 100/DS, Yanco Industries Ltd. Burton, Canada, was used. Ozone was absorbed in water in a standard mechanically stirred reactor, equipped with Rushton type 6-bladed impeller. The diameter of the tank was 200 mm and the height 400 mm, while the liquid height in the reactor was around 200 mm, and was measured in each experimental run. In this way, the volume of liquid in the reactor was around 6 dm³, but varied from one experiment to another. The impeller speed ranged from 300 to 600 min⁻¹, while the gas flow rate was 0.567 dm³ min⁻¹ for continuous and 0.25 dm³ min⁻¹ for the semi-batch mode of operation. The ozone concentrations in both the liquid and gas phase were measured by standard iodometric titration.

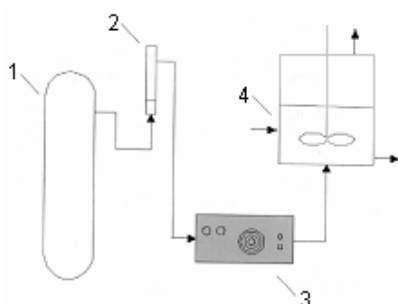


Fig. 1. Experimental set up: oxygen bomb (1), gas flowmeter (2), ozone generator (3) and stirred tank (4).

RESULTS AND DISCUSSION

Continuous mode

The experiments were performed in the same reactor and with the same “clean” water quality as used in the study of Stankovic.¹⁹ We are of the opinion that Stankovic arbitrarily assumed that the ozone decomposition reaction is zero order with respect to ozone and that there were no fast and slow chemical reactions of ozone with substances present in the “clean” water. This approach resulted in too low values of the volumetric mass transfer coefficients obtained.

The experimentally measured values of $c_{G_{IN}}$, $c_{G_{OUT}}$ and c_L , and the two values of $K_L a$, $(K_L a)_{OUT}$, calculated on the basis of the average ozone concentration in the gas bubbles being equal to the ozone concentration in the outlet gas flow, and $(K_L a)_m$, calculated assuming that $\bar{c}_G = (c_{G_{IN}} + 5c_{G_{OUT}})/6$, are summarized in Table II. Only this combination of $c_{G_{IN}}$ and $c_{G_{OUT}}$ assures that $(K_L a)_m$ depends on the square of impeller speed.

TABLE II. Ozone volumetric mass transfer coefficient as a function of impeller speed (gas flow rate: $0.567 \text{ dm}^3 \text{ min}^{-1}$, liquid flow rate: $1.5 \text{ dm}^3 \text{ min}^{-1}$, temperature: $18 \text{ }^\circ\text{C}$, solubility ratio: 0.256). The dependence of $(K_L a)_m$ on impeller speed is shown in Fig. 2.

n min^{-1}	$c_{G_{IN}}$ mg dm^{-3}	$c_{G_{OUT}}$ mg dm^{-3}	c_L mg dm^{-3}	V dm^3	$(K_L a)_{OUT}$ min^{-1}	$(K_L a)_m$ min^{-1}
300	5.480	4.034	0.168	6.23	0.152	0.142
	6.554	4.846	0.226	6.18	0.154	0.144
	7.627	5.648	0.295	6.32	0.154	0.144
400	5.480	3.593	0.271	5.87	0.281	0.250
	6.554	4.314	0.360	5.93	0.288	0.255
	7.627	5.085	0.440	5.81	0.288	0.256
500	4.944	2.888	0.314	5.86	0.468	0.388
	5.480	3.232	0.362	5.76	0.475	0.394
	6.017	3.606	0.411	5.54	0.482	0.401
600	4.944	2.625	0.380	5.92	0.761	0.568
	5.480	2.948	0.436	5.92	0.761	0.568
	6.017	3.277	0.492	5.92	0.756	0.566

The ozone volumetric mass transfer coefficient is neither affected by the ozone concentration in the inlet and outlet gas flow, nor the free ozone concentration in the water. This means that the ozone self-decomposition and slow chemical reactions in the liquid phase do not influence the value of the physical ozone volumetric mass transfer coefficient.

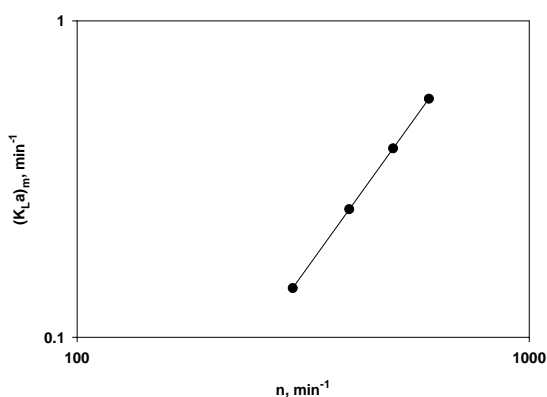


Fig. 2. Dependence of the volumetric mass transfer coefficient on impeller speed.

However, increasing the impeller speed causes a rapid increase of the volumetric mass transfer coefficient. Pejanović¹⁸ determined the oxygen volumetric mass transfer coefficient in the same reactor as used in this work, at 14 °C, and with a gas flow rate of 40 dm³ h⁻¹. These values, converted to the conditions from Table II, are summarized in Table III.

TABLE III. Oxygen volumetric mass transfer coefficient as a function of impeller speed

n / min^{-1}	300	400	500	600
$(K_L a)_{\text{O}_2} / \text{min}^{-1}$	0.175	0.312	0.487	0.706

Pejanović¹⁸ showed that the oxygen volumetric mass transfer coefficient depends on the square of the impeller speed, which also holds for the ozone volumetric mass transfer coefficient $(K_L a)_m$ from Table II. The ratio of these two coefficients is approximately 0.814. This ratio may also be estimated from the expression given in the literature:¹²

$$\frac{(K_L a)_{\text{O}_3}}{(K_L a)_{\text{O}_2}} = \left(\frac{D_{\text{O}_3}}{D_{\text{O}_2}} \right)^n \quad (5)$$

where D_{O_3} and D_{O_2} are the molecular diffusivities of ozone and oxygen in water, respectively, and the exponent n depends on the model of molecular diffusion, being 1 for the two-film model and 0.5 for the surface renewal and penetration model. However, different values of the ozone end oxygen molecular diffusivities are given in the literature. Gottschalk¹² suggests that the ratio between the ozone and oxygen molecular diffusivities in water is 0.622, while Bin²⁰

recommends the value of 0.83. Nevertheless, the value obtained in this work seems to be reasonable.

Therefore, a plug flow for mixing in the gas phase is proposed, which was also reported by Wu *et al.*⁹ The ozone volumetric mass transfer coefficient may now be determined in an open continuous flow stirred reactor, without measuring of ozone concentration in the outlet gas, from Eq. (1) and with $c_L^* = s(c_{G_{IN}} + 5 c_{G_{OUT}})/6$.

Semi-batch mode

Determination of the ozone volumetric mass transfer coefficient from Eq. (2) requires the overall rate of ozone decomposition and slow chemical reactions in the liquid phase to be known. This rate was determined using Eq. (3) and is expressed by the following equation:

$$r_L = -\frac{dc_L}{d\tau} = k_0 + k_1 c_L \quad (6)$$

where k_0 and k_1 are the pseudo rate constants, being $0.05 \text{ mg dm}^3 \text{ min}^{-1}$ and $0.1 \text{ dm}^3 \text{ min}^{-1}$, respectively, for Belgrade drinking water at 20°C .

In a recent paper, Bin²¹ recommended the method of treatment of experimental data assuming that the equilibrium ozone concentration in water is approximately constant during absorption. Since this is not quite true, a different approach is proposed.

It was found that the change in free ozone concentration in drinking water with time, during an absorption run, may be fitted well by the following expression:

$$c_L = a(1 - e^{-b\tau}) \quad (7)$$

Equation (7) indicates that the free ozone concentration in water is an increasing function of the absorption time. Consequently, the driving force for absorption from Eq. (2) decreases with time, causing an increase in the ozone concentration in the outlet gas flow and the ozone equilibrium concentration with absorption time. The form of Eq. (7) suggests that the change of the ozone equilibrium concentration in water with time may be well represented by a linear increase of this concentration with increasing free ozone concentration in water:

$$c_L^* = c_{L_0}^* + A c_L \quad (8)$$

In this way, Eq. (2) becomes:

$$\frac{dc_L}{d\tau} = K_L a (c_{L_0}^* + A c_L - c_L) - k_0 - k_1 c_L \quad (9)$$

and the solution of this equation is:

$$c_L = \frac{K_L a c_{L_0}^* - k_0}{K_L a (1 - A) + k_1} \left[1 - e^{-(K_L a (1 - A) + k_1)\tau} \right] \quad (10)$$

By comparing Eqs. (7) and (10), one may find that:

$$a = \frac{K_L a c_{L_0}^* - k_0}{K_L a (1 - A) + k_1} \quad (11)$$

and:

$$b = K_L a (1 - A) + k_1 \quad (12)$$

The time derivative of Eq. (7) is:

$$\frac{dc_L}{d\tau} = ab e^{-b\tau} \quad (13)$$

This means that this time derivative of the free ozone concentration in water may be found at any given time, if the values of the constants a and b are determined from the best fit of the change of free ozone concentration in water with time. The exact values of $c_{L_0}^*$ and constant A are not necessary to be known.

Calculation of $K_L a$ from Eq. (2) requires that the ozone concentration in the outlet gas flow is also known. It is assumed that this concentration may be calculated from the integral balance, as a mean value over a predefined period of time. Since G_{OUT} differs from G_{IN} by less than 1 %, the integral balance Equation for any 2 minutes duration of absorption is:

$$c_{G_{OUT},n} = \frac{G c_{G_{IN}}^2 - V(c_{L,n+1} - c_{L,n-1}) - \left(k_0 + k_1 \frac{c_{L,n+1} + c_{L,n-1}}{2} \right) V}{G^2} \quad (14)$$

where n is the minutes of absorption time and V is the liquid volume in the reactor. Eq. (14) is valid in time intervals in which the ozone concentration in the liquid phase is close to a linear function of the absorption time, *i.e.*, at the beginning of absorption.

Considering ozone absorption in Belgrade drinking water at 20 °C, the inlet gas flow rate being 0.25 dm³ min⁻¹ and the ozone concentration in the inlet gas 33 mg dm⁻³, the data of the change of the free ozone concentration in water with time given in Table IV are obtained.

TABLE IV. The dependence of free ozone concentration in water ($G_{IN} = 0.25 \text{ dm}^3 \text{ min}^{-1}$, $n = 400 \text{ min}^{-1}$)

τ / min	0	2	4	10	15
$c_L / \text{mg dm}^{-3}$	0	1.30	2.03	3.30	3.62

Fitting of experimental data from Table IV in Origin 5.0 software gives the values of parameters a and b in Eq. (7), as follows: $a = 3.827 \text{ mg dm}^{-3}$ and $b = 0.1962 \text{ min}^{-1}$. In that way:

$$\left(\frac{dc_L}{d\tau} \right)_1 = 0.6171 \frac{\text{mg}}{\text{dm}^3 \text{ min}},$$

$c_{L_1} = 0.682 \text{ mg dm}^{-3}$ and $c_{L_2} = 1.242 \text{ mg dm}^{-3}$, while from Eq. (14), with $V = 6 \text{ dm}^3$ and $n = 1 \text{ min}^{-1}$:

$$c_{G_{\text{OUT},1}} = 15.4056 \frac{\text{mg}}{\text{dm}^3}$$

The ozone volumetric mass transfer coefficient may now be calculated from the following Equation:

$$K_L a = \frac{\left(\frac{dc_L}{d\tau} \right)_1 + k_0 + k_1 c_{L_1}}{s(5c_{G_{\text{OUT},1}} + c_{G_{\text{IN}}})/6 - c_{L_1}} = 0.1977 \text{ min}^{-1}$$

The obtained values of the ozone volumetric mass transfer coefficient agree well with the correlation recommended by Linek *et al.*²² and with the values obtained by Wu and Masten,⁹ but differ from the values given by Bin and Rouston.²³ Since the value obtained in the continuous mode, for a gas flow rate of $0.567 \text{ dm}^3 \text{ min}^{-1}$ at the same impeller speed, corrected to the temperature of $20 \text{ }^\circ\text{C}$ is 0.266 min^{-1} , the correlation given by Pejanović¹⁸ for oxygen transfer in water in stirred vessels seems to hold for ozone transfer as well:

$$K_L a = \text{const}(n^3 d^2)^{2/3} u_G^{1/3} \quad (15)$$

where d is the diameter of turbine impeller and u_G is the superficial gas velocity.

CONCLUSIONS

Investigations of ozone transfer to water in a semi-batch and continuous flow stirred reactor were performed in order to determine the ozone volumetric mass transfer coefficient. The flooding regime and mechanical sucking in the reactor were avoided by the correct choice of impeller speed and gas flow rate. The investigations showed that the value of the ozone volumetric mass transfer coefficient is not affected by the liquid flow rate, since the corresponding values were obtained in both types of operation. However, the ozone volumetric mass transfer coefficient was found to vary with the square of the impeller speed and with the third root of the gas flow rate. The same behavior was previously reported for oxygen transfer to water.

ИЗВОД

АБСОРПЦИЈА ОЗОНА У РЕАКТОРУ СА МЕХАНИЧКИМ МЕШАЊЕМ

ЉИЉАНА ТАКИЋ¹, ВЛАДА ВЕЉКОВИЋ¹, МИОДРАГ ЛАЗИЋ¹, И СРЂАН ПЕЈАНОВИЋ²

¹Универзитет у Нишу, Технолошки факултет у Лесковцу, Лесковац и ²Универзитет у Београду, Технолошко-металуришки факултет, Београд

Испитивана је абсорпција озона у води у шаржном и проточном реактору са механичким мешањем. Развијен је модел за прецизно одређивање коефицијента преноса масе озона у отвореним судовима, без потребе за мерењем концентрације озона у излазном гасу. Пока-

зано је да се споре хемијске реакције озона са полутантима присутним у води, укључујући и спонтану декомпозицију озона, могу третирати као једна укупна хемијска реакција псеудо-првог реда. При оперативним условима коришћеним у овом раду, мешање у течной фази је идеално, док се за мешање у гасној фази може применити модел клипног струјања. Констатовано је да запремински коефицијент преноса масе озона расте пропорционално квадрату броја обртаја мешалице.

(Примљено 19. јуна 2006, ревидирано 27. децембра 2006)

REFERENCES

1. H. Benbelkacem, H. Cano, S. Mathe, H. Debellefontaine, *Ozone Sci. Eng.* **25** (2003) 13
2. M. Kuosa, A. Laari, J. Kallas, *Ozone Sci. Eng.* **26** (2004) 277
3. J. H. Perry, *Chemical Engineers Handbook*, 6th Ed., McGraw-Hill, New York, 1984, p. 3
4. E. Rischbieter, H. Stein, A. Schumpe, *J. Chem. Eng. Data* **45** (2000) 338
5. J. C. Morris, *Ozone News* **1** (1998) 14
6. A. Ouederni, J. C. Mora, R. S. Bes, *Ozone Sci. Eng.* **9** (1987) 1
7. C. A. Jakubowski, B. W. Atkinson, P. Dennis, G. M. Evans, *Ozone Sci. Eng.* **25** (2003) 1
8. J. A. Roth, D. E. Sullivan, *Ind. Eng. Chem. Fundam.* **20** (1981) 137
9. J. Wu, S. Masten, *J. Environ. Eng.* (2001) 1089
10. A. Bin, *Proceedings of the International GLS 7 Conference*, (2005), Strasbourg, France, 2005
11. B. Langlais, D. A. Reckhow, D. R. Brink, Lewis Publishers, 1991
12. C. Gottschalk, J. A. Libra, A. Saupé, *Ozonization of Water and Waste Water*, Wiley-VCH, Germany, 2000
13. G. Anselmi, P. G. Lignola, C. Raitano, G. Volpicelli, *Ozone Sci. Eng.* **6** (1984) 17
14. J. Mallevialle, M. Roustan, H. Roques, Cebedeau, (1975) 175
15. M. Bouaifi, G. Hebrard, D. Bastoul, M. Roustan, *Chem. Eng. Proc.* **40** (2001) 97
16. Y. Qiu, C. H. Kuo, M. E. Zappi, *Environ. Sci. Technol.* **35** (2001) 209
17. F. H. Yocum, *Water* **76** (1979) 135
18. S. Pejanović, Ph.D. Thesis, University of Belgrade, Faculty of Technology and Metallurgy, Serbia and Montenegro, 1992
19. I. Stanković, *Ozone Sci. Eng.* **10** (1988) 321
20. A. Bin, private communications (2006)
21. A. Bin, *Exp. Therm. Fluid Sci.* **28** (2004) 395
22. V. Linek, V. Vacek, J. Sinkul, P. Beneš, Ellis Horwood, Chichester, (1988)
23. A. Bin, M. Roustan, *Proceedings of the International Specialized Symposium IOA 2000, Fundamental and Engineering Concepts for Ozone Reactor Design*, (2000), Toulouse, France, (2000), 89.



Crystalline forms of silver iodide II. Determination of phase transformations

MARIJA R. VUKIĆ^{1*#}, DRAGAN S. VESELINOVIĆ^{2#} and VESNA G. MARKOVIĆ³

¹Institute "Kirilo Savić" a. d., Vojvode Stepe 51, 11000 Belgrade,

²Faculty of Physical Chemistry, Studentski trg 12, P.O.Box 550, 11000 Belgrade and

³ITNMS, Franchet d'Esperey Str. 86, 11000 Belgrade, Serbia

(Received 20 July 2006, revised 21 December 2006)

Abstract: In order to obtain appropriate forms of AgI (β - and γ -), a procedure was developed to synthesize AgI at room temperature (23 °C), whereby samples of varying crystallographic purity and of varying crystallographic contents of the different forms were obtained. This paper presents the results of investigations of the influence of the manner of preparation of β -AgI and γ -AgI samples and the sample heating rate on the phase transformations and their temperatures. During the heating of non-ground, ground and pressed synthesized AgI samples, the phase transformations and the corresponding temperatures for one β -AgI and four γ -AgI samples with different β -AgI contents (representing a crystallographic impurity) were identified. The following phase transformations were observed for the non-ground AgI samples: β -AgI \rightarrow α -AgI at 149.6 °C (for the β -AgI sample) and γ -AgI \rightarrow α -AgI at 148.7 °C or 148.2 °C for the γ -AgI samples with a minimum content of β -AgI (less than 7%), as a crystallographic impurity. The phase transition γ -AgI \rightarrow α -AgI was irreversible because β -AgI was obtained whenever the samples were heated up to 260 °C. Manual sample grinding, as well as pressing at $p_1 = 650$ MPa and $p_2 = 900$ MPa resulted in the β -AgI \rightarrow γ -AgI phase transition in all the investigated cases.

Keywords: silver iodide, heat treatment, mechanical treatment, phase transformation, DSC, X-ray diffractometry

INTRODUCTION

Silver iodide exists in three different crystalline phases.^{1–4} According to literature data,⁴ at ambient conditions, AgI usually exists as a two-phase mixture of the cubic zinc blende-structured γ -phase (F-43m, $a = 6.495$ Å, $Z = 4$)⁵ and the hexagonal wurtzite-structured β -phase (P6₃mc, $a = 4.592$ Å, $c = 7.510$ Å, $Z = 2$).^{6,7} At room temperature, the predominant phase is γ -AgI phase with the zinc-blende face-centered-cubic structure F-43m, although some β -AgI is also usually present with the wurtzite hexagonal structure P6₃mc.⁸ β -AgI becomes the more stable phase above 384 K although the coexistence of the phases may still occur.⁷

* Corresponding author. E-mail: mvukic@infosky.net

Serbian Chemical Society member.

doi: 10.2298/JSC0709857V

Both phases transform to body-centered-cubic α -AgI at 420 K,^{4,8,9} which is stable above this temperature and is the superionic phase.^{10–12}

The literature reveals disagreement among authors about phase transformations of some forms AgI during heating. Parsonage and Staveley¹³ consider that there is only one phase transition at a temperature of 147 °C in the course of heating or cooling, *i.e.*, β -AgI into α -AgI and, *vice versa*, α -AgI into β -AgI, respectively. The authors were of the opinion that a considerable segment of the phase transition is isothermal and that γ -AgI and β -AgI have lattices of very similar thickness and energy and transform into α -AgI at the same temperature (146 – 148 °C). Alpha silver iodide is stable only above 147 °C and transforms very quickly to the beta phase during cooling down to room temperature.^{14,15} According to published data,³ γ -AgI is thermodynamically stable at room temperature and pressure and up to 413 K and 588 MPa; β -AgI is formed above 413 K and pressures of 883 MPa.

It used to be considered that at approximately 410 K (137 °C), β -AgI form transforms into γ -AgI, but this phenomenon was questioned in the literature.¹⁶ Perrott and Fletcher¹⁷ claimed that this phase transformation was absent in samples deviating from stoichiometry by only 1 mol %. Transition temperatures given in the literature¹⁸ are somewhat different and depend on the applied methods and preparation of the samples, which may affect the quality of the nature of the phase transition. Values for phase transformation given in the literature¹⁹ are: β -AgI \rightarrow α -AgI: $t = 147^\circ\text{C}$ and $\Delta H = 26.21 \text{ J g}^{-1}$.

Hanaya *et al.*²⁰ observed a thermal anomaly in the DSC curves at around 150 °C during heating due to the phase transition from β/γ -AgI to α -AgI, as in the case of bulk crystalline AgI ($t = 147^\circ\text{C}$). However, the transition temperature from α -AgI to β/γ -AgI during cooling decreased remarkably with decreasing pore size from 50 to 10 nm.

Previous investigations defined the conditions for obtaining stable samples of γ -AgI with an as low percent as possible of the accompanying β -AgI and of β -AgI containing a low percent of γ -AgI.^{21–23}

The goal of this study was to contribute to the solution of certain dilemmas of the type, number and temperature of the phase transformations occurring during heating and spontaneous cooling, and the effects of grinding/pressing the AgI samples.

EXPERIMENTAL

Synthesis of AgI samples

The synthesis process of both crystallographic forms of AgI, and the employed apparatus were described in detail in earlier papers^{22,23} and only the data of significance for this paper are presented here.

While adding the AgNO_3 solution into the KI solution,²⁴ the reaction of the chemical synthesis occurs in an excess of I^- ions,^{21–23} hence β -AgI (with a hexagonal structure) is the dominant crystal shape obtained in the sample. While adding the solution in the reverse order, the reaction occurs in an excess of Ag^+ ions and γ -AgI (with a cubic, face-centered structure) is obtained as the dominant crystal shape, with different amounts of β -AgI (from 3.3 to 16.0 %). The

percent of β -AgI in the γ -AgI depends on the addition rate and the ratio of the concentrations of the solutions, as well as on the method of drying the sample.^{22,23}

All the procedures were performed almost in darkness, at room temperature under conditions (solution volume and concentration, and dropping rate) defined in previous papers.^{22,23} The amounts of other crystal forms in the synthesized crystalline forms of AgI are given in Table I.

TABLE I. The amount of other crystal form in synthesized crystalline forms of AgI^{22,23}

Crystalline form	No. of the sample	Amount of other crystal form, $I(I_{\max})^{-1} / \%$
β -AgI	1	2.4 γ -AgI
γ -AgI	3	9.9 β -AgI
	4	10.2 β -AgI
	5	16.0 β -AgI
	6	15.6 β -AgI
	7	6.6 β -AgI
	8	3.2 β -AgI
	9	4.2 β -AgI

X-Ray diffraction analysis showed that rather pure crystallographic forms of silver iodide (the β -AgI had a crystallographic purity of 97.6 % and the γ -AgI samples between 84 % and 96.8 %), being simultaneously thermodynamically stable (over a certain time period),^{22,23} were obtained by the developed synthesis procedures.

Methods

The aim of this study was to test the behavior of the synthesized samples of β -AgI and γ -AgI (before and after grinding) on heating from 0 °C to 260 °C and spontaneous cooling back to room temperature, in order to enable adequate conclusions on the thermal stability of such forms to be drawn. Also, the influence of grinding on the changes within the structures of these forms, namely on changes in the behavior at their phase transformations, was studied.

The influence of heating, grinding and pressing of the samples on the stated phenomenon was studied by the following methods: a) crystal powder diffraction (X-ray) and b) differential scanning calorimetry (DSC).

AgI crystal forms were identified by the X-ray diffraction method,²⁵⁻²⁷ and the obtained results were compared with data published in JCPDS cards.²⁸ These investigations consisted of heating non-ground and ground synthesized to a desired temperature and analyzing the obtained diffractograms.

The most adequate method for structural analysis of crystals of polycrystalline samples is the crystal powder diffraction method. The distance between the level d , the parameter of the grid a in a cubic lattice (from the general technical term of Hull and Davey),²⁶ that is, the parameters a and c of a hexagonal lattice (for each pair of 2θ reflections), are given by well-known expressions. The mean values a and c were obtained from the previously calculated single values.

The investigations using the DSC method were performed by heating the synthesized samples (before and after grinding) within the 0–250 °C temperature interval, at heating rates of 1, 2 and 3 °C min⁻¹. Some of the samples were also monitored after the “heating–spontaneous cooling” process.

Apparatus

For testing the influence of heating and grinding of the AgI samples on the change of their structure and on the phase transformations, the following instruments were employed:

- Philips APD 1700 Diffractometer with a PW 1820 vertical goniometer and a graphite monochromator, equipped with a computer system which provides direct value procurement for 2θ , d and I/I_0 ;
- DSC (differential scanning calorimeter) V2. 2A Du Pont 9900.

X-Ray sample characterization was performed both with and without previous mechanical treatment of the samples using the following recording parameters:

- Generator settings: 35 kV and 50 mA;
- Cu-alpha 1, 2 wavelength: 1.54060 Å and 1.54439 Å;
- Step size, sample time: 0.020 step, 0.50 s, 25.00 s per step;
- Monochromator used: Yes;
- Divergence slit: Constant (1 step);
- Analysis program number: 40;
- Peak angle range: (4.010 – 59.990) step;
- Range in D spacing: (1.54083 – 22.0169) Å;
- Cryst. peak width range: (0.00 – 2.00) step;
- Minimum peak significance: 0.75.

The DSC instrument was employed for monitoring the heat flow during the heating of the non-ground and ground silver iodide samples, *i.e.*, for identifying the influence of grinding on their structural changes and phase transitions.

RESULTS AND DISCUSSION

The influence of heating rate on the phase transformations

The DSC curves shown in Fig. 1 were obtained by heating non-ground sample 1 (curve a) and ground sample 1 (curve b) at a heating rate of 2 °C min⁻¹ (see part c).

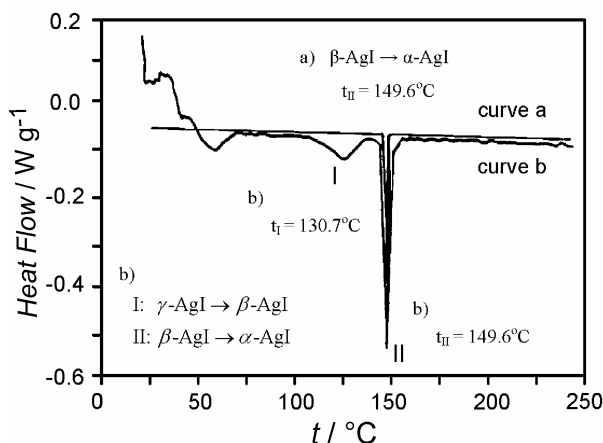


Fig. 1. DSC Curves of β-AgI (sample 1) recorded at a heating rate of 2 °C min⁻¹: a) non-ground synthesized powder (hexagonal structure) and b) after grinding (cubic, face-centered structure).

Figure 1 (curve a) shows the presence of only one phase transformation at a temperature of 149.6 °C (β-AgI → α-AgI) for sample 1 (with the maximum amount of 97.6 % β-AgI and 2.4 % γ-AgI, as a crystallographic impurity). This phase transformation temperature of 149.6 °C deviates from the values given in the literature.¹³ This was the motivation to study the dependence of the phase transformation temperature on the sample heating rate (for sample 1, β-AgI). The results obtained for the thermal stability testing of β-AgI at different heating rates (1, 2 and 3 °C min⁻¹) are given in Table II.

From the results given in Table II, it is obvious that reducing the sample

heating rate (from 3 to 1 °C min⁻¹) lowered the values of the phase transition temperature (from 151.8 °C to 148.6 °C). This leads to the conclusion that this may be the reason for the different values of the phase transition temperature given in the literature.

TABLE II. Dependence of phase transformation (β -AgI \rightarrow α -AgI) temperatures on rate of heating of non-pulverized sample 1^{22,23}

Sample heating rate, ν / °C min ⁻¹	Phase transformation temperature t / °C
1.0	148.6
2.0	149.6
3.0	151.8

The influence of thermal treatment on the phase transformations

Determination of phase transitions temperatures was performed by differential scanning calorimeter (DSC) on non-ground samples 1 (β -AgI), and 3, 5, 7 and 9 (γ -AgI), at a heating rate of 2 °C min⁻¹. The curves obtained for samples 1, 3 and 9 are shown in Figs. 1,2 and 3 (curves a), while the corresponding data for the phase transition temperatures and other characteristics of the tested samples are given in Table III.

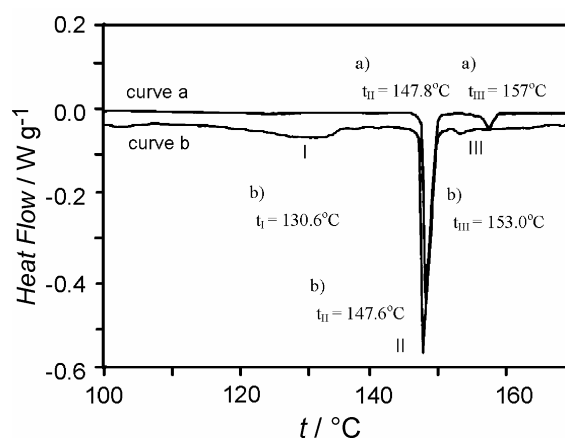


Fig. 2. DSC Curves of γ -AgI (sample 3); a) non-ground synthesized powder and b) after grinding.

The obtained results indicate that sample 1, with the maximum content β -AgI (97.6 %), exhibited only one phase transition at 149.6 °C over the whole range of investigated temperatures (from room temperature to 180 °C). For the samples 7 and 9, with the maximum content of γ -AgI and the minimum content of β -AgI (6.6 % and 4.2 %, respectively), a transition was observed at 148.7 °C, respectively 148.2 °C (over the same temperature range). However, with samples 3 and 5, which contained a larger percent of β -AgI (9.9 % and 16.0 %, respectively) compared with samples 7 and 9 (Tables I and III), two peaks appeared on the DSC

curves, as can be seen in Fig. 2 (curve a) for sample 3. The more expressed maximum were at 147.8 °C (sample 3, curve a in Fig. 2) and 148.5 °C (sample 5, curve a in Fig. 5), and the lower maximum were at 157.0 °C (sample 3, curve a in Fig. 2) and 154.1 °C (sample 5, curve a in Fig. 5).

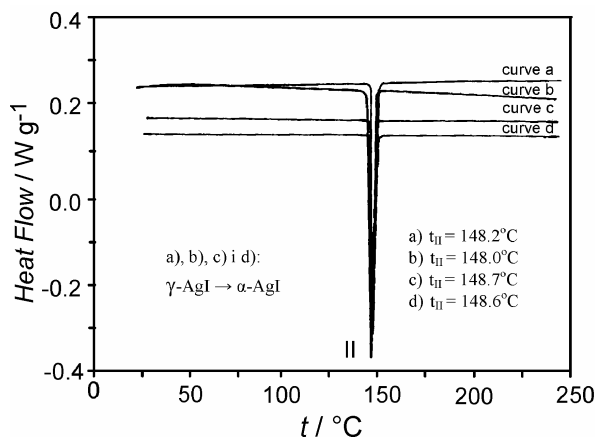


Fig. 3. DSC Curves of γ -AgI (sample 9); a) non-ground synthesized powder, b) after grinding, c) pressed at a pressure $p_1 = 650$ MPa and d) pressed at a pressure $p_2 = 900$ MPa.

TABLE III. Phase transformations and their temperatures* for adequate crystallographic forms** of AgI obtained from DSC method, without and after mechanical and heat treatment of samples (heating rate, $\nu = 2$ °C min^{-1})²²

Sample No.	Crystallographic form before heating	Content of β -AgI %	Phase transformations during mechanical and heat treatment		
			γ -AgI \rightarrow β -AgI	1) β -AgI \rightarrow α -AgI	
				$2) \gamma$ -AgI \rightarrow α -AgI	M-AgI ^e \rightarrow α -AgI
$t_I / ^\circ\text{C}$	$t_{II} / ^\circ\text{C}$	$t_{III} / ^\circ\text{C}$			
1	β -AgI ^a	97.6	–	1) 149.6	–
	γ -AgI ^b	22.09	130.7	1) 149.6	–
3	γ -AgI ^a	9.9	125.0	3) 147.8	157.0
	γ -AgI ^b	36.59	130.6	3) 147.6	153.0
5	γ -AgI ^a	16.0	122.3	3) 148.5	154.1
	γ -AgI ^b	–	–	2) 148.6	–
7	γ -AgI ^a	6.6	–	2) 148.7	–
	γ -AgI ^b	–	–	2) 148.5	–
9	γ -AgI ^a	4.2	–	2) 148.2	–
	γ -AgI ^b	–	–	2) 148.0	–
	γ -AgI ^c	–	–	2) 148.7	–
	γ -AgI ^d	–	–	2) 148.6	–

^aNon-pulverized; ^bpulverized; ^cpressed at a pressure $p_1 = 650$ MPa; ^dpressed at a pressure $p_2 = 900$ MPa; ^eM = $\alpha + \beta + \gamma$ (a mix of all three forms)

* The temperatures of phase transformations correspond to the peak positions on obtained DSC diagrams.

** The crystalline form of samples at certain temperatures was defined by diffractographic method.

A series of X-ray diffraction patterns were therefore recorded at different temperatures, *i.e.*, at 23, 123, 140, 152 and 160 °C or 170 °C, as well as at 23 °C after cooling.

The presence of the different forms of AgI at these temperatures are given in Table IV for samples 1, 3, 5 and 9 and in Fig. 4 for sample 5 only.

TABLE IV. Phase compositions of synthesised AgI samples at different temperatures recorded on diffractogram²²

Sample No.	Composition before heating	Composition						Composition after cooling to 23 °C
		t / °C						
		23	123	140	152	160	170	
1	β -AgI with 2.4 % γ -AgI	$\beta^*+\gamma$	$\beta^*+\gamma$	$\beta^*+\gamma$	α^*	α^*	α^*	$\beta^*+\gamma$
3	γ -AgI with 9.9 % β -AgI	$\gamma^*+\beta$	$\gamma^*+\beta$	$\gamma^*+\beta$	–	α^*	–	$\beta^*+\gamma$
5	γ -AgI with 16.0 % β -AgI	$\gamma^*+\beta$	$\gamma\downarrow+\beta\uparrow$	$\beta^*+\gamma+\alpha$	α^*	–	α^*	$\beta^*+\gamma$
9	γ -AgI with 4.2 % β -AgI	$\gamma^*+\beta$	$\gamma\downarrow+\beta\uparrow$	$\beta^*+\gamma+\alpha$	M**	–	α^*	$\beta^*+\gamma$

* Prevailing structure; \downarrow reduced content; \uparrow increased content; ** M = $\beta + \gamma + \alpha$ (a mix of all three forms)

The diffraction patterns of sample 5 at five different temperatures are presented in Fig. 4. Pattern a was obtained at 23 °C and corresponds to the initial γ -AgI form with the maximum content of the accompanying β -AgI form (16.0 %), while pattern b obtained at 123 °C shows the presence of two forms of AgI (the dominant γ -AgI with an increased content of β -AgI). The patterns c and d, recorded at 140 °C and 152 °C, respectively, exhibit reflections showing the presence of all three forms of silver iodide (α , β and γ) in the samples at these temperatures, implying that a mixture of all three forms of the salt was obtained. At the temperature of 170 °C (pattern e), only α -AgI was present.

With sample 3 (γ -AgI with 9.9 % β -AgI), only α -AgI was present at 152 °C and with sample 9 (γ -AgI with 4.2 % β -AgI), α -AgI was present at 160 °C. In the other cases, the other two forms (β -AgI and γ -AgI) were present, but their relative amounts at 123 °C was changed compared to those in the initial sample (obtained by means of synthesis). Such a situation was registered with samples containing greater amounts of the accompanying β -AgI form in mainly γ -AgI.

The obtained results show that the initial content of β or γ form of AgI in a mixture has an influence on the phase content and the phase transitions of AgI at the investigated temperatures.

It was concluded that the basic criteria for the explanation of such a phenomenon is the percent β -AgI, as a crystallographic impurity, in γ -AgI.^{22,29} The conducted studies showed that samples of γ -AgI containing a higher percent of β -AgI (samples 3 and 5, with 9.9 – 16 % of β -AgI) underwent the phase transformation γ -AgI \rightarrow β -AgI, whereas such a transformation did not occur to a significant extent in samples 7 and 9 (with a β -AgI content within the range 4.2 – 6.6 %). It is assumed that a higher content of β -AgI (> 7 %) in γ -AgI represents a “germ”

that, along with the heating process, causes an easier transformation of the γ form into the β form, resulting in such a transformation to occur in the temperature range from 122.3 °C to 125.0 °C (Table III). In our opinion, the content of β -AgI is relatively low (< 7 %) in the γ -AgI samples 7 and 9 and is not sufficient to act as a “germ” for the phase transition γ -AgI \rightarrow β -AgI on heating. For this reason, only the direct phase transformation γ -AgI \rightarrow α -AgI occurred at the temperatures 148.2 °C and 148.7 °C, respectively (Table III).

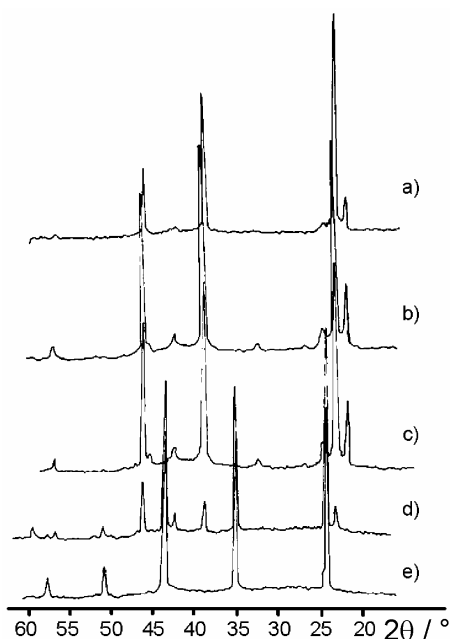


Fig. 4. X-Ray diffraction patterns of sample 5 (γ -AgI) obtained at different temperatures:

- a) 23 °C – γ -AgI,
- b) 123 °C – (γ + β)-AgI,
- c) 140 °C – (γ + β + α)-AgI,
- d) 152 °C – (γ + β + α)-AgI and
- e) 170 °C – α -AgI.

It can be seen from the data in Table III, that the transition temperature at 149.6 °C (sample 1) corresponds to the phase transition β -AgI \rightarrow α -AgI, and that the temperatures 148.7 °C and 148.2 °C (the mean temperature 148.5 °C) for the samples 7 and 9, respectively, correspond to phase transition γ -AgI \rightarrow α -AgI. The literature data¹⁹ for the transitions β -AgI \rightarrow α -AgI and γ -AgI \rightarrow α -AgI gives a value of 147 °C, which is near the values for experimentally obtained phase transitions of 147.8 °C for sample 3 (Table III). The more expressed maximum at 147.8 °C and 148.5 °C for samples 3 and 5, respectively, correspond to the phase transitions γ -AgI \rightarrow (γ + β + α)-AgI, and the lower maximum at 157.0 °C and 154.1 °C, respectively, could probably correspond to the transitions (γ + β + α)-AgI \rightarrow α -AgI because it was determined by X-ray diffraction analysis (Table IV) that all three forms of AgI were present at 152 °C. This also means that in the transition γ -AgI \rightarrow β -AgI. This also confirms the previous assumption that the γ -AgI form is the metastable state of this salt. Simultaneously, the very small differences in the temperatures of phase transitions explain the facts that transition γ -AgI in β -AgI

is not clearly defined in the literature.^{13,17} For these reasons, the less expressed peaks on the diagrams for samples 3 (Fig. 2, curve a) and 5 may not be the result of a new phase transition but also the result of other processes during the larger representation of β , γ and α form AgI.

The influence of sample treatment on phase transition temperature is in accordance with literature data,²⁰ *i.e.*, on the crystallite size. In all cases, as was already stated in previous papers,^{22,23} after spontaneous cooling of the heated samples to 23 °C, β form AgI was obtained, which indicates that the transition γ -AgI \rightarrow β -AgI is irreversible, namely that γ -AgI is a metastable state of this compound. This is an additional reason for the greater stability of β -AgI. Thus, the previous statements¹³ that only one phase transition exists in case of β -AgI (β -AgI \rightarrow α -AgI) were confirmed.

It was also proved that in neither case does the phase transition β -AgI \rightarrow γ -AgI appear, which has also been discussed by other authors.¹⁶

The influence of the manual pulverization on phase transformation

The influence of grinding of β -AgI and γ -AgI on the appearance of the different phase transitions was also studied in this work.

The effects of grinding on the phase transitions was followed by the DSC method (heating from 0 to 250 °C at a heating rate of 2 °C min⁻¹), for sample 1 (β -AgI) and samples 3, 5, 7 and 9 (γ -AgI).

DSC Curve with one phase transition (β -AgI \rightarrow α -AgI) was obtained heating non-ground sample 1, which was proved by X-ray diffraction analysis to have a hexagonal structure (β -AgI) after synthesis (Fig. 1, curve a).

The structure of the sample was changed to γ -AgI by manual grinding of the sample 1 (β -AgI) in an agate mortar and by repeated recording of the DSC curves over the temperature interval from 0 to 250 °C, whereby a change of the phase transformations occurred. In this case, the DSC curve exhibited two phase transitions, *i.e.*, γ -AgI \rightarrow β -AgI and β -AgI \rightarrow α -AgI, at the temperatures of 130.7 °C and 149.6 °C, respectively, which is illustrated in Fig. 1 by curve b. Thus, the X-ray diffraction results of the influence of grinding β -AgI on the structural change were also confirmed by DSC.

The samples 3, 5, 7 and 9 (γ -AgI, containing the amounts of β -AgI given in Table I) were treated in the same way as the sample 1 (β -AgI).

No change of the structure of the dominant γ -form into the β -form was observed with samples 7 and 9 (containing 6.6 % and 4.2 % of β -AgI, respectively), but a reduction of the amount of β -AgI (due to already discussed influence of grinding on the structural change of β -AgI) was registered. Hence, after mechanical treatment of these samples, DSC curves with only one peak, corresponding to the phase transition γ -AgI \rightarrow α -AgI, were obtained. This is illustrated in Fig. 3 by curves a and b using sample 9 as an example. Using the results of previous

studies,^{22,29} and the demonstrated influence of the amount of β -AgI, as a crystallographic impurity in the dominating γ -AgI form, it can be concluded that grinding does not influence the phase transitions if the content of β -AgI is less than 7 %.

The DSC curves for samples 3 and 5 (containing 9.9 % and 16.0 % of β -AgI, respectively) with two or three phase transitions were obtained for the ground and non-ground samples^{22,29}(Figs. 2 and 5).

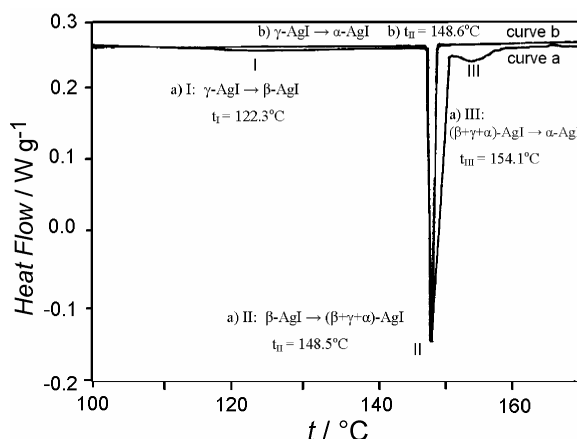


Fig. 5. DSC Curves of γ -AgI (sample 5); a) non-ground synthesized powder (curve a) and b) after grinding (curve b).

In a previous study,²² the influence of larger amounts of β -AgI, shown to be an impurity in the dominating γ -AgI, on the appearance of the two or three transitions during the thermal treatment of non-ground samples was investigated. X-Ray diffraction analysis (Fig. 4, Tables III and IV) showed that the three peaks on the DSC curve (Fig. 5, curve a) for non-ground sample 5 correspond to the phase transitions γ -AgI \rightarrow β -AgI (at $t_I = 122.3$ °C), β -AgI \rightarrow ($\beta+\gamma+\alpha$)-AgI (at $t_{II} = 148.5$ °C) and ($\beta+\gamma+\alpha$)-AgI \rightarrow α -AgI (at $t_{III} = 154.1$ °C). Grinding of this sample in an agate mortar caused the already discussed change of β -AgI into γ -AgI, which lead to the reduction of the content of this form in the dominating form γ -AgI and the elimination of the so-called “germ”, which resulted in the appearance of only the one-phase transition γ -AgI \rightarrow β -AgI (at t_I) and ($\beta+\gamma+\alpha$)-AgI \rightarrow α -AgI (at t_{III}). For this reason, after grinding and heating of sample 5 (from 0 to 250 °C), the peaks I and III were absent on the DSC curve (Fig. 2, curve b), which means that the grinding of γ -AgI containing more than 7 % β -AgI has an influence on the phase transitions. The final result of grinding in this case is the complete absence of the phase transition γ -AgI \rightarrow β -AgI, so that the immediate phase transition γ -AgI \rightarrow α -AgI developed.

An interesting phenomenon was registered with sample 3 (γ -AgI containing 9.9 % of β -AgI). On the DSC curve of the non-ground sample (Fig. 2 curve a),

two peaks at 147.8 and 157.0 °C corresponding to the phase transitions $\beta\text{-AgI} \rightarrow (\beta+\gamma+\alpha)\text{-AgI}$ and $(\beta+\gamma+\alpha)\text{-AgI} \rightarrow \alpha\text{-AgI}$, respectively, are clearly manifested. After the sample had been ground, a peak corresponding to the phase transition $\gamma\text{-AgI} \rightarrow \beta\text{-AgI}$ appeared at 130.6 °C, whereas the peak at 153.0 °C almost completely disappeared (curve b, Fig. 2). Considering the previously established influence of mechanical grinding on the structural change of $\beta\text{-AgI}$ into $\gamma\text{-AgI}$, a decrease of the amount of $\beta\text{-AgI}$ in the dominantly $\gamma\text{-AgI}$ sample would also have occurred in this case after grinding. However, quantitative X-ray diffraction analysis showed that the content of $\beta\text{-AgI}$ in the dominant $\gamma\text{-AgI}$ had increased from 9.9 to 16.5 % after grinding. This result was evidenced for sample 3 only.

After having analyzed all the results, the conclusion was reached that the peak at 153 °C corresponds to a sample structure which is a combination of all three crystallographic forms ($\gamma+\beta+\alpha$)-AgI. Only after heating above 160 °C is the $\alpha\text{-AgI}$ form obtained (BCC).

The influence of the pressure on the structure and phase transitions

The influence of pressing on the structure and the phase transitions was studied with the sample 9 ($\gamma\text{-AgI}$, with 4.2 % of $\beta\text{-AgI}$). The experiment consisted of pressing the sample at two different pressures ($p_1 = 650$ MPa and $p_2 = 900$ MPa). X-Ray diffraction analysis showed that in this case a transformation of $\beta\text{-AgI}$ into $\gamma\text{-AgI}$ occurs, resulting in a reduction of amount of $\beta\text{-AgI}$ in the dominating $\gamma\text{-AgI}$, but that there is no influence on the phase transition $\gamma\text{-AgI} \rightarrow \alpha\text{-AgI}$ (which was present with the as synthesized sample, without the influence of the mechanical treatment or the increased pressure). Considering that this sample contained a small amount of $\beta\text{-AgI}$ (smaller than 7 %), only one peak for the phase transition $\gamma\text{-AgI} \rightarrow \alpha\text{-AgI}$ (Fig. 3, curves c and d) were observed on the DSC curves, practically at the same temperature as for the non-ground ground samples (Fig. 3, curve a and b, respectively).

It is assumed that $\beta\text{-AgI}$ was transformed under pressure into cubic $\gamma\text{-AgI}$ and, hence, the peak for the phase transformation $\gamma\text{-AgI} \rightarrow \beta\text{-AgI}$ was completely absent direct transformation of $\gamma\text{-AgI}$ into $\alpha\text{-AgI}$ occurred.

ИЗВОД

КРИСТАЛОГРАФСКИ ОБЛИЦИ СРЕБРО ЈОДИДА II. ОДРЕЂИВАЊЕ ФАЗНИХ ПРЕЛАЗА

МАРИЈА Р. ВУКИЋ¹, ДРАГАН С. ВЕСЕЛИНОВИЋ² и ВЕСНА Г. МАРКОВИЋ³

¹Историјски "Кирило Савић" д.д., Војводе Силеје 51, 11000 Београд, ²Факултет за физичку хемију, Студентски брз 12, 11000 Београд и ³ИТНМС, Франше Дејереа 86, 11000 Београд

У циљу добијања одговарајућих облика сребро јодида ($\beta\text{-AgI}$ и $\gamma\text{-AgI}$) развијене су методе њихове синтезе на собној температури од 23 °C, при чему су добијени узорци различите кристалографске чистоте и састава. У овом раду су приказани резултати испитивања утицаја начина припреме и брзине загревања узорака $\beta\text{-AgI}$ и $\gamma\text{-AgI}$ на фазне прелазе и

njihove temperature. При загревању неспрашених, спрашених и пресованих испитиваних синтетизованих узорака AgI идентификовани су фазни прелази и њихове temperature за један узорак β -AgI и четири узорка γ -AgI са различитим садржајем β -AgI у себи (као кристалографске нечистоће). Евидентирани су следећи фазни прелази за неспрашене узорке AgI: β -AgI \rightarrow α -AgI на 149,6 °C и γ -AgI \rightarrow α -AgI на 148,7 °C односно 148,2 °C за узорке γ -AgI са минималним садржајем β -AgI (до 7 %), као кристалографске нечистоће. Прелаз γ -AgI \rightarrow α -AgI је иреверзибилан, јер се при хлађењу узорака, загрејаних до 260 °C, добија увек β -AgI. Ручно спрашивање узорака, као и пресовање на $p_1 = 650$ МПа и $p_2 = 900$ МПа, доводи до фазног прелаза β -AgI \rightarrow γ -AgI у свим испитиваним случајевима.

(Примљено 20. јула 2006, ревидирано 21. децембра 2006)

REFERENCES

1. D. A. Keen, *J. Phys. Condens. Matter* **14** (2002) R 819
2. J. S. Lee, S. Adams, J. Maier, *J. Phys. Chem. Solids* **61** (2000) 1607
3. J. R. G. Patnaik, C. S. Sunandan, *J. Phys. Chem. Solids* **59** (1998) 1059
4. S. Hull, D. A. Keen, P. Berastegui, *J. Phys. Condens. Matter* **14** (2002) R 13579
5. G. Burley, *J. Chem. Phys.* **38** (1963) 2807
6. L. H. Adams, B. L. Davis, *Proc. Natl. Acad. Sci.* **48** (1962) 983
7. T. H. James, *The Theory of the Photographic Process*, Macmillan, New York, 1977
8. Atom Indonesia, <http://digilib.batan.go.id/atom-indonesia/fulltex/v31-n1-1-05/E-kartini.pdf>
9. J. B. Boyce, B. A. Huberman, *Phys. Rep.* **51** (1979) 189
10. S. Chandra, *Superionic Solids*, North Holland, Amsterdam, 1981
11. M. B. Salamon, *Physics of Superionic Conductors*, Springer, Berlin, 1979
12. S. Chandra, A. L. Laskar, *Superionic Solids and Solid Electrolytes-Recent Trends*, Academic Press, New York, 1989
13. N. Parsonidzh, L. Steivli, *Besporjadok v kristallakh*, Tom I, Izd. Mir, Moskva, 1982, p. 214
14. M. Tatsumisago, K. Okuda, N. Itakura, T. Minami, *Solid State Ionics* **121** (1999) 193
15. K. Funke, *Prog. Solid State Chem.* **11** (1967) 345
16. M. Natarajan, C. N. R. Rao, *J. Chem. Soc. A* (1970) 3087
17. C. M. Perrott, N. H. Fletcher, *J. Chem. Phys.* **50** (1969) 2344
18. W. C. Hamilton, *Phys. Rev.* **110** (1958) 1050
19. *Spravochnik khimika I*, GHI, II izd., Red. B. P. Nikol'skii, Moskva, 1962
20. M. Hanaya, I. Osawa, K. Watanabe, *J. Therm. Anal.s Calorim.* **76** (2004) 529
21. M. Vukić, D. Veselinović, V. Marković, M. Mirjanić, O. Stojanović, M. Momirović, *Book of Abstracts*, in *Proceeding of XXXV Conference of the Serbian Chemical Society*, (1993), Belgrade, Yugoslavia, (1993), p. 209 (in Serbian)
22. M. Vukić, *PhD Thesis*, University of Belgrade, Faculty of Physical Chemistry, Belgrade, 1996
23. D. S. Veselinović, M. R. Vukić, V. G. Marković, M. D. Mirjanić, *J. Serb. Chem. Soc.* **61** (1996) 31
24. G. Brauer, *Handbuch der präparativen anorganischen Chemie*, Hrsg. V. G. Brauer, BII-15, F. Enke, Stuttgart, 1954, p. 770
25. W. Friedrich, P. Knipping, M. Laue, *Interferenz-Ershheinungen bei Roentgenstrahlen*, Sitzungsberichte der Bayerischen Akademie der Wissenschaften, Math. Phys. Klasse, München, 1912, p. 303
26. H. S. Peiser, H. P. Rooksby, A. J. C. Wilson, *X-Ray Diffraction by Polycrystalline Materials*, The Institute of Physics, London, 1955
27. F. C. Phillips, *An Introduction to Crystallography*, 3rd Ed., Wiley, New York, 1963
28. *Powder diffraction file*, Sets 9, 20, 22, JCPDS, 1601 Park Lane, Swarthmore, Pennsylvania, 1990
29. M. R. Vukić, V. G. Marković, M. Momirović, *Proceedings*, in *Proceeding of 5th International Conference on Fundamental and Applied Aspects of Physical Chemistry "Physical Chemistry 2000"*, (2000), Belgrade, Yugoslavia, (2000), p. 447.



Properties and efficiency of a Pt/Al₂O₃ catalyst applied in a solid fuel thermo-accumulating furnace

SRDJAN BELOŠEVIĆ¹, RASTKO MLADENOVIĆ¹, DRAGOLJUB DAKIĆ¹,
MILIJANA PAPRIKA¹, ALEKSANDAR ERIĆ¹, DEJAN DJUROVIĆ¹,
MIRKO KOMATINA², BOŠKO GRBIĆ^{3#} and NENAD RADIĆ^{3**}

¹Vinča Institute of Nuclear Sciences, Laboratory for Thermal Engineering and Energy, P.O. B. 522, 11001 Belgrade, ²Faculty of Mechanical Engineering, Kraljice Marije 16, 11000 Belgrade and ³Institute of Chemistry, Technology and Metallurgy, Njegoševa 12, 11000 Belgrade, Serbia

(Received 14 June 2006, revised 14 February 2007)

Abstract: A prototype of a solid fuel thermo-accumulating furnace has been developed. In order to achieve a higher combustion efficiency, a Pt/Al₂O₃ catalyst in the form of 3 ± 0.3 mm spheres was applied, which enabled further combustion of flue gases within the furnace. Experimental investigation of the influence of the catalyst on the conversion of CO has been done for different operation regimes and positions of the catalyst. Paper presents selected results regarding CO emission during wood and coal combustion. Investigations suggest a considerable effect of the catalyst and a strong influence of the catalyst position to CO emission reduction. The microstructure of the catalyst beads, characterized by selective chemisorption of CO, has shown the decrease of the number of Pt sites as a consequence of blockage by coke deposits formed during the combustion of solid fuel.

Keywords: Pt/Al₂O₃ catalyst, emission reduction, solid fuel, thermo-accumulating furnace.

INTRODUCTION

The usual problems found in solid fuel household heating systems are low combustion efficiency, small heat transfer intensity and high emission. The problems in residential heating are treated nowadays from various aspects,^{1–4} with emission of pollutants being one of the most important.^{2–4}

A prototype of an innovative thermo-accumulating solid fuel furnace, aimed for residential heating purposes, has been developed and tested. The furnace provides efficiency over 75 %, considerable energy savings, emission of pollution that meets European standards and possibility of firing both low- and high-rank solid fuels. The basis for the development of the furnace was a registered patent.⁵ The furnace is presented and described in details in Ref. 6.

* Corresponding author. E-mail: nradic@nanosys.ihtm.bg.ac.yu

Serbian Chemical Society member.

doi: 10.2298/JSC0709869B

In order to achieve higher combustion efficiency, a Pt/Al₂O₃ catalyst, in the form of 3 ± 0.3 mm spheres, was applied in the furnace prototype, providing further combustion of flue gases within the furnace. An experimental investigation of the influence of the catalyst on the conversion of CO into CO₂ was performed for different operation regimes and positions of the catalyst. All furnace tests were performed in accordance with the European Standard for solid fuel-fired furnaces (EN 12815). The microstructure of the catalyst beads, characterized by selective chemisorption of CO, was studied and compared to the structure of the beads after use in the furnace.

EXPERIMENTAL

Catalyst preparation

The employed support was commercial (γ+θ)-Al₂O₃ in the form of spheres with a diameter of 3 ± 0.3 mm, from Rhone Poulenc. The platinum catalyst was prepared by impregnation of a dry support with an aqueous solution of chloroplatinic acid. Before the Pt deposition, the support was dried for 4 h at 120 °C. An adequate amount of an aqueous solution of hexachloroplatinic acid was added to the support (about 5 cm³ g⁻¹ support) by the incipient wetness method. The concentration of chloroplatinic acid in the impregnating solution was 1 × 10⁻² mol l⁻¹. After the adsorption of chloroplatinic acid during 3 min, the catalyst was filtered, rinsed with distilled water, air-dried at 110 °C for 2 h and finally reduced in a flow of H₂/N₂ mixture. The reduction was performed under a stepwise increase of temperature up to 500 °C. At this temperature the catalyst was reduced during 5 h. A catalyst with the following characteristics was synthesized: Pt amount 0.12 wt. %; specific area – S_{BET} – 110 m² g⁻¹; pore volume – 0.68 cm³ g⁻¹ and supported Pt layer thickness – 100 μm.⁷

Catalytic activity test

The Pt/Al₂O₃ catalyst was tested for combustion of a gas mixture designed to simulate the approximate concentrations of pollutants in the furnace. The activity tests were performed in the apparatus presented earlier.⁸ The activity of the catalyst was investigated in the temperature range 100–400 °C, with a space velocity of 17 500 h⁻¹, defined as the ratio between the gas flow rate and the volume of catalyst. The synthetic gas mixture composition was: CO, 1.17 vol. %; C₃H₆, 800 ppm; H₂, 1.36 vol. %; NO_x, 1120 ppm.; CO₂, 6 vol. %; H₂O, 5 vol. %; O₂, 4.6 vol. % and N₂, the rest. The composition of feed stream corresponds to a redox potential of 0.4 V, which was calculated according to the equation presented in Ref. 8.

Catalytic activity in the furnace

The furnace operating at different regimes, firing wood and coal, with and without catalyst, was experimentally tested. The furnace and the experimental set-up are shown in Fig. 1.

The flue gases flow through the three drafts (1a–1c), while combustion of solid fuel (wood biomass, coal) occurs on a horizontal grate (2). The air enters the furnace through the opening under the grate. In order to examine the influence of the position of the catalyst on its ability to reduce CO emission, the catalyst (3) was placed in two vertical positions (denoted as upper and lower), within the central draft (1b), with flue gases flowing downward and around the catalyst. The flue gases leave the furnace through the stack (4), used for flue gas sampling and temperature and flow rate measurements. The airflow rate is controlled by changing the flue gas fan speed. This fan is connected to a variable (0–220 V) ac supply (5). During the experiments, when the furnace had attained a steady state (after the initial firing), the ac voltage was kept constant at 110 V. This enabled the whole amount of fuel (about 1.5 kg) in the combustion chamber (1a) to burn out before the next fuel feeding an hour later. The furnace as a whole was placed on a high-precision balance (±10 g), in order to monitor the weight loss between consecutive fuel feedings, *i.e.*, the combustion dynamics.

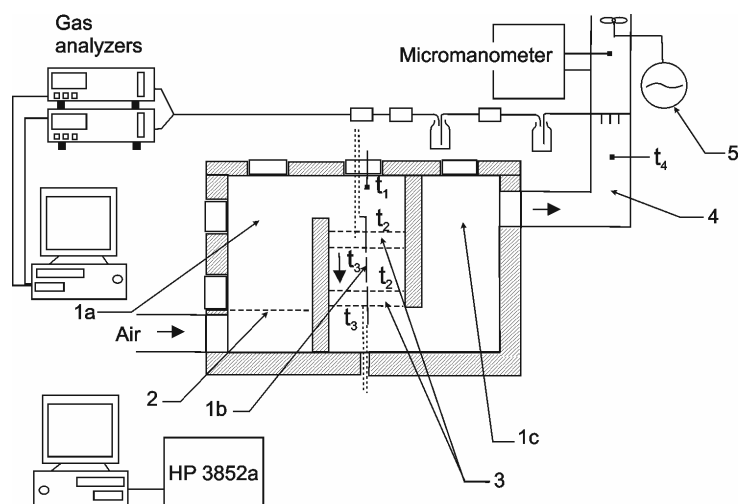


Fig. 1. The solid fuel furnace with the experimental set-up; 1a – combustion chamber; 1b – central draft; 1c – third draft; 2 – grate; 3 – catalyst; 4 – stack; 5 – variable (0 – 220 V) ac power supply.

Gas samples were taken from the stack and continuously analyzed. The gas sampling probe, made according to EN 12815 Standard, was water-cooled on the outside of the stack, in order to dry the flue gas samples. The gas analyzers were controlled by a PC, memorizing the measured concentrations data every three seconds. The flue gas temperatures were measured with type K, class I thermocouples at a number of points, such as at the top of the middle draft (t_1), at the catalyst entrance and exit sections (t_2 and t_3) and at the furnace exit (t_4). The thermocouple signals were measured with a digital voltmeter on an HP3852a data acquisition system, and memorized every 5 seconds.

CO uptake measurements

The CO uptake of the catalysts before and after the catalytic activity tests in the furnace was obtained at a temperature of 24 ± 0.2 °C. The measurements were performed on a pulse gas chromatographic apparatus. Before the chemisorption measurements, the catalyst samples (about 0.5 g) were treated at 500 °C in a helium flow for 1 h. After cooling in a helium flow to room temperature, the CO was pulsed (pulse volume 0.1 cm³) into the helium stream (30 cm³ min⁻¹) through the adsorption cell. The catalyst adsorbed the CO pulses until saturation and the fraction of CO not adsorbed was detected by a thermal conductivity detector (TCD).

RESULTS AND DISCUSSION

In order to compare different operation regimes of the furnace, with different air excess, the measured values of the CO concentration in the dry flue gases CO_{meas} were converted to concentration values at referent oxygen content in the flue gases CO_{ref} , all given in vol. %, according to Eq. (1):

$$CO_{\text{ref}} = \frac{20.9 - O_{2\text{ref}}}{20.9 - O_{2\text{meas}}} CO_{\text{meas}} \quad (1)$$

The referent oxygen content in the flue gases, according to the EN 12815 Standard, is $O_{2\text{ref}} = 13$ vol. %. The measured oxygen content in the flue gases is $O_{2\text{meas}}$. The flow rate of CO (released carbon-monoxide in time, given in mg s^{-1}) is calculated as:

$$\dot{m}_{\text{CO}} = \dot{V}_{\text{fg}} \text{CO}_{\text{ref}} \quad (2)$$

where \dot{V}_{fg} , $\text{m}^3 \text{s}^{-1}$, is the volume flow rate of the flue gases and CO_{ref} , mg m^{-3} , is the referent CO concentration, previously converted from vol. % to mg/m^3 . Since the flue gas sampling was performed (with the results memorized) every three seconds, the mass of CO released in 3 s is:

$$m_{\text{CO}}(3\text{s}) = 3\dot{m}_{\text{CO}} \quad (3)$$

and the cumulative CO emission (given in g) from the beginning of the test until the moment of observation τ , $E_{\text{CO}}(\tau)$ is calculated by the expression in Eq. (4):

$$E_{\text{CO}}(\tau) = \frac{1}{1000} \sum_0^{\tau} m_{\text{CO}}(3\text{s}) \quad (4)$$

Experiments with synthetic gas mixture

From Fig. 2, it is evident that the $\text{Pt/Al}_2\text{O}_3$ catalyst showed satisfactory performances for the removal CO and propylene.

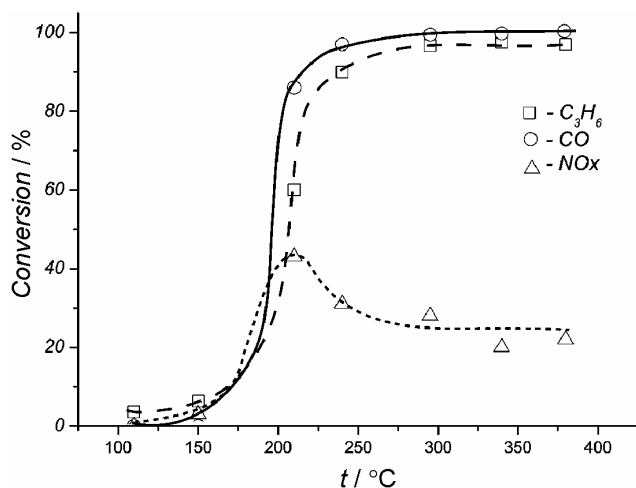


Fig. 2. The performance characteristics of the $\text{Pt/Al}_2\text{O}_3$.

Their conversions exceeded 90 % at temperatures above 225 °C. Although oxidizing conditions were applied (with a redox potential $R = 0.4$ V), a conversion of NO_x was registered. The NO_x conversion curve passed through a maximum at 210 °C and then decreased to a value of 20 %. This is the result of competitive reactions of CO and propylene with NO_x and oxygen. Probably, above 210 °C oxidation reactions of CO and propylene prevailed and NO_x removal was hindered due to a shortage of the reducing agents.

Experiments with wood

The furnace was examined in three operation regimes, with fuel consumption of about 1.5 kg h⁻¹ in each. For the basic one (without the catalyst), wood was supplied to the furnace every 30 minutes (0.750 kg) in the beginning, but it was found that this amount of fuel was optimal for 40 minutes of operation and fuel feeding was adjusted accordingly. In the other two regimes, the catalyst was mounted in the upper and the lower position, respectively. The changes of temperature of the flue gases at the catalyst entrance section and CO concentration in the outlet flue gases at 13 vol. % O₂ with time are shown in Figs. 3 and 4, for both operation regimes with the catalyst.

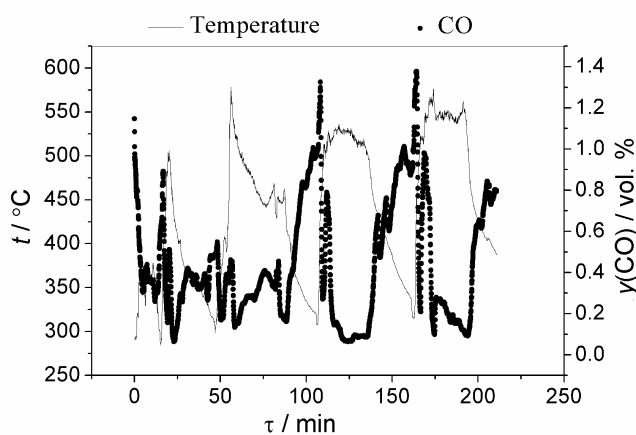


Fig. 3. Time dependence of the flue gases temperature at the entrance section of the catalyst in the upper position and the CO concentration in the outlet flue gases, for wood combustion.

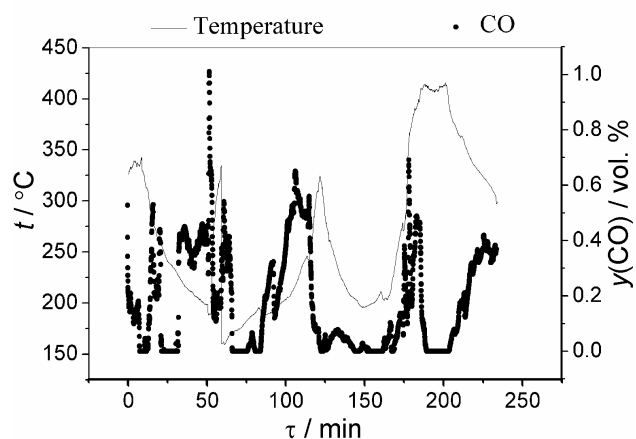


Fig. 4. Time dependence of the flue gases temperature at the entrance section of the catalyst in the lower position and the CO concentration in the outlet flue gases, for wood combustion.

The experimental results for the effect of the catalyst on the CO concentration in the flue gases at 13 vol. % O₂ (averaged over the fuel feeding intervals) and on the cumulative CO emission are given in Figs. 5 and 6.

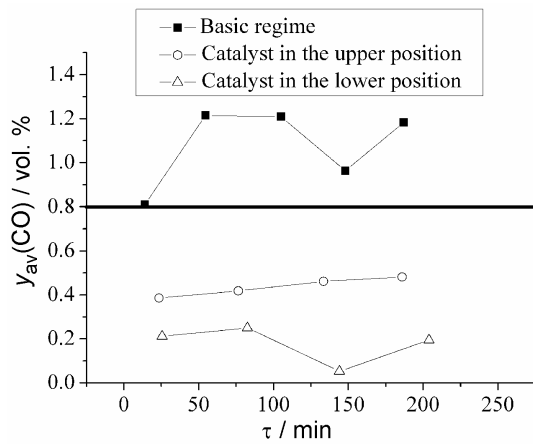


Fig. 5. Effect of the catalyst on the CO concentration in the flue gas, averaged over fuel feeding intervals, for wood combustion.

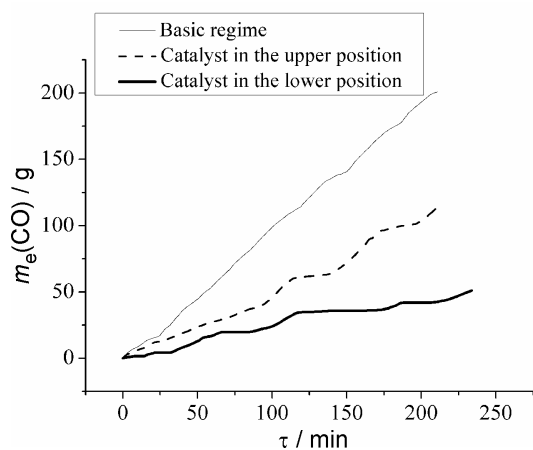


Fig. 6. Effect of the catalyst on the cumulative CO emission, $m_e(\text{CO})$, for wood combustion.

Compared to the basic regime, both those with the catalyst were obviously advantageous. After a quick and very intense increase immediately after fuel feeding, the CO concentration decreased very soon to a value of 0.8 vol. % (Figs. 3 and 4), permitted by the EN 12815 Standard. The average CO concentration (Fig. 5) in the case of the catalyst in the upper position was around 0.4 vol. %, *i.e.*, much lower than the permitted value. Further enhancement was obtained by mounting the catalyst in the lower position, when the presence of the catalyst completely removed CO for a significant period of time between two fuel feedings (Fig. 4) and the average CO concentration was about or lower than 0.2 vol. % (Fig. 5). The positive effects of the catalyst on the reduction of CO emission were even more obvious when the cumulative CO emission during the experiments were considered (Fig. 6). The cumulative emission after 200 minutes of operation for the catalyst in the lower position was 5 times lower compared to the basic regime and for the catalyst in the upper position it was reduced to one half.

The catalyst proved to be more efficient when placed in the lower position than in the upper one (in the zone with higher temperatures). The performance characteristics of the catalyst (Fig. 2) showed that the temperature interval of maximum catalyst efficiency for CO conversion was at temperatures above 200–225 °C, while Figs. 3 and 4 show that for both regimes with the catalyst, the temperatures at the catalyst entrance section was, most of the time, also higher than these. Thus, the better efficiency of the catalyst in the lower position can not be assigned to temperature but most probably to the flow conditions. In this regime, the flue gases enter the catalyst zone and flow over catalyst beads uniformly, so the catalyst is utilized more efficiently. The catalyst in the upper position disturbs the flow and the temperature field in the central draft considerably and it is likely that an intense recirculation zone exists above the catalyst zone (Fig. 1).

Experiments with coal

The experiments were carried out for two operation regimes, the basic one (without the catalyst) and the regime with the catalyst in the upper position. The amount of air supplied in both regimes was sufficient for the combustion of 1.5 kg h⁻¹ of coal. In the basic regime, 1.5 kg of coal was supplied once an hour. It was noted during the experiment that with time the grate became covered with a huge amount of unburnt fuel and ash. In order to avoid this in the regime with catalyst, the furnace was supplied with 0.750 kg of coal every 30 minutes.

The CO concentration was low, almost zero, for most of the time between fuel feedings (Fig. 7). The flue gas temperature at the catalyst entrance section did not change considerably, in the range of 320–365 °C, and probably did not affect the catalytic conversion of CO much. The results for cumulative CO emission (Fig. 8) showed that the presence of the catalyst, even in the upper position (less suitable for reducing CO), significantly contributed to a lowering of the CO concentration levels in the flue gases. After 120 minutes of operation, the CO emission was 20 % lower with the catalyst than without.

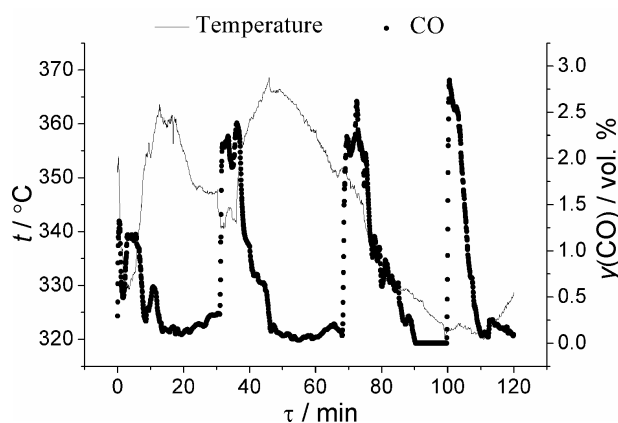


Fig. 7. Time dependence of the flue gases temperature at the entrance section of the catalyst in the upper position and the CO concentration in the outlet flue gases, for coal combustion.

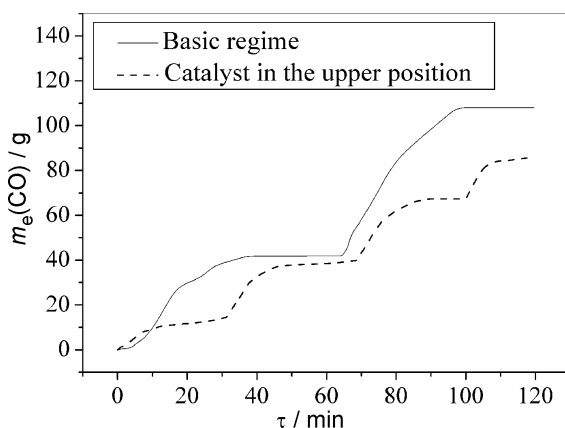


Fig. 8. Effect of the catalyst on the cumulative CO emission, for coal combustion.

Microstructure of the Catalyst Beads

CO uptake measurements (Table I) clearly show that the number of exposed Pt sites which can participate in the surface reactions significantly decreased, by about 50 %, regardless of the type of employed solid fuel.

TABLE I. CO uptake for the Pt/Al₂O₃ catalyst samples

Pt/Al ₂ O ₃ catalyst samples	Fresh	After wood combustion	After coal combustion
CO uptake μmol g ⁻¹	1.51	0.84	0.80

There are several possible mechanisms for the reduction of the exposed Pt sites, such as sintering of the Pt due to the high temperature treatment, physical blockage of the Pt sites by deposits formed during the combustion of the solid fuels or catalyst coking caused by surface reactions. Bearing in mind the applied temperature range (150–500 °C), it is unlikely that sintering of the Pt occurred. Previous investigations showed that sintering of Pt commences above 600 °C.⁹ Therefore, the drop of CO uptake is ascribed to the blockage of the Pt sites. Furthermore, a visual survey of the discharged catalyst showed black deposits only on the half of the sphere facing the flue gases stream. The other half of the sphere retained the appearance of the fresh catalyst. These facts could lead to the conclusion that the deposits originated from the flue gases stream. The deposits were not formed during reaction on the catalyst surface; otherwise the whole sphere would be covered with the black deposits. Also, it should be noted that the black-colored deposits were more pronounced when coal combustion was applied. Although a decrease in the available Pt sites was registered, there is no evidence of a decrease of the catalyst performances in the furnace. However, for long-term application of the catalyst, removal of the deposits by a suitable method (washing, controlled incineration) should be considered.

CONCLUSION

A series of experiments were performed on a prototype of a thermo-accumulating solid fuel furnace, to investigate the possibility of increasing the combustion efficiency (with respect to the transformation of CO) by means of a Pt/Al₂O₃ catalyst, employed in the form of 3 ± 0.3 mm spheres. Tests were performed in accordance with the corresponding European Standard for solid fuel-fired furnaces. Selected results regarding the activity of the catalyst during wood and coal combustion in the furnace, as well as of a catalytic activity test with a synthetic gas mixture are presented. The measured and average values of the concentration of CO, as well as the cumulative emission of CO, showed that the presence of the catalyst considerably reduces CO emission, for both employed fuels – wood and coal. Investigations also suggest a strong influence of catalyst position to reduction of CO emission, as well as the importance of the flow conditions within the furnace. The microstructure of the catalyst beads, characterized by selective chemisorption of CO, evidenced a decrease in the number of Pt sites as a consequence of blockage by coke deposits formed during the combustion of the solid fuels.

Acknowledgement: This work has been supported by the Ministry of Science and Environmental Protection (Republic of Serbia), within Ministry projects.

ИЗВОД

ОСОБИНЕ И ЕФИКАСНОСТ Pt/Al₂O₃ КАТАЛИЗАТОРА У ТЕРМО-АКОМУЛАЦИОНОЈ ПЕЋИ НА ЧВРСТО ГОРИВО

СРЂАН БЕЛОШЕВИЋ¹, РАСТКО МЛАДЕНОВИЋ¹, ДРАГОЉУБ ДАКИЋ¹, МИЛИЈАНА ПАПРИКА¹, АЛЕКСАНДАР ЕРИЋ¹, ДЕЈАН ЂУРОВИЋ¹, МИРКО КОМАТИНА², БОШКО ГРБИЋ³ и НЕНАД РАДИЋ³

¹Институт за нуклеарне науке "Винча", Лабораторија за термоможењеринг и енерџију, п. бр. 522, 11001 Београд, ²Машински факултет, Краљице Марије 16, 11000 Београд и ³Институт за хемију, технологију и металургију, Нjegoшева 12, 11000 Београд

У прототипу термо-акумулационе пећи на чврсто гориво, примењен је Pt/Al₂O₃ катализатор, у облику сфера величине 3 ± 0.3 mm, са циљем да повећа ефикасност сагоревања и накнадно сагори гасове унутар пећи. Утицај катализатора на конверзију CO је експериментално испитан при различитим операционим режимима пећи и позицијама катализатора. Приказани су резултати промене емисије CO у току сагоревања дрвета и угља. Истраживања су показала значајан ефекат катализатора на смањење емисије CO, као и значај положаја катализатора. Микроструктура катализатора, испитана селективном хемисорпцијом CO, је показала да у току сагоревања чврстих горива у пећи долази до депоновања угљеника на катализатору што доводи до блокирања и смањења броја Pt активних центара.

(Примљено 14. јуна 2006, ревидирано 14. фебруара 2007)

REFERENCES

1. R. D. Edwards, K. R. Smith, J. Zhang, Y. Ma, *Energy Policy* **32** (2004) 395
2. J. O. Jaber, *Energy and Buildings* **34** (2002) 311
3. J. Zhang, K. R. Smith, Y. Ma, S. Ye, F. Jiang, W. Qi, P. Liu, M. A. K. Khalil, R. A. Rasmussen, S. A. Thorneloe, *Atmospheric Environ.* **34** (2000) 4537

4. R. D. Edwards, K. R. Smith, J. Zhang, Y. Ma, *Chemosphere* **50** (2003) 201
5. D. Dakic, S. Ilic, Patent No. P-146/00, 9th March 2000, Protected in the Federal Institution for Intellectual Property, Serbia and Montenegro
6. S. Belosevic, M. Paprika, M. Komatina, Z. Stevanovic, R. Mladenovic, N. Oka, D. Dakic, *Energy and Buildings* **37** (2005) 325
7. N. Radic, B. Grbic, A. Terlecki-Baricevic, *Appl. Catal. B* **50** (2004) 153
8. P. Stefanov, I. Avramova, D. Stoichev, N. Radic, B. Grbic, Ts. Marinova, *Appl. Surf. Sci.* **245** (2005) 65
9. B. Grbic, N. Radic, A. Terlecki-Baricevic, *Sci. Sinter.* **30** (1998) 179.



Headspace solid phase microextraction in the analysis of pesticide residues – kinetics and quantification prior to the attainment of partition equilibrium

RADA DJUROVIĆ^{1*}, MIRJANA MARKOVIĆ¹ and DRAGAN MARKOVIĆ^{2#}

¹Institute of Pesticide and Environmental Protection, Banatska 31b, P.O.B. 163, 11080 Belgrade and ²Faculty of Applied Ecology FUTURA, Bulevar Kralja Aleksandra 79, 11000 Belgrade, Serbia

(Received 9 February 2006, revised 12 March 2007)

Abstract: A new theoretical approach to the headspace/solid phase microextraction (HS/SPME) process is proposed and tested by the analysis of pesticide residues of water samples. The new approach focuses on mass transfer at the sample/gas phase and gas phase/SPME polymer interfaces. The presented model provides a directly proportional relationship between the amount of analytes sorbed by the SPME fiber and their initial concentrations in the sample. Also, the expression indicates that quantification is possible before partition equilibrium is attained. Experimental data for pesticides belonging to various classes of organic compounds were successfully interpreted by the developed model. Additionally, a linear dependence of the amount of pesticide sorbed on the initial analyte concentration in aqueous solution was obtained for a sampling time shorter than that required to reach sorption equilibrium.

Keywords: HS/SPME, theoretical model, pesticide residues.

INTRODUCTION

Solid phase microextraction (SPME) is a solvent-free and equilibrium sample preparation technique in which a fused silica fiber coated with a thin polymer film is introduced into a sample or the headspace above the sample. After partitioning between the polymer layer and the sample matrix, organic analytes are selectively extracted by the active film. Developed by Pawliszyn and coworkers,^{1,2} it has wide applications in the analysis of different types of organic residue samples of various origin. Using the headspace mode of SPME, complex matrix effects are reduced and the fiber lifetime is prolonged.

Hitherto, several theoretical models have been proposed to explain the SPME process. Pawliszyn and coworkers proposed models based on diffusion processes in both the direct and headspace modes.^{3,4} The analytical solution was obtained only for perfectly agitated samples with an infinite volume where only the diffu-

* Corresponding author. E-mail: radda@ptt.yu

Serbian Chemical Society member.

doi: 10.2298/JSC0709879D

sion inside the SPME fiber was considered.³ In the case of static aqueous phase and HS/SPME, only numerical solutions were obtained.^{3,4} There was no analytical expression relating the amount of the analyte sorbed by the fiber to its initial concentration in the sample. Hence, Ai proposed an SPME model for a two-phase system consisting of a sample solution and an SPME fiber.⁵ Solving the problem of a more complex three-phase HS/SPME system with two interfaces (sample solution/gas phase and gas phase/fiber) is more complex. Two models have therefore been proposed. The first one is based on steady state kinetics assuming that the mass transfer rates at the two interfaces are the same.⁶ Since analyte transfer rates across the interfaces may not be the same in real systems, Ai proposed an improved model for non-steady state mass transfer.⁷ Providing a better description of the experimental data, the latest theoretical approach assumed that the analyte concentration in the headspace varies with the extraction time. The time variation of the analyte concentration in the headspace results in different rates of analyte evaporation from the solution and its extraction by the SPME fiber.

In trying to clarify the complex HS/SPME process and prove the practical benefit of general agreement between theory and experiment, the kinetic aspect of the process was included and a theoretical approach based on the HS/SPME kinetics is presented in this work. Experimental results obtained for pesticide residues extraction from water samples using the HS/SPME method were interpreted in terms of the developed model.

THEORETICAL TREATMENT

An HS/SPME process involving analyte mass transfer in three phases across two interfaces can be presented by the Equation:



where S , H and F are the analyte concentrations in the sample solution, headspace (gas phase) and SPME polymer film (fiber), respectively; k_1 , k_2 , k_3 and k_4 are the rate constants of the processes occurring during the HS/SPME, namely analyte evaporation, condensation, sorption and desorption, respectively.

The rates of analyte migration in this system are:

$$-\frac{dS}{dt} = S' = k_1S - k_2H \quad (2)$$

$$\frac{dH}{dt} = H' = k_1S - (k_2 + k_3)H + k_4F \quad (3)$$

$$\frac{dF}{dt} = F' = k_3H - k_4F \quad (4)$$

where t is extraction time.

If S_0 represents the initial concentration of analyte in the sample, and V_s , V_h and V_f are the volumes of the sample, headspace and fiber, respectively, then:

$$S_0V_s = SV_s + HV_h + FV_f \quad (5)$$

Differentiating Eq. (4) and substituting H' and F' from Eqs. (3) and (4), the resulting equation becomes:

$$F'' = k_3[k_1S - (k_2 + k_3)H + k_4F] - k_4[k_3H - k_4F] \quad (6)$$

S and H can be expressed in terms of F and F' using Eqs. (5) and (4) and, therefore, Eq. (6) can be expressed as:

$$F'' + p_1F' + q_1F = k_1k_3S_0 \quad (7)$$

with the coefficients p_1 and q_1 having the form:

$$p_1 = k_1 \frac{V_h}{V_s} + k_2 + k_3 + k_4 \quad (8)$$

$$q_1 = k_1k_4 \frac{V_h}{V_s} + k_1k_3 \frac{V_f}{V_s} + k_2k_4 \quad (9)$$

Eq. (7) is a second-order non-homogeneous linear differential equation. Its general solution, with integration constants C_1 and C_2 , is:

$$F = C_1e^{-at} + C_2e^{-bt} + \frac{k_1k_3S_0V_s}{k_1k_3V_f + k_1k_4V_h + k_2k_4V_s} \quad (10)$$

with

$$a = \frac{p_1 - \sqrt{p_1^2 - 4q_1}}{2} \quad (11)$$

and

$$b = \frac{p_1 + \sqrt{p_1^2 - 4q_1}}{2} \quad (12)$$

Applying the initial condition, $F|_{t=0} = 0$, and replacing C_1 and C_2 with new constants, α and β , ($\alpha = -C_1$, $\beta = -C_2$), one obtains:

$$\alpha + \beta = \frac{k_1k_3S_0V_s}{k_1k_3V_f + k_1k_4V_h + k_2k_4V_s} \quad (13)$$

When the extraction time goes to infinity, Eqs. (10) and (13) become:

$$F^\infty = \frac{k_1k_3S_0V_s}{k_1k_3V_f + k_1k_4V_h + k_2k_4V_s} = \alpha + \beta \quad (14)$$

According to Eq. (13), Eq. (10) can be rewritten as:

$$F = \alpha(1 - e^{-at}) + \beta(1 - e^{-bt}) \quad (15)$$

In the treatment presented above, the mass transfers at both interfaces were taken as the rate determining steps. In reality, the mass transfer at one of the interfaces may play the major role and becomes the rate determining step.

DIFFUSION IN THE SPME FIBER AS THE RATE DETERMINING STEP

When diffusion of an analyte from the fiber surface to its inner layers is a much slower process than its evaporation from the sample, this diffusion can be taken as the rate determining step. It can be assumed that analyte partition equilibrium always exists between the sample and its headspace and that the analyte concentration in the headspace remains constant. According to Eq. (2), the partition constant of an analyte between the sample solution and its headspace (K_1) can be expressed as:

$$K_1 = \frac{S^\infty}{H^\infty} = \frac{k_2}{k_1} \quad (16)$$

Using Eqs. (5) and (16), H can be expressed as a function of F . On substituting the resulting expression for H in Eq. (4), the following relationship is obtained:

$$F' + p_2 F = \frac{k_3 S_0 V_s}{V_h + V_s \frac{k_2}{k_1}} \quad (17)$$

with

$$p_2 = k_4 + \frac{k_3 V_f}{V_h + V_s \frac{k_2}{k_1}} \quad (18)$$

The solution of this non-homogeneous linear differential equation is:

$$F = e^{-p_2 t} \left[C + \frac{k_3 S_0 V_s}{p_2 (V_h + V_s \frac{k_2}{k_1})} e^{p_2 t} \right] \quad (19)$$

where C is an integration constant.

Applying the initial condition, $F|_{t=0} = 0$, the following expression is obtained:

$$F = \frac{k_3 S_0 V_s}{p_2 (V_h + V_s \frac{k_2}{k_1})} (1 - e^{-p_2 t}) \quad (20)$$

When extraction time goes to infinity, Eq. (20) becomes:

$$F^\infty = \frac{k_3 S_0 V_s}{p_2 (V_h + V_s \frac{k_2}{k_1})} = \frac{k_1 k_3 S_0 V_s}{k_1 k_3 V_f + k_1 k_4 V_h + k_2 k_4 V_s} \quad (21)$$

Finally, Eq. (20) can be rewritten as:

$$F = \frac{k_1 k_3 S_0 V_s}{k_1 k_3 V_f + k_1 k_4 V_h + k_2 k_4 V_s} (1 - e^{-p_2 t}) \quad (22)$$

Eq. (22) can be applied to the HS/SPME of volatile or semi-volatile analytes when the sample is heated above ambient temperature.

EVAPORATION FROM THE SAMPLE AS THE RATE DETERMINING STEP

Most analytes have low volatility when the HS/SPME is performed at room temperature. If evaporation of the analyte is much slower than its diffusion in the fiber, partition equilibrium is rapidly attained at the gas/fiber interface, with the evaporation process being the rate determining step. According to Eq. (4), the following solution follows:

$$F^\infty = \frac{k_3}{k_4} H^\infty \quad (23)$$

Using Eqs. (5) and (23) and expressing S and F in terms of H , Eq. (3) becomes:

$$H' + p_3 H = k_1 S_0 \quad (24)$$

with the coefficient p_3 expressed as:

$$p_3 = \frac{k_1 V_h}{V_s} + \frac{k_1 k_3 V_f}{k_4 V_s} + k_2 \quad (25)$$

If the initial and boundary conditions are $H|_{t=0} = 0$ and $H|_{t=\infty} = H^\infty$, respectively, the following solution of Eq. (24) is obtained:

$$H = \frac{k_1 k_4 S_0 V_s}{k_1 k_3 V_f + k_1 k_4 V_h + k_2 k_4 V_s} (1 - e^{-p_3 t}) \quad (26)$$

Finally, according to Eq. (23), the analyte concentration in the fiber is given as:

$$F = \frac{k_1 k_3 S_0 V_s}{k_1 k_3 V_f + k_1 k_4 V_h + k_2 k_4 V_s} (1 - e^{-p_3 t}) \quad (27)$$

EXPERIMENTAL

Materials

The fiber used (Supelco) was a fused silica fiber coated with a 100 μm poly(dimethyl siloxane) (PDMS) film. Before use, the fiber was conditioned in a gas chromatograph injection port as recommended by the manufacturer. A magnetic stirrer (Roth RCT Basic, Germany) and 8 \times 3 mm stirring bars were used to mix the samples during extraction. The extraction was performed in 4 cm^3 vials (Supelco).

Standards

Pesticide standards, HCB (I), tefluthrin (II), heptachlor (III), aldrin (IV), chlorpyrifos (V), fen-thion (VI) and bifenthrin (VII), (Dr Ehrenstorfer, Germany) were of 96–99.5 % purity.

Stock standard solutions of 1 mg cm^{-3} of each pesticide were prepared in acetone (J. T. Baker, USA). Working standard mixed solutions were prepared by diluting the stock solution with aceto-

ne. Water standard solutions were used for all SPME measurements. Highly purified deionized water (Purelab Option-R7, Elga, UK) was used for diluting the acetone standard solutions.

Apparatus

A gas chromatograph/mass spectrometer (GC/MS) was used as the detection device (CP-3800/Saturn 2200, Varian, Australia). A 30 m \times 0.25 mm \times 0.25 μ m, VF-5ms column (Varian) was used. The injection port (1079 Universal capillary injector) temperature was set at 270 °C. After operating in the splitless mode for 9 min. (desorption time), the injector was set to the split mode (1:60). The GC was programmed as follows: initial temperature 120 °C, then increased to 170 °C at 10 °C min⁻¹ and held for 20 min, increased to 280 °C at 15 °C min⁻¹ and held for 2 min, increased to 290 °C at 10 °C min⁻¹ and held for 10 min. Helium was used as the carrier gas at a flow rate of 1.1 ml min⁻¹.

The ion trap mass spectrometer was operated in the electron impact/selected ion monitoring (EI/SIM) mode. The ion trap and transferline temperatures were set to 220 °C and 250 °C, respectively. One specific pesticide ion was selected for detection and quantification, while a second one was used for confirmation. The ions inspected were as follows: 284 (214) for HCB, 177 (141) for tefluthrin, 274 (272) for heptachlor, 66 (293) for aldrin, 314 (286) for chlorpyrifos, 278 (109) for fenitron and 181 (165) for bifenthrin.

Procedure (sample preparation and analysis)

In order to determine the optimum extraction temperature, a one-hour extraction procedure was performed in the temperature range from 23 to 90 °C with the standard aqueous solution at a concentration level of 15 ng cm⁻³ of each pesticide. A linearity test was performed in the concentration range from 0.05 to 40 ng cm⁻³. To confirm the proposed theoretical models, an aqueous standard solution of 10 ng cm⁻³ was used.

The aqueous standard solutions were prepared with an acetone content not higher than 1 % v/v, so as not to affect the extraction procedure.^{2,8-10} In all experiments, 4 cm³ vials were filled with 2 cm³ of the standard aqueous samples. Each sample was analyzed in triplicate.

RESULTS AND DISCUSSION

On comparing Eq. (15) developed in this work with the Ai equation obtained for non-steady-state mass transfer, it is evident that both equations have the same form with two exponential terms, clearly confirming the correctness of the approach applied. When the diffusion of the analyte in the fiber was considered as the rate determining step, Eq. (22) was obtained, referring to the HS/SPME at elevated temperatures. In the case of analyte evaporation from the sample as the rate determining step, Eq. (27) was the final solution describing the extraction process at ambient temperatures.

In order to determine the optimum extraction temperature for each of the studied pesticides, extraction-temperature profiles were obtained in a temperature range from 23 to 90 °C and presented in Fig. 1. Increasing the extraction temperature obviously enhanced the amount of analyte sorbed by the fiber, which may be explained by increasing values of k_1 and k_3 . In correlation with rapidly increasing values of k_2 and k_4 , the amount extracted decreased at temperatures exceeding 80 °C for most of the investigated pesticides. For most of the studied pesticides, the maximum amount extracted in a single multi-residue analysis was achieved within the 60–80 °C temperature range and 60 °C was identified as the general optimum extraction temperature.

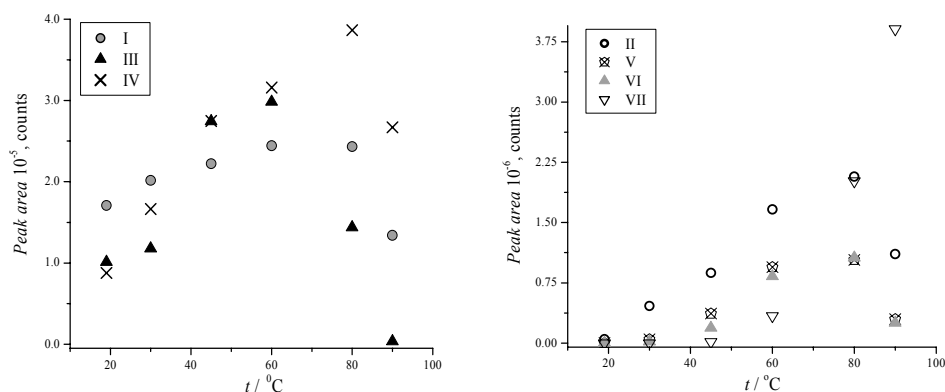


Fig. 1. HS/SPME-temperature profiles of the investigated pesticides (HCB (I), tefluthrin (II), heptachlor (III), aldrin (IV), chlorpyrifos (V), fenthion (VI) and bifenthrin (VII)); concentration: 15 ng cm^{-3} , extraction time: one hour.

The amounts of tefluthrin and aldrin extracted at $60 \text{ }^\circ\text{C}$ in relation to the extraction time are shown in Fig. 2. The obtained extraction time profiles had a shape well known in the literature and their dependences revealed a similar pattern for all the studied pesticides. Partition equilibrium was attained in periods up to 90 min. for all the studied pesticides, with the exception of bifenthrin.

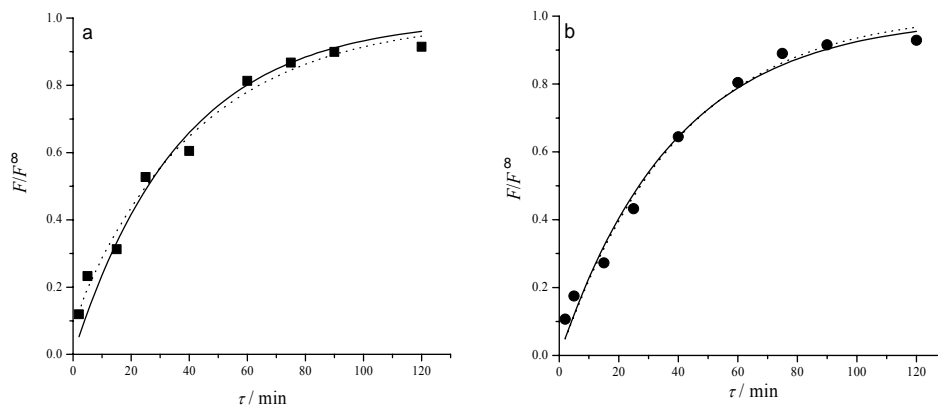


Fig. 2. HS/SPME-time profiles for a) tefluthrin and b) aldrin; extraction volume: 2 ml of aqueous standard solution, concentration: 10 ng cm^{-3} , mixing, temperature: $60 \text{ }^\circ\text{C}$. The solid and dotted lines represent the fits of Eqs. (15) and (22), respectively.

Using a standard fitting procedure (OriginPro 6.1), the experimental data given in Fig. 2 were fitted to both Eqs. (15) and (22). Evidently, the experimental time profiles can be successfully interpreted using both theoretical equations. From the fitting procedures, and according to Eqs. (11) and (12), the parameters p_1 , q_1 and p_2 were calculated and are listed in Table I. These parameters are dependent on the rate constants of the processes involved in the HS/SPME, and an increase

in temperature may be assumed to influence their increase. Evaporation of the analyte at the optimum extraction temperature becomes a very fast process and the model presented by Eq. (15) can be approximated with the simplified model given by Eq. (22).

TABLE I. List of parameters p and q derived from the experimental data fitted to Eqs. (15) and (22)

Pesticide	Eq. (15)		Eq. (22)
	$(p_1 \pm \Delta p_1) / \text{min}^{-1}$	$(q_1 \pm \Delta q_1) / \text{min}^{-2}$	$(p_2 \pm \Delta p_2) / \text{min}^{-1}$
HCB	0.453 ± 0.027	0.029 ± 0.006	0.103 ± 0.022
Tefluthrin	0.962 ± 0.043	0.023 ± 0.002	0.030 ± 0.002
Heptachlor	0.596 ± 0.089	0.024 ± 0.003	0.032 ± 0.003
Aldrin	0.026 ± 0.003	0.026 ± 0.003	0.026 ± 0.001
Chlorpyrifos	0.024 ± 0.002	0.024 ± 0.002	0.019 ± 0.001
Fenthion	0.013 ± 0.001	0.013 ± 0.001	0.0056 ± 0.0002

It is obvious from Eq. (15) that the amount of extracted analyte can be expressed as a function of extraction time in the form of two exponential terms. According to Eq. (14), α and β should be proportional to S_0 . Therefore, if t is held constant, $F \propto S_0$ in Eq. (15).

This relation is the key for quantitative analysis because it indicates that SPME quantification is possible before sorption equilibrium is attained. Also, having the same final form with a different parameter p included, the simplified models (Eqs. (22) and (27)) provide for quantification before absorption equilibrium is attained. Since partition equilibrium was attained within 90 min., practical application of the conclusion drawn was confirmed by relating the sorbed amounts to the initial analyte concentration in the sample over the 60-minute extraction time. Linear dependences, with regression coefficients ranging from 0.9895 to 0.9996, were obtained for pesticide concentrations in the ranges: 0.05–15 ng cm⁻³ (I), 0.05–25 ng cm⁻³ (II), 0.05–40 ng cm⁻³ (III), 0.05–40 ng cm⁻³ (IV), 0.05–40 ng cm⁻³ (V), 0.05–25 ng cm⁻³ (VI) and 0.05–15 ng cm⁻³ (VII). Relative standard deviation values for triplicate measurements were not higher than 19 %.

CONCLUSIONS

A kinetics-based theoretical treatment of the HS/SPME process was proposed. The same form of analytical expression as known from the literature was obtained. Simplified models, including analyte evaporation from the sample or analyte diffusion inside the fiber as the rate determining steps, were also presented. The HS/SPME experiments were performed with standard aqueous solutions of pesticides and the model developed successfully described the experimental data. Theoretical equations provide a linear relationship between the amount of analyte sorbed by the fiber and its initial concentration in the sample, enabling analyte quantification before sorption equilibrium is attained. The theoretical conclusion was confirmed experimentally by the linear dependences obtained for all the studied pesticides.

Acknowledgements: This work was part of the project No. TR-6890 B, supported by the Ministry of Science of the Republic of Serbia.

ИЗВОД

МИКРОЕКСТРАКЦИЈА У ЧВРСТОЈ ФАЗИ («HEADSPACE» ТИП) У АНАЛИЗИ
ОСТАТАКА ПЕСТИЦИДА – КИНЕТИКА И КВАНТИФИКАЦИЈА ПРЕ
УСПОСТАВЉАЊА ПАРТИЦИОНЕ РАВНОТЕЖЕРАДА ЂУРОВИЋ¹, МИРЈАНА МАРКОВИЋ¹ И ДРАГАН МАРКОВИЋ²

¹Институт за пестициде и заштитну животну средину, Банатска 316, 11080 Београд и ²Факултет за примењену екологију ФУТУРА, Универзитет Синџиџинум, Булевар Краља Александра 79, 11000 Београд

Нови приступ теоријском разматрању процеса микроекстракције у чврстој фази (HS/SPME) је предложен и примењен у анализи остатака пестицида у воденим растворима. Модел се базира на трансферу масе кроз границе фаза, узорак/гасна фаза и гасна фаза/SPME полимер. Предложени модел даје директну пропорционалност између количине анализата апсорбоване на SPME влакну и његове почетне концентрације у узорку. Добијени израз указује да је квантификација могућа и пре достизања партиционе равнотеже. Модел је тестиран на екстракцији пестицида који припадају различитим класама органских једињења и добијено је очекивано слагање. Такође, линеарне зависности сорбоване количине пестицида од њихове почетне концентрације у раствору су добијене за време екстракције краће од оног потребног за достизање апсорпционе равнотеже.

(Примљено 9. фебруара 2006, ревидирано 12. марта 2007)

REFERENCES

1. C. L. Arthur, J. Pawliszyn, *Anal. Chem.* **62** (1990) 2145
2. C. L. Arthur, L. M. Killam, K. D. Buchholz, J. Pawliszyn, *Anal. Chem.* **64** (1992) 1960
3. D. Louch, S. Motlagh, J. Pawliszyn, *Anal. Chem.* **64** (1992) 1187
4. Z. Zhang, J. Pawliszyn, *Anal. Chem.* **65** (1993) 1843
5. J. Ai, *Anal. Chem.* **69** (1997) 1230
6. J. Ai, *Anal. Chem.* **69** (1997) 3260
7. J. Ai, *Anal. Chem.* **70** (1998) 4822
8. L. Urruty, M. Montury, *J. Agric. Food Chem.* **44** (1996) 3871
9. R. Eisert, K. Levsen, *Fresenius J. Anal. Chem.* **351** (1995) 555
10. R. Eisert, K. Levsen, *J. Am. Soc. Mass Spectrom.* **6** (1995) 1119.



The characteristics of the air pollution of a transition economy city: the example of Belgrade

ALEKSANDRA M. ŽUJIĆ^{1*#}, BOJAN B. RADAK^{1#} and DRAGAN A. MARKOVIĆ^{2#}

¹*Vinča Institute of Nuclear Sciences, Laboratory for Physical Chemistry, P.O. Box 522, 11001 Belgrade and* ²*Faculty of Applied Ecology, Singidunum University, Bulevar Kralja Aleksandra 70, 11000 Belgrade, Serbia*

(Received 2 October 2006, revised 28 February 2007)

Abstract: The results of sulphur dioxide (SO₂), nitrogen dioxide (NO₂) and black smoke (BS) levels in the Belgrade metropolitan area, the only pollutants measured at almost all 20 monitoring stations set up in the area, were critically analysed, the most reliable ones select and the pollution characteristics were defined in these terms. Belgrade was found to have pollution typical for a city in economical transition – still high SO₂ and BS levels, with seasonal variation, while moderate NO₂ levels. This is discussed in terms of sources, as well as spatial and temporal distribution.

Keywords: urban air pollution, air quality, monitoring, Belgrade.

INTRODUCTION

Urban air pollution and its impact on urban air quality is a world-wide problem. It manifests itself differently in different regions depending on the economical, political, and technological developments, on the climate and topography and on the nature of the available energy sources. Although the air quality in European cities has generally improved in recent decades, air pollution is still considered a top priority environmental problem with both urban and large scale impacts. Air pollution in a developing urban area initially increases, passes through a maximum and then decreases when pollution abatement becomes effective.¹ Cities in the industrialized western world are in some respects at the last stage of this development. In transition economies, many cities are in the stabilization stage. In developing countries, the pollution levels are still rising.

In order to provide a database for determining the air quality in major metropolitan areas, to observe pollution trends in urban and non-urban areas and to assess the compliance or progress made towards meeting air quality standards, it is necessary to have a reliable air pollution monitoring network. The current urban Belgrade air monitoring features 20 monitoring stations belonging to two networks.

*Corresponding author. E-mail: zuic@vin.bg.ac.yu

Serbian Chemical Society member.

doi: 102298/JSC0709889Z

The objective of the present study was to analyse and characterise the air quality in the Belgrade metropolitan area in terms of the three most commonly monitored parameters, SO₂, NO₂, and BS, based on measurements from the official monitoring networks.

AIR POLLUTION MONITORING IN BELGRADE

Geography and climate

Belgrade (population about 1.6 million) is situated at the crossing of the communication paths between eastern and western Europe, on the Balkan Peninsula. It has grown around the banks of two rivers (Fig. 1), the Sava and the Danube, at their confluence, and has an average elevation of 116.75 m, with the characteristics of a hilly city. The Belgrade metropolitan area combines two different natural settings: the Pannonian Plain to the north and the hilly Šumadija to the south.

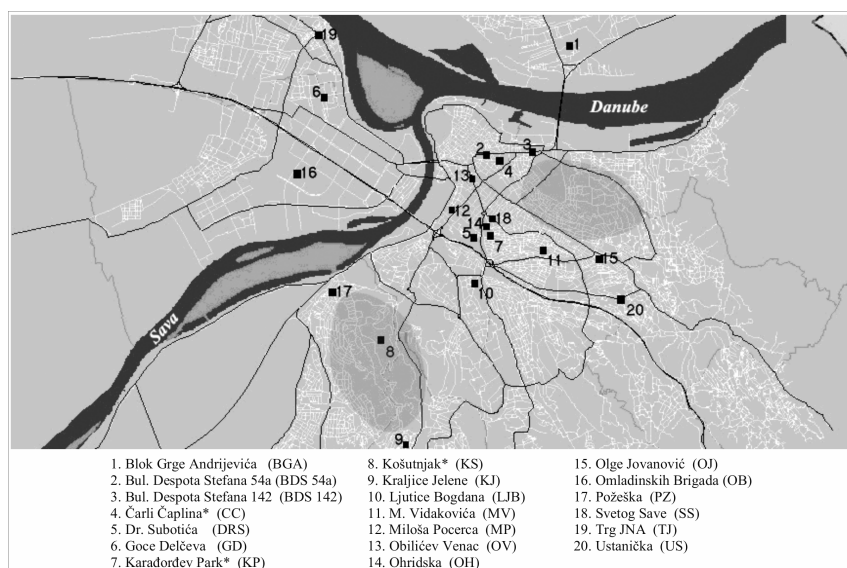


Fig. 1. Belgrade metropolitan area with the locations of the air-monitoring stations of IPH (unmarked) and HSRS (marked with *). Gray ellipses represent the major elevations of the terrain.

The climate is moderate continental, with four seasons; the average annual air temperature is 11.9 °C, January is the coldest month (average 0.4 °C) and July the hottest (average 21.7 °C); an annual average of 139 days with precipitation (annual average 667.9 mm).

As in many big cities, the Belgrade climate is characterised by the “heat island” phenomenon, where the central part of the city shows higher average temperatures (up to 3 °C) than its surroundings. During the winter months, lakes of cool air form in the lower parts of the city during nights, causing the phenomenon known as temperature inversion.²

Belgrade monitoring network

The monitoring of air pollution levels in Belgrade was established by the National Health Service in 1953 and was conducted by the Institute of Public Health (IPH). At this moment, there are 20 monitoring stations, combined between IPH (17 stations) and the Hydrometeorology Service of the Republic of Serbia (HSRS-3 stations), measuring various air pollutants. They are presented in Fig. 1. Of these stations, 14 are semi-automatic and 6 are automatic, with on-line monitoring since 2003 (BDS 54a, OH, OB, KP, CC, and KS in Fig. 1).

The monitoring stations are set up in five distinctive areas: central area with heavily saturated day traffic, mixed residential and industrial areas, primarily residential areas, prevailing industrial areas, landscape area with no traffic (urban background). The stations monitor various pollutants, but almost all of them monitor SO₂, NO₂, and BS.

EXPERIMENTAL

The semi-automatic stations collect samples as 24-hour averages and the pollutant concentrations are determined in the laboratory (SO₂ by the tetrachloromercurate (TCM) method ISO 4221, NO₂ by the triethanolamine (TEA) method ISO 6768 and BS by reflectometry of the collecting filter). The automatic monitors collect SO₂ and NO₂ samples continuously, analyse by ultraviolet (UV) fluorescence ISO 1996 and chemiluminescence ISO 1985, respectively, and generate values as 3 min or 30 min averages.

RESULTS AND DISCUSSION

Outline of the data

The observations are based on the daily averages of the concentrations of SO₂, NO₂, and BS in the period 2003–2005, inclusive. They were analysed in terms of temporal and spatial variations, which reveal characteristics and sources of the pollution.

Prior to detailed analyses, the whole body of available data of the 1999 – 2005 period was scrutinised for consistency and reliability. This revealed that most of the SO₂ data from the semi-automatic stations were not sufficiently reliable in the low concentration range, when the values fell below the detection limit of the employed TCM method. Also, in many cases, the semi-automatic stations gave generally lower values than the more reliable automatic stations. This is consistent with comparisons at Schauinsland, Germany.³ The stability of unprotected TCM samples is affected by temperature and light. This suggests that the data quality could be inconsistent across the sites. National comparisons in Germany showed that the TCM method gave slightly lower results than the impregnated filter method, even during winter. A national comparison in Turkey, February–November (1997), indicated that the low SO₂ results obtained by TCM may be caused by interference from ozone or some other oxidant.⁴ In addition, some semi-automatic SO₂ data do not even follow the real seasonal annual variation, or are a possible victim of the

arrangement of street canyon building.^{5,6} For these reasons, all further considerations involving SO₂ are based primarily on SO₂ data from the automatic stations. Excluded are the stations: BGA, BDS 142, KJ, LJB, OJ, SS, and US.

The data for NO₂ and BS show more overall consistency and no significant differences exist between the automatic and semi-automatic data.

Seasonal and spatial variations

The SO₂ data show very regular variability, with high concentrations in winter (October–March), the cold season, and a gradual decrease to minimum values in summer. Black smoke shows similar, albeit less expressed, seasonal changes. NO₂ does not show significant seasonal variations.

Since spatial variation of pollutants is expected over the whole area,^{7,8} the spatial distribution of the pollutants across a Belgrade street map was plotted using Golden Software Surfer (Version 6), a contouring and surface mapping software. The input data were the geographic coordinates of the stations and the average concentrations of the chosen pollutants at those locations during summer (June–August) and winter (October–March) in the period 2003–2005. Only the stations with reliable data in that period were included into the consideration, as discussed. This Surfer software creates contour maps which identify different ranges of data by automatically assigning a different colour to each data range. The most relevant features in the plots are the indications of maxima or minima defined by the iso-concentration curves.

Average SO₂ concentrations for summer and winter periods during 2003–2005 for the chosen stations are given in Table I. The summer data from stations OB, DRS, TJ, GD, and MV were not reliable enough to be taken into account, due to the reasons already discussed.

TABLE I. Average summer and winter SO₂ concentrations during 2003 – 2005 at the chosen monitoring stations

Station	BDS 54a	CC	KP	KS	OH	OB	DRS	TJ	GD	MV
Summer	17	30	35	25	49	*	*	*	*	*
Winter	73	83	149	45	141	33	101	28	19	50

The plots of SO₂ (Fig. 2) indicate that the maximum in winter months is concentrated around the area with several poorly filtered large heating systems near the centre of the city. In summer, the maximum is shifted more to the Industrial area near the Danube riverbank.

The data show that the SO₂ values exceed the limit value only during the winter season, almost exclusively in the central city zones.

The average NO₂ summer and winter concentrations for 2003–2005 were calculated from 14 monitoring stations (Table II).

The plots of NO₂ (Fig. 3) feature open iso-concentration curves in some parts, which may be an artefact due to lack of data in those parts, but the winter superpo-

sition (Fig. 3a) indicates the contribution of the district heating plants located more prevalently in the western parts of the city. This contribution is absent in summer (Fig. 3b), and the summer plot basically indicates the traffic density distribution.

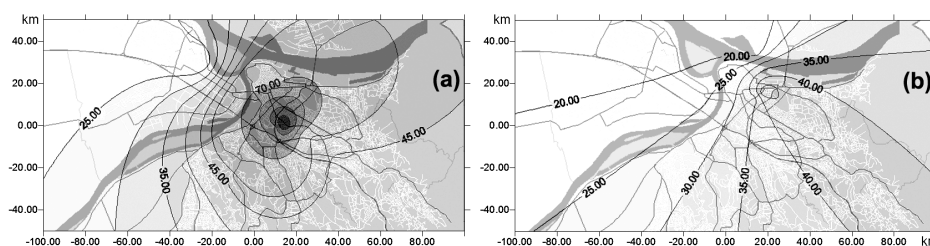


Fig. 2. Spatial distribution of SO_2 in (a) winter and (b) summer. Based on the measurements from the OB, KS, BDS 54a, CC, OH and KP stations (for the summer period) plus the DRS, TJ, GD and MV (for winter) stations, the iso-concentration lines are indicated in $\mu\text{g m}^{-3}$.

TABLE II. Average summer and winter NO_2 concentrations during 2003 – 2005 at the chosen monitoring stations

Station	BGA	BDS 54a	BDS 142	CC	KP	KS	MV	MP	OV	OH	OB	PZ	SS	TJ
Summer	11	34	29	24	22	21	30	42	31	38	16	24	22	35
Winter	13	48	33	21	34	18	26	35	31	74	35	26	24	34

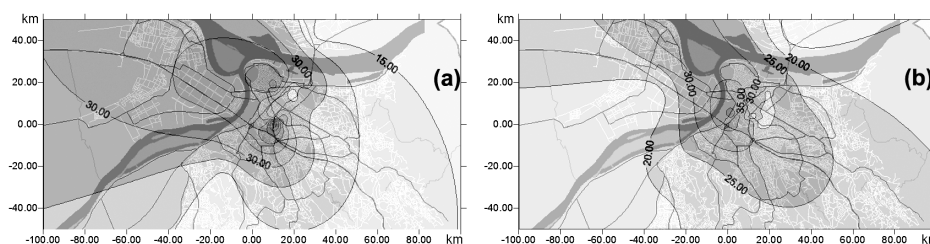


Fig. 3. Spatial distribution of NO_2 in (a) winter and (b) summer. Based on the measurements of the BGA, BDS142, MV, MP, OV, PZ, SS, TJ, OB, KS, BDS54a, CC, OH and KP stations, the iso-concentration lines are indicated in $\mu\text{g m}^{-3}$.

The NO_2 limits are rarely exceeded (1 % to 9 %, in Fig. 4). More do so during the heating season for stations near the district heating plants (OH, BDS 54a, KP, OV, OB), or in the non-heating season, the stations where traffic is the predominant source of NO_2 (MP, MV).

Both the winter and the summer plots of BS (Fig. 5a and 5b, respectively) show a clear “island” of “clean” air around the monitoring station KS, which is expected, as it is situated at an elevated urban background point. Generally, high BS concentrations seem to be confined to the lower parts of the city, where particulate matter naturally accumulates. That indicates natural and traffic sources of this pollution. High summer BS concentrations to the north from the main city area also indicate a strong natural source of this parameter – natural dust, which is quite present in the north, towards the Pannonian Plain. In winter, there is an

“island” of high BS pollution around the city centre, where most of the individual and poorly filtered heating sources are situated (Fig. 5a). In this period, district heating plants in the western parts of the area apparently add to the seasonal contribution as well.⁹

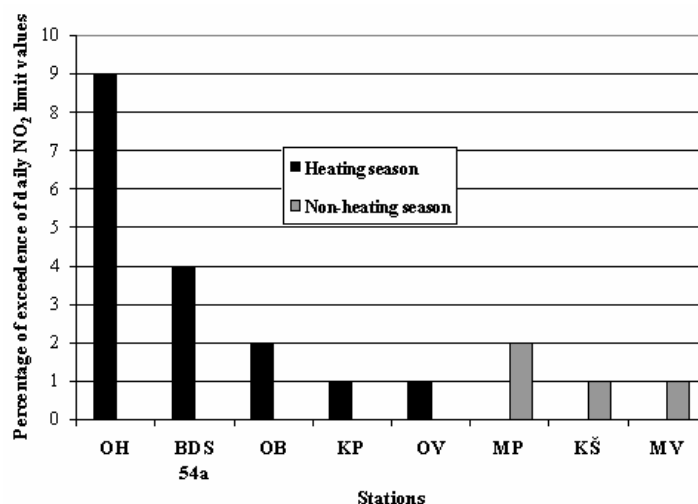


Fig. 4. Exceedence of daily the NO_2 limit values ($85 \mu\text{g m}^{-3}$) in 2005 during the heating and non-heating season.

The most extensive set of data was available for BS, which was measured at 17 locations in Belgrade (Table III).

This is in agreement with data on BS exceedences which show that in the heating season they occur in the central, northern, and western parts roughly twice as much as they do in the non-heating season. Heating is obviously still a major BS source in winter.

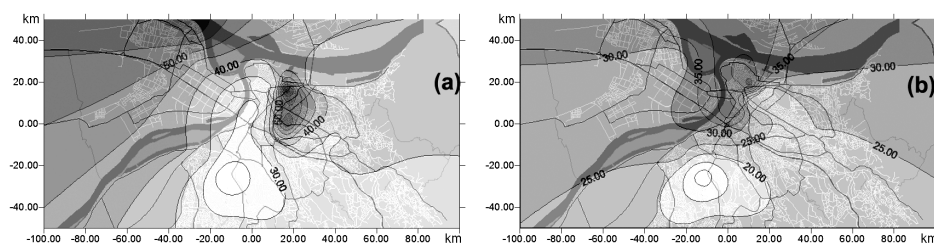


Fig. 5. Spatial distribution of BS in (a) winter and (b) summer. Based on the measurements of the BDS 142, DRS, GD, KJ, LJB, MV, MP, OV, OJ, PZ, SS, TJ, US, KS, BDS 54a, CC and KP stations, the iso-concentration lines are indicated in $\mu\text{g m}^{-3}$.

The situation is somewhat different at station BDS 54a, where the BS exceedence percentage is not significantly different in the two seasons and is even higher during the non-heating season. This is an indication that at this particular

spot, the dominant source of BS is traffic, which adds to the complexity of the BS sources. In order to shed more light onto the nature of the BS measurements, some available PM₁₀ (particles below diameter 10 µm) data were examined.

TABLE III. Average summer and winter BS concentrations during 2003 – 2005 at the chosen monitoring stations

Station	BDS 54a	BDS 142	CC	DRS	GD	KP	KS	KJ	LJBM	MP	OV	OJ	PZ	SS	TJ	US	
Summer	53	28	22	27	25	30	6	23	*	23	45	20	25	27	*	38	23
Winter	39	38	76	42	44	67	20	32	33	38	30	37	34	39	42	63	37

Unlike BS values, those of PM₁₀ show a great difference between the seasons, such that heating adds a significant contribution to the overall concentration of PM₁₀ particles. Some studies have shown that mineral based particles (diameter around 50 µm) originate from either combustion processes (*e.g.* lead compounds from gasoline engines) or from brake and clutch lining wear.¹⁰ These larger particles than 10 µm can appear in the material measured as BS, but not in the filtered PM₁₀ material. PM₁₀ particles mostly originate from various stationary combustion processes, transport, wind erosion, and resuspended road dust.¹¹ The results in Fig. 6 show that at this location the dominant source of PM₁₀ in winter is stationary combustion (heating). This means that PM₁₀ is here a better indicator of combustion processes than BS itself, which actually reflects traffic activity better.

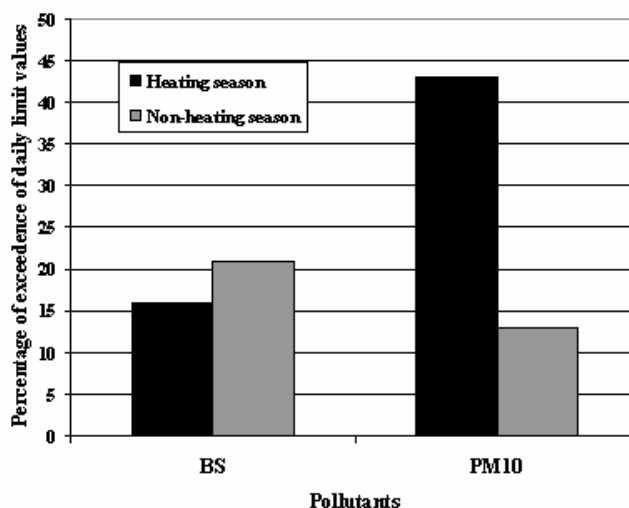


Fig. 6. Exceedence of the daily limit values for BS and PM₁₀ in 2005 during the heating and non-heating season at the BDS 54a station.

Comparisons with other European cities

In comparison to some other European cities, the Belgrade situation is apparently the worst in terms of SO₂ and BS levels, and moderate in terms of NO₂ le-

vels (Fig. 7).¹² Since SO₂ and BS are pollution parameters associated with outdated technologies, the situation reflects the lagging behind of technical developments of heating, industrial, and traffic practices in Belgrade. On the other hand, moderate NO₂ levels indicate that traffic is apparently still not as dense as in the more developed cities.

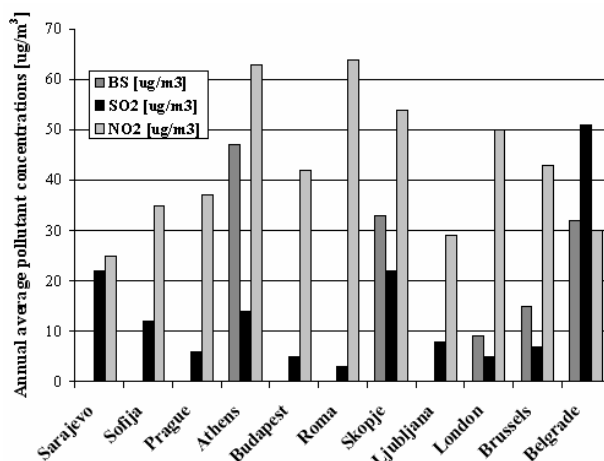


Fig. 7. Average annual BS, SO₂ and NO₂ concentrations in some European cities in 2004.

During the 1990s, the industrial “hot spots” shifted from western Europe to the central and eastern Europe (CEE), where heavy industry, use of low-quality fuels and outdated production technologies resulted in high emission levels. As a consequence, the emissions of NO_x and SO₂ per unit gross domestic product (GDP) in the CEE were more than 4 times higher, and emissions of particles and volatile organic compounds (VOC) considerably higher.¹³ A transition period characterized the second part of the 90s in the CEE countries, when a series of management procedures were introduced, such as closing inefficient industries and power plants, fuel switching from brown coal to natural gas, and the introduction of flue gas desulphurization. The result was significant air-quality improvements.¹⁴

The ratio of the concentrations NO_x/SO₂ is apparently an indicator of the structure of pollution.¹⁵ Nitrogen oxides are mainly produced by mobile sources, the role of which increases with the development of the economy. Simultaneously, the employment of sulphur-rich fuels typically decreases with modernisation of the technologies. Consequently, the value of this index significantly increases in urban areas with economic development. Cities in western Europe have a dominant traffic contribution to air pollution, and the resulting index has high values (Amsterdam, London, Helsinki, Milan, in Fig. 8). Cities of eastern and south-eastern Europe, which in the 1990s underwent rapid economic developments, show intermediate values of this index (Vilnius, Tallinn, Budapest, Prague, Warszawa, Ljubljana, Nicosia), whereas most of the Balkan cities (Skopje, Sofija, Sarajevo, Belgrade) show values below 5, typical of transition economy cities.

In most respects, air pollution in Belgrade has the characteristics of most East European cities in the past decade, of countries in transition in which economic conditions have a strong effect on the atmospheric environment (the quality of the car fleet and the types of environmental protection related to installations at stationary sources, as well as the type of home heating).¹⁶

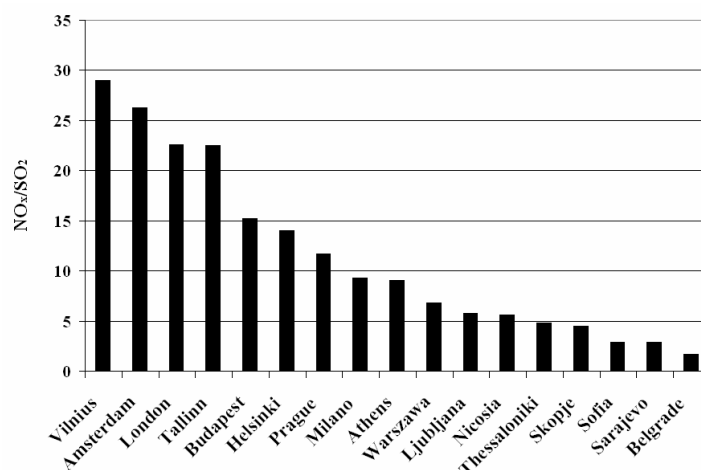


Fig. 8. Average annual concentration ratio of NO_x/SO₂ in some European cities in 2004.

CONCLUSIONS

Analysis of the data from twenty monitoring stations in the Belgrade metropolitan area showed that the TCM method used for SO₂ detection in the semi-automatic stations is quite unreliable, especially in the low concentration range. It follows that only the automatic stations can be trusted in this respect. This leaves only three reliable stations in the Institute of Public Health network, clearly indicating the need for modernisation of the equipment. Fortunately, the Hydrometeorology Service contributes to the available data with its additional three automatic stations.

The most significant characteristics of air-pollution in Belgrade are: high SO₂ and elevated BS pollution in the cold season, mainly caused by domestic heating; NO₂ pollution which follows the temporal and spatial variations of traffic emissions, with some seasonal contributions from heating; and indications of significant traffic and natural contributions to BS generally. It should be interesting to follow these indications by more detailed research which would answer important questions about the origin, and more importantly, characteristics and health impact capacity of the particulate matter in Belgrade generally, with possible mapping of the natural/anthropogenic influences across the whole area. Monitoring of the classical "Black Smoke" parameter obviously cannot answer these questions alone and has to be appended by monitoring parameters such as PM₁₀, PM_{2.5}, and PM₁, together with chemical analyses.

Since mapping requires inclusion of as many measuring points as possible, in the present study it was confined only to the pollutants monitored by all the available stations of the existing networks. Also, the obtained average concentration ratio of NO_x/SO_2 below the value of 5 clearly classifies Belgrade as a transition economy city.

Substitution individual heating with coal and heavy oil by gas district heating would help enable considerable decreases in the SO_2 and BS levels. Better traffic organisation should contribute to a lowering or containment of NO_2 levels, which are not so critical in comparison with other European cities.

Acknowledgements: This work was supported by the Serbian Ministry of Science and Environmental Protection, project No. 142065. We are also grateful to the Belgrade Institute of Public Health and Hydrometeorology Service of the Republic of Serbia for the data utilised in this study.

ИЗВОД

КАРАКТЕРИСТИКЕ АЕРОЗАГАЂЕЊА ГРАДОВА ЗЕМАЉА У ЕКОНОМСКОЈ ТРАНЗИЦИЈИ: ПРИМЕР БЕОГРАДА

АЛЕКСАНДРА М. ЖУЈИЋ¹, БОЈАН Б. РАДАК¹ и ДРАГАН А. МАРКОВИЋ²

¹Институт за нуклеарне науке Винча, Лабораторија за физичку хемију, п. бр. 522, 11001 Београд и

²Факултет за примењену еколозију, Универзитет Синџидунум, Булевар Краља Александра 70, 11000 Београд

У раду су критички анализирана мерења нивоа SO_2 , NO_2 и чађи на територији града Београда. Концентрације ових загађивача се мере на већини од 20 мерних станица мониторинг мреже постављене на широј територији града, од којих су одабране само оне најпоузданије и на основу тих мерења дефинисане су основне карактеристике аерозагађења у Београду. Нађено је да Београд карактерише аерозагађење типично за градове земаља са економијом у транзицији – високи нивои SO_2 и чађи који показују знатне сезонске варијације и умерено високи нивои NO_2 . Разматрани су извори, просторна и временска расподела ових аерополутаната.

(Примљено 2. октобра 2006, ревидирано 28. фебруара 2007)

REFERENCES

1. J. Fenger, *Atmos. Environ.* **33** (1999) 4880
2. S. Matic-Besarabic, S. Kostoski, *Air pollution in the Republic of Serbia 2000*, Republic of Serbia, Ministry of Health and Environmental Protection, Belgrade, 2001, p. 16
3. European Monitoring and Evaluation Programme (EMEP), EMEP/CCC-Report 6/2000. Kjeller, Norway, 1999, p. 22
4. European Monitoring and Evaluation Programme (EMEP), EMEP/CCC-Report 6/2003. Kjeller, Norway, 2003, p. 24
5. K. Kemp, F. Palmgren, *Sci. Total Environ.* **189/190** (1996) 33
6. P. Mestayer, R. Almbauer, O. Tehepel, in *SATURN-Studying Atmospheric Pollution in Urban Areas – Final Report*, N. Moussiopoulos, Ed., Springer, Berlin, 2003, p. 53
7. P. Kassomenos, A. N. Skouloudis, S. Lykoudis, H. A. Flocas, *Atmos. Environ.* **33** (1999) 1868
8. L. Morawska, D. Vishvakarman, K. Mengersen, S. Thomas, *Atmos. Environ.* **36** (2002) 3545
9. S. Matic-Besarabic, M. Gojkovic, V. Dudic, G. Pantelic, in *The Quality of the Environment of the City of Belgrade*, M. Grubacevic, R. Mijić, M. Tanasković, U. Miloradović, Eds., Regional Environmental Centre, Belgrade, 2006, p. 60

10. Z. Samaras, S. C. Sorensen, in *Urban Air Pollution: European Aspects*, J. Fenger, O. Hertel, F. Palmgren, Eds., Kluwer Academic Publishers, Dordrecht, 1998, p. 72
11. H. Horvath, in *Urban air pollution: European aspects*, J. Fenger, O. Hertel, F. Palmgren, Eds., Kluwer Academic Publishers, Dordrecht, 1998, p. 161
12. Airbase (2006), *European Topic Centre of Air and Climate Change*, <http://air-climate.eu.int/databases>. Data downloaded in April 2006
13. J. C. Bollen, J. P. Hettelingh, R. J. M. Maas, *Scenarios for economy and environment in Central and Eastern Europe*, RIVM report no. 481505002, Netherlands Institute of Public Health and the Environment, 1996
14. H. A. Bridgman, T. D. Davies, T. Jickells, I. Hunova, K. Tovey, K. Bridges, V. Surapipith, *Atmos. Environ.* **36** (2002) 3388
15. V. Kimmel, H. Tammet, T. Truuts, *Atmos. Environ.* **36** (2002) 4142
16. L. Bozo, H. Eerens, S. Larssen, M. M. Millan, N. Moussiopoulus, S. Papalexiou, Z. Samaras in *Urban air pollution: European aspects*, J. Fenger, O. Hertel, F. Palmgren, Eds., Kluwer Academic Publishers, Dordrecht, 1998, p. 457.



Thermodynamics and phase diagram calculation of some sections in the Ag–Bi–Sn system

DRAGANA ŽIVKOVIĆ^{1*#}, IWAO KATAYAMA², DRAGAN MANASIJEVIĆ^{1#},
HIROMI YAMASHITA² and NADA ŠTRBAC^{1#}

¹University of Belgrade, Technical Faculty, Bor, Serbia and ²Osaka University,
Graduate School of Engineering, Osaka, Japan

(Received 9 February 2007)

Abstract: The thermodynamic properties and characteristic phase diagrams of some sections in the Ag–Bi–Sn system were calculated. The thermodynamic functions, such as Gibbs excess energy, activity and enthalpy of formation, were calculated using the RKM model and compared with experimental data reported in the literature. Iso-activity diagrams for all three components at 900 K have been constructed. The calculated phase diagrams of the vertical sections Sn–AgBi, Ag–BiSn and Bi–AgSn, obtained using the ThermoCalc program, were compared and confirmed with the results of DTA measurements from the present work.

Keywords: thermodynamics, phase diagrams, ternary alloys, Ag–Bi–Sn system, lead-free solders.

INTRODUCTION

Although originally commenced as an environmental issue, lead-free soldering is rapidly evolving into an important issue for the worldwide electronic industry.^{1,2} A contribution to this topic at the European level has been given in the frame of the COST 531 Action “Lead-free solder materials”,³ during which, based on a recent version 4.4 SGTE,⁴ a new thermodynamic database for lead-free solder alloys was developed.⁵ It also contains data for carefully tested binary phase diagrams, suitable for the prediction of phase equilibria in multicomponent solder systems.

Among the lead-free solder alternatives for surface mount assembly, systems based on Ag–Sn were considered as the most promising. Especially the Ag–Bi–Sn system was determined to be a very applicable one, since its solderability was positively assessed among a range of lead-free alloys.²

Considering the thermodynamic description of the Ag–Bi–Sn system, there are few papers dealing with experimental investigations of thermodynamics properties of the ternary Ag–Bi–Sn system. Hassam *et al.*⁶ determined mixing enthal-

* Corresponding author. E-mail: dzivkovic@tf.bor.ac.yu

Serbian Chemical Society member.

doi: 10.2298/JSC0709901Z

pies of liquid alloys by direct reaction calorimetry. Recently, Katayama *et al.*⁷ measured activities of tin using the fused salt EMF method.

A thermodynamic optimization of the Ag–Bi–Sn ternary system, was performed by Zabdyr *et al.*,⁵ while a phase equilibria investigation of this system was presented by Ohtani *et al.*,⁸ who established that the investigated system includes three ternary invariant reactions – two ternary transitory peritectics at 263.6 °C and 262.5 °C, and one ternary eutectic at 139.2 °C.

In this work, the results of a calculation of the thermodynamic properties and phase diagram in the chosen sections of the Ag–Bi–Sn system are compared with experimental DTA data, from this work and the literature, as a contribution to more complete comprehension of the thermodynamics and phase equilibria of this ternary system.

Theoretical fundamentals

The Gibbs energies of liquid and substitutional solid phases in ternary system are described by the sub-regular solution model with the Redlich–Kister–Muggianu model⁹ as follows:

$$G_m^\phi = \sum_{i=1}^3 x_i^\phi G_i^\phi + RT \sum_{i=1}^3 x_i^\phi \ln x_i^\phi + G^E(T, x_2) \quad (1)$$

$$G^E(T, x_2) = x_1^\phi x_2^\phi L_{1,2}^\phi + x_2^\phi x_3^\phi L_{2,3}^\phi + x_3^\phi x_1^\phi L_{1,3}^\phi + x_1^\phi x_2^\phi x_3^\phi L_{1,2,3}^\phi \quad (2)$$

where $L_{1,2}^\phi, L_{2,3}^\phi, L_{1,3}^\phi$ are binary temperature-dependent interaction parameters, and $L_{1,2,3}^\phi$ presents the ternary interaction parameter, expressed in the form:

$$L_{1,2,3}^\phi = x_1 L_{123}^0 + x_2 L_{123}^1 + x_3 L_{123}^2 \quad (3)$$

and optimized on the basis of the available thermodynamic and phase diagram data.

EXPERIMENTAL

Alloys of the Ag–Bi–Sn system were prepared from the pure metals (99.999 %) by melting together weighed amounts of tin, silver and bismuth in evacuated and sealed quartz tubes. After melting, the samples were annealed at 300 °C for 200 h and slowly cooled inside the furnace to room temperature.

The DTA measurements were performed using a Derivatograph (MOM Budapest) apparatus equipped with a Pt/Pt 10 % Rh thermocouples under the following conditions: air atmosphere, heating rate 5 K min⁻¹ using sintered Al₂O₃ as the reference specimen.

RESULTS AND DISCUSSION

Starting data

The basic data for the calculation of the thermodynamic properties and the phase diagrams were the optimized thermodynamic parameters for the Ag–Bi–Sn system compiled elsewhere,⁵ including all binary subsystems, *i.e.*, Ag–Sn,¹⁰ Ag–Bi^{11,12} and Bi–Sn.^{13,14}

The pure solid elements at 298.15 K and 1 bar in their stable form were chosen as the reference state for the systems (SER) and, therefore, Version 4.4 of the

SGTE Unary Database (Scientific Group Thermodata Europe) of the phase stabilities for the stable and metastable states of pure elements² was employed.

The following phases from the constitutive binary subsystems, considered in the COST 531 Database⁵ and presented in Table I, were used in the calculations in this work: liquid phase, the Sn-rich bct phase (denoted as BCT_A5), the Ag-rich fcc phase (denoted as FCC_A1), the Bi-rich rhombohedral phase (denoted as RHOMBOHEDRAL_A7), the orthorhombic order structure Ag₃Sn (denoted as AGSB_ORTHO) and the hcp phase (denoted as HCP_A3).

TABLE I. Optimized thermodynamic parameters for the Sn–Ag–Bi ternary system from the literature⁵

LIQUID	
EXCESS MODEL IS REDLICH-KISTER_MUGGIANU	
CONSTITUENTS: AG,BI,SN	
L(LIQUID,AG,BI;0)	=+3340.81+39.16749*T-5.969876*T*LN(T)
L(LIQUID,AG,BI;1)	= -5485.45-1.07133*T
L(LIQUID,AG,BI;2)	= -3055.34+1.77449*T
L(LIQUID,AG,SN;0)	= -399.49-31.42004*T+3.081837*T*LN(T)
L(LIQUID,AG,SN;1)	= -18150.65+5.87501*T
L(LIQUID,AG,SN;2)	= -12009.03+5.18355*T
L(LIQUID,BI,SN;0)	=+500+1.5*T
L(LIQUID,BI,SN;1)	=-100-0.135*T
L(LIQUID,AG,BI,SN;0)	= +4093.27+63.407508*T
L(LIQUID,AG,BI,SN;1)	= +11188.52-8.978544*T
L(LIQUID,AG,BI,SN;2)	=+17072.3-21.742545*T
AGSB_ORTHO	
2 SUBLATTICES, SITES .75: .25	
CONSTITUENTS: AG : AG,BI,SN	
G(AGSB_ORTHO,AG:AG;0)-H298(FCC_A1,AG;0)	=+GHSERAG+4750-0.5*T (298.14<T<3000.00)
G(AGSB_ORTHO,AG:BI;0)-0.75 H298(FCC_A1,AG;0)-0.25 H298(RHOMBOHEDRAL_A7,BI;0)	=+0.75*GHSERAG+0.25*GHSERBI+5 (298.14<T<3000.00)
G(AGSB_ORTHO,AG:SN;0)-0.75 H298(FCC_A1,AG;0)-0.25 H298(BCT_A5,SN;0)	= -11085.3+110.01471*T-23.18*T*LN(T)-0.00359*T ² +4389.5*T ⁽⁻¹⁾
L(AGSB_ORTHO,AG:AG,BI;0)	= 0.0
L(AGSB_ORTHO,AG:AG,SN;0)	= 0.0
L(AGSB_ORTHO,AG:BI,SN;0)	= -1000
FCC_A1	
2 SUBLATTICES, SITES 1: 1	
CONSTITUENTS: AG,BI,SN : VA	
L(FCC_A1,AG,BI:VA;0)	=+25077.78-12.05475*T
L(FCC_A1,AG,SN:VA;0)	= +745.45+11.498027*T
L(FCC_A1,AG,SN:VA;1)	= -36541.5
L(FCC_A1,BI,SN:VA;0)	= 2000

TABLE I. Continued

HCP_A3 2 SUBLATTICES, SITES 1: .5 CONSTITUENTS: AG,BI,SN : VA
L(HCP_A3,AG,BI,VA;0) = +25077.78-12.05475*T L(HCP_A3,AG,BI,SN:VA;0) = 50000 L(HCP_A3,AG,SN:VA;0) = +1046.1+10.23693*T L(HCP_A3,AG,SN:VA;1) = -40505.5 L(HCP_A3,BI,SN:VA;0) = 2000
BCT_A5 1 SUBLATTICE CONSTITUENTS: AG,BI,SN
L(BCT_A5,AG,BI;0) = +25077.78-12.05475*T L(BCT_A5,AG,SN;0) = 18358.8 L(BCT_A5,BI,SN;0) = +3500-1.038*T L(BCT_A5,BI,SN;1) = -3710
RHOMBOHEDRAL_A7 EXCESS MODEL IS REDLICH-KISTER_MUGGIANU CONSTITUENTS: BI,SN
L(RHOMBOHEDRAL_A7,BI,SN;0) = +19720-22.6*T L(RHOMBOHEDRAL_A7,BI,SN;1) = -5760+11.834*T

Calculation of the thermodynamic properties of liquid Ag–Bi–Sn alloys

Katayama *et al.*⁷ recently measured the activity of tin using the fused salt EMF method at 900 K along the isoconcentration sections of Sn ($x_{Ag}/x_{Bi} = 1/3, 1/1$ and $3/1$). Based on these results, the concentration dependences of the excess Gibbs energy of mixing were obtained using the Darken Equation.¹⁵ These experimentally based results were used for comparison with the data from the present work, which were calculated using the optimized thermodynamic parameters for the constitutive binary systems. The excess Gibbs energies of mixing at 900 K for the ternary Ag–Bi–Sn system were calculated on the basis of the Redlich–Kister–Muggianu Model⁹ from the binary data only and using ternary parameters from the literature.⁵ Comparison between the Gibbs energy calculated from the binary prediction using ternary parameters and the experimental results⁸ is shown in Fig. 1.

It may be seen that experimental data could be thermodynamically very well described using ternary interaction parameters in the calculation procedure. Binary prediction alone did not give satisfactory results. The same trend of good agreement between the results calculated in this work and experimental data⁷ is shown in Fig. 2, in which the activities in three investigated isoconcentration sections from the tin corner with $x_{Ag}/x_{Bi} = 1/3, 1/1$ and $3/1$ at 900 K are presented.

Fair agreement between the experimental and the calculated values is observed for all the studied compositions. The calculated isoactivity curves at 900 K for every component are shown in Fig. 3.

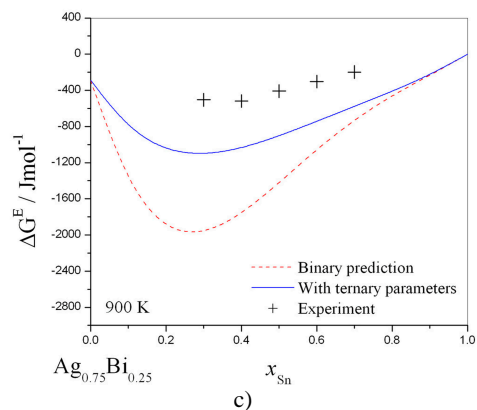
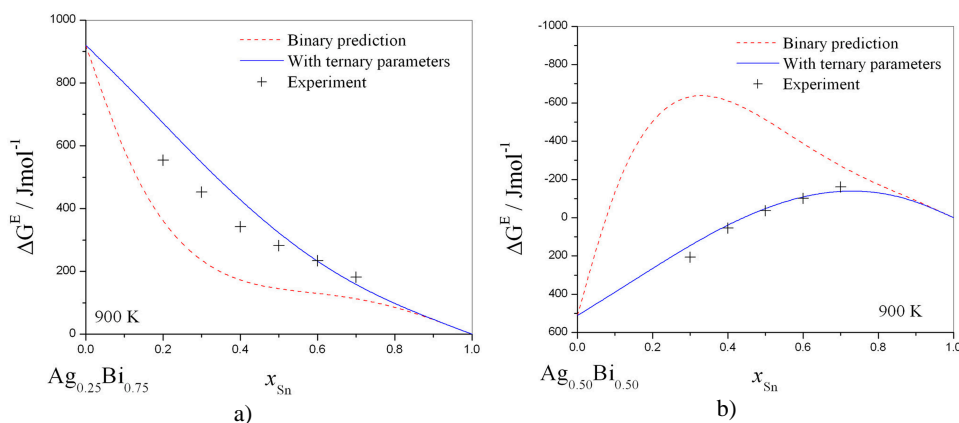


Fig. 1. Calculated and experimental integral molar Gibbs excess energy⁷ concentration dependences based on Calphad calculations and derived from experimental measurements for isoconcentration section from tin corner at 900 K with: a) $x_{Ag}/x_{Bi} = 1/3$; b) $x_{Ag}/x_{Bi} = 1/1$; c) $x_{Ag}/x_{Bi} = 3/1$.

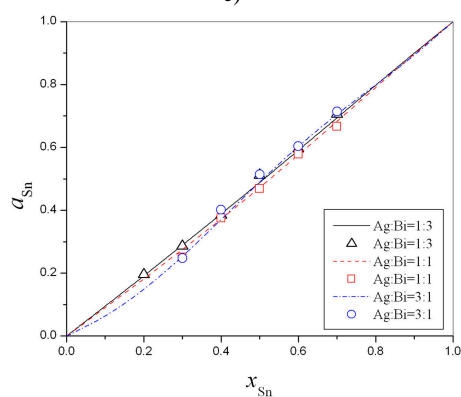


Fig. 2. Comparison of calculated tin activity (lines) and experimental values⁷ (symbols) in the Ag–Bi–Sn system at 900 K.

Furthermore, mixing enthalpies for some alloys in the Ag–Bi–Sn system were calculated and compared with mixing enthalpies of liquid alloys experimentally determined using direct reaction calorimetry.⁶ The results of the comparison between the enthalpies of formation calculated using ternary parameters and experimental values determined at 878 K (for two sections with molar ratio of $x_{Ag}/x_{Bi} = 1/3$ and $x_{Bi}/x_{Sn} = 1/3$), showing fair mutual agreement, are shown in Fig. 4.

mental values determined at 878 K (for two sections with molar ratio of $x_{Ag}/x_{Bi} = 1/3$ and $x_{Bi}/x_{Sn} = 1/3$), showing fair mutual agreement, are shown in Fig. 4.

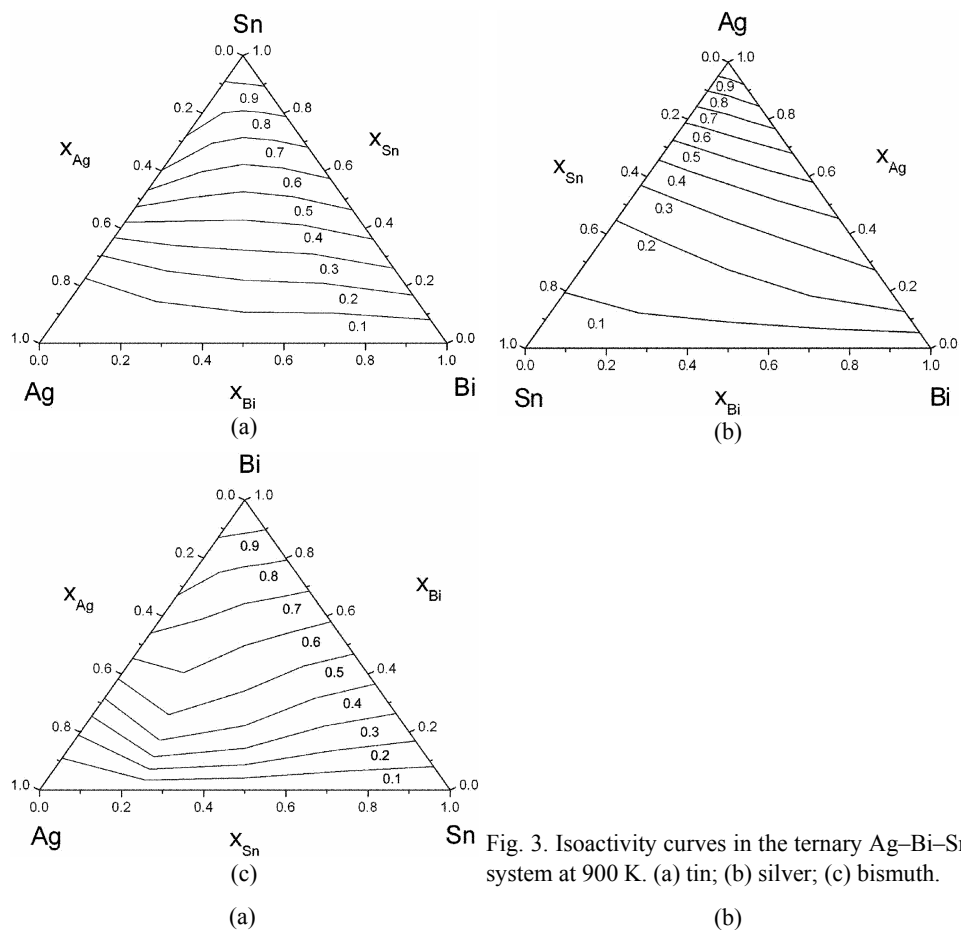


Fig. 3. Isoactivity curves in the ternary Ag–Bi–Sn system at 900 K. (a) tin; (b) silver; (c) bismuth.

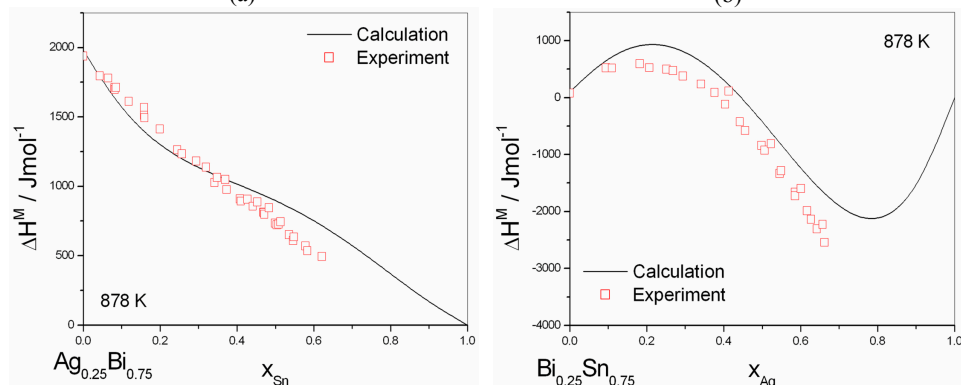


Fig. 4. Enthalpy of formation of Ag–Bi–Sn liquid alloys at the section of: a) $x_{Ag}/x_{Bi} = 1/3$; b) $x_{Bi}/x_{Sn} = 1/3$.

Investigation of the phase equilibria of the Ag–Bi–Sn ternary system

The phase diagrams for three vertical sections in this ternary system, Sn–AgBi, Ag–BiSn and Bi–AgSn, were calculated using optimized thermodynamic parameters⁵ from Table I. DTA measurements were used to check and confirm the calculated phase boundaries. The experimental results of thermal analysis, including the characteristic temperatures of the endothermic peaks, which occur during heating of the investigated samples in the three chosen sections, are presented in Table II.

TABLE II. The temperatures of liquidus and other phase transformations obtained by DTA for the samples in Ag–Bi–Sn system

Sample composition at. %	Temperature of the DTA peak / K	
	Liquidus	Other phase transformations
Ag:Bi=1:1		
Sn10Ag45Bi45	505	262
Sn20Ag40Bi40	495	136, 243, 411
Sn40Ag30Bi30	443	137, 167
Sn60Ag20Bi20	401	138, 172
Sn80Ag10Bi10	312	137, 194
Bi:Sn=1:1		
Sn45Ag10Bi45	381	139
Sn35Ag30Bi35	444	140, 180
Sn25Ag50Bi25	482	139, 183
Sn20Ag60Bi20	537	260, 373
Sn15Ag70Bi15	558	262
Sn5Ag90Bi5	814	–
Ag:Sn=1:1		
Sn45Ag45Bi10	481	138, 164
Sn35Ag35Bi30	485	138, 167
Sn25Ag25Bi50	476	139, 205
Sn15Ag15Bi70	428	139, 260
Sn5Ag5Bi90	271	141

The phase diagrams for three sections in the investigated system, Sn–AgBi, Ag–BiSn and Bi–AgSn, calculated using ThermoCalc software¹⁶ and including the obtained DTA results, are presented in Fig. 5.

As can be seen in Fig. 5, there is a good agreement between the calculated phase diagrams of the investigated sections and the experimental results obtained by DTA.

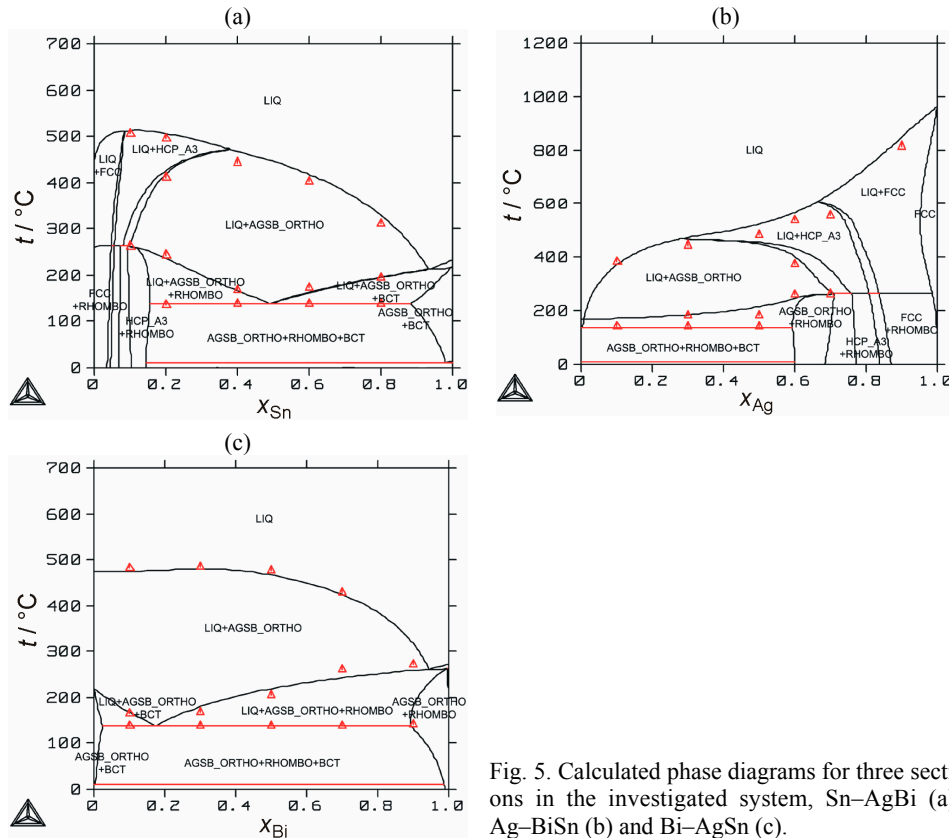


Fig. 5. Calculated phase diagrams for three sections in the investigated system, Sn–AgBi (a), Ag–BiSn (b) and Bi–AgSn (c).

CONCLUSIONS

The results of the calculation of thermodynamic properties and phase diagram in the Ag–Bi–Sn system are presented in this paper. The Gibbs excess energy was calculated using the Redlich–Kister–Muggianu model from binary data only and by applying a ternary correction term, using starting data given in the literature.⁵ It was shown that the ternary term significantly improves the agreement between the calculated and experimental-based results. The calculated results were compared with available experimental data reported in the literature. The phase diagrams for the vertical sections Sn–AgBi, Ag–BiSn and Bi–AgSn were calculated using ThermoCalc software. The calculated phase diagrams were compared with experimental DTA data from the present study. Good mutual agreement was noticed.

Acknowledgement: The authors from Serbia gratefully acknowledge the support of the Ministry of Science of the Republic of Serbia, under Project No.142043. This work was also conducted in the frame of the European action COST 531 on lead-free solder materials.

ИЗВОД

ПРОРАЧУН ТЕРМОДИНАМИЧКИХ ВЕЛИЧИНА И ФАЗНИХ ДИЈАГРАМА
У НЕКИМ ПРЕСЕЦИМА Ag–Bi–Sn СИСТЕМА

ДРАГАНА ЖИВКОВИЋ¹, IWAO KATAYAMA², ДРАГАН МАНАСИЈЕВИЋ¹,
HIROMI YAMASHITA² и НАДА ШТРБАЦ¹

¹Технички факултет, Универзитет у Београду, ВЈ 12, 19210 Бор и

²Osaka University, Graduate School of Engineering, Osaka, Japan

У раду је извршен прорачун термодинамичких величина и фазних дијаграма у неким пресецима Ag–Bi–Sn система. Термодинамичке функције су прорачунате применом RKM модела и упоређене са експерименталним резултатима из литературе. Дијаграми изо-активних линија су конструисани за све три компоненте на 900 К. Прорачунати фазни дијаграми вертикалних пресека Sn–AgBi, Ag–BiSn и Bi–AgSn применом ThermoCalc програма су упоређени и потврђени резултатима ДТА мерења из овог рада.

(Примљено 9. фебруара 2007)

REFERENCES

1. http://www.pb-free.com/ica_authored_papers/low_alpha_solders.pdf
2. N. C. Lee, *Adv. Microelectronics* **26** (1999) 29
3. <http://www.univie.ac.at/cost531>
4. Version 4.4 SGTE Unary Database. (<http://www.sgte.org>)
5. A. T. Dinsdale, A. Kroupa, J. Vizdal, J. Vrestal, A. Watson, A. Zemanova: COST531 Database for Lead-free Solders, Ver. 2.0, (2006)
6. S. Hassam, M. Gambino, J. P. Bros, *Z. Metallknd.* **85** (1994) 460
7. I. Katayama, T. Tanaka, S. Akai, K. Yamazaki, T. Iida, *Mater. Sci. Forum* **502** (2005) 129
8. H. Ohtani, I. Satoh, M. Miyashita, K. Ishida, *Mater. Trans. JIM* **42** (2001) 722
9. O. Redlich, A. T. Kister, *Ind. Eng. Chem.* **24** (1948) 345
10. C. S. Oh, J. H. Shim, B. J. Lee, D. N. Lee, *J. Alloys Comp.* **238** (1996) 155
11. B. Zimmerman, *Optimisation by experimental and calculation of the binary and ternary systems of Ag, Bi, Pb and Tl*, PhD Thesis, University of Stuttgart, 1976
12. H. L. Lukas, B. Zimmermann: Unpublished Work, 1998
13. H. Ohtani, K. Ishida, *J. Electronic Mater.* **23** (1994) 74
14. D. Malakhov, X. J. Liu, I. Ohnuma, R. Kainuma, H. Ohtani, K. Ishida, *Mater. Trans.* **43** (2002) 1879
15. L. S. Darken, *J. Am. Chem. Soc.* **72** (1950) 2909
16. www.thermocalc.se (ThermoCalc TC4A – Version 2.0, ©1993-1998 Foundation of Computational Thermodynamics, ThermoCalc AB, 1998).



Influence of grain size on chalcopyrite ore leaching in acidic medium

M. M. ANTONIJEVIĆ*, G. D. BOGDANOVIĆ, S. M. ŠERBULA and S. M. MILIĆ

University of Belgrade, Technical Faculty Bor, Department of Chemistry and
Chemical Technology, P.O. Box 50, 19210 Bor, Serbia

(Received 3 October 2006, revised 14 March 2007)

Abstract: This work presents an investigation of column leaching of a chalcopyrite ore using sulphuric acid where dissolved oxygen and iron(III) ions play the role of oxidants. The investigations were carried out in PVC columns, diameter 110 mm and height 1000 mm, by percolation of the leaching solution through the ore layer. The influence of ore grain size on the degree of leaching and acid consumption was examined. The formation of gypsum on limestone results in the comminution of the initial raw material during leaching. The grain size of chalcopyrite was found to have no important influence on the leaching rate of copper. A higher consumption of sulphuric acid was found for the fractions (–3+1) mm, (–5+0) mm and (–5+3) mm than for the fractions (–10+5) mm, (–20+10) mm and (–20+0) mm.

Keywords: chalcopyrite ore, column leaching, grain size.

INTRODUCTION

Classic methods of copper recovery from chalcopyrite ores are associated with the formation of large quantities of out-of-balance raw materials. Further treatment of such raw materials and copper recovery from them is possible by leaching these minerals and subsequent copper extraction from the leaching solutions. Leaching of such out-of-balance raw materials is carried out on heaps, dumps and *in situ*. Both oxide and sulphide copper ores are leached, whereby acid leaching^{1,2} and bioleaching^{3–6} are the most often employed methods. However, if CuFeS_2 is the most common copper mineral in the dumps and heaps, the leaching rate is lower than for other minerals because this mineral is not very reactive. Due to this, stronger oxidants have to be used for the decomposition of chalcopyrite. On the laboratory scale, for this purpose, strong oxidants have to be employed, such as: chlorine,⁷ nitric acid,⁸ ozone,⁹ and chromium(VI)^{10,11} but, decomposition of chalcopyrite may also occur in the presence of some weak oxidants, *i.e.*, iron(III)^{12–15} and oxygen,¹⁶ which are more favourable for direct use.

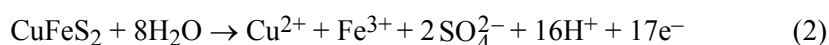
* Corresponding author. E-mail: mantonijevic@tf.bor.ac.yu
doi: 10.2298/JSC0709911A

Previous investigations have shown that the oxidation process of chalcopyrite is very complex, where dissolution is assumed to occur *via* the following Equations:¹⁷

– oxidation to elementary sulphur



– oxidation to sulphate



For potential values > 700 mV, massive dissolution of the chalcopyrite occurred according to Eq. (1) or (2).¹⁸ Oxygen and Fe^{3+} ion can oxidize the mineral because the redox pairs $\text{O}_2/\text{H}_2\text{O}$ ($\text{O}_2(\text{g}) + 4\text{H}^+ + 4\text{e}^- \rightarrow 2\text{H}_2\text{O}$) and $\text{Fe}^{3+}/\text{Fe}^{2+}$ ($\text{Fe}^{3+} + \text{e}^- \rightarrow \text{Fe}^{2+}$) have a standard redox potential of 1.23 V and 0.77 V, respectively.

Both, elementary sulphur and sulphates may be obtained as the final products of chalcopyrite oxidation. Sulphur formation retards the dissolution of this mineral due to passivation.^{19–22} Many factors influence the dissolution rate: the nature of the passive layer,¹⁴ galvanic interactions on the surface of the mineral,^{23,24} activation of the mineral,²⁵ particle size,^{26,27} *etc.* Using electrochemical methods, important data were obtained and employed to explain the behaviour of chalcopyrite in solution (the nature and existence of a passive layer, the influence of reactants on the dissolution rate, *etc.*), indicating the complexity of the chalcopyrite oxidation process.^{28–31}

In this work, the oxidation of chalcopyrite ore from the Bor River ore body was analysed using sulphuric acid solutions as the leaching solution and dissolved oxygen as the oxidant, as well as the iron(III) formed during the leaching. The influence of grain size on the dissolution rate of chalcopyrite was investigated using sulphuric acid solutions (pH 1.0) at a solid/liquid ratio of 1:1. The experiments were performed in columns by percolation of the leaching solution through the ore. In addition to the content of copper, those of iron, silicon, aluminium, magnesium and calcium were determined in the leaching solutions. The untreated sample and the solid residues obtained after the leaching process were analysed by X-ray diffraction analysis.

EXPERIMENTAL

Material

Samples for laboratory investigation were taken from the Bor River ore body, East Serbia. The sample was crushed to $(-20+0)$ mm and samples for study were prepared by additional crushing and sieving. The following fractions were used in this study: $(-3+1)$ mm, $(-5+3)$ mm, $(-5+0)$ mm, $(-10+5)$ mm, $(-20+10)$ mm and $(-20+0)$ mm. The results of the chemical analyses of the ore samples of various size ranges are presented in Table I.

The grain size distributions of an untreated and treated sample within the size range of $(-20+0)$ mm are presented in Fig. 1.

It was estimated using mineralogical and X-ray analysis of the samples that the most common copper mineral was chalcopyrite and pyrite, whereby the ratio of chalcopyrite/pyrite 1:3. Based on

qualitative mineralogical analyses, the amounts of magnetite, hematite, rutile, leucoxene and limonite, as well as of trace amounts of chalcocite, covellite and bornite were estimated. The background minerals in the analysed sample were based on quartz-carbonate-silicate.

TABLE I. Chemical analysis of the ore samples

Constituents	Content / %					
	Size range / mm					
	-3+1	-5+0	-5+3	-10+5	-20+10	-20+0
Cu _{uk}	0.51	0.58	0.53	0.57	0.48	0.64
Cu _{ox}	0.007	0.01	0.013	0.009	0.019	0.027
Fe	4.00	3.92	4.60	3.67	3.84	3.93
S	5.18	5.57	5.09	5.76	4.80	3.74
CaO	4.31	6.3	4.59	5.25	5.52	5.94
MgO	1.56	1.69	1.70	1.67	1.48	1.76
SiO ₂	57.64	53.10	55.90	54.4	53.48	54.06
Al ₂ O ₃	12.48	12.97	13.19	12.71	12.05	12.89

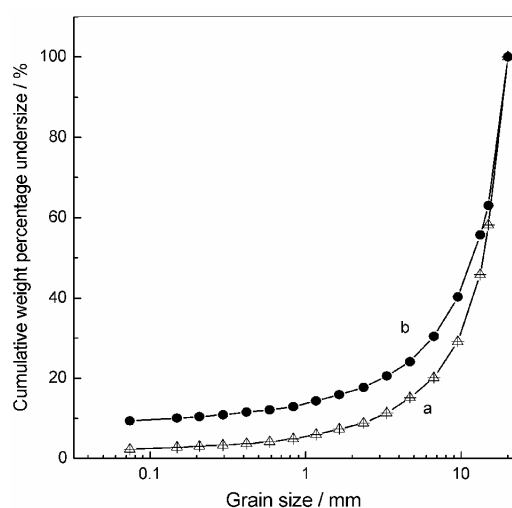


Fig. 1. Grain size distribution for the size range (-20+0) mm, a) untreated sample, b) treated sample.

Column leaching experiments

Dissolution of all the samples was carried out in PVC columns of, diameter 110 mm and height 1000 mm, using sulphuric acid solutions as the leaching solution. Eight kilograms of ore of a definite size range, (-3+1) mm, (-5+3) mm, (-5+0) mm, (-10+5) mm, (-20+10) mm or (-20+0) mm, was loaded into a column. A bed of silicon dioxide of about 1 cm thickness was layered over the ore in order to assure uniform distribution of the solution. Sulphuric acid solution of pH 1.0, at ratio of solid/liquid of 1:1, was used as the leaching solution. The pH values were adjusted by addition of sodium hydroxide, and the output solutions were re-circulated upon adjustment of the pH. The sulphuric acid consumption was calculated based on the sodium hydroxide consumption. At definite time intervals, 5 ml of leaching solution was taken and transferred into a 100 ml volumetric flask. The solutions were made up to a volume of 100 ml with distilled water and the amounts of copper and iron were measured using atomic absorption spectrophotometry (AAS). Aluminium and

silicon were measured by inductively coupled plasma–atomic emission spectroscopy (ICP–AES). Upon 90 days of leaching of following fractions: -20+10 mm, -20+0 mm and -5+3 mm, the contents of Ca and Mg were determined in the output leaching solutions by atomic absorption spectrophotometry (AAS).

The liquid flow rate through column was $3.3 \text{ cm}^3 \text{ min}^{-1}$. The all leaching experiments lasted three months under atmospheric conditions.

RESULTS AND DISCUSSION

Influence of grain size on the dissolution rate of chalcopyrite was analysed for six size fractions, *i.e.*, (-3+1) mm, (-5+3) mm, (-5+0) mm, (-10+5) mm, (-20+10) mm and (-20+0) mm). The results of the leaching experiments are presented in Figs. 2 – 7.

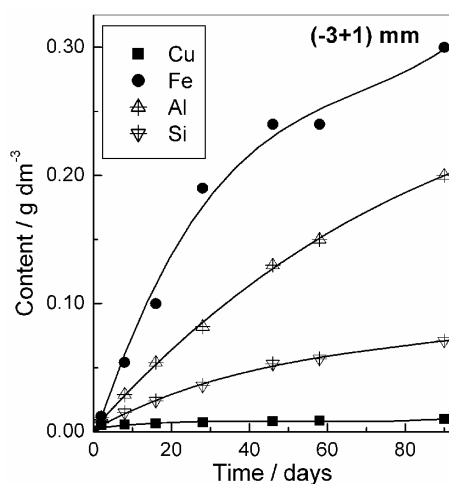


Fig. 2. Dependence of the concentrations of copper, iron, aluminium and silicon in the leaching solution on time after copper ore treatment with sulphuric acid (pH 1.0, S:L = 1:1) for the size range: (-3+1) mm.

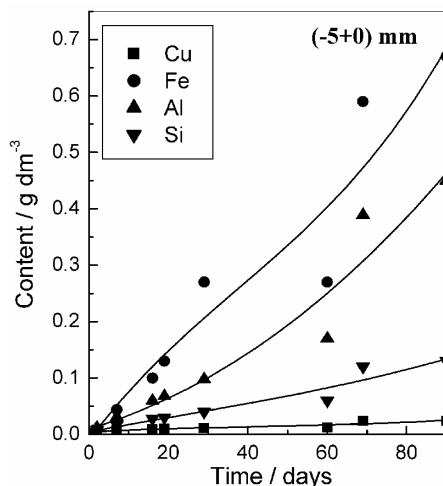


Fig. 3. Dependence of the concentrations of copper, iron, aluminium and silicon in the leaching solution on time after copper ore treatment with sulphuric acid (pH 1.0, S:L = 1:1) for the size range: (-5+0) mm.

From the dissolution curves (Figs. 2 – 7), it can be seen that concentration of the selected elements increased with time. The copper(II) concentration in these solutions after leaching for three months was in the range of $0.011 - 0.024 \text{ g dm}^{-3}$; iron, aluminium and silicon in the range $0.22 - 0.68 \text{ g dm}^{-3}$, $0.14 - 0.45 \text{ g dm}^{-3}$ and $0.039 - 0.13 \text{ g dm}^{-3}$, respectively. The calcium(II) concentration was in the range of $0.030 - 0.062 \text{ g dm}^{-3}$, and of magnesium $0.134 - 0.460 \text{ g dm}^{-3}$.

Low calcium concentration can be explained by the formation of sparingly soluble calcium sulphate.¹⁵ The experimental results show that the grain size of the ore, for these size ranges, had a minor influence on the dissolution rate. Also, the oxidation rate of chalcopyrite under these conditions was low, as shown by the low copper(II) ions concentration in the output solutions (Fig. 8).

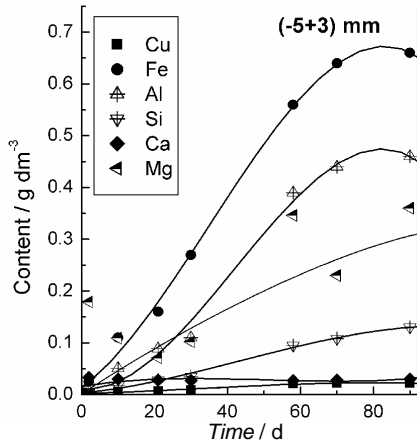


Fig. 4. Dependence of the concentrations of copper, iron, aluminium, silicon, calcium and magnesium on time after copper ore treatment with sulphuric acid (pH 1.0, S:L = 1:1) for the size range: (-5+3) mm.

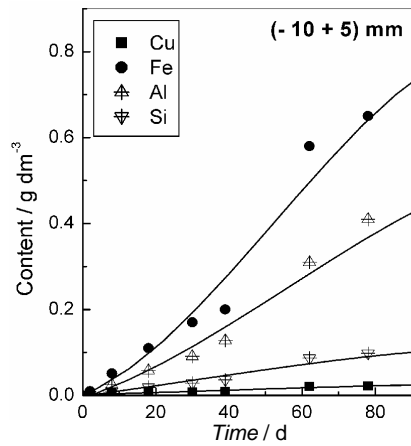


Fig. 5. Dependence of the concentrations of copper, iron, aluminium and silicon in the leaching solution on time after copper ore treatment with sulphuric acid (pH 1.0, S:L = 1:1) for the size range: (-10+5) mm.

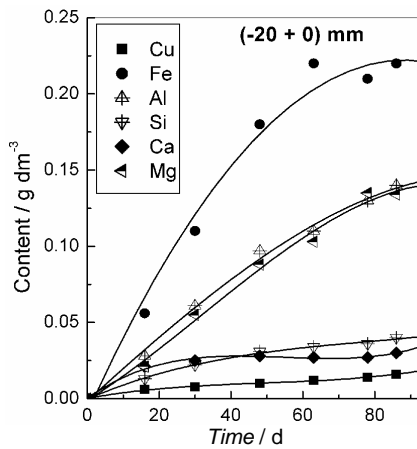


Fig. 6. Dependence of the concentrations of copper, iron, aluminium, silicon, calcium and magnesium on time after copper ore treatment with sulphuric acid (pH 1.0, S:L = 1:1) for the size range: (-20+0) mm.

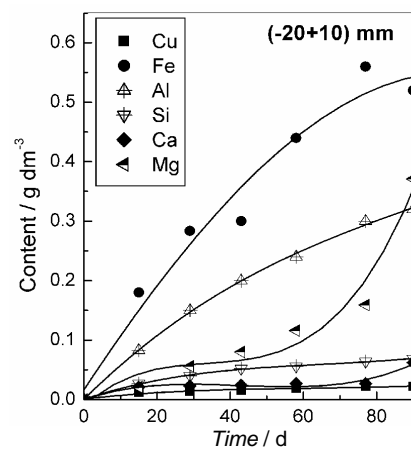


Fig. 7. Dependence of the concentrations of copper, iron, aluminium, silicon, calcium and magnesium on time after copper ore treatment with sulphuric acid (pH 1.0, S:L = 1:1) for the size range: (-20+10) mm.

Insignificant influence of grain size on the dissolution rate of chalcopyrite may be explained as follows: in the initial period of leaching, oxidation of chalcopyrite occurs on the surface of the ore grains. Due to the reaction between sulphuric acid and the matrix minerals, calcium ions are released, which react with the sulphate anions forming calcium sulphate (gypsum) as a precipitate. The

formation of this compound during leaching was confirmed by X-ray diffraction analysis of the solid residue (Fig. 9). Precipitate formation may occur when the formation front moves to the interior of the ore grains. Due to the large volume of the precipitate, small cracks form in the grain exposing new chalcopyrite surfaces. This phenomenon results in a comminution of the initial raw material during leaching, which may be seen from the curve of the grain size distribution of the solid residue (Fig. 1, curve b). Ritsema and Groenenberg³² in 1993 proposed that the following reaction occurs on limestone in acidic medium in the presence of iron(III) (during pyrite oxidation):

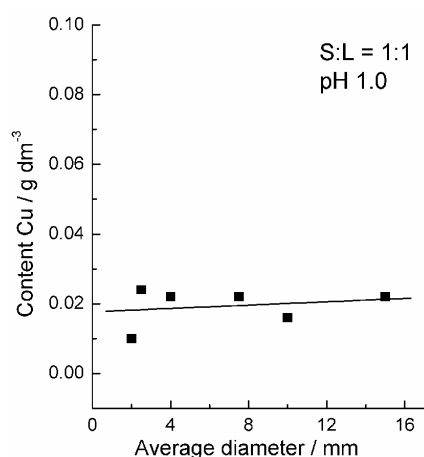
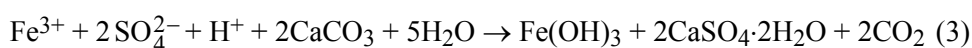


Fig. 8. Dependence of copper concentration on the average diameter of ore grains after leaching (pH 1.0, S:L = 1:1, leaching time: 90 days).

They found that carbonate particles become coated with gypsum and amorphous ferric oxyhydroxides are formed in reaction (3). Simon *et al.*³³ showed tabular crystals composed of S and Ca (gypsum), based on SEM-EDS analysis of the coatings. These facts are in accordance with the present results.

Mineralogical analysis showed that carbonate minerals existed in the initial raw material. These minerals react with sulphuric acid forming a porous layer, which enables contact of leaching solution with minerals in the grain interior. Auck and Wadsworth¹ found that, during acid leaching of copper ore, the copper leaching rate increases with decreasing ore grain size, but the leaching rate was not proportional to the reciprocal value of diameter. Lu *et al.*²² found that for chalcopyrite leaching particles of a various diameters in solutions of 0.8 M H₂SO₄ containing 1 M NaCl, identical copper concentrations were obtained in the solution after 9 h of leaching. A lack of dependence of the concentrations of leached ions on the size of the ore was also registered for other raw materials. For example, during the oxidation of As-bearing gold ore, it was found out that the grain size had no influence on the arsenic and iron concentrations in the leaching solutions.³³ The differences in behaviour are probably due to the variable composition of the ores.

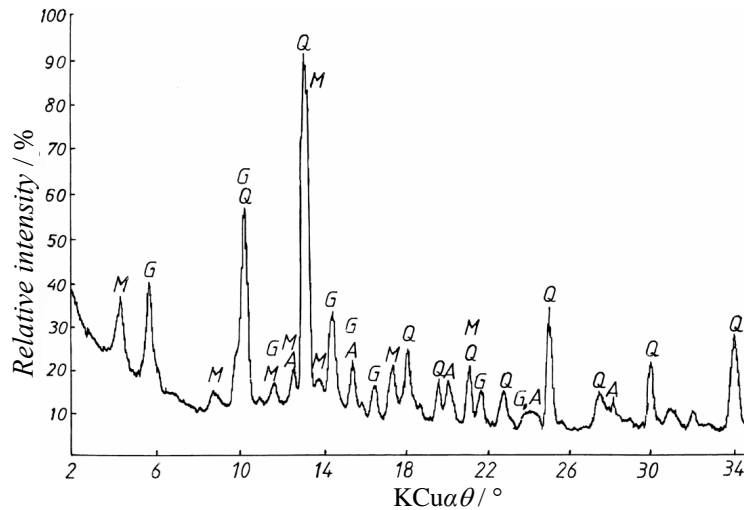


Fig. 9. X-Ray diffraction pattern of the residue after 90 days of leaching: gypsum (G), quartz (Q), anhydrite (A) and muscovite (M). Conditions: H_2SO_4 (pH 1.0), S:L = 1:1; for size range (-3+1) mm.

The ore grain size had a small influence on the consumption of acid. As seen in Table II, the acid consumption was in the range of $56 - 73 \text{ g kg}^{-1}$ ore, for various grain sizes. Ahonen and Tuovinen⁴ performed experiments of bacterial leaching of a complex sulphide ore containing chalcopyrite and obtained an average acid consumption of 43 g kg^{-1} ore.

TABLE II. Influence of grain size on the consumption of sulphuric acid (pH 1.0) after 90 days of leaching

Fraction / mm	-3+1	-5+0	-5+3	-10+5	-20+10	-20+0
Consumption / g kg^{-1} ore	73	65	67	56	57	61

Siliceous and aluminosiliceous minerals may be altered into other mineral forms during leaching.³⁵ Some siliceous minerals may be partly dissolved during long-term acid leaching experiments. Siliceous (Me_2SiO_4) leaching rates are much slower than those for carbonates, but their contribution to acid consumption may be important such as shown by the following reaction:



The experimentally determined acid consumption (Fig. 10 and Table II) show an increased acid consumption with time. This suggests that reactions between basic components and sulphuric acid are continuously contributing to the formation of leaching channels. This result leads to approximately equal leaching rates regardless of the ore grain size. Consumption of sulphuric acid is higher for the fractions (-3+1) mm, (-5+0) mm and (-5+3) mm than for the coarser fractions (-10+5) mm, (-20+10) mm and (-20+0) mm, Fig. 10.

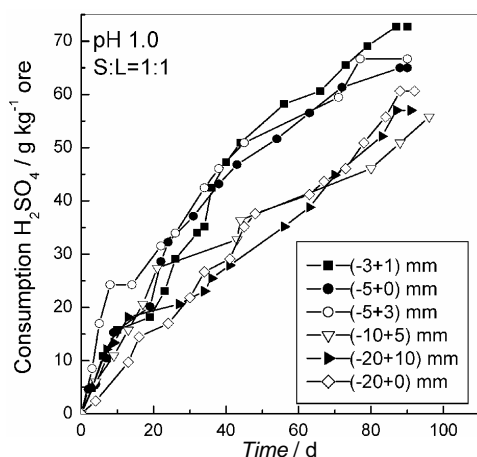


Fig. 10. Dependence of acid consumption on leaching time for various size ranges (pH 1.0, S:L = 1:1).

CONCLUSIONS

Based on experimental data, the following could be concluded:

1. Grain size of chalcopyrite ore has a minor influence on the leaching rate of this mineral in sulphuric acid solution.
2. The copper(II) concentration in the leaching solutions after leaching for three months is in the range of $0.011 - 0.024 \text{ g dm}^{-3}$. The concentrations of iron, aluminium and silicon are in the range of $0.22 - 0.68 \text{ g dm}^{-3}$, $0.14 - 0.45 \text{ g dm}^{-3}$ and $0.039 - 0.13 \text{ g dm}^{-3}$, respectively.
3. The formation of gypsum on limestone results in the comminution of the initial raw material during leaching.
4. A higher consumption of sulphuric acid was found for the fractions of $(-3+1)$, $(-5+0)$ and $(-5+3)$ mm than for the fractions $(-10+5)$, $(-20+10)$ and $(-20+0)$ mm, due to the presence of finer ore particles.

Acknowledgements: The authors are grateful to the Ministry of Science of Serbia for financial support (Project No: 142012).

ИЗВОД

УТИЦАЈ ВЕЛИЧИНЕ ЗРНА НА РАСТВОРАЊЕ ХАЛКОПИРИТНЕ РУДЕ У КИСЕЛОЈ СРЕДИНИ

М. М. АНТОНИЈЕВИЋ, Г. Д. БОГДАНОВИЋ, С. М. ШЕРБУЛА и С. М. МИЛИЋ

Универзитет у Београду, Технички факултет у Бору, бр. 50, 19210 Бор

У раду су приказани резултати лужења халкопиритне руде сумпорном киселином где су улогу оксиданаса имали растворени кисеоник и јони гвожђа(III). Испитивања су вршена у колонама од ПВЦ материјала пречника 110 mm и висине 1000 mm, перколацијом раствора кроз слој руде. Испитиван је утицај величине зрна руде на степен излужења и потрошњу киселине. У току лужења халкопиритне руде дешава се уситњавање полазне сировине услед грађења минерала гипса. Величина зрна руде халкопирита, у испитиваном опсегу крупноће, нема велики утицај на брзину лужења тог минерала у раствору сумпорне киселине. Нађено

je da je veća potrošnja sumporne kiseline za klase крупноће (−3+1), (−5+0) и (−5+3) mm него што je код klasa крупноће (−10+5), (−20+10) и (−20+0) mm.

(Примљено 3. октобра 2006, ревидирано 14. марта 2007)

REFERENCES

1. Y. T. Auck, M. E. Wadsworth, *International Symposium on Hydrometallurgy Chicago*, Illinois, February 25–March 1, The American Institute on Mining and Metallurgical and Petroleum Engineers, AIME, New York (1973) p.645
2. J. Frenay, P. Dufresne, *Acta Technica Belgica* **26** (1986)147
3. T. Brewis, *Mining Magazine* **173** (1995) 5
4. L. Ahonen, O. H. Tuovinen, *Hydrometallurgy* **37** (1995) 1
5. J. M. Casas, J. Martinez, L. Moreno, T. Vargas, *Metallurg. and Mater. Trans. B* **29** (1998) 899
6. H. Yuehua, Q. Guanzhou, W. Jun, W. Dianzuo, *Hydrometallurgy* **64** (2002) 81
7. S. Colak, M. Alkan, M. M. Kocakerim, *Hydrometallurgy* **18** (1987) 183
8. F. Habashi, *Chalcopyrite, Its Chemistry and Metallurgy*, McGraw Hill, London, 1978
9. T. Havlik, M. Skrobjan, *Canadian Metallurgical Quarterly* **29** (1990) 133
10. M. M. Antonijević, Z. Janković, M. Dimitrijević, *Hydrometallurgy* **35** (1994) 187
11. M. M. Antonijević, *J. Serb. Chem. Soc.* **60** (1995) 233
12. J. E. Dutrizac, R. J. C. MacDonald, *Canadian Metallurgical Quarterly* **12** (1973) 409
13. F. B. Mateos, I. P. Perez, F. C. Mora, *Hydrometallurgy* **19** (1987) 159
14. C. Klauber, A. Parker, W. Bronswijk, H. Watling, *Internat. J. Mineral Process.* **62** (2001) 65
15. M. M. Antonijević, G. D. Bogdanović, *Hydrometallurgy* **73** (2004) 245.
16. P. H. Yu, C. K. Hansen, M. E. Wadsworth, *International Symposium on Hydrometallurgy*, Chicago, Illinois, February 25–March 1. The American Institute on Mining and Metallurgical and Petroleum Engineers, AIME, New York (1973) p. 375
17. T. Biegler, D. A. Swift, *J. Appl. Electrochem.* **9** (1979) 545
18. A. Lopez-Juarez, N. Gutierrez-Arenas, R. E. Rivera-Santillan, *Hydrometallurgy* **83** (2006) 63
19. P. B. Munoz, J. D. Miller, M. E. Wadsworth, *Metallurg. Trans. B* **10** (1979) 149
20. J. E. Dutrizac, *Metallurg. Trans. B* **12** (1981) 371
21. R. P. Hackl, D. B. Dreisinger, E. Peters, J. A. King, *Hydrometallurgy* **39**(1995) 25
22. Z. Y. Lu, M. I. Jeffrey, F. Lawson, *Hydrometallurgy* **56** (2000) 189
23. B. P. Gantayat, P. C. Rath, R. K. Paramguru, S. B. Rao, *Metallurg. Mater. Trans. B* **31** (2000) 55
24. N. B. Devi, M. Madhuchanda, K. Rao Srinivasa, P. C. Rath, R. K. Paramguru, *Hydrometallurgy* **57** (2000) 57
25. E. Godocikova, P. Balaz, Z. Bastl, L. Brabec, *Appl. Surf. Sci.* **200** (2002) 36
26. A. Bruynesteyn, D. W. Duncan, *Medical Progress Through Technology, Solution Min. Symp. Proc. 103rd AIME Annu. Meet*, Feb. 25–27, Dallas, TX, USA (1974) p. 324
27. M. M. Antonijević, Z. D. Jankovic, M. D. Dimitrijevic, *Hydrometallurgy* **71** (2004) 329
28. C. Gomez, M. Figueroa, J. Munoz, M. L. Blazquez, A. Ballester, *Hydrometallurgy* **43** (1996) 331
29. N. Hiroyoshi, S. Kuroiwa, H. Miki, M. Tsunekawa, T. Hirajima, *Hydrometallurgy* **74** (2004) 103
30. Y. L. Mikhlin, Y. V. Tomashevich, I. P. Asanov, A. V. Okotrub, V. A. Varnek, D. V. Vyalikh, *Appl. Surf. Sci.* **225** (2004) 395
31. M. Farquhar, P. L. Wincott, R. A. Wogelius, D. J. Vaughan, *Appl. Surf. Sci.* **218** (2003) 34
32. C. J. Ritsema, J. E. Groenenberg, *Soil Sci. Soc. Am. J.* **57** (1993) 968
33. M. Simon, F. Martin, I. Garcia, P. Bouza, C. Dorrnsoro, J. Aguilar, *Environ. Pollut.* **135** (2005) 65
34. M. Mihaljevic, L. Sisir, V. Ettler, O. Sebek, J. Prusa, *J. Geochemic. Explor.* **81** (2004) 59
35. P. Oliva, B. Dupre, F. Martin, J. Viers, *Geochim. Cosmochim. Acta* **68** (2004) 2223.